

Institut für Neurowissenschaften  
der Technischen Universität München  
Klinikum rechts der Isar  
(Direktor: Univ.-Prof. Dr. A. Konnerth)

## **In Vivo Analysis of the Neuronal Calcium Signaling in the Developing Visual Cortex**

Ruxandra-Iulia Miloş

Vollständiger Abdruck der von der Fakultät für Medizin der Technischen Universität  
München zur Erlangung des akademischen Grades eines  
Doktors der Medizin  
genehmigten Dissertation.

Vorsitzender: Univ.-Prof. Dr. D. Neumeier

Prüfer der Dissertation:

1. Univ.-Prof. Dr. A. Konnerth
2. apl. Prof. Dr. Th. Kleppisch
3. apl. Prof. Dr. O. Garaschuk

Die Dissertation wurde am 22.01.2008 bei der Technischen Universität München  
eingereicht und durch die Fakultät für Medizin am 07.05.2008 angenommen.

Abstract (German)

## **In vivo Analyse neuronaler Kalziumsignal-Aktivität während der Frühentwicklung des visuellen Cortex**

Im visuellen Cortex der Maus wurden neuronale Kalziumsignale mittels der Zwei-Photonen Mikroskopie *in vivo* untersucht. Es wurden entweder kleinmolekulare, anorganische Kalzium-Indikatoren oder der genetisch-kodierte Kalzium-Biosensor CerTN-L15 eingesetzt. Acht Tage nach der Geburt (P8) wurden erstmals spontane Kalziumwellen beobachtet. Zum Zeitpunkt des Augenöffnens (P12-P14) änderte sich das Aktivitätsmuster zügig von unspezifisch-global zu spezifisch-karg. Ursache dafür war die Reifung der synaptischen Hemmung. Die Kalziumwellen erforderten die Aktivierung spannungsgesteuerter Natrium-Kanäle, aktive glutamaterge Synapsen und besonders die Aktivierung von NMDA-Rezeptorkanälen. Auch für die lichtevozierten Kalziumsignale waren die NMDA-Rezeptorkanäle von entscheidender Bedeutung. Die Ergebnisse dieser Untersuchungen enthüllen die wesentlichen kortikalen Aktivitätsmuster einer kritischen Phase der Frühentwicklung der Sehrinde.

Abstract (English)

## **In Vivo Analysis of the Neuronal Calcium Signaling in the Developing Visual Cortex**

Neuronal calcium ( $\text{Ca}^{2+}$ ) activity in the *in vivo* mouse visual cortex was studied by means of two-photon imaging. Signal reporters were either small molecule  $\text{Ca}^{2+}$  indicators or the genetically encoded  $\text{Ca}^{2+}$  biosensor CerTN-L15. The data revealed a novel type of large scale spontaneous  $\text{Ca}^{2+}$  waves, that emerged in the visual cortex around postnatal day 8 (P8). Around eye opening (P12-14) the pattern of  $\text{Ca}^{2+}$  waves changed from profuse to sparse in line with the development of GABAergic inhibition. The  $\text{Ca}^{2+}$  waves required activation of voltage-gated  $\text{Na}^+$  channels, glutamatergic synaptic transmission and, importantly, relied upon activation of NMDA receptor-channels. The activation of NMDA receptors was also essential for light-evoked  $\text{Ca}^{2+}$  signals. Taken together, the results reveal on the single-cell level the essential activity patterns during a critical phase in the development of the visual cortex.

## Contents

Abstract (German).....	2
Abstract (English).....	2
Contents.....	3
Abbreviations.....	6
<b>1. Introduction</b> .....	<b>8</b>
1.1. <i>In Vivo</i> Calcium Imaging in the Mammalian Brain.....	8
1.1.1. Goals.....	8
1.1.2. <i>In Vivo</i> Two-Photon Fluorescence Microscopy.....	9
1.1.2.1. Underlying Principle of Two-Photon Fluorescence Microscopy.....	9
1.1.2.2. A Two-Photon Microscope Setup.....	12
1.1.2.3. <i>In Vivo</i> Applications of Two-Photon Microscopy.....	14
1.1.3. <i>In Vivo</i> Labeling with Fluorescent Calcium Indicators.....	14
1.1.3.1. Different Classes of Fluorescent Calcium Indicators and Their <i>In Vivo</i> Brain Labeling Techniques.....	15
1.1.3.1.1. The Small Molecule Calcium Indicators (SMCIs).....	16
1.1.3.1.2. The Genetically Encoded Fluorescent Calcium Indicator Proteins (FCIPs).....	18
1.2. The Mouse Visual System.....	21
1.2.1. Architecture of the Mouse Visual System.....	22
1.2.2. Functional Properties of Neurons in the Mouse Visual Cortex.....	24
1.2.3. Patterns of Neuronal Activity and their Roles in the Developing Visual System.....	25
1.2.3.1. Patterns and Importance of Spontaneous Activity for the Visual System Development.....	26
1.2.3.2. Early Patterned Visual Experience and the Development of Visual System.....	29
<b>2. Aim of the Study</b> .....	<b>31</b>
<b>3. Methods</b> .....	<b>33</b>
3.1. Animals.....	33
3.2. Anesthesia.....	33
3.3. Surgical Procedure.....	34
3.4. <i>In Vivo</i> Loading of Cortical Cells with Small Molecule Fluorescent Calcium Indicator Dyes.....	36
3.5. <i>In Vivo</i> Two-Photon Calcium Imaging.....	39

3.6. <i>In Vivo</i> Application of Pharmacological Substances.....	40
3.7. Visual Stimulation.....	41
3.8. Identification of the Recording Position and Data Analysis.....	42
<b>4. Results</b>	<b>44</b>
4.1. Improvements of the Methodology for <i>In Vivo</i> Two-Photon Calcium Imaging in the Mammalian Brain.....	44
4.1.1. Progress in Imaging Neuronal Networks <i>In Vivo</i> Using Small Molecule Calcium Indicators.....	44
4.1.1.1. Cell Loading Using a Low Concentration of the Calcium Indicator Solution.....	46
4.1.1.2. <i>In Vivo</i> Monitoring of Cellular Calcium Signals from New Born to Aged Brain.....	48
4.1.1.3. Multicolor Imaging for Identification of Different Cell Types .....	49
4.1.2. <i>In Vivo</i> Imaging Using Genetically Encoded Fluorescent Calcium Indicator Proteins.....	51
4.1.2.1. <i>In Vivo</i> Two-Photon Imaging of CerTN-L15 Transgenic Mouse.....	51
4.1.2.2. <i>In Vivo</i> Calcium Measurements from Cell Somata and Spiny Dendrites in CerTN-L15 Transgenic Mouse.....	54
4.2. Spontaneous Network Activity in the Developing Visual Cortex .....	55
4.2.1. Emergence of Spontaneous Calcium Waves at the Beginning of the Second Postnatal Week.....	55
4.2.2. Mechanisms Underlying the Spontaneous Calcium Waves.....	61
4.2.2.1. Spontaneous Calcium Waves Require Firing of Action Potentials.....	61
4.2.2.2. <i>In Vivo</i> Spontaneous Calcium Waves Require Synaptic Glutamatergic Synaptic Transmission.....	63
4.2.2.3. The Spontaneous Calcium Waves Involve Postsynaptic AMPA Receptor Activation.....	64
4.2.2.4. NMDA Receptor-Channels Activation Play a Critical Role for the Spontaneous Calcium Waves.....	66
4.2.3. Attempts to Chronically Block the Spontaneous Calcium Waves.....	70
4.2.4. Global Nature of Cell Activation before Eye Opening.....	71
4.2.5. Switch from Global to Sparse Cellular Activation at Eye Opening.....	71
4.2.5.1. Mechanism Underlying the Sparsification of Spontaneous Neuronal Activity: Role of GABA <sub>A</sub> -Receptor Dependent Inhibition.....	74
4.2.5.2. Mechanism Underlying the Sparsification of Spontaneous Neuronal Activity: No Role for Visual Experience.....	77
4.3. Development of the Light Evoked Activity in the Mouse Visual Cortex.....	79
<b>5. Discussion</b>	<b>85</b>
5.1. New Applications of the Multi-Cell Bolus Loading Technique.....	85
5.2. Advances in Imaging Calcium Signals Using the New Genetically Encoded Fluorescent Calcium Biosensor CerTN-L15.....	88
5.3. Endogenous Network Activity in the Developing Visual Cortex.....	89
5.3.1. Patterns of Spontaneous Network Activity in the Developing Visual Cortex.....	90
5.3.2. Possible Physiological Function of the Spontaneous Calcium Waves .....	92
5.4. Maturation of Neuronal Responses to Light Stimulation in the Mouse Visual Cortex.....	94
<b>Bibliography</b> .....	<b>97</b>

<b>Appendix A: List of Publications and Original Papers</b> .....	111
<b>Appendix B: Curriculum Vitae</b> .....	135
<b>Acknowledgements</b> .....	136

## Abbreviations:

3D	three-dimension
ACSF	artificial cerebrospinal fluid
Alexa 594	Alexa 594 hydrazide sodium salt
AM	acetoxymethyl
AMPA	$\alpha$ -amino-3-hydroxyl-5-methyl-4-isoxazole-propionat
AP	action potential
APD	avalanche photo diodes
APV	D-2-amino-5-phosphonovaleric acid
BAPTA	1,2-bis-[2-aminophenoxy]ethane-N,N,N',N'-tetraacetic acid
BW	body weight
°C	grade Celsius
$[Ca^{2+}]_i$	intracellular free calcium concentration
$Ca^{2+}$	calcium
$CaCl_2$	calcium chloride
CaM	calmodulin
CFP	cyan fluorescent protein
CGP	(E)-( $\pm$ )-2-amino-4-methyl-5-phosphono-3-pentenoic acid
$Cl^-$	chloride
Cm	centimeter
CNQX	6-Cyano-7-nitroquinoxaline-2,3-dione
$CO_2$	carbon dioxide
dLGN	dorsal lateral geniculate nucleus
DMSO	dimethylsulfoxid
DR	dark rearing (more precisely mice reared in the dark)
EEG	electroencephalography
EGFP	enhanced green fluorescent protein
ENOs	early network oscillations
EYFP	enhanced yellow fluorescent protein
FCIP	genetically encoded fluorescent calcium indicator protein
fMRI	functional magnetic resonance imaging
FRET	fluorescent resonance energy transfer
Fsec	femtosecond
g	gram
GABA	$\gamma$ -aminobutyric acid
$GABA_A$	$\gamma$ -aminobutyric acid type A receptor
GFP	green fluorescence protein
GVD	group velocity dispersion
HEPES	4-(2-hydroxyethyl)-1-piperazineethanesulfonic acid
Hz	Hertz
$IP_3$	inositol 1, 4, 5-triphosphat
KCl	potassium chloride
kD	kilodalton

kg	kilogram
kW	kilowatt
MCBL	multi-cell bolus loading
mg	milligram
MgCl <sub>2</sub>	magnesium chloride
MHz	megahertz
min	minute
MK-801	(+)-5-methyl-10,11-dihydro-5H-dibenzo-[a,d]cyclohepten-5,10-imine hydrogen maleate
ml	milliliter
mm	millimeter
mM	millimolar
ms	millisecond
mW	milliwatt
MW	megawatt
MΩ	megaohm
n	number
NA	numerical aperture
nAChR	nicotinic acetylcholine receptor
NaCl	sodium chloride
NaH <sub>2</sub> PO <sub>4</sub>	sodium hydrogen phosphate
NaHCO <sub>3</sub>	sodium hydrogen carbonate
nm	nanomolar
NMDA	N-methyl-D-aspartate
NR	normal rearing (more precisely mice reared under normal lighting condition)
μl	microliter
μm	micrometer
μM	micromolar
O <sub>2</sub>	oxygen
OG-1 AM	Oregon Green 488 BAPTA-1 AM
P	postnatal day
PET	positron emission tomography
pH	
PMT	photomultiplier tubes
RGCs	retinal ganglion cells
S.D.	standard deviation
S.E.M.	standard error of mean
SMCI	small molecule calcium indicator
SR101	sulforhodamine 101
TnC	troponin C
TPLSFM	two-photon laser scanning fluorescence microscopy
TTX	tetrodotoxin
UV	ultraviolet
V1	primary visual cortex
YFP	yellow fluorescent protein
ΔF/F	the relative change in fluorescence over time
ΔR/R	ratio of Citrine/ Cerulean fluorescence

# Chapter 1

## Introduction

The focus of the work presented in this thesis was the analysis of *in vivo* calcium signaling in the developing visual cortex of rodents using calcium fluorescence markers and two-photon microscopy. The introductory chapter includes three sections which provide the basic information required for an understanding of the methods and the general approach. The first section outlines the principle, instrumentation and applications of two-photon microscopy, as well as the techniques used for *in vivo* labeling of neuronal tissue with fluorescence calcium indicators. Section two gives an overview of the anatomical and functional organization of the mouse visual system, while the final section provides a brief review on up to date data regarding the presence and significance of patterned activity in the developing visual system.

### 1.1. *In vivo* Calcium Imaging in the Mammalian Brain

#### 1.1.1. Goals

The brain is constantly active even in the absence of sensory information, exhibiting patterns of spontaneous activity that start before birth and last until death. Understanding the mechanisms that generate the spontaneous brain activity and its modulation by external sensory inputs is of critical importance in understanding information processing. The ideal approach to study brain activity are intact *in vivo* preparations, which preserve all the circuits that connect the different parts of the nervous system and maintain the integrity of the incoming sensory inputs, outgoing motor commands, and internal association processes. Brain activity depends both on the intrinsic electrophysiological properties of single neurons



(Llinas, 1988) and also on synaptic interactions in the neural networks (Steriade, 2000). On the other hand, there is a rich diversity of neuronal and glial cell types that serve different functions. Therefore, a comprehensive method appropriate to study the mechanisms governing brain activity demands the fulfilling of several conditions, such as the ability (i) to examine the intact, living, organism, (ii) to visualize and identify the cellular types involved in the process, (iii) to investigate their properties at single cell level and, if possible simultaneously, (iv) to analyze their involvement in the spatiotemporal pattern of neuronal networks dynamics.

So far, the function of large scale neuronal assemblies has been studied *in vivo* with different electrical and imaging techniques, including electroencephalography (EEG), functional magnetic resonance imaging (fMRI), positron emission tomography (PET), extracellular multielectrode recordings (Nicolelis and Ribeiro, 2002), intrinsic optical signal recordings (Grinvald et al., 1986; Bonhoeffer and Grinvald, 1991), and voltage-sensitive dye-based imaging (Orbach et al., 1985). However, these techniques do not allow recordings with single-cell resolution. A major step forward in overcoming this limitation was the development, more than a decade ago (Denk et al., 1990), of the two-photon laser scanning fluorescence microscopy (TPLSFM). Combined with *in vivo* fluorescence labeling techniques, TPLSFM has been proved to represent a powerful new technique for the visualization and investigation of the physiological processes that take place both at cellular and neural network levels in living animals.

## 1.1.2. *In Vivo* Two-Photon Fluorescence Microscopy

### 1.1.2.1. Underlying Principle of Two-Photon Fluorescence Microscopy

Fluorescence microscopy is based on the absorption of light with a specific wavelength by the molecules of a fluorescent marker (referred to also as fluorophore), followed by the emission of light with a longer wavelength (of a different color than the absorbed light). The absorption process or the excitation brings the fluorescent molecule from its electronic ground state to an excited electronic state (**Fig. 1**). Each of these electronic states is composed of a manifold of vibrational substates, which broadens the range of photon energies (wavelengths) that can cause this transition. An excited-state fluorescent molecule

quickly ends up in the lowest vibrational level of the excited electronic state, a process called internal conversion. Fluorescence is observed when a photon is emitted by the fluorescent molecule as it returns directly to the ground state. Excited-state lifetimes are usually in the nanoseconds range. Because of the energy loss that accompanies the initial internal conversion, fluorescence occurs at a lower photon energy (longer wavelength) than excitation (Lanni and Keller, 2000).

In traditional fluorescence microscopy techniques, including confocal microscopy, the elementary process involves the absorption of a single “blue” photon (also called linear absorption), which has high enough energy to bridge the gap between the ground and excited states of a fluorophore. In two-photon excitation, the quantum energies of two photons have to be combined quasi-simultaneously (within  $\sim 0.5$  fs, Helmchen and Denk, 2005) in order to promote an electronic transition that would otherwise require a single photon of approximately twice the energy. This is achieved with the use of near-infrared (red) photons that have double wavelength and half the energy of blue photons (**Fig. 1**).

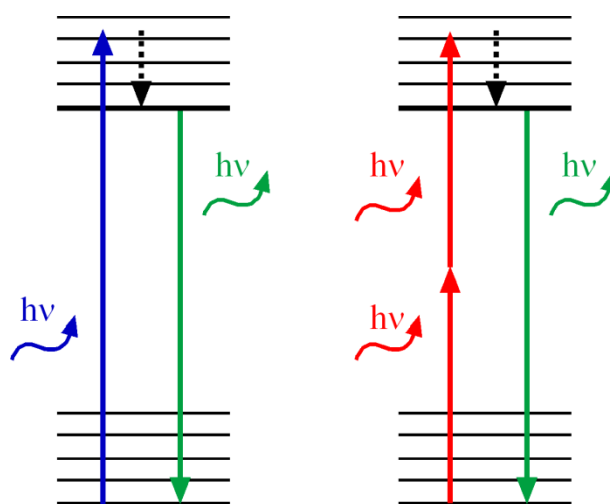


**Figure 1: Scheme of one-, respectively two-photon excitation.**

In one-photon microscopy a fluorophore is brought from its ground to the excited state by the absorption of a blue photon. The fluorophore relaxes down in the lowest vibrational level of the excited electronic state (internal conversion) and usually returns to the ground state by emission of one photon having a lower energy (longer wavelength, green) than the excitation photon. In two-photon microscopy, two red photons interact simultaneously with a fluorescent molecule to excite it and produce an electronic transition corresponding to twice the energy of the single photon. The emitted photon has now a higher energy than the absorbed ones and the excitation and emission wavelengths are typically separated by several 100 nm.

The rate of one photon absorption per fluorophore  $W_1$  is linearly related to the average photon flux density  $\langle \phi \rangle$  by the one-photon cross section  $\sigma$  (a measure of how efficiently the fluorophore converts excitation light to emitted fluorescence),  $W_1 = \sigma \langle \phi \rangle$ . The rate of two-photon absorption  $W_2$ , however, depends on the density of pairs of photons

and is thus proportional to the average squared photon flux density,  $W_2 = \sigma \langle \phi^2 \rangle$ . This requires that pairs of photons energies can combine only if these photons happen to pass through a small enough area within a small enough time (Williams et al., 1994). Therefore, the efficiency of two-photon absorption depends on the spatial and temporal distribution of the excitation light. High spatial density can be generated by focusing a laser beam through a high numerical aperture objective (Helmchen and Denk, 2005). Concentration in time is achieved by the use of “mode-locked” lasers that emit repetitive ultrashort pulses (in the femtoseconds range) that deliver the photons quasi-simultaneous. During the pulse a very high instantaneous power is produced (kW, MW) while the average power incident on the sample is low, only 1 Watt (Wise, 2000). Lasers used in TPLSM provide pulse length around 100 fsec and repetition rates of approximately 100MHz.

Living tissues are characterized by severe scattering due to inhomogeneities in the index of refraction present in the tissue (Denk and Svoboda, 1997). Scattering leads to degradation of the resolution and contrast and for traditional, including confocal, fluorescence microscopy it limits the possibility of high-resolution deep imaging within the tissue. Two-photon microscopy overcomes this limitation due to two unique properties of two-photon excitation. First, it has a highly localized fluorescence excitation that allows efficient fluorescence collection. Second, it uses longer excitation wavelengths (ranging between 700 to 1000 nm) that lead to better tissue penetration. Both these properties contribute to the ability of two-photon microscopy to provide high resolution images from up to 1 mm deep inside the living brain (Theer et al., 2003).

In one-photon microscopy, the excitation light has to reach the focus and on the way there it illuminates the entire thickness of the sample being examined, before the focal point and beyond, because most excitation light continues to propagate. On the other hand, two-photon absorption depends on the square of the density of photons, specifically of the illumination intensity. The consequence is that two-photon absorption is spatially confined only to the perifocal region, contrasting with one photon microscopy where the absorption occurs within the entire excitation cone (Denk et al., 1990). Absorption of excitation light can cause phototoxicity and photodamage of the tissue. The lack of out of focus excitation in two-photon microscopy increases the tissue viability and allows long time imaging (Williams et al., 1994).

In one-photon microscopy optical sectioning needed for obtaining resolution is based on the rejection, by a confocal pinhole, of all fluorescence light except for that coming from the focus, which means that approximately 99% of the generated fluorescence light is wasted

(Denk, 2000). Only the photons that have not been scattered on their way out of the tissue (ballistic photons) contribute to the signal, while the scattered photons, which form the majority, are rejected by the pinhole (Denk and Svoboda, 1997). Localization of the excitation renders another advantage to two-photon microscopy, namely it provides an optical sectioning effect (Denk et al., 1990), because fluorescence is generated only in the vicinity of the focus (called the focal volume, roughly 1 femtoliter) where the light intensity is high enough to excite the fluorophores. Scattered excitation photons are too dilute to excite, and they produce negligible background or photodamage. Therefore, in two-photon excitation there is almost a complete utilization of the excited fluorescence because only those fluorophores are excited from which one would collect the fluorescence.

### 1.1.2.2. A Two-Photon Microscope Setup

Two-photon microscopes are commercially available from several providers, but they could also be converted from already existing confocal systems (Majewska et al., 2000). The latter option require only the replacement of optics for adaptation to the different excitation wavelength of two-photon microscopy (Denk and Svoboda, 1997) and, since out of focus fluorescence is not a concern in two-photon microscopy, the confocal pinhole is no longer necessary. There are quite a few advantages for the custom-built systems, including price, the flexibility to choose the components specifically needed for the applications, and understanding of the complete system functioning (Majewska et al., 2000).

The main components of a two-photon microscope are the light source, scanning mirrors and optics, a fluorescence detector and a data acquisition system (**Fig. 2**). The light source is represented by “mode-locked” lasers, of which the most widely used is the Titanium-sapphire (Ti:sapphire) laser, because of the greatest performance in terms of power capability ( $\sim 1-5$  W), broad wavelength tunability (700-1100nm) and short pulse duration ( $\sim 100$ fs) (Wise, 2000). It has a repetition rate of  $\sim 100$  MHz that matches the nanoseconds fluorescence lifetime of the fluorophores (Helmchen and Denk, 2005). After the laser beam has traveled through the optical glass components of the microscope, the short pulses are longer at the sample due to group velocity dispersion (GVD). GVD is the result of the difference in propagation speed for wave packets of different wavelengths in different optical materials and results in decreased two-photon excitation efficiency (Denk, 2000). This can be compensated by a prism or grating arrangement (Soeller and Cannell, 1996) that restores the initial pulse width at the sample and optimize the two-photon absorption.

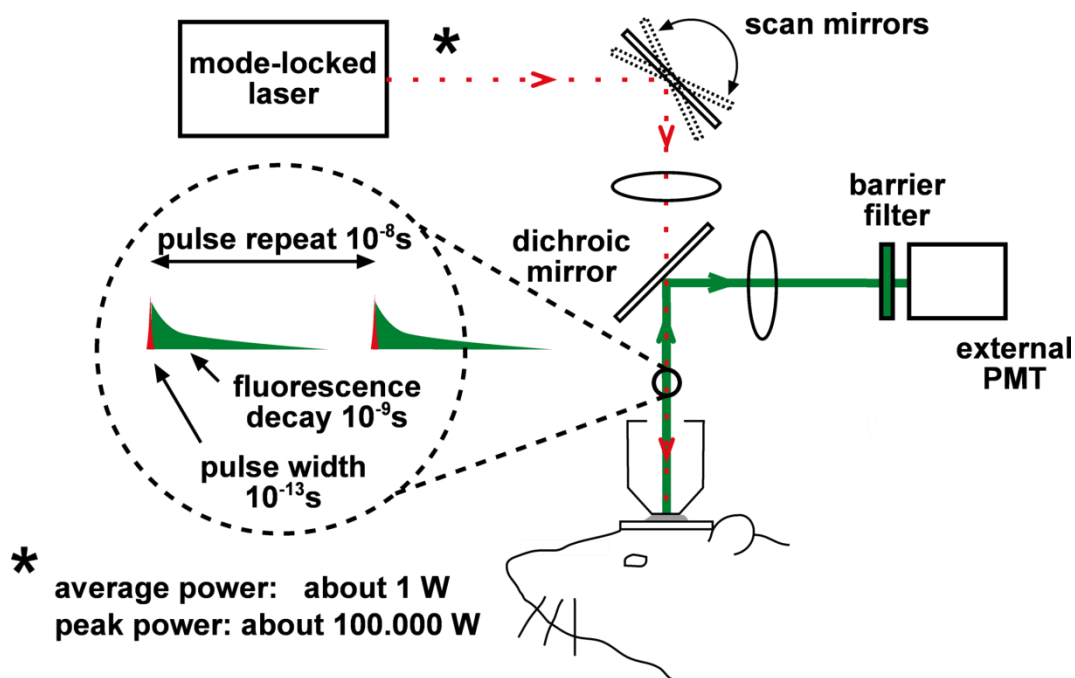


**Figure 2: Scheme of a two-photon microscope setup for *in vivo* experiments.**

A mode-locked laser provides the excitation light with wavelengths in the red portion of the spectrum in form of ultrashort pulses (the pulse width is 100fsec). The laser beam is guided to enter the objective and raster scanned across the specimen by scanning mirrors. Fluorescent light emitted by the sample is collected through the same objective, separated from the excitation light by a dichroic mirror and subsequently detected by an external PMT. For *in vivo* experiments the animal should be accommodated in the setup. modified from (Svoboda et al., 1997)

The scanning mirrors and the optics of the microscope that direct the excitation light to the sample are selected for high throughput in the infrared light. The excitation intensity can be adjusted by a laser intensity modulator (for example a Pockels cell). The laser beam is scanned usually by a pair of galvanometric scanning mirrors and further adjusted in order to fill the back aperture of the microscope objective, which focuses the light into the sample. The same objective collects the emitted fluorescence, which is further separated from the excitation light by a dichroic mirror, and then guided onto the detector, which can be either photomultiplier tubes (PMT) or avalanche photo diodes (APD). Because in the two-photon microscopy the emitted photons are generated only in the focus point, even the highly scattered signal photons carry useful information. Therefore, the whole-field detection is the preferred modality that enables the detection system to collect as many fluorescence photons emerging from the specimen as possible.

### 1.1.2.3. *In vivo* Applications of Two-Photon Microscopy

Based on its unique advantage of depth penetration and reduced photodamage, TPLSFM opened a new avenue for the *in vivo* analysis of different biological tissues. Its applicability expanded extremely fast to investigate the behavior of various tissues in their natural environment, like for example, lymph nodes (for review see (Cahalan and Parker, 2006; Cahalan et al., 2003)), kidney (Ashworth and Tanner, 2006; Ashworth et al., 2007), muscle (Rudolf et al., 2006), embryo (Squirrell et al., 1999), blood flow (Kleinfeld et al., 1998), and skin (Masters et al., 1998). Furthermore, TPLSFM was used *in vivo* to study the characteristics and possible treatment therapies for the development and progression of pathological processes, like tumors (Wessels et al., 2007; Boissonnas et al., 2007) and Alzheimer disease (Takano et al., 2007).

The emergence of TPLSFM contributed also substantially to the advances achieved in the investigation of the intact mammalian brain on the subcellular, cellular and network scale. Two-photon microscopy for the first time enabled *in vivo* recordings from subcellular compartments like dendrites of pyramidal neurons in anesthetized rats (Svoboda et al., 1997), deep layer cortical pyramidal neurons (Helmchen et al., 1999), as well as functional imaging from entire neuronal networks (Stosiek et al., 2003).

### 1.1.3. *In vivo* Labeling with Fluorescent Calcium Indicators

As a fluorescence imaging technique, TPLSM depends on suitable fluorescent labeling methods that would facilitate the visualization of the biological structures and monitoring of their function. A large number of fluorescent indicators have been developed for measuring different ion concentrations. Notably, a lot of effort has been invested to design calcium indicators because of the important role of calcium in cellular function and in particular in neuronal activity. Calcium ( $\text{Ca}^{2+}$ ) is one of the most important intracellular messengers in the brain. It is essentially involved in the mechanisms responsible for neuronal development, like neuronal migration (Komuro and Kumada, 2005), neurite outgrowth (Redmond et al., 2002; Konur and Ghosh, 2005; Lohmann et al., 2005), gene expression (Fields et al., 2005) and the regulation of various metabolic pathways.  $\text{Ca}^{2+}$  signaling is also indispensable for synaptic transmission (Evans and Zamponi, 2006) and plasticity (Liu and Zukin, 2007), processes responsible for the induction of memory and learning. Furthermore,

dysregulation of intracellular  $\text{Ca}^{2+}$  signaling is involved in many pathophysiological events, such as cell apoptosis and the pathogenesis of Alzheimer's (LaFerla, 2002), and Huntington (Bezprozvanny and Hayden, 2004) disease, or autism spectrum disorders (Krey and Dolmetsch, 2007).

Functional imaging of  $\text{Ca}^{2+}$  dynamics takes advantage of the properties of  $\text{Ca}^{2+}$  homeostasis inside brain cells. In resting conditions, the concentration of  $\text{Ca}^{2+}$  is very low inside the neuronal cells, typically 50-100 nanomolar, whereas the  $\text{Ca}^{2+}$  ions concentration outside cells is several orders of magnitude higher than inside, several millimolar in the bloodstream or cerebrospinal fluid (Purves, 2004). Upon depolarization, there is an intracellular  $\text{Ca}^{2+}$  influx, which is attributed to the activation of different types of voltage-gated  $\text{Ca}^{2+}$  channels and NMDA receptors present in the cellular membrane and abundantly expressed in the nervous system. This  $\text{Ca}^{2+}$  influx produces a transient rise in the cytoplasmic  $\text{Ca}^{2+}$  concentration, which can be further amplified by the release of  $\text{Ca}^{2+}$  from the intracellular stores, (e.g. the endoplasmic reticulum) through a process referred to as  $\text{Ca}^{2+}$  induced  $\text{Ca}^{2+}$  release. The fluorescence properties of  $\text{Ca}^{2+}$  indicators are sensitive to the intracellular free-  $\text{Ca}^{2+}$  concentration.

### 1.1.3.1 Different Classes of Fluorescent Calcium Indicators and Their *In Vivo* Brain Labeling Techniques

One class of  $\text{Ca}^{2+}$  indicators consist of a metal-binding site (or sensor) coupled to a fluorescent molecule. At present there is a wide variety of fluorescent  $\text{Ca}^{2+}$  indicators available that are classified into two categories: chemical  $\text{Ca}^{2+}$  indicators (or “dyes”) based on the  $\text{Ca}^{2+}$  specific chelator 1,2-bis-[2-aminophenoxy]ethane-N,N,N',N'-tetraacetic acid (BAPTA) (Tsien, 1989), and genetically encoded fluorescent  $\text{Ca}^{2+}$  indicator proteins (FCIPs), which use  $\text{Ca}^{2+}$  sensor proteins (Garaschuk et al., 2007). Indicators signal  $\text{Ca}^{2+}$  binding by generating changes in their fluorescence through mechanisms leading to the following three outcomes: (i) a shift in excitation and sometimes emission fluorescence peaks, (ii) changes in fluorescence intensities or (iii) changes in fluorescent resonance energy transfer (FRET) (Adams, 2000). The change in fluorescence upon  $\text{Ca}^{2+}$  binding is registered as a  $\text{Ca}^{2+}$  transient, which has a fast raise time, due to  $\text{Ca}^{2+}$  entering inside the cell through voltage-gated  $\text{Ca}^{2+}$  channels, and a slower decay time, due to  $\text{Ca}^{2+}$  removal from the cells by the  $\text{Ca}^{2+}$  pumps.

### 1.1.3.1.1 The Small Molecule Calcium Indicators (SMCIs)

The chemical  $\text{Ca}^{2+}$  indicators (also called small molecule  $\text{Ca}^{2+}$  indicators, SMCIs) are charged molecules that do not cross the cellular membranes and therefore require delivery into cells by microinjection. This problem was overcome by the synthesis of acetoxymethyl (AM) ester derivatives of these indicators (Tsien, 1981). This design masks the negative charges of the indicator with AM esters, which render the molecule lipophilic and membrane permeant, allowing the indicator to passively diffuse across the cell membrane inside the cell. Once inside the cells, the AM esters are cleaved by cytoplasmic esterases and the free indicator loses its lipophilicity and remains trapped inside the cell because it is once again charged. Thus, the indicator accumulates intracellularly at higher concentrations compared to the extracellularly residual AM ester (Yuste et al., 2000).

As already mentioned,  $\text{Ca}^{2+}$  indicators change their fluorescence with changes in the intracellular free calcium concentration,  $[\text{Ca}^{2+}]_i$ . There is a strong relationship between the electrical activity and the changes in  $[\text{Ca}^{2+}]_i$ , and subsequently, the changes in the fluorescence of the small molecule  $\text{Ca}^{2+}$  indicators (Yuste and Denk, 1995; Helmchen et al., 1996; Smetters et al., 1999; Mao et al., 2001). Therefore, labeling of neuronal cells with SMCIs provides a sensitive tool for real-time analysis of neuronal activity *in vivo* and the combination with the TPLSM enables deep imaging in the intact mammalian brain (Helmchen and Waters, 2002). To investigate the spatio-temporal neuronal  $[\text{Ca}^{2+}]_i$  dynamics different loading techniques evolved for *in vivo* delivery of the indicator molecules inside the brain cells.

The first method developed to label brain cells *in vivo* with SMCIs was the intracellular dye loading of individual neurons via sharp microelectrodes or patch pipettes (Svoboda et al., 1997; Helmchen et al., 1999; Svoboda et al., 1999), which were inserted at a shallow angle inside the brain. By using this approach simultaneous *in vivo* electrophysiological intracellular recordings and  $\text{Ca}^{2+}$  imaging were made possible. These studies measured the generation of  $\text{Ca}^{2+}$  transients in dendrites of neurons located either in layer 2/3 or in deep layer 5 in the barrel cortex during spontaneous and evoked action potential firing, as well as during sensory stimulations. A similar approach was used also for monitoring odor and action potential-dependent dendritic  $\text{Ca}^{2+}$  signals in mitral cells of the rat olfactory bulb (Charpak et al., 2001; Debarbieux et al., 2003).

However, this loading procedure restricts the *in vivo* high-resolution  $\text{Ca}^{2+}$  imaging to a single neuron at the time and therefore is not applicable for monitoring entire neuronal



networks. A versatile method was developed that circumvented this limitation and enabled *in vivo* simultaneous loading of large population of neuronal cells with SMCI (Stosiek et al., 2003; Garaschuk et al., 2006a). This method is termed multi-cell bolus loading (MCBL). It is based on targeted pressure ejection of a concentrated solution of the AM, membrane-permeant, form of  $\text{Ca}^{2+}$  indicators into the brain region of interest via a pipette inserted into the brain through a small skull craniotomy. It can be used for a large spectrum of indicator dyes, including Oregon Green 488 BAPTA-1 AM, Fura-2 AM, Fluo-4 AM, Indo-1 AM. This procedure enables the homogeneous staining of hundred of cells present in a brain region with a diameter of approximately 300  $\mu\text{m}$  (Stosiek et al., 2003). Due to its minimal invasive protocol, it is suited for real-time analysis of intact neuronal circuits with the resolution of single cells. For example, Göbel et al. reported recently the development of a new three-dimensional (3D) scanning technology for two-photon microscopy that allowed fast fluorescent measurements from several hundred cells distributed in 3D space and MCBL-loaded with the  $\text{Ca}^{2+}$  indicator Oregon Green 488 BAPTA-1 AM (Göbel et al., 2007). In the mammalian brain, MCBL was successfully applied to stain *in vivo* cortical cells in mouse (Stosiek et al., 2003; Nimmerjahn et al., 2004; Garaschuk et al., 2006a; Garaschuk et al., 2006b; Sohya et al., 2007;), rat (Nimmerjahn et al., 2004; Kerr et al., 2005; Ohki et al., 2005; Göbel et al., 2007), and cat (Ohki et al., 2005; Ohki et al., 2006), as well as cerebellar neurons (Sullivan et al., 2005).

Another approach for *in vivo*  $\text{Ca}^{2+}$  imaging from populations of cortical cells is represented by the topical application of the  $\text{Ca}^{2+}$  indicator Fluo-4 AM on the exposed surface of the brain with its subsequent diffusion into the cortex. By this method only glial cells are stained *in vivo* (Hirase et al., 2004; Takano et al., 2007), the investigation possibility being restricted only to the study of cortical astrocytic networks.

The latest reported method for loading of individual neurons and small neuronal networks *in vivo* with  $\text{Ca}^{2+}$  indicators is local electroporation (Nagayama et al., 2007; Nevian and Helmchen, 2007). Electroporation is based on the application of electric pulses that briefly disrupt the cell membrane and create pores that allow charged indicator molecules to enter inside the cells. This procedure enables  $\text{Ca}^{2+}$  imaging at neuronal population level and it also has an exquisite subcellular resolution down to dendritic spines and axonal boutons (Nagayama et al., 2007).

### 1.1.3.1.2. The Genetically Encoded Fluorescent Calcium Indicator Proteins (FCIPs)

The genetically encoded fluorescent  $\text{Ca}^{2+}$  indicator proteins (FCIPs) have been constructed by fusing fluorescent proteins to functional  $\text{Ca}^{2+}$  sensor proteins that are normally involved in physiological  $\text{Ca}^{2+}$  signaling. The probes are introduced into an intact organism by gene transfer techniques. The development of FCIPs followed two distinct strategies (Garaschuk et al., 2007; Griesbeck, 2004; Kotlikoff, 2007).

The first approach for engineering FCIPs was pioneered by the development of the so-called ‘cameleons’ (Miyawaki et al., 1997; Miyawaki et al., 1999), and was based on fluorescence resonance energy transfer (FRET) occurring between two different mutants of the green fluorescence protein (GFP). FRET is a quantum-mechanical phenomenon that occurs between a fluorescence donor and a fluorescence acceptor that are in molecular proximity of each other ( $<80 \text{ \AA}$  apart). The transfer of energy or FRET occurs from the excited state of the donor fluorophore to the ground state of the neighboring acceptor fluorophore. In order for FRET to take place the acceptor must absorb light at roughly the same wavelengths as the donor emits (Tsien, 2000; Zhang et al., 2002). In cameleons, the  $\text{Ca}^{2+}$  sensor protein calmodulin (CaM) and the calmodulin binding peptide M13 from myosin light chain kinase are sandwiched between cyan fluorescent protein (CFP) and yellow fluorescent protein (YFP) as donor and acceptor proteins. Binding of  $\text{Ca}^{2+}$  to CaM initiates an intramolecular interaction between CaM and M13 domains causing CaM to wrap around the M13. Thus the donor (CFP) and acceptor (YFP) fluorophores are brought together and the energy transfer between the two fluorescent proteins is enhanced. Therefore, cameleons react to increases in the intracellular  $\text{Ca}^{2+}$  concentration with increases in their FRET response. The readout of FRET, and subsequently of changes in intracellular  $\text{Ca}^{2+}$  concentration, is the ratio of acceptor to donor fluorescence. Because they allow emission ratioing, and hence, are less susceptible to movement artifacts, the FRET based indicators are well suited for *in vivo*  $\text{Ca}^{2+}$  imaging.

The second approach was to create single-fluorophore-based, non-ratiometric  $\text{Ca}^{2+}$  indicators (for detailed reviews about single-fluorophore  $\text{Ca}^{2+}$  indicators consult (Zhang et al., 2002; Kotlikoff, 2007). They exploited the property of GFP and its mutants to remain fluorescent despite a variety of circular permutations (in which the amino and carboxyl portions are interchanged and rejoined with a short spacer connecting the original termini) and insertions of foreign proteins at certain locations within the GFP (Baird et al., 1999). For

example, insertion of CaM within a yellow mutant (enhanced yellow fluorescent protein, EYFP) of GFP resulted in an indicator protein (named camgaroo1) whose fluorescence could be enhanced several fold upon  $\text{Ca}^{2+}$  binding and could be used to monitor cytosolic  $\text{Ca}^{2+}$  in single mammalian cells (Baird et al., 1999). Similar CaM and M13 grafts into circularly permuted GFPs yielded  $\text{Ca}^{2+}$  indicators known as pericams (Nagai et al., 2001) or GCaMPs (Nakai et al., 2001).

When transgenically expressed in organisms, the genetically encoded fluorescent  $\text{Ca}^{2+}$  indicators should avoid interfering with the biochemistry of the host cell and, likewise, the indicators should not be modified by the biochemical machinery of the host cell, so that they can report reliably. Most of the FCIPs rely on CaM as  $\text{Ca}^{2+}$  binding moiety. On the other side, CaM is an ubiquitous signaling protein that is highly regulated on many levels and activates numerous  $\text{Ca}^{2+}$ -dependent responses within cells (Griesbeck, 2004). These interferences could be responsible for the deficiencies of the CaM-based FCIPs when they were expressed in the central nervous system of transgenic animals, such as reduced dynamic range or lack of  $\text{Ca}^{2+}$  sensitivity (Nagai et al., 2004). This CaM-related impediment was overcome by the generation of a new family of ratiometric, FRET-based  $\text{Ca}^{2+}$  biosensors, which replaced CaM with variants of Troponin C, the specialized  $\text{Ca}^{2+}$  sensor protein from skeletal and cardiac muscle (Heim and Griesbeck, 2004; Mank et al., 2006; Heim et al., 2007). The only known function of Troponin C is to regulate muscle contraction. Therefore, Troponin C-based sensors have the potential to interfere minimally with the host cell biochemistry and to be more suited for transgenic expression in model organisms (Garaschuk et al., 2007).

The first successful attempt that allowed monitoring FCIP-mediated  $\text{Ca}^{2+}$  signals in the central nervous system of mammals *in vivo* was carried out by Hasan et al. (Hasan et al., 2004). They produced stable transgenic mouse lines with two different functional  $\text{Ca}^{2+}$  indicators, namely inverse pericam and camgaroo-2, under the control of the tetracycline-inducible promoter. FCIP-positive cells included, beside hippocampal and neocortical pyramidal cells, the main olfactory receptor neurons, the granule cells and a few mitral cells in the olfactory bulb. FCIP-mediated  $\text{Ca}^{2+}$  signals could be reliably detected in the olfactory bulb *in vivo*, allowing to construct maps of afferent glomerular activity. Each odor evoked a unique activity map, and odors known to evoke similar maps of glomerular afferent activity produced analog activity patterns in the transgenic mice (Hasan et al., 2004).

Another study that described functional *in vivo*  $\text{Ca}^{2+}$  measurements based on FCIPs in transgenic mice was reported by Diez-Garcia et al. (Diez-Garcia et al., 2007). The authors

generated transgenic mice expressing the single-fluorophore-based indicator protein GCaMP2 in cerebellar granule cells under the control of Kv3.1 potassium channel promoter (Diez-Garcia et al., 2005). This allowed imaging of parallel fiber activity transcranially *in vivo*.  $\text{Ca}^{2+}$  transients were induced by direct electrical stimulation in the molecular layer and could be measured from beams of parallel fibers through the skull of living mice. Thus, the potential of FCIPs for imaging activity from populations of neurons in living animals was confirmed. Nevertheless, in these studies FCIPs were used for large-scale mapping of electrically- and sensory-driven neuronal activity *in vivo*, but they could not report functional  $\text{Ca}^{2+}$  measurements at single cell or subcellular resolution.

Significant progress in this direction was achieved by the generation of a novel transgenic mouse line, constitutively expressing a Troponin C-based  $\text{Ca}^{2+}$  indicator, CerTN-L15 (Heim et al., 2007). The sensor protein had an increased brightness and was based on the FRET signals between the donor protein Cerulean and the acceptor protein Citrine (**Fig. 3**). It was exclusively expressed under the Thy-1 promoter in neurons in many major areas of the central nervous system. The onset of CerTN-L15 expression was around birth and remained stable for up to 11 months, the longest time point tested. CerTN-L15 enabled not only the *in vivo* visualization of individual layer 2/3 cortical neurons, their dendrites and dendritic spines, but it also allowed *in vivo* measurements of glutamate-evoked  $\text{Ca}^{2+}$  transients in somata and dendrites (results also presented in the Section 4.1.1.4. of this thesis).

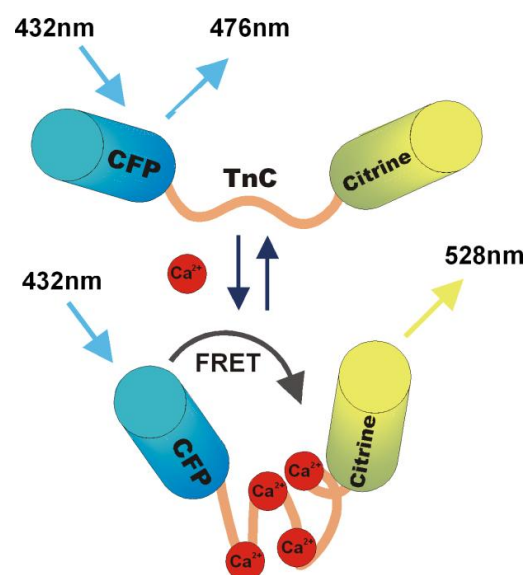


**Figure 3: Troponin C-based  $\text{Ca}^{2+}$  sensor proteins.**

Schematic representation of the FRET-based mechanism of sensor function. Troponin C is sandwiched between the donor protein (CFP or Cerulean) and the acceptor protein (Citrine). Upon  $\text{Ca}^{2+}$  binding, the molecule undergoes a conformational change that brings the donor and the acceptor proteins closer, thus enhancing FRET between the two fluorophores.

(taken from Garaschuk et al., 2007)

In comparison to SMCIIs, the use of FCIPs for *in vivo* monitoring of neuronal function presents several advantages (Miyawaki, 2005; Knöpfel et al., 2006), which include (i) targeted-expression to cell types or subcellular organelles of interest, (ii) ‘sparse’ labeling that provides imaging contrast necessary to study  $\text{Ca}^{2+}$  signals in dendrites and spines, (iii) the possibility for emission ratioing, being less susceptible to movements artifacts. Nevertheless, SMCIIs are still superior to FCIPs when  $\text{Ca}^{2+}$  sensitivity, dynamic range or response dynamics of the indicator are considered (Garaschuk et al., 2007).

In conclusion, the recent advances achieved in designing fluorescent  $\text{Ca}^{2+}$  indicators, paralleled by the technical development of two-photon fluorescent microscopy, significantly enlarged the resources for *in vivo* brain imaging. On one side the use of SMCIIs enabled (i) *in vivo* visualization of single cells and their processes down to a millimeter below the brain surface (Theer et al., 2003), (ii) *in vivo* recordings from subcellular compartments like dendrites of pyramidal neurons (Svoboda et al., 1997), (iii) two- and three-dimensional imaging of cortical network activity with single-cell resolution (Stosiek et al., 2003; Garaschuk et al., 2006a; Göbel et al., 2007), (iv) recordings from unanesthetized, behaving animals (Adelsberger et al., 2005). In addition, FCIPs facilitated specific neuronal labeling that was expressed throughout the entire lifetime of the animals, and the possibility of *in vivo*  $\text{Ca}^{2+}$  imaging with single-cell and even subcellular resolution (Heim et al., 2007).

## 1.2. The Mouse Visual System

Over the past years, the visual system of the mouse has gained increased attention for the neurophysiologists due to the development of transgenic mouse technology (Hübener, 2003), the mouse being currently the only mammal in which manipulations of specific genes are performed routinely. Gene technology allows assessing the involvement of specific genes and proteins in the function, development and plasticity of the visual system. It was also shown that the cells in the mouse visual cortex exhibit the presence of all the major functional properties that have been described in higher mammals, such as cats or monkeys. Taken together, these aspects render the mouse visual system a valuable model system for studies that aim to understand the mechanisms governing visual perception and integration.

### 1.2.1 Architecture of the Mouse Visual System

In the visual system, the main pathway leading from the retina (which contains the photoreceptors) to the cortex (where visual information is perceived and processed) is arranged in a relatively straightforward fashion and it has been intensively studied both anatomically and physiologically. Visual information is transmitted from the retina to the dorsal lateral geniculate nucleus (dLGN) of the thalamus and from here to the primary visual cortex (also called striate cortex, area 17 or V1) in the occipital lobe. Outside the striate cortex there exists also a set of visually responsive regions, generally termed extrastriate areas. Another target of the retinal input is the superior colliculus.

**Fig. 4** illustrates schematically the mouse visual system. The eyes are laterally positioned in mice, and hence, the binocular field of vision is relatively small, being larger in the upper than in the lower half of the visual field (Dräger, 1975). Only the central 30-40° of the upper portion of each visual hemifield is seen by the retinas of both eyes (Wagor et al., 1980; Gordon and Stryker, 1996). The axons of the ganglion cells leave the retina and form the optic nerves that join at the optic chiasm. In mouse, about 90% of the ganglion cells axons decussate at the optic chiasm and proceed into the contralateral optic tract, while the remaining axons continue in the ipsilateral tract. The visual system of the mouse is thus, essentially crossed (Valverde, 1968).

Retinal ganglion cell axons from the two eyes project into distinct eye-specific regions in dLGN (Godement et al., 1984; Hübener, 2003; Jaubert-Miazza et al., 2005). The eye-specific regions emerge from an initially overlapping distribution of ipsilateral and contralateral projecting retinal ganglion cell axons that last during the first postnatal week (Godement et al., 1984). These initially diffuse retinal projections retract and segregate to form eye-specific regions, process which is completed by the time of natural eye-opening at postnatal day 12-14 (P12-14) (Jaubert-Miazza et al., 2005). From the dLGN the fibers of the optic radiation proceed rostralward to bend immediately dorsalward entering the internal capsule and continuing dorsomedially in the white matter to end massively in layer 4 or lamina granularis of the primary visual cortex of the mouse (Valverde, 1968).

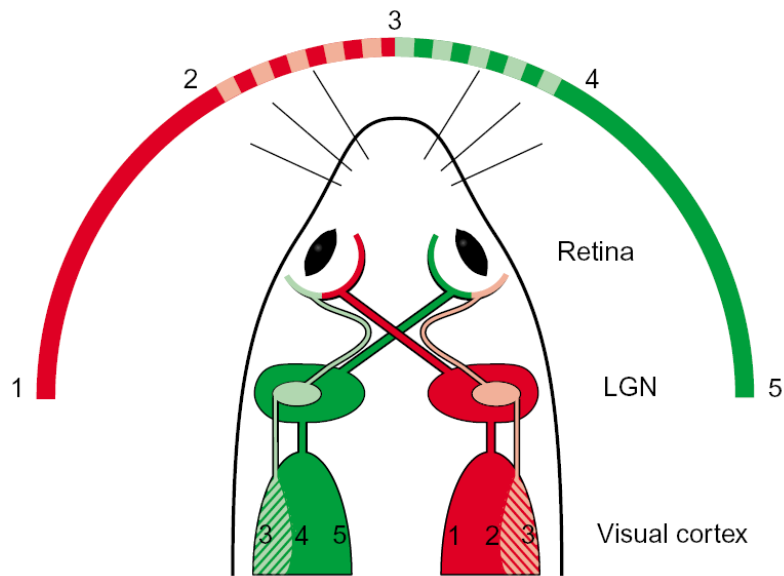


**Figure 4: Scheme of the mouse visual system.**

The extent of the visual field seen by both retinas of the mouse comprises the central 30-40°. The retinal ganglion cells from the most temporal region of each retina (marked with light red and green colors) project their axons to a small eye-specific region of the dLGN on the same hemisphere. The majority of retinal ganglion cell axons (approximately 90%) cross to the other hemisphere at the optic chiasm and project to the contralateral dLGN. The geniculocortical afferents carrying information from both eyes project to the lateral one third of the primary visual cortex in the binocular zone. taken from (Hübener, 2003)

The mouse primary visual cortex contains a complete and continuous retinotopic map of the visual field. The retinotopic map is arranged such that the upper visual field is projected posterior, while the nasal part is mapped onto the lateral border of the primary visual cortex (Dräger, 1975; Schuett et al., 2002). Geniculocortical projections carrying information from both eyes converge in the lateral one third of the primary visual cortex (Dräger, 1975) in the ‘binocular zone’. In this region the majority of neurons (around 70%) usually respond to inputs from both eyes, but overall there is a strong dominance of the contralateral eye, only 5% of the cells being exclusively driven by the ipsilateral eye (Dräger, 1975; Metin et al., 1988; Gordon and Stryker, 1996). By transneuronal labeling it was showed that in mice the bulk of the geniculocortical projections is confined to the primary visual cortex and it does not invade the surrounding extrastriate areas (Antonini et al., 1999).

## 1.2.2 Functional Properties of Neurons in the Mouse Visual Cortex

The functional analysis of the neurons in the mouse primary visual cortex revealed that they possess all of the major receptive field properties described previously in higher mammals such as cats (Hubel and Wiesel, 1959, 1962) or monkeys (Hubel and Wiesel, 1968). Electrophysiological investigations (Dräger, 1975; Mangini and Pearlman, 1980; Metin et al., 1988) showed that many neurons are orientation selective (around 40% of the total sampled cells), i.e. they respond best to stimuli (bars) presented at a particular orientation within the cell's receptive field. A fraction of the oriented cells show also direction selectivity, responding stronger to a bar (or spot) moving in one direction perpendicular to the preferred orientation (Dräger, 1975; Metin et al., 1988). The cells with oriented receptive fields were recorded mostly in the upper part of cortical layer 2/3, while direction selectivity was a property equally widespread in the supra- and infragranular layers, but less common in layer 4 (Metin et al., 1988). For the non-oriented cells different criteria and classifications were used, and therefore they do not represent a homogenous group.

It was also shown that the mouse brain is able to undergo plastic changes similar to those of higher mammals. One of the most used manipulations to induce cortical plasticity is monocular deprivation, during which a single eye is sutured and closed and the other eye remains open. After few days of monocular deprivation there is an increase in the number of individual neurons in the primary visual cortex that respond preferentially to the open eye in comparison to the number of neurons that respond to the deprived eye (Wiesel and Hubel, 1963). These readjustments occur during a relatively short time window in early postnatal life called critical period. In mice monocular deprivation results also in a shift of the ocular dominance distribution of cortical neurons located in the binocular zone, that is strongest at P28 (Gordon and Stryker, 1996). These physiological changes are followed also by anatomical rearrangements that consist in growth arrest of the geniculocortical afferents from the closed eye and expansion of the ones belonging to the open eye (Antonini et al., 1999). Recent studies on transgenic mice have provided strong evidence that the beginning of the critical period for monocular deprivation is triggered as soon as the inhibitory circuits in the visual cortex are mature enough to provide a certain level of inhibition (Hensch, 2005).

Besides the similarity, there are also differences between cat or monkey and mouse neurons in the primary visual cortex. One of those is the difference in the receptive field size. The average receptive field diameter for the mouse is around 14° (Metin et al., 1988), in contrast to around one degree in the cat and below one degree in the macaque. In addition,



many cells in the mouse visual cortex can be activated by stimuli placed anywhere in a region half the size of one hemifield (Hübener, 2003). In higher mammals, such as cats (Hubel and Wiesel, 1962) or monkeys (Hubel and Wiesel, 1968, 1969), a characteristic of the functional architecture of the visual cortex is that cells are organized in columns extending vertically from surface to the white matter. These columns are based on the response properties of the cells, like orientation preference or ocular dominance. In mice, neither anatomical studies based on transneuronal labeling after tracer injections into the eye (Antonini et al., 1999), nor functional studies like optical imaging of intrinsic signals (Schuett et al., 2002) were able to detect such structures in the mouse visual cortex. Nevertheless, the appearance of some cellular clustering has been remarked, both for orientation selective cells, as well as for ocular dominance (Dräger, 1975; Metin et al., 1988).

### 1.2.3. Patterns of Neuronal Activity and their Roles in the Developing Visual System

One of the most intriguing issues in the development of the visual system is the role and balance between innate, genetic factors (nature) and adaptation to early experience (nurture) in the establishment of the neuronal circuits. Most of the activity-dependent hypothesis of circuits formation have been based on Hebb's postulate which states that synapses are strengthened when pre- and post-synaptic cells are simultaneously active ("Neurons that fire together wire together"). Hebb's postulate has been expanded to include the converse: asynchronously active synapses are weakened and eventually eliminated (Torborg and Feller, 2005). Models based on Hebb's postulate predict that activity plays an "instructive role", meaning that the information required to drive the refinement of neuronal circuits is contained in the activity patterns (Torborg and Feller, 2005). In this context, one area of investigation has concentrated on the role of correlated, synchronous neuronal activity, patterned either by intrinsic mechanisms or by early sensory experience, for neuronal circuit formation and refinement.

### 1.2.3.1. Patterns and Importance of Spontaneous Activity for the Visual System Development

In the visual system, several features of visual cortical functional architecture, such as orientation tuning and ocular dominance columns are present even before any visual experience has occurred (Chapman and Stryker, 1993; Chapman et al., 1996; Horton and Hocking, 1996; Chapman et al., 1999; Weliky, 1999). It has been proposed that internally generated spontaneous correlated activity, a hallmark of the developing neural networks (Ben-Ari, 2001), may replace sensory-evoked activity in the initial steps of cortical circuits formation and maturation during the early stages of development (Katz and Shatz, 1996; McCormick, 1999; Sur et al., 1999; Weliky, 1999, 2000). Therefore, a lot of effort has been invested in characterizing the spatio-temporal patterns and the role of neuronal spontaneous activity within the different levels of the developing visual pathway.

One well-described example of how endogenous activity can shape circuits organization in the early stages of the visual system development is represented by the spontaneously generated waves of activity present in the immature, light-insensitive mammalian retina (for review see Wong, 1999; Torborg and Feller, 2005). Several weeks before eye-opening and even before maturation of the photoreceptors, retinal ganglion cells (RGCs) spontaneously fire periodic bursts of action potentials, which were first observed *in vivo* in the fetal rat retina (Galli and Maffei, 1988; Maffei and Galli-Resta, 1990). The synchronous bursts last a few seconds and are separated by 1 to 2 minutes of silence (Meister et al., 1991). Simultaneous recordings *in vitro* from large populations of RGCs and amacrine cells (Meister et al., 1991; Wong et al., 1993; Wong et al., 1995) revealed that these bursts are correlated among neighboring cells. They generate waves sweeping across restricted retinal domains of activity (Feller et al., 1996). The domain boundaries alter with time, which implies that there are no pacemaker regions and that all regions can participate equally (Feller et al., 1996).

Intriguingly, the fine structure of waves and their underlying mechanisms alter with maturation. In mice retinal waves develop through three distinct stages, as assessed by  $\text{Ca}^{2+}$  imaging (Bansal et al., 2000). First, between embryonic day 16 and birth, large propagating waves sensitive to nicotinic acetylcholine receptor (nAChR) antagonists were detected together with nonpropagated, nAChR-independent,  $\text{Ca}^{2+}$  oscillations displayed by small clusters of cells. Second, between P0 and P11, only large propagating waves that were abolished by toxins specific to  $\alpha 3$  and  $\beta 2$  subunit-containing nAChR were detected. Third,

between P11 and P14, the propagating activity was abolished by ionotropic glutamate receptor antagonists.

Retinal waves exist only during a specific period of development and in mice it has been demonstrated that they begin to break down shortly after eye opening, around P15. By P21 waves have already disappeared (Demas et al., 2003). They are present throughout the period during which the RGC axon terminals are refined both according to eye preference and topographic position within their target structures. Modulations of retinal waves during the first postnatal week result in alteration of retinal projections to their subcortical targets, suggesting an instructive role for the correlated retinal activity in the development of retinogeniculate connectivity. Using an *in vitro* preparation in which the mouse visual system from the retina to the dLGN remained intact, Mooney et al. demonstrated that spontaneous retinal activity is transmitted via the optic nerve to the dLGN, where it drives bursts of activity (Mooney et al., 1996). Furthermore, mice lacking the  $\beta 2$  subunit of the nAChR ( $\beta 2^{-/-}$  mice) have no retinal waves (Bansal et al., 2000), but have maintained uncorrelated firing of individual retinal ganglion cells (McLaughlin et al., 2003) for the first postnatal week. In these mice retinogeniculate axons fail to segregate into the normal eye-specific areas in the dLGN (Rossi et al., 2001; Muir-Robinson et al., 2002). The correlated spontaneous retinal waves are also necessary for retinotopic map refinement in the superior colliculus (McLaughlin et al., 2003; Chandrasekaran et al., 2005; Mrcic-Flogel et al., 2005). Also the higher relays in the visual pathway, the thalamocortical connections, are affected when the waves of spontaneous activity in the retina are disrupted genetically or pharmacologically during the first postnatal week (Cang et al., 2005). Using optical imaging and microelectrode recording, Cang et al. demonstrated that in the  $\beta 2^{-/-}$  mice the anatomical mapping of geniculocortical projections is imprecise and cortical retinotopic maps are functionally defective.

These findings raised the question if retinal waves are transmitted to and trigger activity in the developing visual cortex. Using simultaneous recordings from the rat retina and visual cortex during the first postnatal week *in vivo*, Hanganu et al. found that spontaneous retinal bursts are correlated with bursts in the contralateral visual cortex (Hanganu et al., 2006). However, blocking propagation of retinal activity or removing the retina only reduced the frequency, but did not completely eliminate the cortical bursts. Experiments using mono- and binocular enucleation during early ferret development also suggest that retinal input may not be needed for the initial establishment of ocular dominance columns (Crowley and Katz, 1999, 2000). Hence, the eventual patterns of spontaneous activity that underlie the

development of visual cortical functional architecture may differ from those predicted only by retinal activity alone (Weliky and Katz, 1999).

In parallel to the “bottom-up” type of retinal activity influences on the developing of the higher stations in the visual system, there is also growing evidence that suggests that “top-down” cortical influences are crucial in regulating the spontaneous activity in the thalamus and the organization of visual cortical functional architecture. For example, multielectrode recordings in the developing dLGN of ferrets *in vivo* demonstrated that prior to eye opening, synchronous bursts of action potentials are produced within all dLGN layers. By consecutive removal of the ipsilateral visual cortex and of the retinal drive, it was proved that the cortico-thalamic feedback is required for the generation of the correlated activity between the different eye-specific dLGN layers and for sustaining the intrinsic synchronized dLGN oscillatory activity *in vivo* (Weliky, 1999; Weliky and Katz, 1999). Moreover, silencing cortical activity with tetrodotoxin infusion (i) alters the pattern and precision of the geniculocortical projections (Catalano and Shatz, 1998), (ii) blocks the normal development of orientation selective responses (Chapman and Stryker, 1993) or (iii) the development of horizontal connections between cells with similar preferred orientation (Ruthazer and Stryker, 1996) in the visual cortex.

In comparison to the wealth of data regarding the retinal activity, little is known about the *in vivo* patterns of spontaneous activity at early and late developmental ages and their roles in the developing visual cortex. The majority of data concerning the activity in the neonatal cortex were provided by *in vitro* studies. Different patterns of correlated activity have been described, either by using electrical or optical recordings with  $\text{Ca}^{2+}$  sensitive indicators: (i) “neuronal domains” (Yuste et al, 1992; Yuste et al., 1995; Kandler and Katz, 1995, 1998), (ii) “early network oscillations”, ENOs (Garaschuk et al., 2000), (iii) carbachol-induced slow calcium waves (Peinado, 2000) and beta network oscillations (Dupont et al., 2006). The mechanisms underlying these spontaneous cortical activities are significantly distinct, and include: (i) activation of metabotropic glutamate receptors followed by inositol triphosphate ( $\text{IP}_3$ )-dependent  $\text{Ca}^{2+}$  release from intracellular stores and communication via gap junctions (Yuste et al., 1992; Yuste et al., 1995; Kandler and Katz, 1995, 1998), (ii) synaptic transmission through activation of glutamatergic receptors and excitatory GABAergic mechanisms (Garaschuk et al., 2000), (iii),  $\text{Ca}^{2+}$  influx during electrical activity (Corlew et al., 2004), (iv) developmental switch from a subplate-driven, gap-junction coupled synchronized oscillatory activity to a synaptic network acting through NMDA receptors (Dupont et al., 2006). The complexity of neocortical *in vitro* patterns is probably explained by

the diversity of experimental conditions and by age and region differences. Hence, the following question arises: do any of these *in vitro* patterns of endogenous activity in the maturing neocortex resemble the *in vivo* patterns?

*In vivo*  $\text{Ca}^{2+}$  imaging in non-anesthetized mice pups (P3-P4) showed spontaneous, periodically recurring cortical  $\text{Ca}^{2+}$  waves that reflect the correlated activity of thousands of neurons (Adelsberger et al., 2005). These  $\text{Ca}^{2+}$  waves were strongly reminiscent of the ENOs described previously in cortical slices from newborn rats and mice (Garaschuk et al., 2000). This form of spontaneous cortical activity was detected in rodents at embryonic day 16 (Corlew et al., 2004) and persisted approximately until the end of the first postnatal week, during the period at which GABAergic transmission is depolarizing (Garaschuk et al., 2000). The surgical separation of the cortex from the thalamus in slice recordings did not alter the  $\text{Ca}^{2+}$  waves significantly, indicating that they result from intrinsic cortical activity.  $\text{Ca}^{2+}$  waves were expressed primarily during sleep-like resting states and vanished or became inhibited during the animal's movement or under anesthesia (Adelsberger et al., 2005).

Later in development, the adult neocortex is characterized by slow recurring (0.2-0.5 Hz) oscillations composed of a depolarized state (Up) and a hyperpolarized state (Down) (Steriade et al., 1993). These Up-Down fluctuations were observed spontaneously during anesthesia (Steriade et al., 1993; Lampl et al., 1999; Petersen et al., 2003; Kerr et al., 2005), sleep (Steriade and Timofeev, 2003), and quiet wakefulness (Petersen et al., 2003). Analysis of the spiking activity during the spontaneous Up state revealed that spiking is sparse and heterogeneously distributed across neuronal populations (Margrie et al., 2002; Petersen et al., 2003; Kerr et al., 2005). After eye-opening, the spontaneous cortical activity was proved to have an essential role for the integration of stimulus-evoked sensory information through various mechanisms (Anderson et al., 2000; Kenet et al., 2003), including the action of Up-Down states on neuronal firing probability (Petersen et al., 2003; Hasenstaub et al., 2007). However, when or through which mechanisms the early synchronized activity detected at earlier stages of development in the neocortex changes into the sparse activity at the later stages is not known.

### 1.2.3.2. Early Patterned Visual Experience and the Development of Visual System

Until recently, in the studies of the developing mammalian visual system, visual experience before eye-opening was not usually thought to have any developmental

significance. Nevertheless, responses through the naturally closed lids could pattern neural activity in the visual system and thus provide developmentally relevant information which is used in the refinement of connections (Akerman et al., 2002). Some indications that light might pass through the lids and stimulate the visual system before eye-opening in kittens were provided by Huttenlocher already since 1966 (Huttenlocher, 1966, 1967). Recent studies have also shown that in ferrets, as early as two weeks before eye-opening (ferrets open their eyes around P32), visual stimuli presented through the closed eyelids can drive neuronal activity in dLGN and striate cortex (Krug et al., 2001; Akerman et al., 2002). Subsequently, Akermann et al. addressed the developmental significance of this source of activity for the ferret retinogeniculate pathway. The terminals of RGCs that respond to increases in light intensities (“On”) and those that respond to decreases in light (“Off”) are initially intermixed in the ferret dLGN and segregate during development. Rearing ferrets in the dark in the period before eye-opening altered the normal segregation of On and Off retinal inputs in the retinogeniculate pathway (Akerman et al., 2002). This study demonstrated that visual experience through closed eyelids is important for the normal development of functional connections.

Visually evoked activity is not found in the cortical neurons in the immediate neonatal period, P4 for kittens (Huttenlocher, 1966, 1967) and P19 for ferrets (Akerman et al., 2002) being the earliest age at which visual responses have been recorded. It may be that visual experience is less involved in the initial formation of neuronal circuits in the visual system, for which the most significant might be the spontaneous activity, but plays an important role in the subsequent refinement and/or consolidation of them. This culminates with the critical period, phase during which fast and strong adaptive changes of neuronal circuits happen in response to imbalanced binocular input caused by transient lid closure of one eye (Wiesel and Hubel, 1963). Thus, whereas spontaneous activity and perhaps genetic factors play a role in the establishment of the system, visual experience appears necessary for the subsequent phase of its maintenance and stability (Yuste and Sur, 1999).

## Chapter 2

### Aim of the Study

As presented in the introductory chapter,  $\text{Ca}^{2+}$  signaling plays a major role in the physiology of the central nervous system, fact that generated an intensive effort for designing new  $\text{Ca}^{2+}$  indicators and methods to label neural cells with these indicators. The mechanisms of cellular  $\text{Ca}^{2+}$  dynamics were mostly studied *in vitro* using cell cultures or brain slices. Very little data is available at the moment regarding the mechanisms of  $\text{Ca}^{2+}$  signaling in brain *in vivo*. A significant progress for  $\text{Ca}^{2+}$  imaging in living animals was achieved by the technical development of two-photon laser scanning fluorescence microscopy, which enabled imaging deep into brain tissue. By using TPLSFM in combination with loading of brain cells with small molecule  $\text{Ca}^{2+}$  indicators, *in vivo* recordings of  $\text{Ca}^{2+}$  signals from individual neurons and ensembles of neuronal networks were made possible. However, the specific contribution of the different classes of neuronal cells to the network  $\text{Ca}^{2+}$  activity, or the *in vivo*  $\text{Ca}^{2+}$  dynamics in dendrites, the place of synaptic transmission in which  $\text{Ca}^{2+}$  plays a crucial role, are still far from being elucidated. The genetically encoded fluorescent  $\text{Ca}^{2+}$  indicator proteins have the potential to be targeted to specific cell types and/or subcellular organelles of interest, and therefore, seem to represent ideal tools to address these issues.

On the other hand, appropriate model systems for *in vivo*  $\text{Ca}^{2+}$  imaging in the brain have to be designed. Such a system has to match and be relevant for the real system represented by the human brain. In this respect rodent system represents a valuable model system, since it shares many basic biological functions with the human brain. Their gene sequence (encoding the functional proteins) shows remarkable similarities with humans. Mouse availability for transgenic technology allows investigations of the involvement of specific genes and proteins in the function, development and plasticity of the brain. One of the most used models to investigate brain development and plasticity is the visual system. It was

also shown that the cells in the mouse visual cortex exhibit the presence of all the major functional properties that have been described in higher mammals, such as cats or monkeys. The study presented in this thesis focuses on two major issues: first, the search for improvements of the methodology for *in vivo* two-photon  $\text{Ca}^{2+}$  imaging and second, their application in the analysis of the development of the mouse visual cortex. The following specific questions were address in this thesis:

Which additional techniques could be combined with *in vivo* functional  $\text{Ca}^{2+}$  imaging to be able to identify the cellular types one records the  $\text{Ca}^{2+}$  signals from?

- Is there a new type of genetically encoded fluorescent  $\text{Ca}^{2+}$  biosensor better suited than the usual anorganic  $\text{Ca}^{2+}$  indicators to perform *in vivo*  $\text{Ca}^{2+}$  recordings from subcellular structures, like for example, from dendrites?
- Which are the patterns of *in vivo*  $\text{Ca}^{2+}$ -based spontaneous activity in the mouse visual cortex, both at neuronal network and single cell level, during the time when the neuronal circuits are established?
- Which are the mechanisms underlying the spontaneous activity?
- Do the patterns of the spontaneous activity change during development and if so, by which mechanism?
- Which is the first time point when the cortical neurons become responsible to visual stimulation and how are these responses reshaped by the subsequent incoming visual information?



## Chapter 3

### Methods

#### 3.1. Animals

All experiments were carried out according to institutional animal welfare guidelines and were approved by the government of Bavaria, Germany. Balb/c mice of either sex were used, aged between postnatal day 7 (P7) and one year old provided either by Charles-River company (Sulzfeld, Germany) or by the breeding facility of the Technical University Munich. Mice were reared with 12 hours light/dark cycle. In 5 experiments mice were kept in a dark room from birth until postnatal day 22-28 when experiments were performed. The transgenic mice expressing Thy 1-CerTN-L15 were between 2 to 5 months old and were generated in the group of Oliver Griesbeck in Max Planck Institute for Neurobiology in Martinsried, Germany. Two months old transgenic mice expressing enhanced green fluorescent protein (EGFP) in the somatostatin-positive GABAergic interneurons were provided by Jackson Laboratories (Maine, USA).

#### 3.2. Anesthesia

All experiments were carried out on anesthetized animals. Mice were anesthetized by inhalation of isoflurane (Abbot, Wiesbaden, Germany) at concentrations between 1 to 1.5% (vol/vol) in pure oxygen. The delivery of the anesthetic and the regulation of its concentration were performed with the help of a vaporizer specially designed for volatile anesthetic agents and by a flow meter. For the duration of anesthesia the physiological status of the animal was continuously monitored. It is known from the literature that under sedation and anesthesia, body temperature drops abruptly and hypothermia may cause shock and death. Mice have a

rather high surface area to body weight ratios and rapid metabolism, so they lose body heat rapidly (Flecknell, 2000). This is particularly important in young animals. Therefore, after inducing the anesthesia in a closed pre-anesthesia chamber, mice were placed onto a warming blanket (38°C) in front of a mask through which the mixture of anesthetic and oxygen was provided. Animals were supplied with warmed saline solution (subcutaneously or intraperitoneal) to support the cardio-vascular function and to prevent dehydration. In small rodents, the fluid loss during surgical procedure has to be compensated at a rate of 10-15 ml kg<sup>-1</sup> body weight (Flecknell, 2000), which for a 20 g mouse would equal 0.2-0.3 ml.

Anesthesia level was controlled by sensors from an anesthesia-monitoring system that were affixed to the animal. Equipment for small laboratory animals provided by ADI Instruments was used. Body temperature, respiratory and cardiac rate and rhythm, and blood pressure were monitored continuously. Additional care was taken that the color of animals' mucous membranes was kept pink. If any sign of too deep anesthesia appeared (decrease in the respiration or pulse rate and abnormal rhythm, white or cyanotic membranes) the level of the anesthetic was immediately adjusted.

During the surgical preparation and staining procedure animals were kept in a surgical depth of anesthesia resulting in lack of reflexes (righting reflex, pedal or paw pinch withdrawal, eyelid reflexes) and respiration rate of 80-100 per minute. During the recording sessions mice were anesthetized by low doses of isoflurane (0.8-1%), in order to minimize the influence of anesthetic on cortical activity.

### 3.3. Surgical Procedure

All experiments were performed in the visual cortex. Location of this brain area was identified following the stereotactic coordinates (Bregma -3- -4 mm, 2-3 mm lateral to the midline for P18 to one year old mice) described by Paxinos and Franklin (Paxinos and Franklin, 2001) and the architecture of the blood vessels (Antonini et al., 1999). In younger animals, the position of the primary visual cortex (0-1 mm anterior to the lambdoid suture, 1.5-3 mm lateral to the midline) was identified according to the Golgi atlas of the postnatal mouse brain (Valverde, 1998).

The eyes of the animals were protected by application of Isopto-Max crème (Alcon Pharma, Freiburg, Germany). Approximately 15 min after subcutaneous injection of approximately 50-100 µl local anesthetic (2% lidocaine) under the scalp and at surgical level of anesthesia, the skin and muscles above the visual cortex were gently removed with fine

scissors. Also the soft tissue attached to the skull was removed with fine forceps. The exposed skull was then dried with air, thinned under the control of a dissecting microscope by using stainless steel drill bits and polished with a felt polisher (Dr. Ihde Dental, Munich, Germany). The thinned area was circular and had typically a diameter of 1-1.5 mm. The skull was thinned as gently as possible, without pressing onto it, since harsh, inaccurate thinning could cause brain damage. Drilling was carried out intermittently and in the drillings breaks the skull was covered with cold artificial cerebrospinal fluid (ACSF) solution to prevent heat-induced tissue injury. Over-thinning of the skull was avoided, because it can produce cortical injury, most likely due to deformation of the skull under the pressure of the drill and to overheating of the skull and cortical tissue. In adult mice some bleeding from bony canaliculi (Grutzendler and Gan, 2005) could arise during the thinning process. This bleeding usually stopped spontaneously or soon after the skull surface was washed with cold ACSF. Thinning stopped as soon as the bone bended when it was gently touched with tweezers. Imaging through thinned skull provides optimal results when the skull is thinned down to a thickness of about 10-20  $\mu\text{m}$ .

A recording chamber with a diameter of 35 mm and a central access opening, custom-made from a standard tissue-culture dish (See **Fig. 5B**), was then glued on the skull of the animal using cyanoacryl glue (UHU, Buhl-Baden, Germany) (Garaschuk et al., 2006a). The mouse was transferred into the recording setup equipped with a two-photon laser-scanning microscope and placed onto a warming blanket (38°C). The sensors of the anesthesia-monitoring system were affixed to the mouse to ensure that physiological levels of monitored parameters are maintained. The use of the recording chamber had two advantages: it enabled head fixation and the use of water-immersion objectives through perfusion with a warm (37°C) ACSF (containing: 125 mM NaCl, 4.5 mM KCl, 26 mM NaHCO<sub>3</sub>, 1.25 mM NaH<sub>2</sub>PO<sub>4</sub>, 2 mM CaCl<sub>2</sub>, 1 mM MgCl<sub>2</sub>, 20 mM glucose, pH 7.4, when bubbled with 95% O<sub>2</sub> and 5% CO<sub>2</sub>). The rate of the ACSF perfusion was approximately 5 ml/min.

A small craniotomy was performed under visual control (10 or 20x objectives magnification) using fine needles (0.3 mm diameter, 12 mm length). The craniotomy was made above an area devoid of large blood vessels and it was small (under 0.5 mm) for imaging through the skull and larger (or two small craniotomies were performed near each other) if ‘open-access’ imaging was intended. In the case of imaging through the thinned skull, the stability of the preparation is higher because of the lower impact of heart beat and breathing artifacts. Nevertheless, the efficiency of photon detection is better when the skull above the imaging field is removed, producing crisper images and greater imaging depth.

A very important concern during executing the craniotomy was not to damage and remove the dura mater. Its removal was not required for cell staining and it strongly enhanced the breath- and heartbeat- related movement artifacts. Stability of the recordings also critically depended on the diameter of the craniotomy. Thus, openings larger than 1 mm in diameter were often accompanied by large movement artifacts. Furthermore, the regions with a high density of blood vessels and experiments in very young animals (P8-P15) produced recordings with high-frequency vibrations of cells. In these cases, the recording conditions were improved to a certain degree by covering the skull opening with 2% low melting point agarose (e.g., 20 mg in 1 ml standard ACSF; Invitrogen GmbH, Karlsruhe, Germany) which, when hardened, reduced the cardiac and respiratory pulsations. The craniotomy was used for *in vivo* loading of large populations of cortical cells with a small molecule fluorescent  $\text{Ca}^{2+}$  indicator dye and/or for imaging.

### 3.4. *In Vivo* Loading of Cortical Cells with Small Molecule Fluorescent Calcium Indicator Dyes

Cortical cells were loaded with the membrane-permeant acetoxymethyl (AM) esters of the fluorescent  $\text{Ca}^{2+}$  indicator dyes Oregon Green 488 BAPTA-1 AM, OG-1 AM (Molecular Probes, Eugene, Oregon, USA) and Fura-PE3 AM (TefLabs, Austin, Texas, USA). The AM esters were dissolved in a solution containing 20% Pluronic F-127 in dimethylsulfoxid, DMSO (e.g., 2 g Pluronic F-127 in 10 ml DMSO; Sigma-Aldrich, Steinheim, Germany) to yield a dye concentration of 10 mM. This solution was subsequently diluted 1/10 to 1/100 in standard pipette solution (containing 150 mM NaCl, 2.5 mM KCl, and 10 mM HEPES) to prepare the staining solution with a final concentration of the  $\text{Ca}^{2+}$  indicator dye of 0.1-1 mM. The standard pipette solution is a simplified  $\text{Ca}^{2+}$ -free ACSF solution used to minimize precipitation of the  $\text{Ca}^{2+}$  indicator dye. Staining solution was filtered through a Millipore filter with a pore diameter of 0.45  $\mu\text{m}$ , in order to avoid clogging of the micropipette used for dye delivery to the cells.

**Fig. 5** illustrates the basic approach used for *in vivo* loading of cell populations with fluorescent  $\text{Ca}^{2+}$  indicator dyes. The followed protocols were described in (Stosiek et al., 2003) and (Garaschuk et al., 2006a). A staining micropipette was pulled from a borosilicate glass capillary (Hilgenberg GmbH, Malsfeld, Germany) using a pipette puller (PP830 from Narishige, Japan). Pipette resistance was 6-9  $\text{M}\Omega$  (when filled with standard pipette solution). Pipette was filled with the staining solution and inserted into the cortex using a LN-Mini

manipulator (Luigs & Neumann GmbH, Ratingen, Germany) under an angle of 30-40°. Pipette was advanced along its axis until it reached the desired depth, approximately 150-200  $\mu\text{m}$  below the cortical surface. A pressure pulse (2x1 min, 70 kPa) was applied to the pipette using a pressure-application device, either Picospritzer II (General Valve, Fairfield NJ, USA) or a pneumatic drug-ejection system (NPI Electronic GmbH, Tamm, Germany). Approximately 400 femtoliters of the dye-containing solution (Stosiek et al., 2003) was ejected into the cortical tissue during the pressure application. Afterwards the pipette was removed coaxially from the brain. The release of the  $\text{Ca}^{2+}$  indicator dye into the brain was confirmed by briefly imaging the place of its delivery. The presence of a fluorescence cloud indicated that dye was ejected from the pipette. If no fluorescence could be detected in the cortical tissue, the staining procedure was repeated.

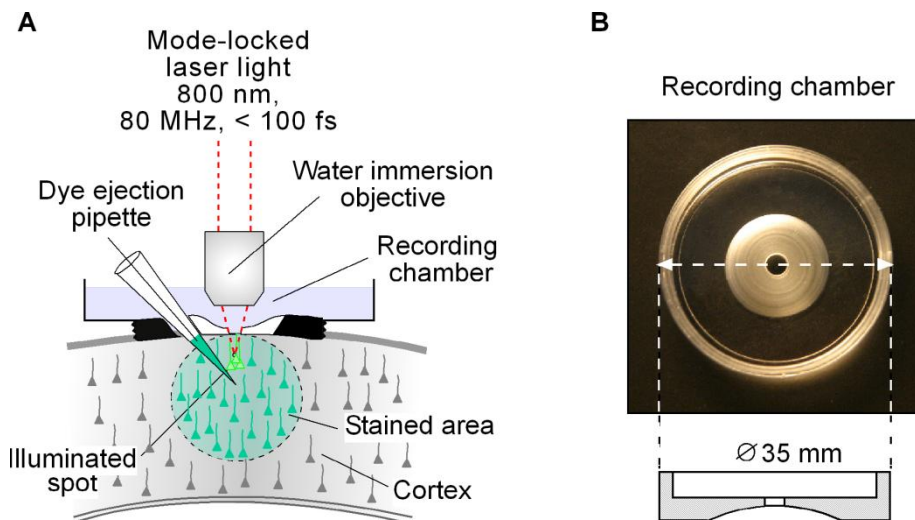


**Figure 5: Schematic representation of the experimental procedure.**

(A) The skin above the cortical area to be imaged is removed and a custom-made recording chamber is glued on the skull. The chamber is perfused with warmed (37°C) ACSF. One small craniotomy is made for insertion of the micropipette containing the staining solution. The micropipette is advanced into the brain and a small amount of staining solution is pressure-ejected into the tissue, yielding a stained cortical area (shown in green) with a diameter of 200-400  $\mu\text{m}$ . A two-photon laser-scanning microscope is used for imaging, which is performed either through the thinned skull or through a second small craniotomy to improve the depth and quality of the recordings. (B) Photograph of the custom-made recording chamber showing its diameter and cross-section. The inside opening of the chamber has a diameter of 3.5 mm and its surrounding circular region is thinned to fit the bend of the animal's skull.

The time needed to reach a stable fluorescence level within the cortical cells loaded with the  $\text{Ca}^{2+}$  indicator was 30-60 min. This protocol yielded an almost spherical stained brain area with a diameter of 200-400  $\mu\text{m}$  (Stosiek et al., 2003) and (Garaschuk et al., 2006b). Note that all cells in the preparation (**Fig. 6A**) were stained with the  $\text{Ca}^{2+}$  indicator. The only dark areas corresponded to blood vessels, which could be easily identified when focusing through the tissue. If the cells were not or only poorly loaded, two scenarios were probable: either the

tissue was intact, but the dye delivery failed, or the tissue was damaged (**Fig. 6B**). The possible reasons for the tissue damage could be the following: inaccurate thinning of the skull, damaging large blood vessels while performing the craniotomy and/or the longevity of the dissection time (therefore in our final protocol we restricted it to less than 2 hours).

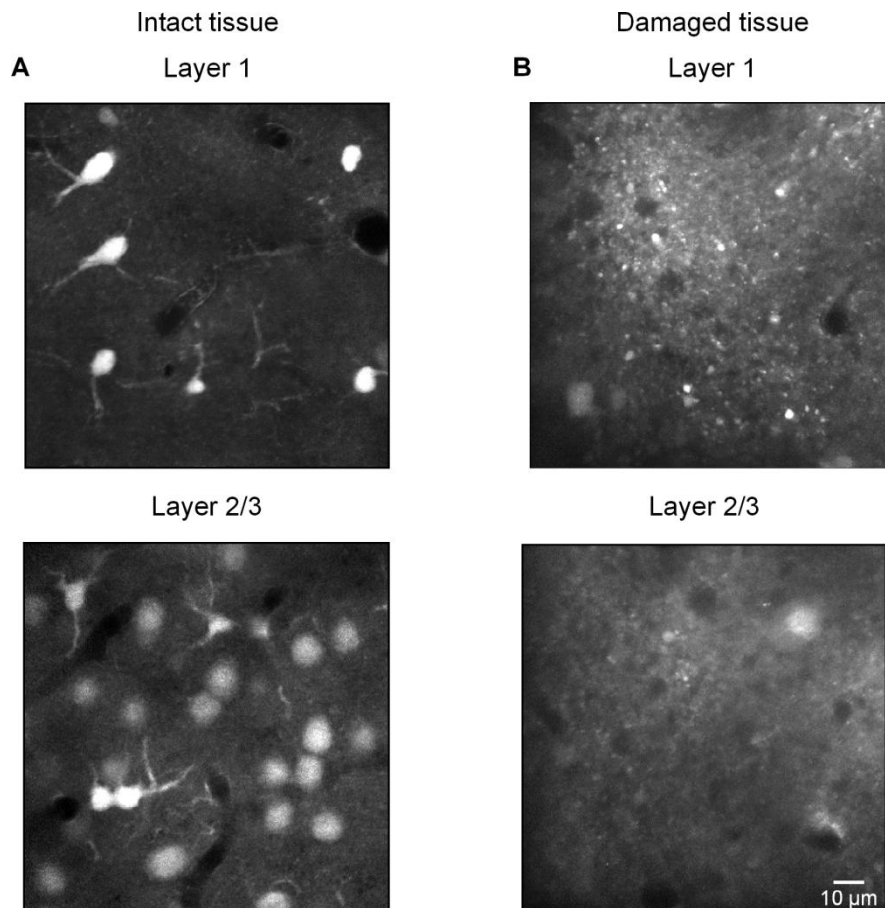


**Figure 6: Evaluation of the staining quality.**

(A, B) Micrographs showing MCBL-loaded cells in layer 1 (*upper panels*) and layer 2/3 (*lower panels*) from 2 different stained regions in a P64 mouse. Both areas were stained following the same procedure. In (A) cells are clearly visible, while in (B) the tissue is damaged due to the injury of a large brain vessel while performing the craniotomy.

To distinguish between neuronal cells and astrocytes the protocol developed by (Nimmerjahn et al., 2004), who established sulforhodamine 101 (SR101) as an astrocyte-specific marker, was used. To allow application of both dyes (OGB-1 and S101) from the same application pipette the protocol was modified as follows: 1 mg of SR101 was diluted in 4 ml standard pipette solution and used further to dilute the concentrated solution containing 10 mM  $\text{Ca}^{2+}$  indicator dye; the combined staining mixture was then injected into the cortex according to the usual procedure. This application resulted in a good loading of neurons and glia cells with the  $\text{Ca}^{2+}$  indicator, and also in specific staining of astrocytes with SR101 within the same brain region.

### 3.5. *In Vivo* Two-Photon Calcium Imaging

For *in vivo* two-photon measurements a custom-built, two-photon laser-scanning microscope based on a mode-locked Ti:sapphire laser system (Mai Tai, Spectra Physics, Mountain View, CA) was used. The laser system generates the excitation light with a pulse width of 100 femtoseconds, wavelength ranging between 710- 920 nm, and repetition rates of 80 MHz. The laser-scanning system (Olympus Fluoview, Tokyo, Japan) was coupled to an upright microscope (either BX51WI or BX61WI, Olympus, Tokyo, Japan) and equipped with one of the following water-immersion objectives:  $\times 10$ , 0.3 numerical aperture (NA);  $\times 20$ , 0.5 NA; both from Olympus (Tokyo, Japan),  $\times 60$ , 1.0 NA from Nikon (Tokyo, Japan), and  $\times 40$ , 0.8 NA and  $\times 63$ , 0.9 NA from Leica (Bensheim, Germany). The average power of the excitation light under the objective was approximately 50-70 mW. The excitation power was reduced to the minimum when the high resolution objectives ( $\times 40$  and  $\times 60$ ) were focused onto the brain surface. In order to avoid dye bleaching, the excitation power was carefully raised as the objective was lowered to inspect the upper cortical layers. The following structures became clearly visible: large epithelial cells on the surface of the cortex; cortical layer 1 cells from the surface down to the depth of 100-200  $\mu\text{m}$ , depending on the age of the animal (**Fig. 6A**, *upper panel*); and cortical layer 2/3 cells (**Fig. 6A**, *lower panel*).

Data acquisition was performed using a Fluoview 300 software from Olympus (Tokyo, Japan). Data was sampled with different frequencies, depending on the aim of the experiment: the high resolution images were taken with a frame rate of 1 Hz, the time lapse  $\text{Ca}^{2+}$  measurements of spontaneous activity were taken with a frame rate of 5-10 Hz, while the light-evoked  $\text{Ca}^{2+}$  transients were sampled at 200 Hz using the line-scan mode (in which the image that builds up is made by scanning the same line from a region of the sample at successive points in time).

The wavelength of the excitation light was chosen depending on the  $\text{Ca}^{2+}$  indicator used and the excitation spectrum of EGFP and SR101. Excitation light of 800 nm was used for the visualization of cortical cells loaded with the  $\text{Ca}^{2+}$  indicator dyes OG-1 AM and Fura-PE3 AM. SR101 emits fluorescence light at wavelengths between 550-750 nm, which are significantly longer than those of common  $\text{Ca}^{2+}$  indicators. Thus, in the double staining experiments with OG-1 AM and SR101, the emitted light was split at 575 nm using a dichroic mirror and two photomultipliers. The fluorescence resulting from OG-1 AM was directed to the green channel and the one deriving from sulforhodamine 101 to the red channel. For imaging the CerTN-L15 fluorescence, the biosensor was excited either at 860 or

at 890 nm. For ratiometric measurements of FRET between Citrine and Cerulean the emitted fluorescence light was split at 515 nm. In the experiments with transgenic mice expressing EGFP-labeled somatostatin-positive GABAergic interneurons both OG-1 AM and EGFP were excited at 900 nm and the emitted fluorescence was split at 515 nm.

### 3.6. *In Vivo* Application of Pharmacological Substances

The craniotomy was used not only for loading and imaging the cells, but also for drug delivery to the cortical region under study. Two techniques were used: (i) local application of drugs directly to the cells of interest by inserting an iontophoresis or a pressure-application pipette, procedure similar to the insertion of the staining pipette and (ii) bath application by adding the drugs to the preheated ACSF, used to perfuse the recording chamber. The latter method is similar to the bath application of drugs in conventional brain slice experiments (Garaschuk et al., 2006b).

The following substances were used as described in the results section: (i) the sodium channel blocker tetrodotoxin (TTX, Calbiochem, Schwalbach, Germany); (ii) the  $\alpha$ -amino-3-hydroxyl-5-methyl-4-isoxazole-propionat (AMPA) receptor antagonist 6-Cyano-7-nitroquinoxaline-2,3-dione (CNQX); (iii) the N-methyl-D-aspartat (NMDA) receptor antagonists: D-2-amino-5-phosphonovaleric acid (APV), (E)-( $\pm$ )-2-Amino-4-methyl-5-phosphono-3-pentenoic acid (CGP 37849, Tocris, Northpoint, Avonmouth, UK), (+)-5-methyl-10,11-dihydro-5H-dibenzo-[a,d]cyclohepten-5,10-imine hydrogen maleate (MK-801); (iv) N-Methyl-D-aspartic acid (NMDA); (v) (-)-the  $\gamma$ -aminobutyric acid type A receptor (GABA<sub>A</sub>) antagonists bicuculline methobromide (Axxora, Lörrach, Germany) and gabazine (SR 95531); and (vi) glutamate. Unless otherwise indicated, all chemicals were purchased from Sigma-Aldrich (Steinheim, Germany).

The following drugs were delivered by bath application: TTX (1-2  $\mu$ M), CNQX (50 $\mu$ M) together with APV (50-100 $\mu$ M), APV alone (50-100 $\mu$ M), CGP (25-50 $\mu$ M) and MK-801 (100-150 $\mu$ M). Under *in vivo* conditions the small craniotomy was sufficiently large to allow an effective access of drugs to the cortical parenchyma. The water-soluble drugs (e.g. APV or TTX) produced their effect very soon after they were present in the recording chamber, and, therefore, within time frames comparable to those observed in slices. However, to achieve *in vivo* drug effects similar to those observed in slices, a two- to threefold increase in the concentration of the drug was required (Garaschuk et al., 2006b).



For the local application, either a MVCS-C-01 iontophoresis system, or a pressure drug-ejection system (PDES-02D) were used, both from NPI, Electronic, Tamm, Germany. In some of these experiments, 12.5-500  $\mu\text{M}$  of the red, cell-impermeant, fluorescent dye Alexa 594 hydrazide sodium salt (Alexa 594) (Molecular Probes, Eugene, Oregon, USA) was added to the drug-containing solution that was filled into the application pipette. Addition of Alexa 594 allowed visualization of the pipette and improved the precision of the pipette positioning.

TTX (2.5-5 $\mu\text{M}$ ) was delivered by low pressure application. The following agents were ejected iontophoretically: CNQX (1mM), APV (10-25mM), bicuculline (20mM), NMDA (10mM), gabazine (500 $\mu\text{M}$ ), and glutamate (100mM). In all solutions pH was adjusted to 7.4 with the help of a buffer (HEPES). Retaining currents of 8-15 pA were used to delay drug leakage from the pipette. APV, CNQX and glutamate were ejected with negative currents of -1nA. In the case of bicuculline and gabazine the retain current was higher and negative, -40 to -100 pA and the drugs were often applied just by switching off the retain current. In a few remaining cases when switching off the retain current was ineffective, small ejecting currents (+40 to +60 pA) were applied to release the drug into the tissue. This application method was chosen in order to avoid triggering seizures by ejecting a too large amount of the GABA<sub>A</sub> receptor antagonists. In each particular experiment the application duration that elicited an unambiguous effect of the drug was used.

### 3.7. Visual Stimulation

In all experiments recordings were done in a dark adapted state. A photo-diode was used as light source, and it was mounted on an adjustable support in front of the mouse's eye. The visual stimuli consisted of 100 ms long light flashes produced by the photo-diode which was placed at a distance of about 35-40 cm and at an angle of 35-50° laterally from the eye of the mouse (see **Fig. 34A**). For recording of the light-evoked Ca<sup>2+</sup> transients, the stimulus was presented to the same cells in series of 10-20 trials, and afterward the procedure was repeated with other selected cells within the same experiment. These series were generally acquired between separate blocks of spontaneous activity recordings. In very young animals (P7-P10) the visual responses could not be elicited with the photo-diode placed at the normal distance and therefore it had to be positioned very close (approximately 5 cm) in front of the mouse's eye.

### 3.8. Identification of the Recording Position and Data Analysis

To document the exact position of the recorded regions, at the end of the experiments mice were sacrificed, the brains were removed and coronal slices were cut. Images of the brains and slices were obtained using CCD cameras, either Orca-ER (Hamamatsu Photonics, Herrsching, Germany) or pixelfly (PCO, Kelheim, Germany) mounted on a microscope (IX70 and MVX10, Olympus, Tokyo, Japan). Fluorescent images were acquired using a fluoresceine filter set and overlaid with the transmitted light images (**Fig. 7**). The location of the recorded cortical area was then identified using the relation between the fluorescent spot and the other identified anatomical structures on the slices described in the mouse brain atlas of Paxinos and Franklin (Paxinos and Franklin, 2001).

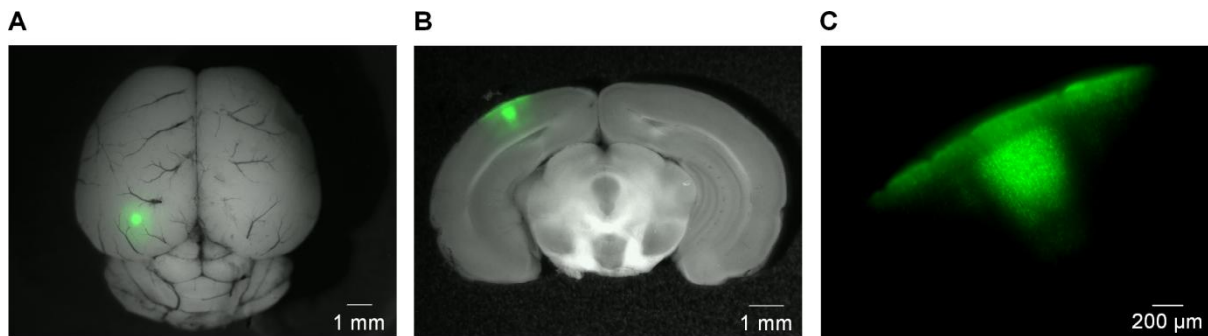


**Figure 7: Macroscopic view of the stained cortical region.**

Whole brain (A) and slice (B, C-higher magnification) photographs of the stained region taken after the brain of a P16 mouse was removed and sliced at the end of the experiment. The fluorescence images are overlaid with the transmitted light images as green false color images, and therefore the green spots indicate the stained region in the visual cortex of the mouse.

Image analyses were done off-line with a LABVIEW-based custom-made software package (National Instruments, Austin, Texas, USA), ImageJ (<http://rsb.info.nih.gov/ij/>) and Igor Pro (Wavemetrics, Lake Oswego, Oregon, USA) software. The neuronal  $\text{Ca}^{2+}$  transients were measured by drawing regions of interest (ROIs) that included cell soma. The baseline fluorescence was calculated from a region of interest drawn within a blood vessel and was subsequently subtracted. Throughout the analyses data are presented as the relative change in fluorescence over time as  $\Delta F/F = (F_0 - F_1)/F_0$ . For the ratiometric measurements of FRET between Citrine and Cerulean results are given as the relative change in the ratio of Citrine/Cerulean fluorescence ( $\Delta R/R$ ). A  $\text{Ca}^{2+}$  transient was identified as an event if its amplitude was larger than 3 times standard deviation (S.D.) of the baseline fluorescence noise. For calculating the decay time constant, the decaying portion of the  $\text{Ca}^{2+}$  transient was fitted with a mono-exponential function using Igor Pro. The decay time constant of the Alexa 594-

induced fluorescence transient was measured in a similar way, but in this case a double-exponential function was used.

In the experiments where local drug applications were carried out, the time window and the localization of the drug effect were calculated based on the Alexa 594-induced fluorescence transient. Alexa 594 is cell-impermeant, so it was assumed that both the applied agent and Alexa 594 would be similarly washed out from the tissue by the microcirculation. The Alexa 594 transient was measured by drawing a ROI on the extracellular space situated near the application pipette. Duration of the drug effect was then measured between the moment of drug application (the beginning of Alexa 594 transient) and the time point when the Alexa 594 transient decreased to 95% of its maximal amplitude. In the cases of bicuculline and gabazine applications, their effect was quantified within the time window in which the Alexa 594 transient was higher than 70% of its maximal amplitude. Values are given as mean  $\pm$  standard error of mean (S.E.M.).

## Chapter 4

### Results

#### 4.1. Improvements of the Methodology for *In Vivo* Two-Photon Calcium Imaging in the Mammalian Brain

##### 4.1.1. Progress in Imaging Neuronal Networks *In Vivo* Using Small Molecule Calcium Indicators

*In vivo* recordings of network  $\text{Ca}^{2+}$  activity from populations of cortical cells loaded with small molecule fluorescent  $\text{Ca}^{2+}$  indicators were made possible due to the technique first described by Stosiek et al. (Stosiek et al., 2003) and termed multi-cell bolus loading (MCBL). To understand the mechanisms underlying MCBL first this process was characterized in more detail. Cells located in the mouse visual cortex were bulk-loaded with small molecule fluorescent  $\text{Ca}^{2+}$  indicators using MCBL and imaged *in vivo* with two-photon laser scanning microscopy. MCBL is based on the pressure-injection of a concentrated (1 mM) solution containing the membrane-permeant, AM form of the fluorescent  $\text{Ca}^{2+}$  indicator dye into a brain region of interest. **Fig. 8A** illustrates the MCBL staining procedure in the visual cortex of a P14 mouse using a solution of Fura PE3, a  $\text{Ca}^{2+}$  indicator dye which is fluorescent also in the AM form. The left panel on **Fig. 8A** shows an image of the cortical region only one minute after the dye was ejected into the tissue. Immediately after dye delivery, the fluorescent dye molecules are located diffusely in the extracellular space. Subsequently, the molecules of the AM form of the indicator dye passively diffuse across the cellular membranes and become incorporated intracellularly. There the AM esters are cleaved by the intracellular esterases and the  $\text{Ca}^{2+}$  indicator loses its lipophilicity, remaining trapped inside the

cells. As a result, within few minutes cells start to accumulate the dye and become brighter, while the dye becomes gradually removed from the extracellular space, which becomes dimmer (**Fig. 8A**, middle and right panel).

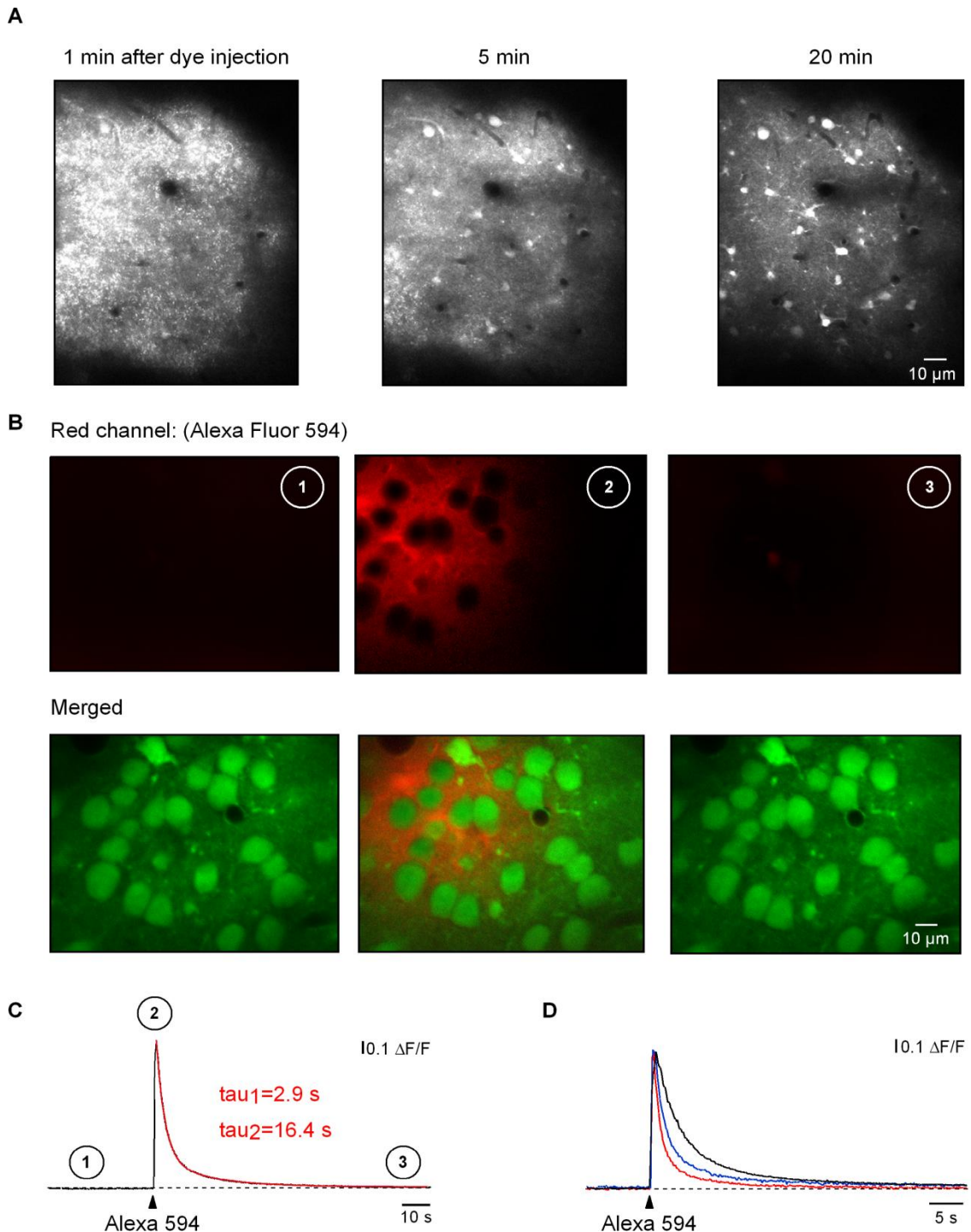


**Figure 8: Kinetics of the MCBL staining and removal of the extracellular dye molecules by the vascular system.**

(A) Images taken *in vivo* in layer 2/3 of a mouse visual cortex at different times (1, 5, and 20 min) after the bolus-injection of the fluorescent  $\text{Ca}^{2+}$  indicator dye Fura PE3 AM. Note that just after injection the dye molecules are predominantly located in the extracellular space. At the later time points, they gradually disappear from the extracellular space and the cells become brighter. (B) Consecutive images acquired *in vivo* before (1), during (2), and after (3) a 500 ms long iontophoretic application of the cell-impermeant dye Alexa

594 (*upper panels*). Merged images on the *lower panels* show no overlapping between the extracellular fluorescence caused by Alexa 594 application (*red*) and the cortical neurons loaded with OG-1 AM (*green*). (C) Time course of the Alexa 594-induced fluorescence transient. The numbers on the trace correspond to the time points at which the images in (B) were taken. (D) Three Alexa 594-induced fluorescence transients recorded in different experiments, covering the entire range of kinetics observed.

The process of dye removal from the extracellular space results also from the clearing of the extracellular space by the vascular system. To estimate the kinetics of this clearing process, the membrane-impermeant fluorescent dye Alexa 594 was locally ejected into the mouse cortex by iontophoresis and its removal from the extracellular space was monitored with the use of two-photon imaging (**Fig. 8B**). As shown on **Fig. 8B**, Alexa is briefly present in the extracellular space immediately after the application (**Fig. 8B**, middle panel) and within few seconds it is rapidly removed. The Alexa 594-induced fluorescence transient had a double exponential time course, with the mean decay time constants of  $2.3 \pm 0.1$  s and  $13.3 \pm 0.7$  s ( $n=33$  events), respectively (**Fig. 8C and D**).

In conclusion, the *in vivo* conditions, in which microcirculation is preserved, provide the basis for an efficient and rapid removal of the fluorescent  $\text{Ca}^{2+}$  indicator molecules from the extracellular space. This removal process teams up with the intracellular dye accumulation to produce a good contrast between the stained cells and the surrounding tissue in the MCBL loading technique.

#### 4.1.1.1. Cell Loading Using a Low Concentration of the Calcium Indicator Solution

Initially, the MCBL technique used 1mM solution of a fluorescent  $\text{Ca}^{2+}$  dye inside the application pipette (Stosiek et al., 2003). As detailed in the Methods section, the acetoxymethyl esters of the  $\text{Ca}^{2+}$  indicator dyes are dissolved in DMSO, a detergent, and therefore the final staining solution contained also 10% DMSO (vol/vol). Although the staining solution is quickly diluted within the brain and similar and/or higher DMSO concentrations were regularly used also by other groups (Hirase et al., 2004; Wong, 2000), there still remained the question regarding the putative negative influence of the detergent on the neuronal function.

To investigate the influence of DMSO and dye concentrations on the quality of the staining and on the dynamics of somatic  $\text{Ca}^{2+}$  transients, ten times lower concentrations of the  $\text{Ca}^{2+}$  indicator were tested. The MCBL procedure yielded staining of the very good quality also with 100  $\mu\text{M}$  OG-1 AM and 1% DMSO (vol/vol)-containing pipette solution (**Fig. 9A**

and **B**). Nevertheless, the staining with a diluted solution was less reproducible and required increased care for performing the preparation.

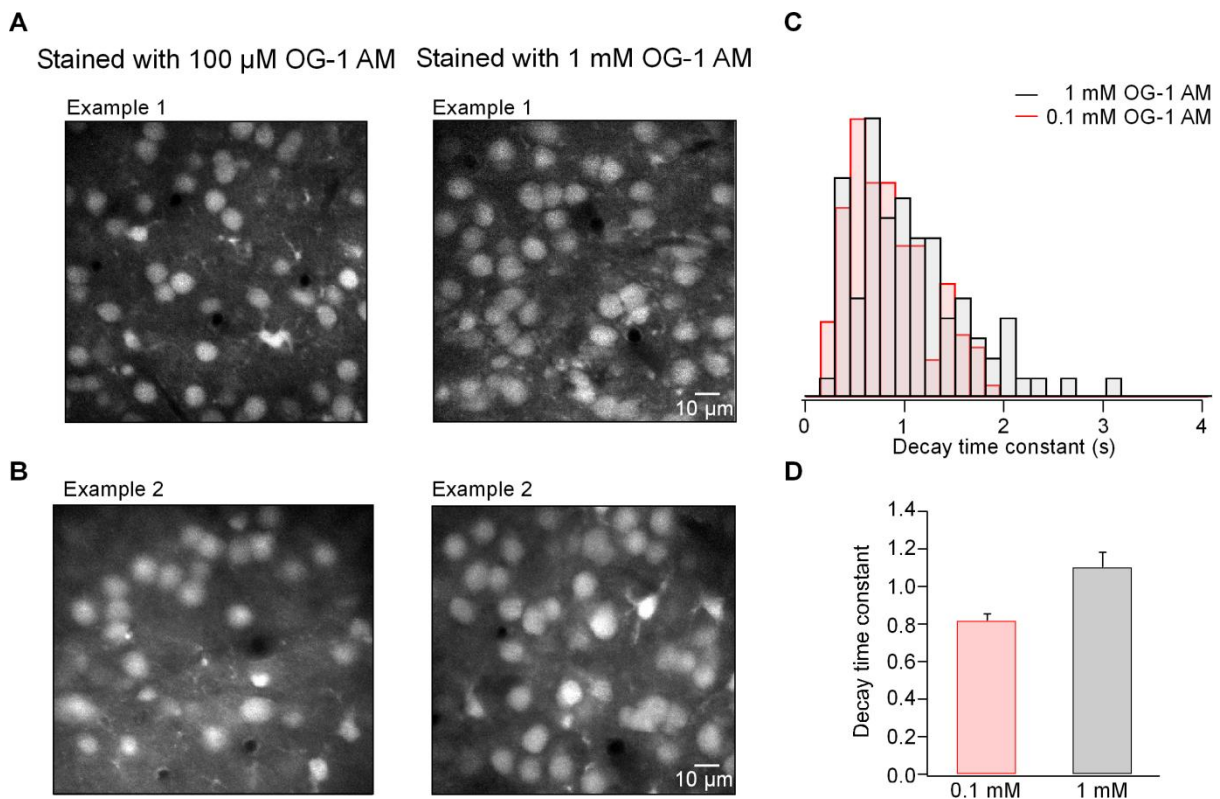


**Figure 9: MCBL using a low concentration of the indicator dye.**

(**A**, **B**) High-magnification images of layer 2/3 individual neurons acquired in the visual cortex from two different mice, aged P16 and P18, respectively. In each animal two separate areas were stained with OG-1 AM at different concentrations, either 100  $\mu\text{M}$  (*left panels*) or 1 mM (*right panels*). (**C**) Normalized histograms showing the distribution of decay-time constants of spontaneously occurring  $\text{Ca}^{2+}$  transients in the neurons stained with 1mM (*black*) and 100 $\mu\text{M}$  (*red*) of OG-1 AM. (**D**) Bar graphs presenting the mean values of the respective decay time constants.

Interestingly, the time courses of the spontaneous cellular  $\text{Ca}^{2+}$  transients were not considerably changed by the use of lower concentration dye (**Fig. 9C** and **D**). When both concentrated and diluted staining solutions were used in the same experiment, the average decay time constants were  $0.81 \pm 0.04$  s ( $n=123$  events) in cells stained with 100 $\mu\text{M}$  OG-1 AM and  $1.10 \pm 0.08$  s ( $n=88$  events) in cells stained with 1mM OG-1 AM. These findings suggested furthermore that the intracellular dye concentrations obtained using staining solutions containing either 100  $\mu\text{M}$  OG-1 AM, or 1mM OG-1 AM were comparable (approximately 20  $\mu\text{M}$  (Stosiek et al., 2003)).

#### 4.1.1.2. *In Vivo* Monitoring of Cellular Calcium Signals from New Born to Aged Brain

MCBL method was successfully used to stain cortical tissue at virtually all the developmental stages in which it was tested. **Fig. 10** shows examples of MCBL-based staining of layer 2/3 in the visual cortex of mice at four different ages, ranging from new born (P8, **Fig. 10A**), juvenile (P23, **Fig.10B**), adult (two-month old, **Fig. 10C**) until one year old (**Fig. 10D**).

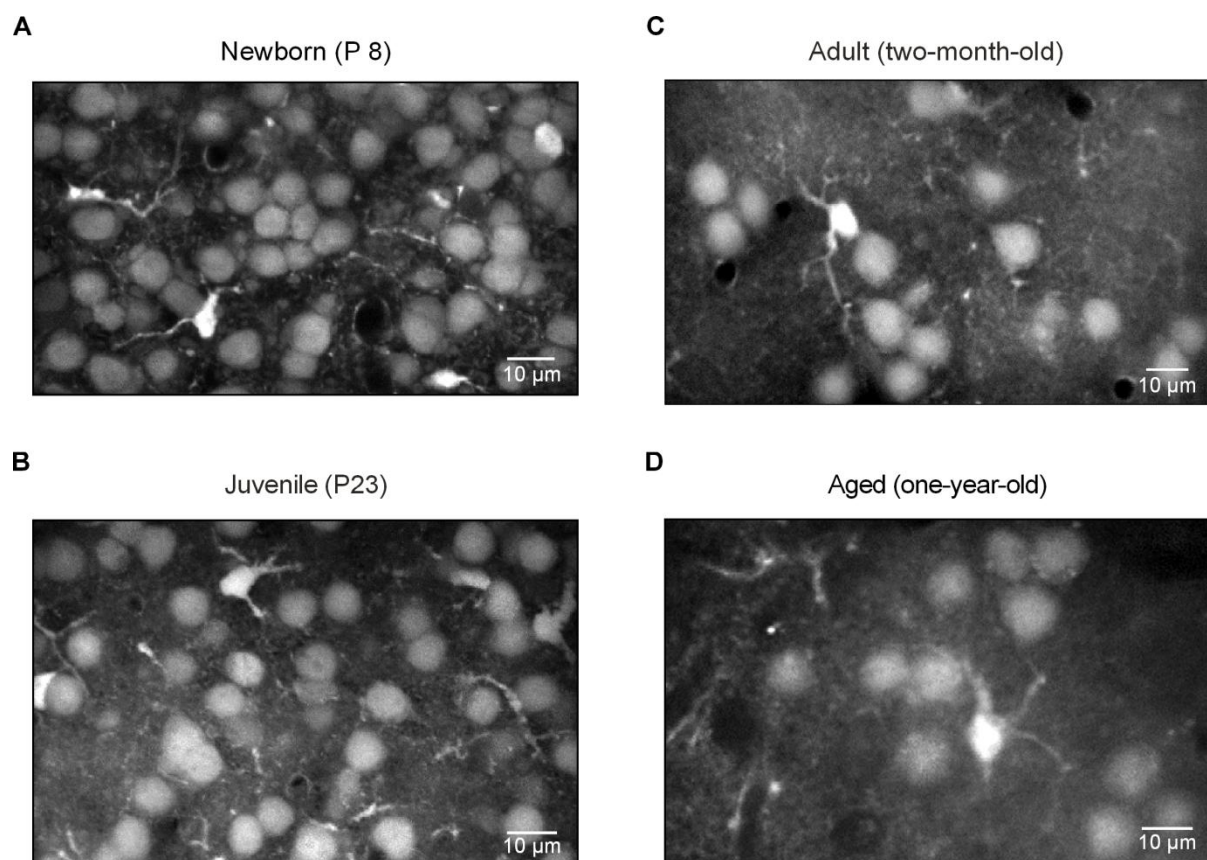


**Figure 10: Staining and imaging of cortical tissue at various developmental stages.**

High-magnification micrographs showing MCBL-loaded cells in layer 2/3 of the visual cortex at different ages during development. In all experiments cells were stained with OG-1 AM.

In all ages tested, the quality of the staining yielded similarly good results, allowing  $\text{Ca}^{2+}$  imaging with single-cell resolution deep within the tissue (up to 300-400  $\mu\text{m}$  under the brain surface), and recording of spontaneous and sensory evoked  $\text{Ca}^{2+}$  transients from individual cells. The maximal depth at which individual cells could be clearly identified depended on the shape and density of the cells, and the density of the blood vessels in the imaged region. Because the cell density in very young mice is higher, the depth below the



cortical surface at which single cells could be resolved was slightly decreased. Additionally, the preparation requirements differed depending on the age of the animals. In new born and young mice (P7-P12) the thickness of the skull was very small and supplementary attention should be paid not to damage the brain when the recording chamber was attached to the skull. Conversely, in old mice longer drilling was necessary because their increased skull thickness, that necessitated multiple brakes to avoid overheating of the skull and subsequent cortical tissue injury.

Thus, MCBL technique can be applied *in vivo* for studying the functional properties of neuronal networks with single-cell resolution at all desired developmental stages.

#### 4.1.1.3. Multicolor Imaging for Identification of Different Cell Types

The MCBL procedure is not cell type specific. It provides a relatively homogeneous loading of virtually all cells in the target brain region, although glia cells have the tendency to accumulate higher concentration of the indicator dye, and therefore appear somewhat brighter than neurons. In order to differentiate between the various cellular types present in the stained area additional markers (for example, cell-type specific expression of green fluorescent protein, GFP) and simultaneous recordings of these different indicators (multicolour imaging) were required.

To separate neurons from glia cells a specific astroglial marker, sulforhodamine 101 (S101), can be used (Nimmerjahn et al., 2004). Upon excitation S101 emits light in the red portion of the spectrum, at wavelengths between 550-750 nm (Garaschuk et al., 2006a), which are significantly longer than those of the common  $\text{Ca}^{2+}$  indicators (OG-1 AM; Fura PE3). Therefore the emission of S101 and OG-1 AM, can be easily separated using a corresponding dichroic mirror.

The double staining method described by Nimmerjahn et al.(2004) was modified in order to accelerate the loading procedure. The two indicators dyes were combined as described in the Methods section and co-ejected into the brain from the same pipette, resulting in a simultaneous labeling of the cells with S101 and OG-1 AM. When this protocol was applied to stain the visual cortex of the mouse in layer 2/3, astrocytes were double loaded, with S101 and OG-1 AM, and they appeared yellow on the merged image, while neurons stained only with OG-1 AM appeared green (**Fig. 11A**).

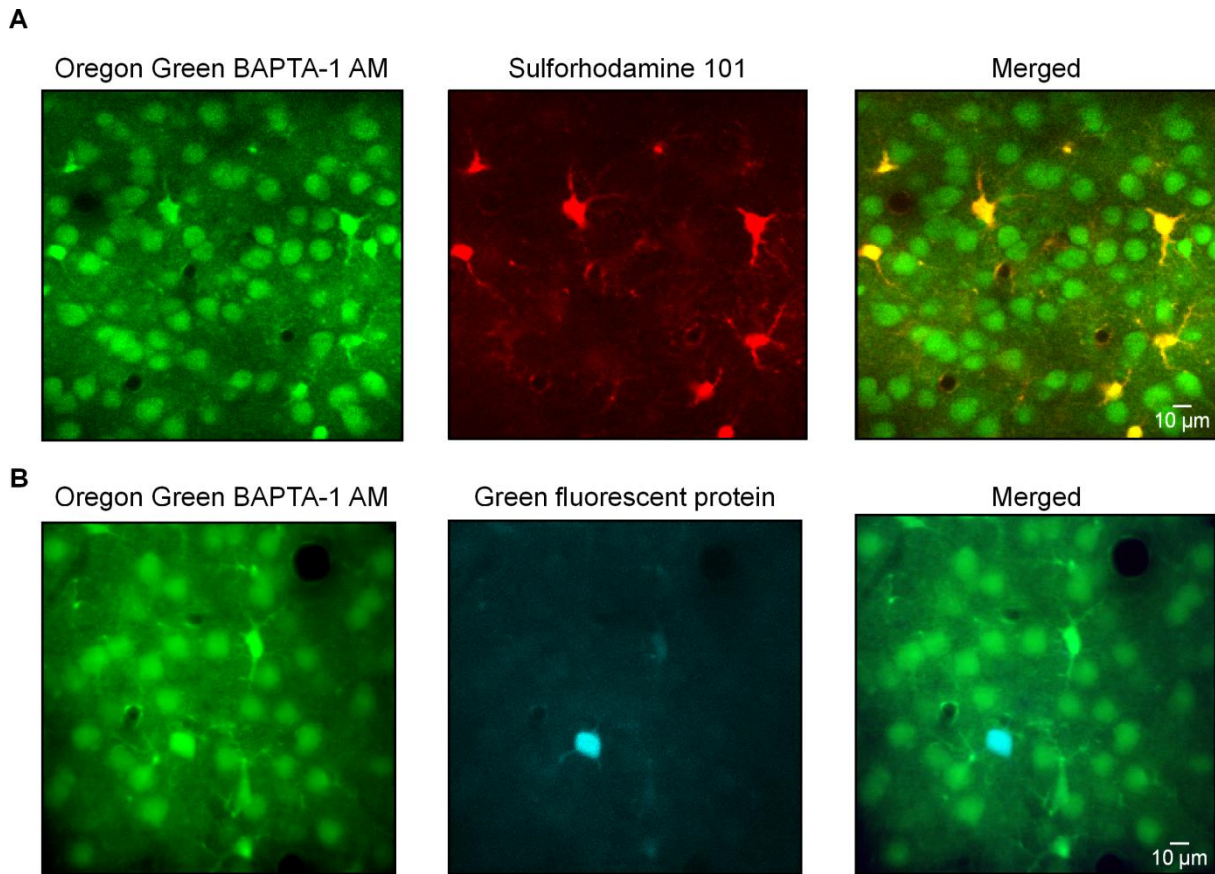


**Figure 11: Double staining and multicolour imaging of specific cell types.**

(A) Images of MCBL-loaded cells in layer 2/3 of mouse visual cortex stained simultaneously with a dye mixture containing OG-1 AM and the astroglial marker sulforhodamine 101. The fluorescence resulting from OG-1 AM is directed to the green channel (*left*) and the one from sulforhodamine 101 to the red channel (*middle*). On the merged image (*right*) the neurons appear in green and astrocytes in yellow. (B) Images of cortical layer 2/3 cells stained with OG-1 AM (*left*) in a transgenic mouse in which the somatostatin-positive GABAergic interneurons were labeled with the enhanced green fluorescent protein (EGFP) (*middle*). The merged image (*right*) shows all cells in green and the EGFP-positive interneuron in blue. Mouse age was P30 in (A) and P57 in (B).

Alternatively, cells of the specific subtype were recognized using mutant mice expressing a genetically encoded indicator, like, for example, the enhanced green fluorescent protein (EGFP). In **Fig. 11B** MCBL was applied in the visual cortex of transgenic mice expressing EGFP-labeled somatostatin-positive GABAergic interneurons. In this preparation, all cells were bolus loaded with OG-1 AM, while the presence of GABAergic interneurons was documented based on the EGFP labeling. Both OG-1 AM and EGFP were excited at 900 nm and the emitted light was split with a dichroic mirror at 515 nm and recorded in two separated channels. **Fig. 11B** shows an image taken from the layer 2/3 of the mouse visual cortex where one EGFP-positive interneuron (blue) was identified from the other surrounding cells stained with OG-1 AM (green).

Thus, in combination with other techniques which specifically label a certain cell type, MCBL loading is a very valuable tool to study cell-type specific morphological and functional properties of cortical cells.

### 4.1.2. *In Vivo* Imaging Using Genetically Encoded Fluorescent Calcium Indicator Proteins

Beside the small molecule  $\text{Ca}^{2+}$  indicators, genetically encoded fluorescent calcium indicator proteins (FCIPs) are another class of  $\text{Ca}^{2+}$  biosensors used for studying  $\text{Ca}^{2+}$  dynamics in living cells. Recently, a new transgenic mouse line expressing a FRET (fluorescence resonance energy transfer)-based  $\text{Ca}^{2+}$  biosensor was developed (Heim et al., 2007). The biosensor used troponin C (TnC), the  $\text{Ca}^{2+}$  sensor protein in skeletal and cardiac muscle (Heim and Griesbeck, 2004; Mank et al., 2006), as the  $\text{Ca}^{2+}$ -binding moiety. To increase the brightness of the sensor the donor cyan fluorescent protein was replaced by Cerulean and the common folding mutations V163A and S175G were introduced into the acceptor protein Citrine to enhance the folding and brightness. The resulting sensor was termed CerTN-L15. To generate transgenic mice, CerTN-L15 was expressed under the control of the neuron-specific Thy-1 promoter, and subsequently it was present in neurons of many brain regions, including neocortical and hippocampal pyramidal cells (Heim et al., 2007). Here the analysis of the biosensor's cortical expression pattern and its *in vivo*  $\text{Ca}^{2+}$  signaling properties are presented.

#### 4.1.2.1. *In Vivo* Two-Photon Imaging of CerTN-L15 Transgenic Mouse

Two-photon imaging of the layer 2/3 in the visual cortex of CerTN-L15 transgenic mouse (**Fig. 12A**) revealed a characteristic pattern of the cellular fluorescence signals. The fluorescence of CerTN-L15 was confined to ring-like structures with the diameter of 10-15  $\mu\text{m}$  (most probably cell somata) and highly-fluorescent bright spots (dendrites) 1-2  $\mu\text{m}$  in diameter (**Fig. 12A** and **Fig. 13B**, middle panel, some of the bright spots are marked with asterisks). In addition, the images contained non-fluorescent areas. Some of these non-fluorescent areas were blood vessels surrounded by astrocytic processes (arrowheads on **Fig. 12A**), as was shown by complementary staining with astrocyte-specific fluorescent marker sulforhodamine 101 (Nimmerjahn et al., 2004). The others (arrows on **Fig. 12A**) were most probably somata of cells which did not express CerTN-L15. There was no overlap between fluorescence of CerTN-L15 and that of S101 (**Fig. 12A, B**) confirming that CerTN-L15 was expressed exclusively in neurons.

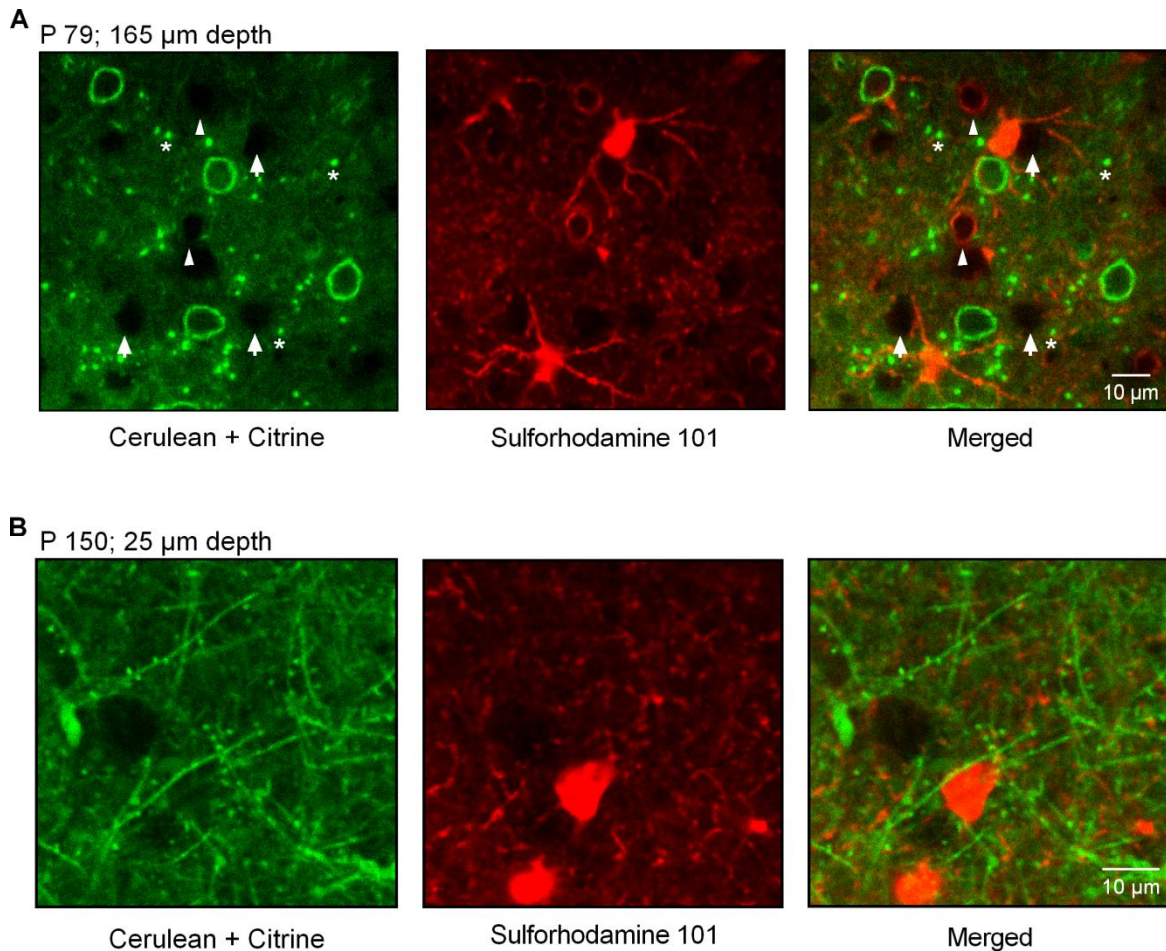


**Figure 12: *In vivo* expression pattern of CerTn-L15 in the mouse cortex.**

(A, B) Micrographs taken *in vivo* in the visual cortex of two Thy 1-CerTn-L15 transgenic mice at different depths below the cortical surface. Images on the right show the selective neuronal expression of the biosensor in layer 2/3 individual neurons (A), in dendrites and in the dendritic spines of layer 1 (B), proved by counterstaining with the astroglia-selective marker sulforhodamine 101. Fluorescence of Cerulean and Citrine is directed to the green channel (*left panels*) and fluorescence of sulforhodamine 101 to the red channel (*panels in the middle*). The merged pictures (*right panels*) demonstrate no overlap between sulforhodamine-positive astroglial cells and CerTn-L15 fluorescence. Arrowheads indicate blood vessels surrounded by glial processes, arrows point out neurons that do not express CerTn-L15, and asterisks outline CerTn-L15-positive dendritic processes.

Secondary-tertiary spiny dendrites that were near and parallel to the cortical surface were particularly well suited for imaging. As shown in **Fig. 12B**, in CerTN-L15 expressing mice the concentration of the indicator dye within the dendrites and the dendrite-to-background fluorescence ratio allowed the clear visualization of fine dendrites and their spines. The double staining with S101 proved once again no overlapping between the CerTN-L15 expression in the dendrites and S101 staining of astrocytes and their processes (**Fig. 12B**).

Three-dimensional reconstructions of image stacks showed that within individual neurons the indicator was distributed homogeneously in the cytosol, with no signs of

aggregation. It filled all neuronal processes, thus properly outlining the architecture of the cells (**Fig. 13**). The sensor was excluded from the cell nucleus as expected for a protein with a molecular weight of 69 kD (Talcott and Moore, 1999). This caused a ring-like appearance of cell somata under *in vivo* conditions, where cells were usually viewed from above (**Fig. 12A** and **Fig. 13B**, panel in the middle). The cytosolic localization of the sensor was confirmed by analyzing its distribution inside the cells imaged at high resolution (120x magnification, **Fig. 13B**, upper and lower panels). The three-dimensional reconstructions of the *in vivo* obtained images showed that the abundantly present bright dots ( $\varnothing$  1-2  $\mu\text{m}$ , asterisks on **Fig. 12A** and **Fig. 13B**) corresponded to brightly labeled apical dendrites of pyramidal neurons (**Fig. 13A, C**).

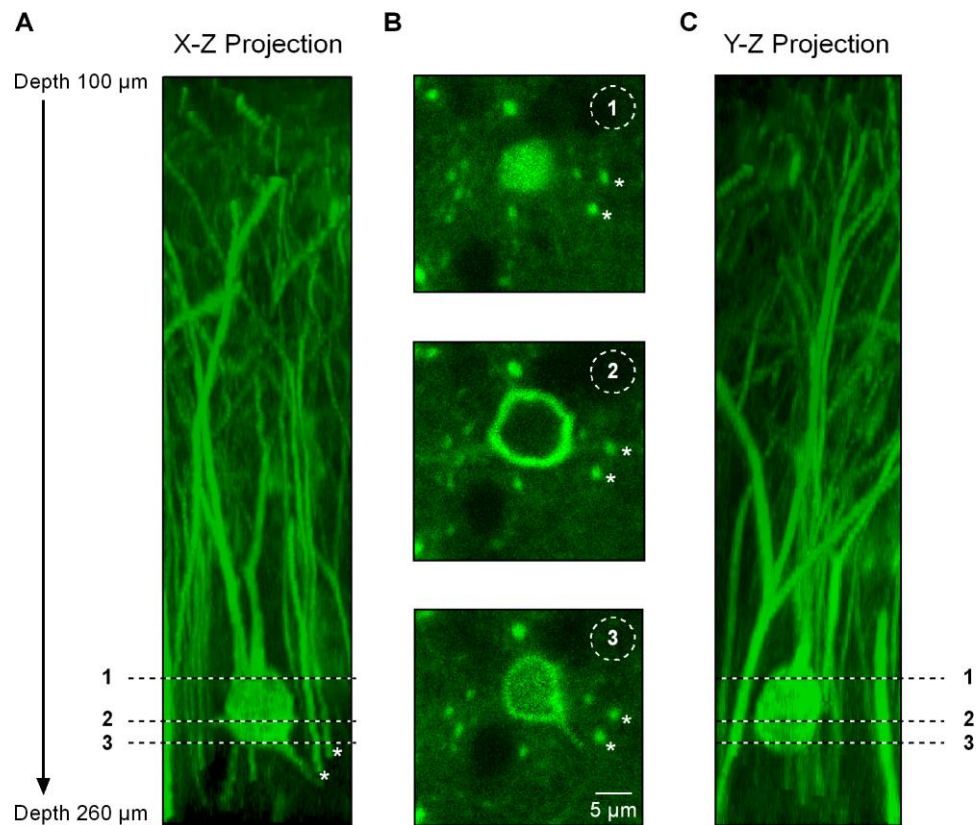


**Figure 13: Three dimensional reconstructions of a layer 2/3 pyramidal neuron and dendritic processes expressing CerTN-L15.**

(A-C) High-resolution images showing one pyramidal neuron in cortical layer 2/3 and dendritic processes of deeper cortical cells (*left and right*) expressing CerTN-L15 and reconstructed from a stack of images taken from 100 to 260  $\mu\text{m}$  below the cortical surface (with 2  $\mu\text{m}$  steps). (B) Three selected sections (each taken at the depth marked by respective number on the left and right) showing that CerTN-L15 is expressed in the cytosol, but not in the nucleus. Asterisks indicate dendritic processes.

#### 4.1.2.2. *In vivo* Calcium Measurements from Cell Somata and Spiny Dendrites in CerTN-L15 Transgenic Mouse

Iontophoretic glutamate applications were performed to probe for the  $\text{Ca}^{2+}$  sensitivity of CerTN-L15 in single neurons and their dendrites *in vivo*. The duration of the stimulation pulses used to evoke somatic  $\text{Ca}^{2+}$  transients was 100-300 ms. The resulting amplitudes ( $\Delta\text{R}/\text{R}$ ) of the  $\text{Ca}^{2+}$  transients were  $63.7 \pm 5.1\%$ ,  $n=11$  events. The time courses of somatic glutamate-evoked  $\text{Ca}^{2+}$  transients were analyzed by measuring the decay time constant (**Fig. 14B** and **C**), which was on average  $1.68 \pm 0.3$  s ( $n=11$  events) *in vivo*. These data yielded similar results to the ones obtained with comparable protocols from the *in vitro* recordings, however, the *in vivo* measurements had higher detection threshold (Heim et al., 2007). The reduced detection sensitivity *in vivo* could partially be due to the less favorable viewing angle for the somatic *in vivo* recordings. Indeed, cell somata appeared as ring-like structures when viewed from above (*in vivo*, **Fig. 12A**, **Fig. 13B** panel in the middle) and more frequently as filled circles when viewed from the side, as it was the case in the *in vitro* conditions (Heim et al., 2007). Therefore, fewer pixels were available for somatic  $\text{Ca}^{2+}$  measurements *in vivo*. In addition, the sensitivity of the *in vivo* measurements was most probably compromised by light scattering (Helmchen and Denk, 2005).

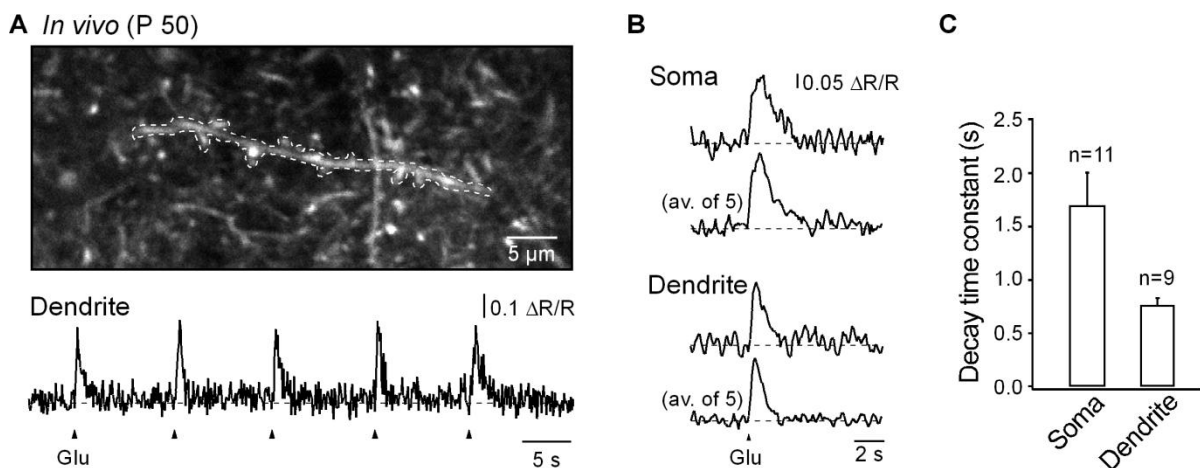


**Figure 14: CerTN-L15-dependent  $\text{Ca}^{2+}$  measurements from somata and dendrites *in vivo*.** (A) High-magnification image of a spiny dendrite at  $30\ \mu\text{m}$  below the cortical surface (*upper panel*). CerTN-L15-based  $\text{Ca}^{2+}$  transients calculated from the region of interest delineated in the upper panel in response to five consecutive 40 ms long iontophoretic glutamate applications (*lower panel*). (B) Individual and average of 5  $\text{Ca}^{2+}$  transients recorded simultaneously in the soma (*upper traces*) and in a neighboring dendrite of another cell (*lower traces*) evoked by 30 ms long iontophoretic glutamate applications. (C) Bar graphs presenting the mean values of the decay time constants of somatic and dendritic glutamate-evoked  $\text{Ca}^{2+}$  transients recorded *in vivo*.

The initial processing of synaptic signals in cortical neurons is likely to take place in spiny dendrites, in the immediate vicinity of synapses (Holthoff et al., 2004; Polsky et al., 2004). Therefore, attempts to measure  $\text{Ca}^{2+}$  signals in these structures were carried out. CerTN-L15 provided discernable  $\text{Ca}^{2+}$  signals from small dendritic segments (approx.  $1 \times 35 \mu\text{m}$ , **Fig. 14A**). Brief (30-50 ms) iontophoretic glutamate pulses evoked dendritic  $\text{Ca}^{2+}$  transients with mean amplitudes of  $48.8 \pm 7 \%$  ( $n=9$  events) and decay time constants of  $0.76 \pm 0.07$  s (**Fig. 14B** and **C**). Remarkably, the signal-to-noise ratio of the glutamate-evoked dendritic  $\text{Ca}^{2+}$  signals was large enough to distinguish individual, nonaveraged  $\text{Ca}^{2+}$  transients from the background noise (**Fig. 14A, B**).

The cellular expression pattern of CerTN-L15  $\text{Ca}^{2+}$  sensor with bright dendrites and sensor-free nuclei renders this indicator particularly appropriate for dendritic recordings. On the other hand, MCBL technique of *in vivo* cells labeling with small molecule  $\text{Ca}^{2+}$  indicators provides good staining of cells somata, but not of dendrites. Taken together, these techniques could complement each other and thus facilitate functional analyses of cortical networks function *in vivo*.

## 4.2. Spontaneous Network Activity in the Developing Visual Cortex

### 4.2.1. Emergence of Spontaneous Calcium Waves at the Beginning of the Second Postnatal Week

Taking advantage of the technical developments described in Section 4.1., the second major aim of this thesis was to characterize the patterns and properties of the spontaneous and flash-evoked activity in the mouse visual cortex in relation to the developmental stage. Our motivation to do so rely on the fact that mouse visual cortex receives increasing attention due to availability of transgenic animals. However, little is known about the development of vision in mice and underlying cellular/ network mechanisms.

The spontaneous activity in layer 2/3 of the mouse visual cortex during development was investigated *in vivo* using two-photon microscopy and the MCBL method for loading the cortical cells with the membrane permeant  $\text{Ca}^{2+}$  indicator OG-1 AM. Mice at different ages were anesthetized with the volatile anesthetic Isoflurane, cells in the visual cortex were stained with OG-1 AM (**Fig. 15A**), and measurements of the spontaneously occurring changes in the intracellular  $\text{Ca}^{2+}$  concentration within the loaded cells were performed. **Fig. 15B** shows

stained cortical layer 2/3 cells located at about 130  $\mu\text{m}$  under the cortical surface of a P9 mouse. Because the imaging procedure is minimally invasive, during recordings the concentration of Isoflurane was maintained at the minimum level necessary to produce a superficial state of the animal's anesthesia, in order to avoid movements. This level was reached with concentrations of about 0.5-1% in pure oxygen. The recording sessions consisted of several imaging periods lasting between 90 to 300 sec. On average 20 to 60 cells were recorded simultaneously. The animals tested were divided into several age groups as shown in **Table 1**.

Under these experimental conditions repetitive, spontaneous wave-like  $\text{Ca}^{2+}$  transients occurred globally throughout the whole recorded cortical region (**Fig. 15B, C**). The  $\text{Ca}^{2+}$  waves were periodically recurrent at slow rates (0.5 waves/min in the example shown in **Fig. 15D** at P9). The discovery of these spontaneous  $\text{Ca}^{2+}$  waves was surprising in view of earlier findings that, in neonates, early network oscillations-associated  $\text{Ca}^{2+}$  changes (Garaschuk et al., 2000) are suppressed by anesthetics (Adelsberger et al., 2005).

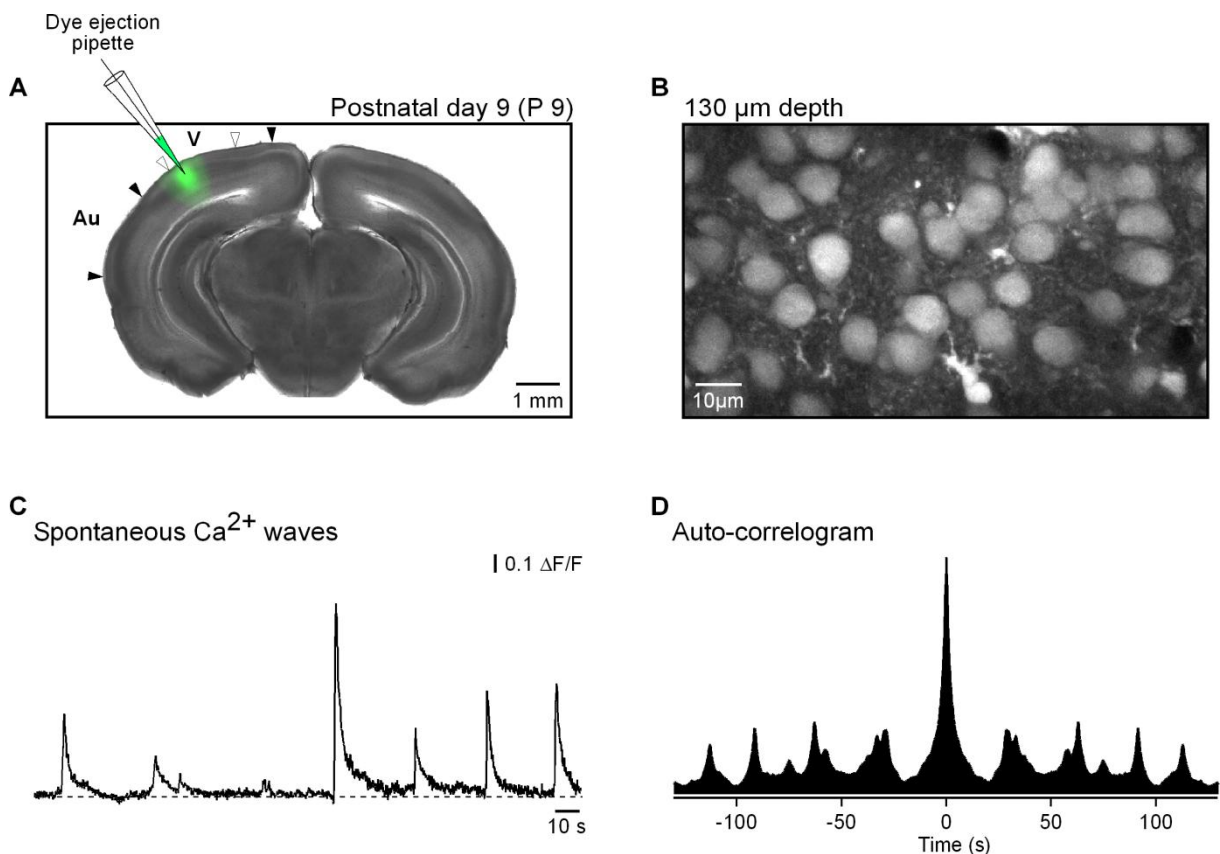


**Figure 15: Recording of slow spontaneous  $\text{Ca}^{2+}$  waves in the mouse visual cortex.**

(A) A combined fluorescence/transmitted light micrograph of a 500  $\mu\text{m}$  thick coronal brain slice from a P9 mouse taken after an *in vivo* experiment. The primary visual cortex stained *in vivo* with OG-1 AM is shown in green. The position of the pipette used for staining the cells with OG-1 AM is shown schematically. The borders of the visual (V) and auditory (Au) cortices are marked by filled arrowheads. Open arrows delineate the primary visual cortex. (B) High-resolution image taken *in vivo* in layer 2/3 of the visual cortex where recordings in (C)



were conducted. (C) Spontaneous  $\text{Ca}^{2+}$  waves recorded from a large region of interest covering the whole area shown in (B). (D) An autocorrelogram of the trace shown in (C). Note that the spontaneous  $\text{Ca}^{2+}$  waves represent an oscillation having at this age (P 9) a period of approximately 30 s.

Cortical layer 2/3 contains not only cell somata, but also cellular processes such as neuronal dendrites, axons and glial processes which form the neuropil. MCBL loading technique stained brightly the cell bodies (**Fig. 15B**) because of the abundant accumulation of the fluorescent indicator into the cytoplasm. In addition, it also stained the neuropil, revealing that various cellular compartments had also taken up the  $\text{Ca}^{2+}$  indicator molecules. Neuropil staining showed no distinguishable structures, most likely because all stained subcellular structures had similar brightness. The  $\text{Ca}^{2+}$  waves were detected within the entire cortical region, both in cells and in neuropil, as global network activation (**Fig. 15B, C**). To investigate the contribution of the cellular and extracellular (neuropil) component to the generation of  $\text{Ca}^{2+}$  waves, the  $\text{Ca}^{2+}$  signals deriving from each of these elements were analyzed separately and the relation between them was examined (**Fig. 16**). This analysis showed that the wave activity was present both in the neuropil (recorded from large regions of interest devoid of cell somata (**Fig. 16A**)) and in the neurons (**Fig. 16A, B**). Remarkably, most of the neurons participated in this spontaneous activity ( $75 \pm 7\%$ ,  $n = 3$  experiments). This dense activation of the vast majority of neurons is in striking contrast with to the results obtained in the somatosensory and motor cortex of older mice, where a sparse activation (10%) of layer 2/3 neurons is encountered (Kerr et al., 2005).

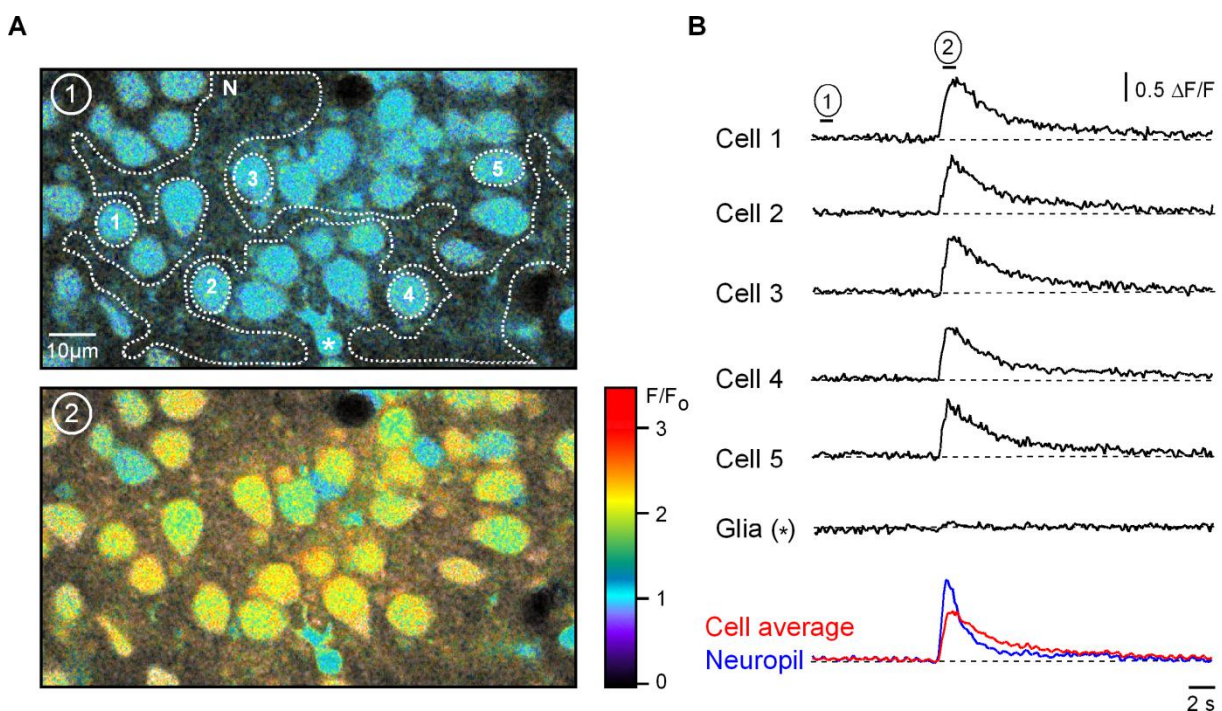


**Figure 16: Contribution of the cellular and neuropil components to the generation of the spontaneous  $\text{Ca}^{2+}$  waves in cortical layer 2/3.**

(A)  $F/F_0$  images illustrating the intracellular  $\text{Ca}^{2+}$  levels before (*upper*) and on the peak (*lower*) of a spontaneous  $\text{Ca}^{2+}$  wave (the time points at which the images in (A) were taken are indicated by circled numbers in (B)). Each image is the result of averaging 5 consecutive frames acquired with 7 Hz. (B)  $\text{Ca}^{2+}$  transients, recorded during the spontaneous  $\text{Ca}^{2+}$  wave illustrated in (A), measured in the individual neurons, a glia cell and in the neuropil (marked in (A) with corresponding numbers, asterisk and the letter N, respectively). Cell average trace (*red*) is the mean of the  $\text{Ca}^{2+}$  transients recorded in all 31 neurons present in the area shown in (A).

The involvement of glia cells in the spontaneous  $\text{Ca}^{2+}$  waves was also investigated. Glia cells could be easily identified due to their brighter staining and their specific morphology with thick processes (Fig. 16), as well as by their positive reaction to the sulforhodamine 101 staining (Fig. 11A, 17). When simultaneous measurements of  $\text{Ca}^{2+}$  signals in both astrocytes and neurons were conducted, it was evident that only neurons produced fast  $\text{Ca}^{2+}$  transients, synchronous with the  $\text{Ca}^{2+}$  waves, while the astrocytes (n=9 cells) were not engaged in the wave activity (Fig. 16, 17). Previous studies (Hirase et al., 2004; Nimmerjahn et al., 2004; Kerr et al., 2005) have shown that  $\text{Ca}^{2+}$  signals in astrocytes have long durations on the minute time scale and are thus markedly different from the fast wave-associated  $\text{Ca}^{2+}$  transients recorded in neurons.

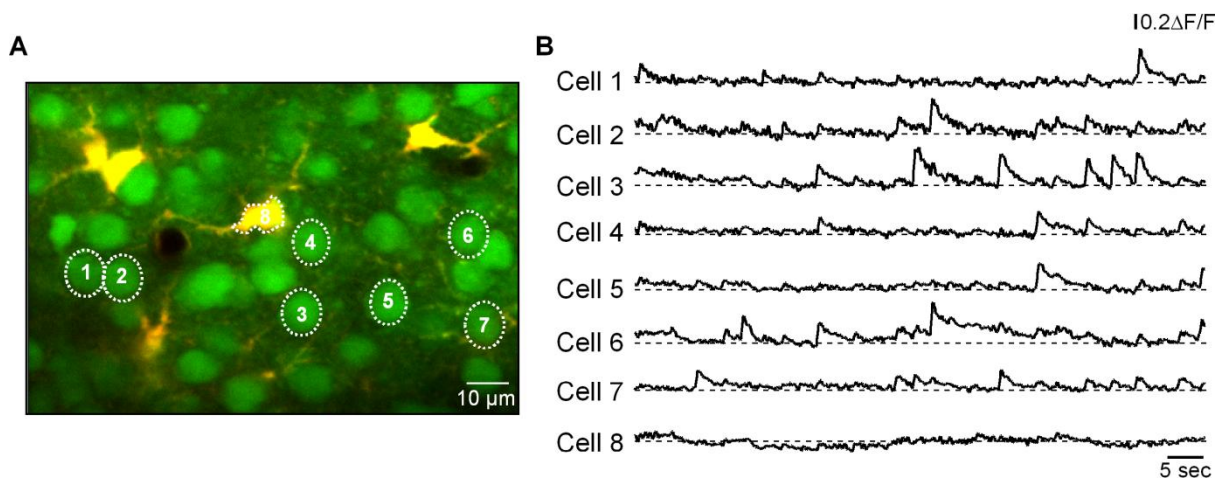


**Figure 17: Astrocytes do not participate in the neuronal  $\text{Ca}^{2+}$  waves.**

(A) *In vivo* image acquired in layer 2/3 of the visual cortex in a P14 mouse showing neurons stained with OGB-1 AM (*green*) and astrocytes stained both with OGB-1 AM and with S101 (*yellow*). Traces in (B) illustrate spontaneous  $\text{Ca}^{2+}$  transients measured in the cells marked with the corresponding numbers in the image.

A detailed developmental analysis revealed that the spontaneous  $\text{Ca}^{2+}$  waves were first detected at P8 (Fig. 18). At P7, the youngest age tested, only in 1 out of 5 experiments performed  $\text{Ca}^{2+}$ -dependent fluorescent changes reminiscent of the spontaneous  $\text{Ca}^{2+}$  waves could be detected. They occurred with very low amplitude and extremely seldom during the prolonged recording session, and therefore this experiment was not included in the final

analysis. Between P8-P9 the  $\text{Ca}^{2+}$  waves were detected with a higher probability. The earliest age at which the spontaneous  $\text{Ca}^{2+}$  waves were reliably detected was P10 (See **Table 1**).

Postnatal age	Experiments in which $\text{Ca}^{2+}$ waves could be detected/total number of experiments performed
P7	1/5
P8	4/7
P9	3/7
P10	4/4
P11	5/5
P12-13	12/12
P14-15	6/6
P16-19	6/6
P20-29	10/10
P30-39	4/4
P48-65	6/6

**Table 1:** Number of experiments at each individual postnatal age in which the spontaneous  $\text{Ca}^{2+}$  waves could be recorded.

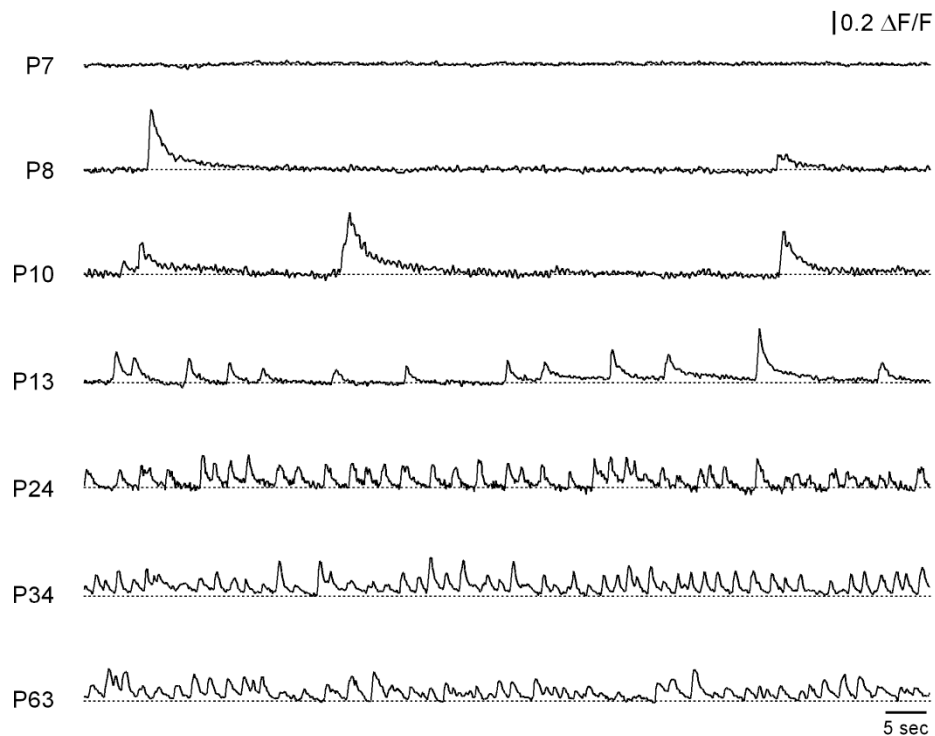


**Figure 18: Development of the slow spontaneous  $\text{Ca}^{2+}$  waves during the maturation of the mouse visual cortex.**

*In vivo* recordings of spontaneous  $\text{Ca}^{2+}$  waves acquired from the cortical layer 2/3 at different ages during development. The  $\text{Ca}^{2+}$  waves were recorded at each age from a large region of interest (as shown in **Fig. 15B**).

At P8 the spontaneous  $\text{Ca}^{2+}$  waves occurred at a low frequency ( $0.5 \pm 0.1$  waves/min) and high amplitude ( $38.4 \pm 4.5\%$ ). During the next developmental days, the frequency of the

waves gradually increased, while the amplitude decreased (Fig. 18, 19). After the end of the third postnatal week, the  $\text{Ca}^{2+}$  waves reached a delta range frequency of about 30 waves/min (or 0.5 Hz). The delta  $\text{Ca}^{2+}$  waves persisted at this frequency in adult mice.

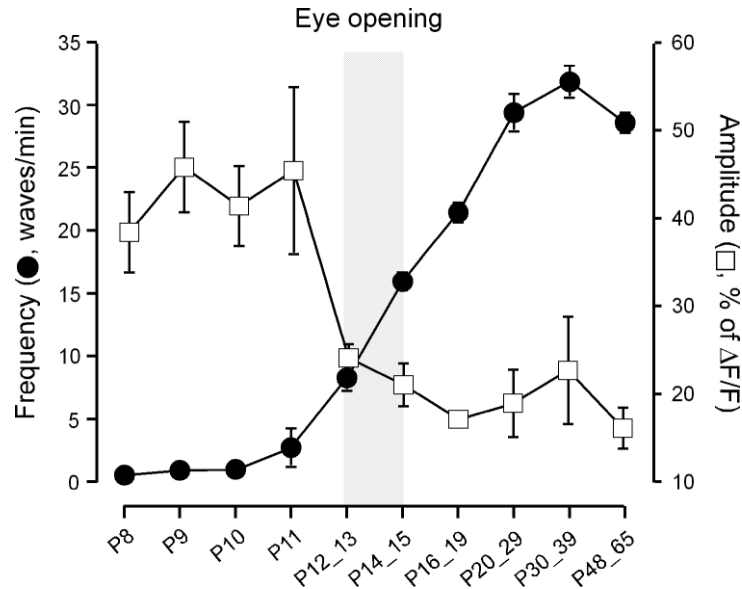


**Figure 19: Developmental profile of the spontaneous  $\text{Ca}^{2+}$  waves.**

A graph illustrating frequencies (filled circles) and amplitudes (open squares) of the spontaneous  $\text{Ca}^{2+}$  waves at different ages (n=4 animals, 3, 4, 5, 12, 6, 6, 10, 4, 6 from left to right).

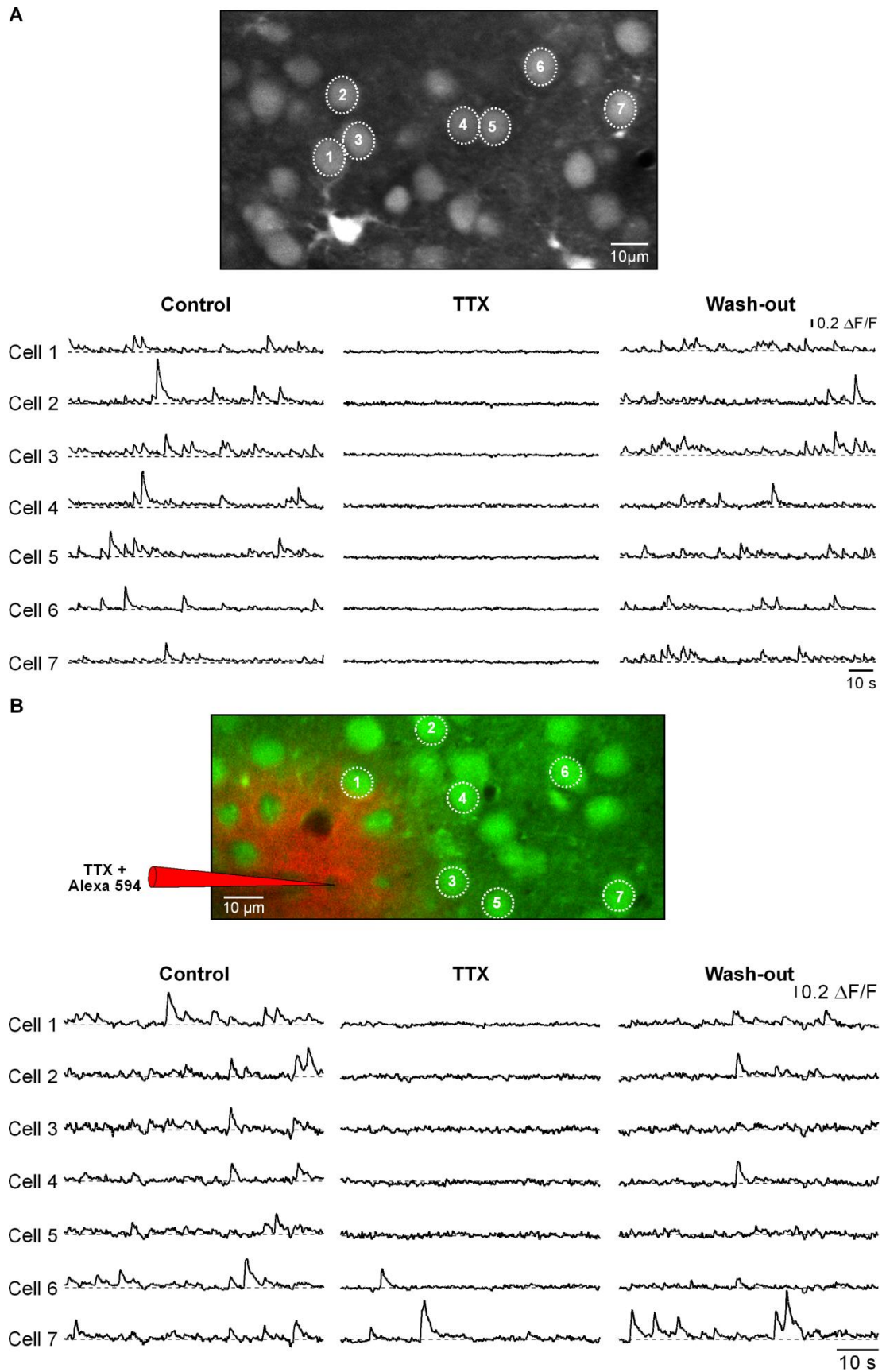
During the first postnatal week the immature neocortical activity *in vivo* is represented by the spontaneous early network oscillations-associated  $\text{Ca}^{2+}$  changes (Garaschuk et al., 2000). These are suppressed by anesthetics (Adelsberger et al., 2005) and by the developmental transition of GABAergic transmission from excitatory to inhibitory (around P7) (Garaschuk et al., 2000). The results presented here reveal a new type of slow spontaneous  $\text{Ca}^{2+}$  waves in the visual cortex that emerge at the beginning of the second postnatal week and increase in frequency during later stages of development from a sub-delta to a delta range of cortical wave activity (Buzsaki and Draguhn, 2004). Distinctive features of the new  $\text{Ca}^{2+}$  wave activity, as compared with the previously reported early network oscillations, are the insensitivity to anesthetics, and the persistence after the switch of GABAergic transmission from excitatory to inhibitory.

## 4.2.2 Mechanisms Underlying the Spontaneous Calcium Waves

To understand the mechanisms underlying the generation of the spontaneous  $\text{Ca}^{2+}$  waves different pharmacological substances were applied *in vivo* to the cells of interest in two different ways. In the so called “bath application” the drugs were added to the preheated ACSF that perfused the recording chamber. Drugs diffused from the surface into the depth of the cortical tissue through the craniotomy used to load the cells with the  $\text{Ca}^{2+}$  indicator. However, in the conditions of bath applied drugs it remained unclear, whether the primary site of drug action was in layer 2/3 or whether it took place in the deeper cortical layers. Therefore, alternatively, the drugs were applied by local application directly to the cells of interest in cortical layer 2/3 by inserting a pipette through the craniotomy and releasing the substance either iontophoretically or by pressure-application. Such local applications allowed a better control of drug effect in the treated area, the effect being restricted only to the cells situated in the close vicinity of the application pipette. The applied substances were “visualized” by addition of the cell-impermeant, fluorescent dye Alexa 594 (Alexa 594, 12.5-500  $\mu\text{M}$  depending on the length of application) to the pipette solution. The presence of Alexa 594 helped to verify the onset, effectiveness and localization of drug application. Thus, in the cells situated near the pipette and within the Alexa 594 cloud an unambiguous drug effect could be observed (**Fig. 20B**, **Fig. 22**, **Fig. 24B** and **Fig. 25**). In all the pharmacology experiments the drug effect was quantified as the mean blockade (expressed in percentage) of the frequency of  $\text{Ca}^{2+}$  transients measured in individual neurons per minute.

### 4.2.2.1 *In Vivo* Spontaneous Calcium Waves Require Firing of Action Potentials

The spontaneous  $\text{Ca}^{2+}$  waves in layer 2/3 of the visual cortex were completely and reversibly blocked by the voltage-gated  $\text{Na}^+$  channels blocker tetrodotoxin (TTX). TTX produces a potent and specific blockade of the  $\text{Na}^+$  channels responsible for action potential (AP) generation. This effect was seen both by using bath (**Fig. 20A**, 1-2 $\mu\text{M}$  TTX, n=5 animals, P16-P22) and local pressure (**Fig. 20B**, 2.5-5 $\mu\text{M}$  TTX, n=6 animals, P16-P35) applications.



pressure (**B**) applications of TTX. In (**A**) 2  $\mu\text{M}$  TTX was used, while in (**B**) the pipette solution contained 5 $\mu\text{M}$  TTX and 50  $\mu\text{M}$  Alexa 594. In the merged image in (**B**) the fluorescence of OG-1 AM is directed to the green channel, while fluorescence of Alexa 594 is directed to the red channel. Mouse age was P21 in (**A**) and P24 in (**B**).

Bath application of TTX completely silenced the entire network. To confine the TTX blockade to the imaged cells in cortical layer 2/3, TTX was also applied locally. The degree of TTX blockade in these conditions reached  $80.87 \pm 8.09\%$  (**Fig. 23**). This value was inferior to the one seen in bath application presumably due to the diffusion gradient of the drug which prevented that the same drug concentration is reached in the vicinity of all cells in the imaged region. The results achieved using both approaches showed that the generation of the spontaneous  $\text{Ca}^{2+}$  waves *in vivo* depends on action potential firing. Similar results proving the dependency upon AP firing *in vivo* were obtained in the rat somatosensory/motor cortex (Kerr et al., 2005). By combining electrical recordings with  $\text{Ca}^{2+}$  imaging this and our own study (Garaschuk et al., 2006b) showed that action potentials correlate with somatic  $\text{Ca}^{2+}$  transients in same cells and that the amplitude of the  $\text{Ca}^{2+}$  transient is proportional with the number of APs.

#### 4.2.2.2 *In Vivo* Spontaneous Calcium Waves Require Glutamatergic Synaptic Transmission

The spontaneous  $\text{Ca}^{2+}$  waves detected in layer 2/3 neurons in the visual cortex were also completely ( $98.86 \pm 1.12\%$ , **Fig. 23**) and reversibly (**Fig. 21**,  $n=6$  experiments, P16-P29) blocked by a mixture of glutamate receptors antagonists CNQX (50 $\mu\text{M}$ ) and APV (50-100 $\mu\text{M}$ ). This result indicates that the recruitment of layer 2/3 neurons into the spontaneous  $\text{Ca}^{2+}$  waves requires active synaptic glutamatergic transmission.

Another set of experiments was performed to investigate which glutamatergic receptor-channels are involved in the  $\text{Ca}^{2+}$  wave activity. The contribution of each subtype of glutamate receptors (AMPA or NMDA receptor-channels) was investigated separately by using specific antagonists.

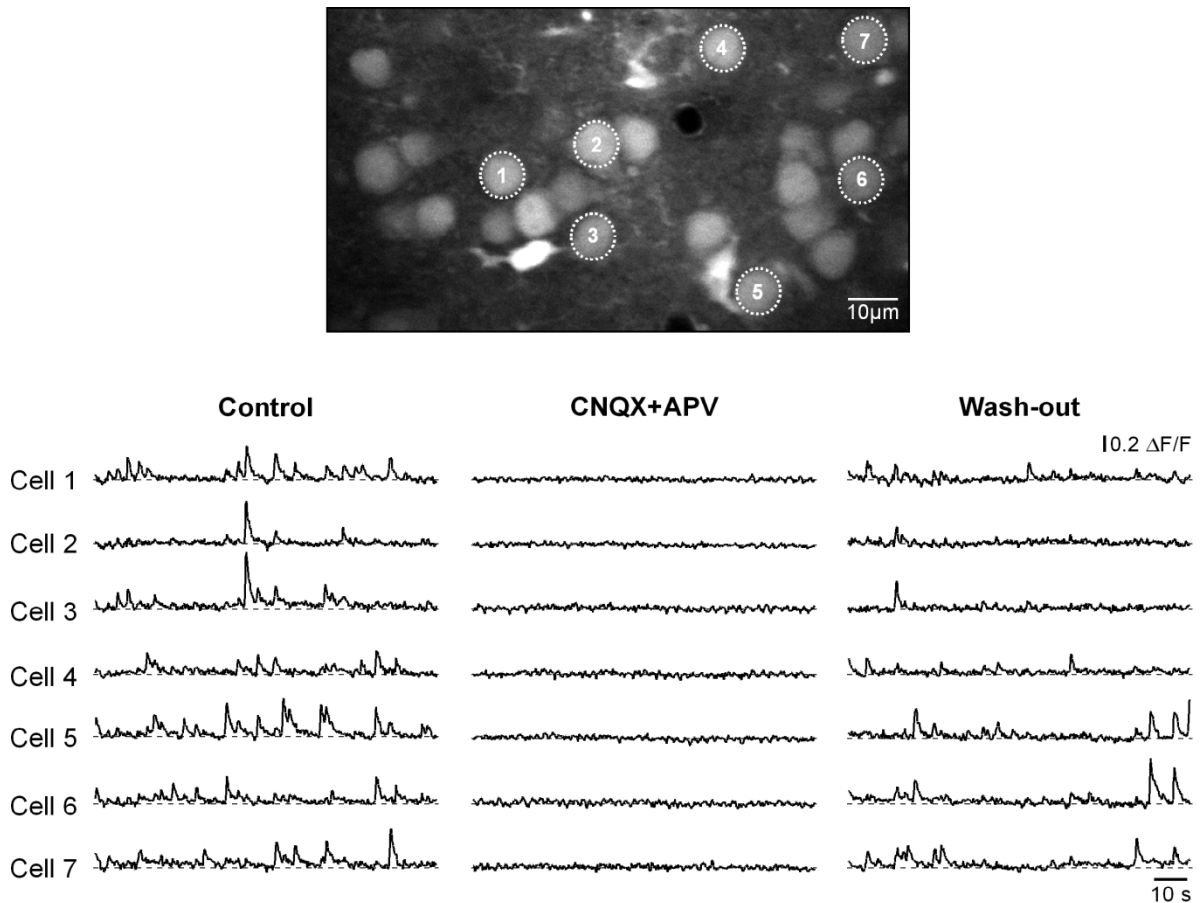


**Figure 21: Spontaneous  $\text{Ca}^{2+}$  waves require glutamatergic synaptic transmission.**

Spontaneous  $\text{Ca}^{2+}$  waves measured in cortical layer 2/3 neurons, marked with respective numbers in the image, in control (*left*), during bath application of a solution containing  $50\mu\text{M}$  CNQX and  $100\mu\text{M}$  APV (*middle*), and after wash out of CNQX and APV (*right*). Mouse age was P16.

#### 4.2.2.3 The Spontaneous Calcium Waves Involve Postsynaptic AMPA Receptor Activation

The role of postsynaptic AMPA receptor activation was tested by local application of the AMPA receptor antagonist CNQX ( $1\text{mM}$ ) to the cortical layer 2/3 cells by iontophoresis (**Fig. 22**,  $n=6$  experiments, P16-P28). As previously reported for the motor and somatosensory cortex (Kerr et al., 2005) also in the visual cortex the  $\text{Ca}^{2+}$  wave activity was abolished by blocking the postsynaptic AMPA receptors. The blocking effect was clear, the frequency of wave-associated spontaneous somatic  $\text{Ca}^{2+}$  transients significantly decreasing with  $90.22 \pm 2.62\%$  during the antagonist application.



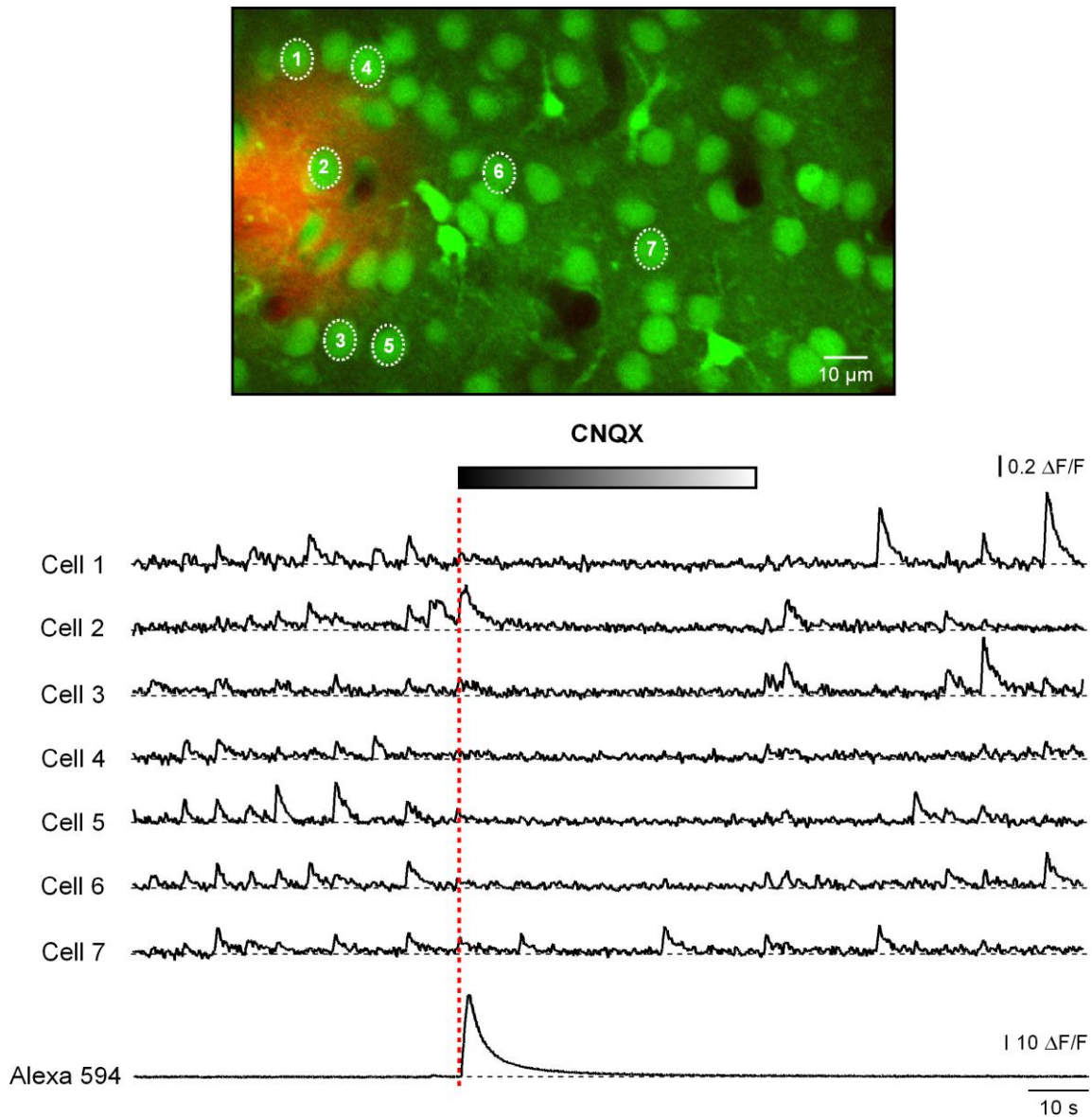


**Figure 22: Postsynaptic AMPA receptors are necessary for the spontaneous  $\text{Ca}^{2+}$  waves.** High-magnification *in vivo* image taken in layer 2/3 of the mouse visual cortex (*upper panel*). Spontaneous  $\text{Ca}^{2+}$  transients measured from the cells marked with corresponding numbers on the image (*middle*), and the time course of Alexa 594-based fluorescent transient recorded before, during and after 1 sec iontophoretic application of 1 mM CNQX. In the application pipette CNQX was mixed with Alexa 594 to mark the place and timing of the application. In the merged image the fluorescence of OG-1 is directed to the green channel, while fluorescence from Alexa 594 is directed to the red channel. Mouse age was P17.

A summary of the pharmacological profile of the slow spontaneous  $\text{Ca}^{2+}$  waves is given in **Fig. 23**.

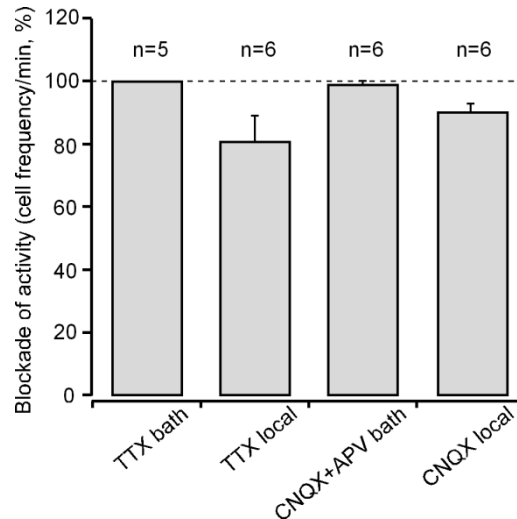


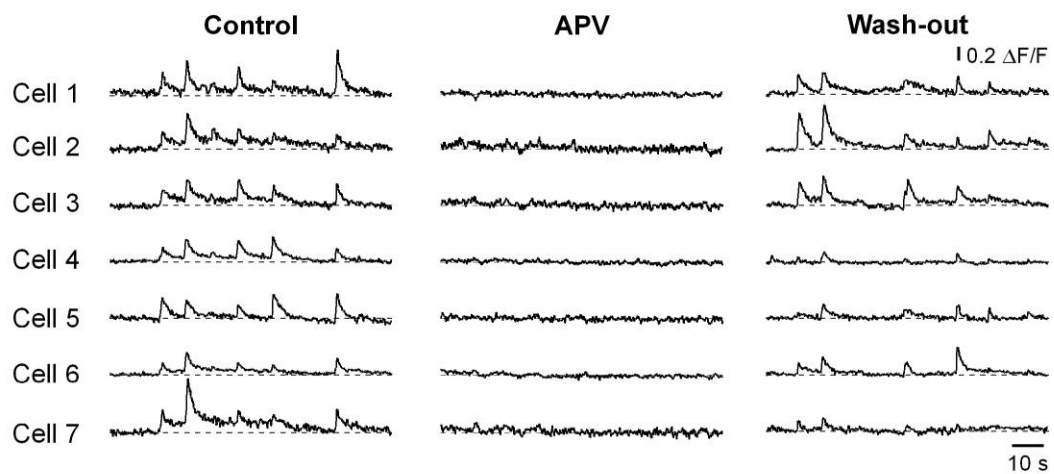
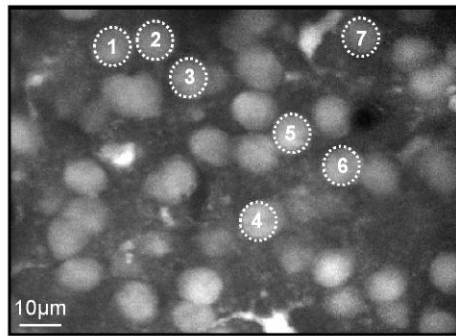
**Figure 23: Pharmacological profile of the spontaneous  $\text{Ca}^{2+}$  waves.**

Bar graphs illustrating the blockade of the frequency of spontaneous  $\text{Ca}^{2+}$  transients per cell (normalized to control) produced by application of different drugs: 1-2  $\mu\text{M}$  TTX in bath application, (n=5 mice); 2.5-5 $\mu\text{M}$  TTX in local pressure application (n=6); 50 $\mu\text{M}$  CNQX and 50-100 $\mu\text{M}$  APV in bath application (n=6); and 1 mM CNQX in iontophoretic application (n=6).

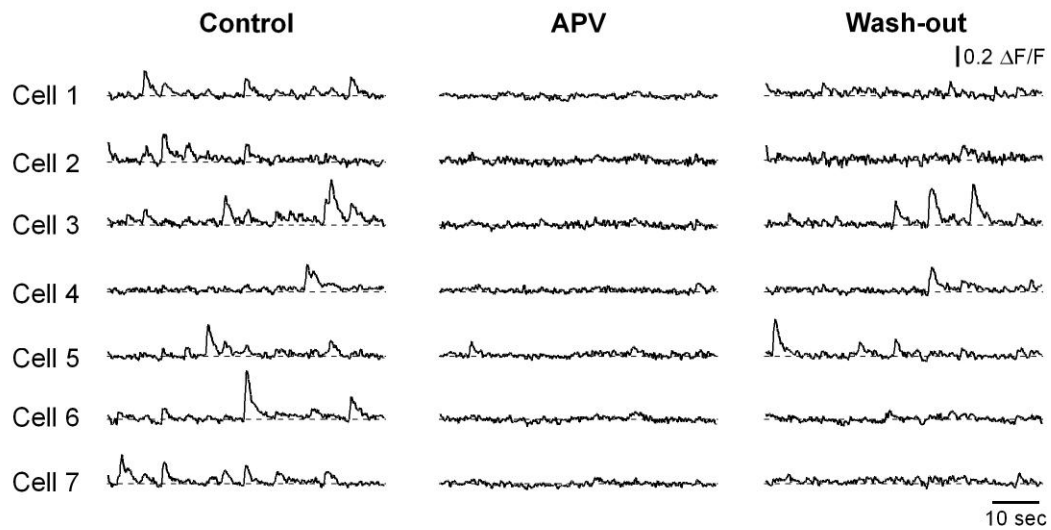
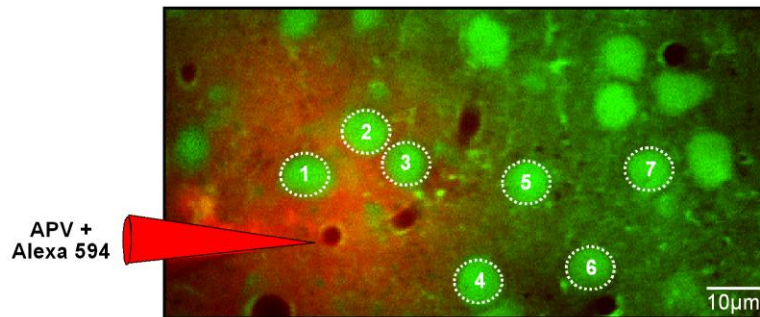
#### 4.2.2.4 NMDA Receptor-Channels Activation Play a Critical Role for the Spontaneous Calcium Waves

NMDA receptors make a major contribution to normal excitatory transmission in adult visual cortex (Miller et al., 1989; Bear et al., 1990). To test whether NMDA receptor-channels play a special role in the spontaneous  $\text{Ca}^{2+}$  waves different types of selective NMDA receptors antagonists were used either in bath or local application. The competitive antagonists APV (**Fig. 24A**, 50-100 $\mu\text{M}$ , n=5 experiments, P11-P17) and CGP (25-50 $\mu\text{M}$ , n=5 experiments, P11-P18) in bath application profoundly and reversibly suppressed the  $\text{Ca}^{2+}$  waves (**Fig. 26**,  $98.35 \pm 1.64\%$  blockade of the cell frequency for APV and  $95.64 \pm 2.12$  for CGP, respectively).

A



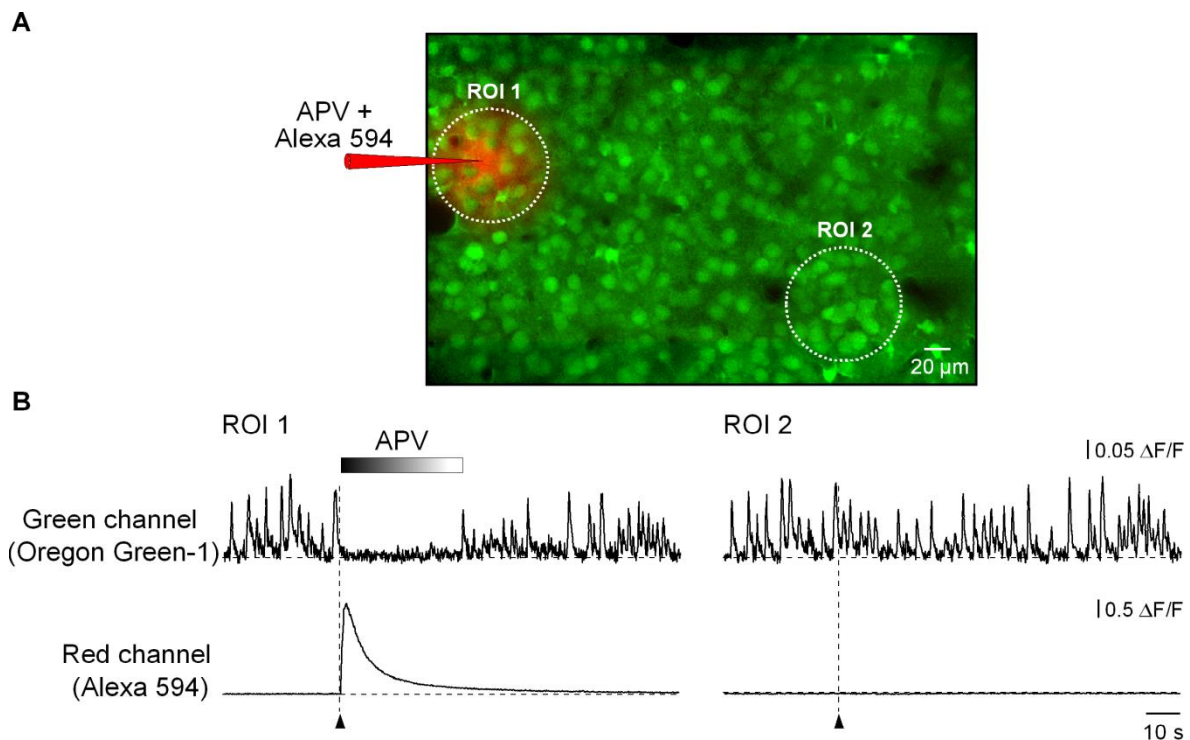
B



**Figure 24: Critical role of NMDA receptors for the spontaneous  $\text{Ca}^{2+}$  waves.**

(A) Spontaneous  $\text{Ca}^{2+}$  waves in individual layer 2/3 neurons, marked with respective numbers in the image above, recorded before (*left*), during (*middle*) and after (*right*) a bath application of 100  $\mu\text{M}$  APV. (B) Similar experiment to the one shown above, but here APV (25mM) was mixed with Alexa 594 and applied locally from a pipette. The extracellular fluorescence caused by Alexa 594 is shown in red and the layer 2/3 cortical neurons loaded with OG-1 AM in green. Mouse age was P13 in (A) and P24 in (B).

Another type of NMDA receptors blocker, the non-competitive, voltage-dependent blocker MK-801 was also tested (100-150 $\mu\text{M}$ , n=5, P14-P20). It irreversibly abolished the spontaneous  $\text{Ca}^{2+}$  waves (**Fig. 26**,  $92.43 \pm 2.85\%$  blockade of the cell frequency), effect that persisted over eight hours, the longest time monitored.

**Figure 25: Blockade of NMDA receptors is confined to the application spot and does not influence the remote network activity.**

(A) Low magnification (x20 objective, zoom 2) recordings from a large area of the primary visual cortex. (B) Spontaneous  $\text{Ca}^{2+}$  waves and Alexa 594-induced fluorescence transient recorded before, during and after a 400 ms iontophoretic application of 10mM APV. In the application pipette APV was mixed with 500  $\mu\text{M}$  Alexa 594 and ejected simultaneously to visualize the area subjected to the drug application and monitor the time course of APV application. The circles delineate the regions of interest from which the spontaneous  $\text{Ca}^{2+}$  waves and Alexa 594 fluorescence was measured. The emitted fluorescence was split into two channels at 575 nm and the fluorescence of OG-1 AM was directed to the green channel, while fluorescence from Alexa 594 was directed to the red channel. Note that only ROI 1 experienced an increase in Alexa 594 fluorescence (**B**, lower panel) causing a selective and transient blockade of the spontaneous  $\text{Ca}^{2+}$  waves (**B**, upper panel). Mouse age was P15.

Similar results were obtained in experiments in which the site of NMDA receptor blockade was restricted to the investigated neurons in cortical layer 2/3 by direct local APV application from a iontophoretic pipette (10-25 mM, n=4 experiments, P14-P24, **Fig. 24B**). APV release blocked effectively the spontaneous  $\text{Ca}^{2+}$  waves locally ( $97.74 \pm 1.30\%$ ; **Fig.**

26). The area of APV blockade was restricted only to the cells in the application spot, while the activity in the more remote cortical regions was not affected (**Fig. 25**).

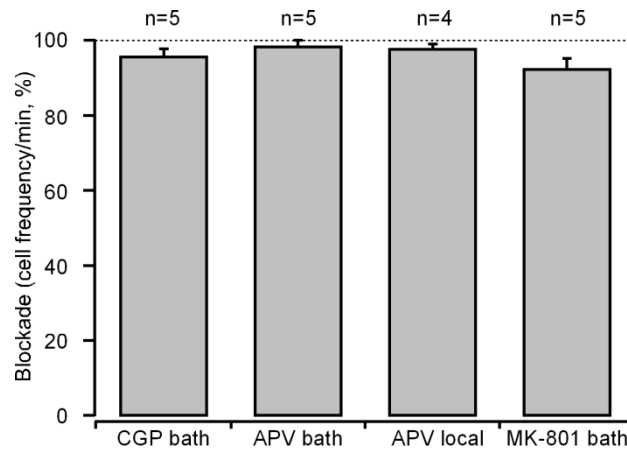


**Figure 26: Effect of NMDA receptors blockers on the spontaneous  $\text{Ca}^{2+}$  waves.**

Summary of the effect of different NMDA-receptor blockers (CGP 25-50  $\mu\text{M}$ , bath application, n=5 mice; APV, 50-100 $\mu\text{M}$ , bath application, n=5; APV, 10-25mM, iontophoretic application, n=4; MK-801, 100-150 $\mu\text{M}$ , bath application, n=5) on the spontaneous  $\text{Ca}^{2+}$  waves. The averaged cell frequency of wave-associated somatic  $\text{Ca}^{2+}$  transients during drug application is normalized in each individual experiment to the control one.

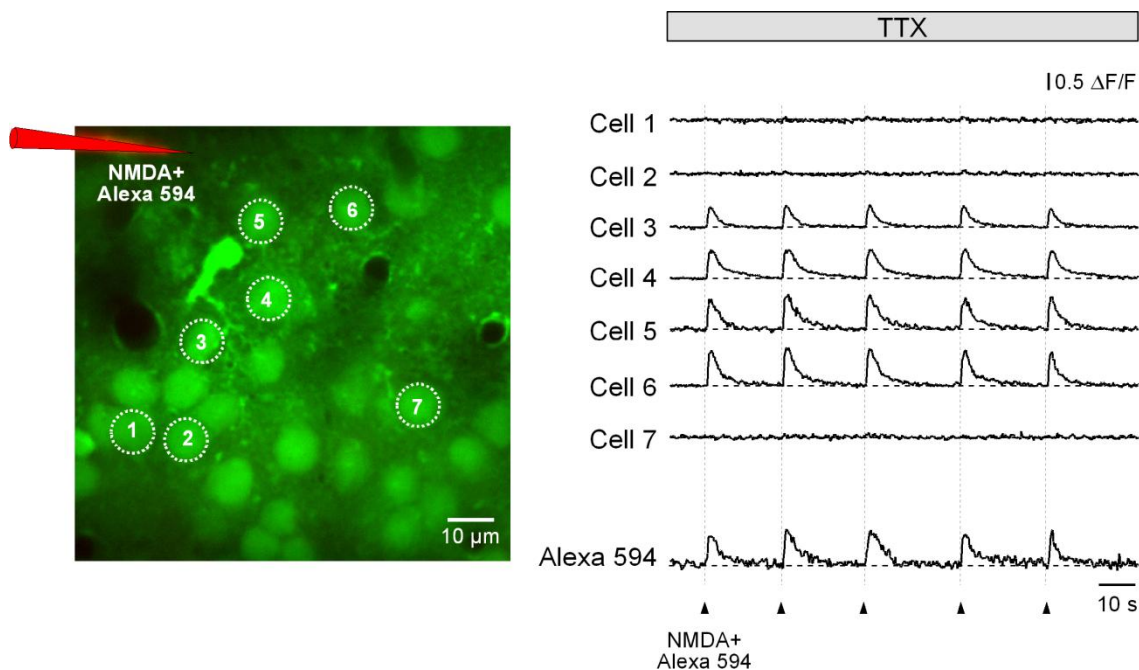


**Figure 27: Mimicking spontaneous  $\text{Ca}^{2+}$  waves by local NMDA application.**

*In vivo* wave-like  $\text{Ca}^{2+}$  transients from layer 2/3 neurons of the mouse visual cortex (marked with the respective numbers in the image) during repetitive 60 ms long iontophoretic co-applications of 10mM NMDA and 0.5 mM Alexa Fluor 594. TTX (1  $\mu\text{M}$  final concentration) was added to the ACSF solution which was perfused in the recording chamber. Note that the cells located close to the tip of the application pipette respond to each NMDA application with  $\text{Ca}^{2+}$  transients similar to the spontaneous ones, while the cells which are further away from the pipette remain silent. Mouse age was P19.

Additional support for the important role of the NMDA receptors activation for the spontaneous  $\text{Ca}^{2+}$  waves came from the fact that application of the NMDA alone (10 mM) successfully mimicked wave-like  $\text{Ca}^{2+}$  transients (**Fig. 27**).

Taken together, these results demonstrate both by blockade with different classes of antagonists and also by agonist stimulation, that the activation of NMDA receptor-channels plays a major and decisive role for the spontaneous  $\text{Ca}^{2+}$  waves in layer 2/3 of the mouse visual cortex.

### 4.2.3 Attempts to Chronically Block the Spontaneous Calcium Waves

To address the role of the spontaneous  $\text{Ca}^{2+}$  waves, their chronic blockade was attempted by chronically inhibiting the NMDA receptors. For this aim, chronic application of the non-competitive NMDA receptor antagonist MK-801 was tested. MK-801 has an open channel-blocking mechanism of action (Wong et al., 1986) by binding to a site located within NMDA receptor-associated ion channel and thus preventing the  $\text{Ca}^{2+}$  influx. It blocks NMDA receptors in a use- and voltage-dependent manner, since the channel must open for the drug to bind inside it. The blocking action of MK-801 on NMDA responses is slow in onset and persistent, with only a partial recovery after a washing period of 3 hours (Woodruff et al., 1987). Therefore, MK-801 was chosen because of its persistent effect on blocking NMDA receptors and hence, the spontaneous  $\text{Ca}^{2+}$  waves, effect also previously tested in bath application.

Different chronic applications paradigms were attempted: repetitive intramuscular injection of 0.1 mg/kg BW (n=2 animals) (Daw et al., 1999), repetitive intraperitoneal injection of 0.4 mg/kg BW (n=1 animal), intraventricular injections of 20mM MK-801 (n=2 animals), local iontophoretic application of 100mM MK-801 (n=1 animal), intracortical injections of 10mM MK-801 (n=2 animals). Implantation of Elvax slices (Smith et al., 1995; Persico et al., 1997; Kakizawa et al., 2005; Reiprich et al., 2005;) containing 16 mM MK-801 placed over the visual cortex (n=3 animals) were also attempted, but the preparations damaged the cortex and the results could not be interpreted. The last trials tried to inject mice intraperitoneally with 0.2mg/kg BW in consecutive days from P8 to P13, but the mice showed weight lost in comparison with their litter mates forcing us to interrupt the experiment.

None of the application protocols was able to fully block the spontaneous cortical  $\text{Ca}^{2+}$  waves for a long enough time period (at least a day). It seemed that the dose of NMDA

receptor antagonists sufficient for chronic blockade of the  $\text{Ca}^{2+}$  waves was very close to the lethal.

#### 4.2.4 Global Nature of Cell Activation before Eye Opening

In experiments performed in young animals before eye opening (in mice eye opening takes place around P12-14 (Demas et al., 2003; Jaubert-Miazza et al., 2005) a particular pattern of cellular activation was observed. Each spontaneous  $\text{Ca}^{2+}$  wave produced the activation of nearly every cell within the field of view (**Fig. 16, 28A, C**). The average fraction of cells participating in a given  $\text{Ca}^{2+}$  wave was high between P8 to P11 ( $71.93 \pm 6.22$  %). Another characteristic of the cellular  $\text{Ca}^{2+}$  signals at their emergence was their large amplitude in individual cells, measured as the relative change in fluorescence,  $\Delta F/F$ . The mean amplitude of  $\text{Ca}^{2+}$  transient in single cells was  $42.86 \pm 1.49\%$  ( $n=201$  events) at P8 and  $54.06 \pm 1.96\%$  ( $n=192$  events) at P9, respectively. These results indicated that at the early ages preceding eye opening the endogenous cortical activity is dense, being characterized by an extensive recruitment of the majority of cortical neurons in the  $\text{Ca}^{2+}$  waves.

#### 4.2.5 Switch from Global to Sparse Cellular Activation at Eye Opening

The generalized, ‘dense’ neuronal responsiveness found in the spontaneous activity in the visual cortex before eye opening was in contrast to the sparse neuronal activity reported previously in other brain regions at later stages of development (Petersen et al., 2003; Kerr et al., 2005). Therefore, in another series of experiments the changes in the pattern of spontaneous  $\text{Ca}^{2+}$  waves as a function of development were followed up. The aim was to find out if and how the endogenous cortical activity matures and which is the pattern of neuronal activation during this process.

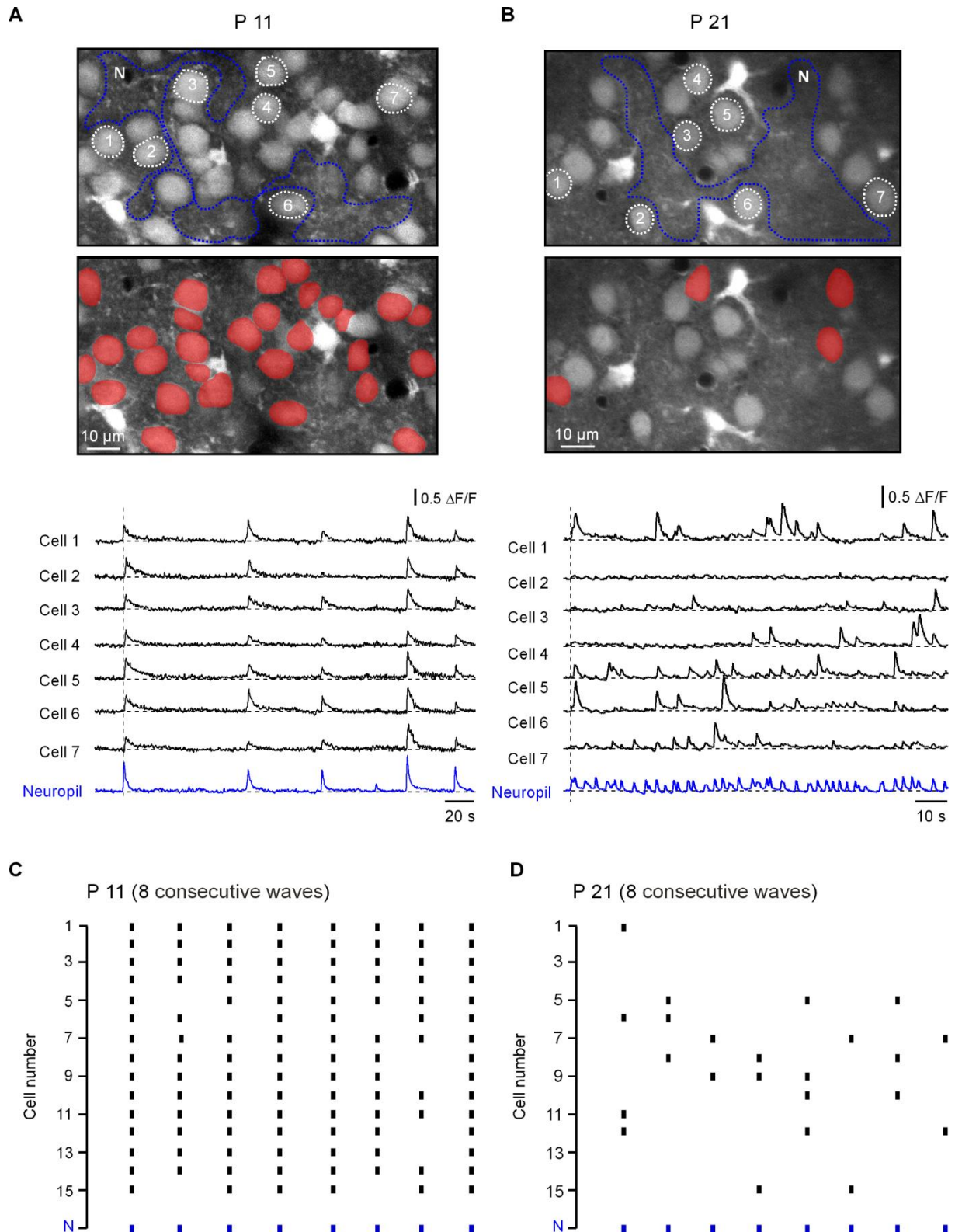


**Figure 28: Sparsification of spontaneous neuronal activity at eye opening.**

(A, B) Images taken *in vivo* from layer 2/3 neurons in the visual cortex in two animals aged P11 (A) and P21 (B), respectively. Middle panel: cells, which were active during the first  $\text{Ca}^{2+}$  wave (vertical broken line in the lower panel), are colored in red. Lower panel: wave-associated spontaneous  $\text{Ca}^{2+}$  transients recorded from individual neurons (marked with respective numbers in the upper panel (black), as well as from neuropil regions (blue), at both ages. (C, D) Raster plots illustrating the activity of all cells recorded in this particular experiment at P21 (D) and of a corresponding number of cells recorded at P11 (C). The first 7 cells in (C) and (D) correspond to those marked with respective numbers in (A) and (B). Each  $\text{Ca}^{2+}$  transient is represented as a dot.



In line with the previously described sparse mode of neuronal activation in adults, in the visual cortex after eye opening the fraction of active neurons per  $\text{Ca}^{2+}$  wave was strongly reduced. **Fig. 28** illustrates the developmental switch in the pattern of neuronal activation by comparing the spatiotemporal distribution of the wave-associated somatic  $\text{Ca}^{2+}$  transients in two separate experiments performed at P11 and at P21, respectively. The raster plots (**Fig. 28C, D**) of eight consecutive  $\text{Ca}^{2+}$  waves show that before eye opening the majority of neurons present in the recorded window were synchronously activated each time a  $\text{Ca}^{2+}$  wave was detected, whereas a week later the cellular activation was sparser and more heterogeneous. This heterogeneity emerged from the fact that the subpopulation of neurons activated during each  $\text{Ca}^{2+}$  wave was continually changing, (as in Kerr et al., 2005).

A closer quantification of the developmental profile of the  $\text{Ca}^{2+}$  waves (**Fig. 29**) revealed the highest fraction of active cells during P8-P11. Around eye-opening a process of ‘sparsification’ is initiated leading to the gradual decrease in the fraction of active cells per wave. This sparsification is nearly completed within one week after eye-opening and reaches a level of about 15% of active cells per wave in adults (fraction of active cells/wave equals  $18.98 \pm 2.7\%$  at P20-29 and  $15 \pm 2.6\%$  at P48-65).

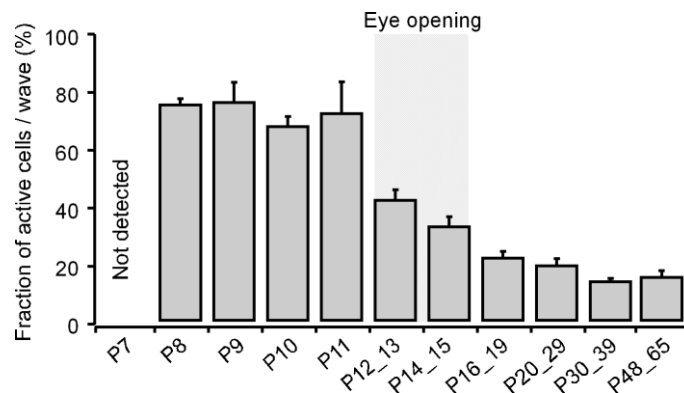


**Figure 29: Developmental profile of the sparsification of spontaneous neuronal activity.**

Bar graph showing at each age tested the fraction of neurons participating in a given  $\text{Ca}^{2+}$  wave (from left to right n=5, 4, 3, 4, 5, 12, 6, 6, 10, 4, and 6 mice).

During development the frequency of spontaneous  $\text{Ca}^{2+}$  waves increased constantly from below one wave per minute at P8 to about 30/min at P20-29. The frequency of  $\text{Ca}^{2+}$  transients measured in individual neurons initially increased from  $0.38 \pm 0.08/\text{min}$  at P8 to  $5.18 \pm 0.39/\text{min}$  at P14-15, but it remained stable thereafter. The difference between the increase in the frequency of spontaneous  $\text{Ca}^{2+}$  waves and the one in individual cell frequency is in line with the decrease in the fraction of activated neurons per  $\text{Ca}^{2+}$  wave after the third postnatal week.

Taken together, the comparison of the spatial and temporal structure of the neuronal activation across the ages studied suggests that the overall pattern of spontaneous activity in layer 2/3 of the visual cortex is changing during development. Before eye opening activity is global, synchronous, whereas after eye opening it changes into a heterogeneous, sparse activation pattern.

#### 4.2.5.1. Mechanism Underlying the Sparsification of Spontaneous Neuronal Activity: Role of GABA<sub>A</sub>-Receptor Dependent Inhibition

The  $\gamma$ -aminobutyric acid (GABA) is the main inhibitory neurotransmitter in the brain. In the primary visual cortex it was shown that the functional maturation of GABA-dependent local inhibitory connections plays a crucial role in the activity-dependent plasticity and cortical circuits consolidation (Hensch et al., 1998; Fagiolini and Hensch, 2000; Hensch, 2005). Therefore, we next tested whether the developing of synaptic inhibition plays a role in the development from a global to a sparse participation of the individual neurons in the spontaneous Ca<sup>2+</sup> waves detected in layer 2/3 of the visual cortex. Thus, the effect of local iontophoretic applications of the GABA<sub>A</sub> receptor antagonist gabazine (SR95531, 500 $\mu$ M) onto the neurons located in the visual cortical layer 2/3 was assessed at early and late developmental stages. Animals were grouped in two age categories: at the age when the majority of neurons were synchronously participating in the Ca<sup>2+</sup> waves (P11-P12, n=4 experiments), and at the age when the neuronal activations was already sparse (P20-P29, n=5 experiments). The application duration of gabazine varied between 40 to 60 sec. The concentration and duration of gabazine release, as well as the diameter of the ejecting pipette (<1  $\mu$ m), were carefully controlled in order to avoid triggering seizures by ejecting a too large amount of the GABA<sub>A</sub> receptor antagonist. The frequency with which Ca<sup>2+</sup> waves occurred was not significantly modified. It was on average 115.04 $\pm$ 20.99% at P11-P12 and 102.68 $\pm$ 7.16% at P20-29 during gabazine application compared to the control frequency (**Fig. 31B**).

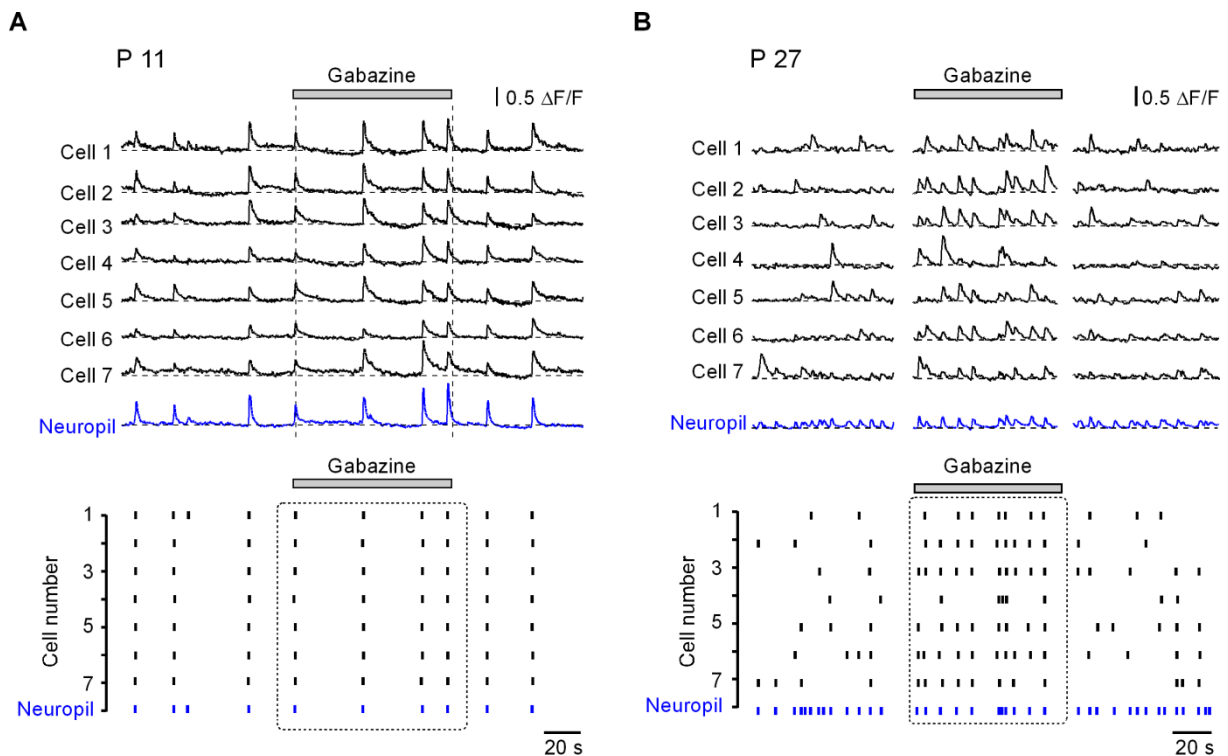


**Figure 30: Role of synaptic inhibition for the sparsification.**

(**A**, **B**) Upper panels: Wave-associated  $\text{Ca}^{2+}$  transients in individual neurons (*black*) and neuropil (*blue*) in one P11 (**A**) and another P27 (**B**) mouse before, during and after a local iontophoretic application of the GABA<sub>A</sub> receptor blocker gabazine (60-s-long, 500 $\mu\text{M}$  in the application pipette). Lower panels: Raster plots calculated from the corresponding traces in (**A**) and (**B**); each dot represents a  $\text{Ca}^{2+}$  transient detected in single cells (*black*) and neuropil (*blue*). Note the absence of any effect of the drug at P11 (**A**) and a strong increase in the fraction of active cells at P27 (**B**).

Gabazine is a selective and competitive GABA<sub>A</sub> receptor antagonist. When gabazine was iontophoretically applied in the young animals, at P11-P12, the activation of cells did not change significantly (**Fig. 30A**). The fraction of cells participating in each spontaneous  $\text{Ca}^{2+}$  wave remained constant at this early age (**Fig. 31A** left panel, 58.45 $\pm$ 5.07% in the control and 58.74 $\pm$ 12.18% during gabazine application). Cellular frequency was only slightly increased (120.21 $\pm$ 16.68% normalized to control frequency, (**Fig. 31C**) when the GABAergic inhibition was removed.

The effects of GABA<sub>A</sub> receptor antagonist application were instead considerably different when its effect was assessed in the older animals group, at P20-29, at the age when the sparsification process was already completed. During the gabazine application, neurons recovered their synchronous activation (**Fig. 30B**), the mean percentage of individual neurons involved in a single  $\text{Ca}^{2+}$  wave increasing from 16.93 $\pm$ 2.12% in control to 58.58 $\pm$ 7.62% during drug application (**Fig. 31A**, right panel). This three-fold increase in cellular synchronicity was due to a massive boost in neuronal activation, the frequency with which

neurons generated  $\text{Ca}^{2+}$  transients raising also during drug application to  $354.93 \pm 46.63\%$  compared to the control frequency (**Fig. 31C**).

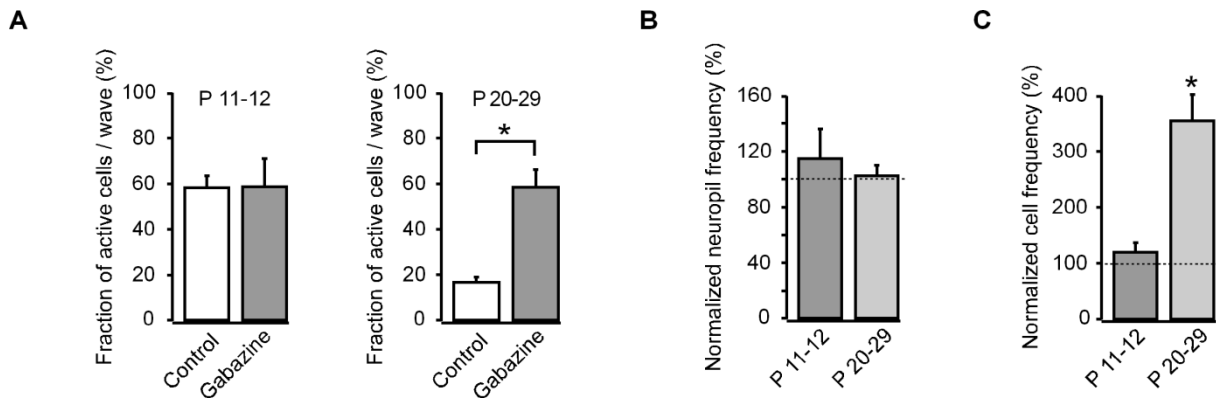


**Figure 31: Removal of  $\text{GABA}_A$  mediated inhibition recovers the neuronal synchronicity.**

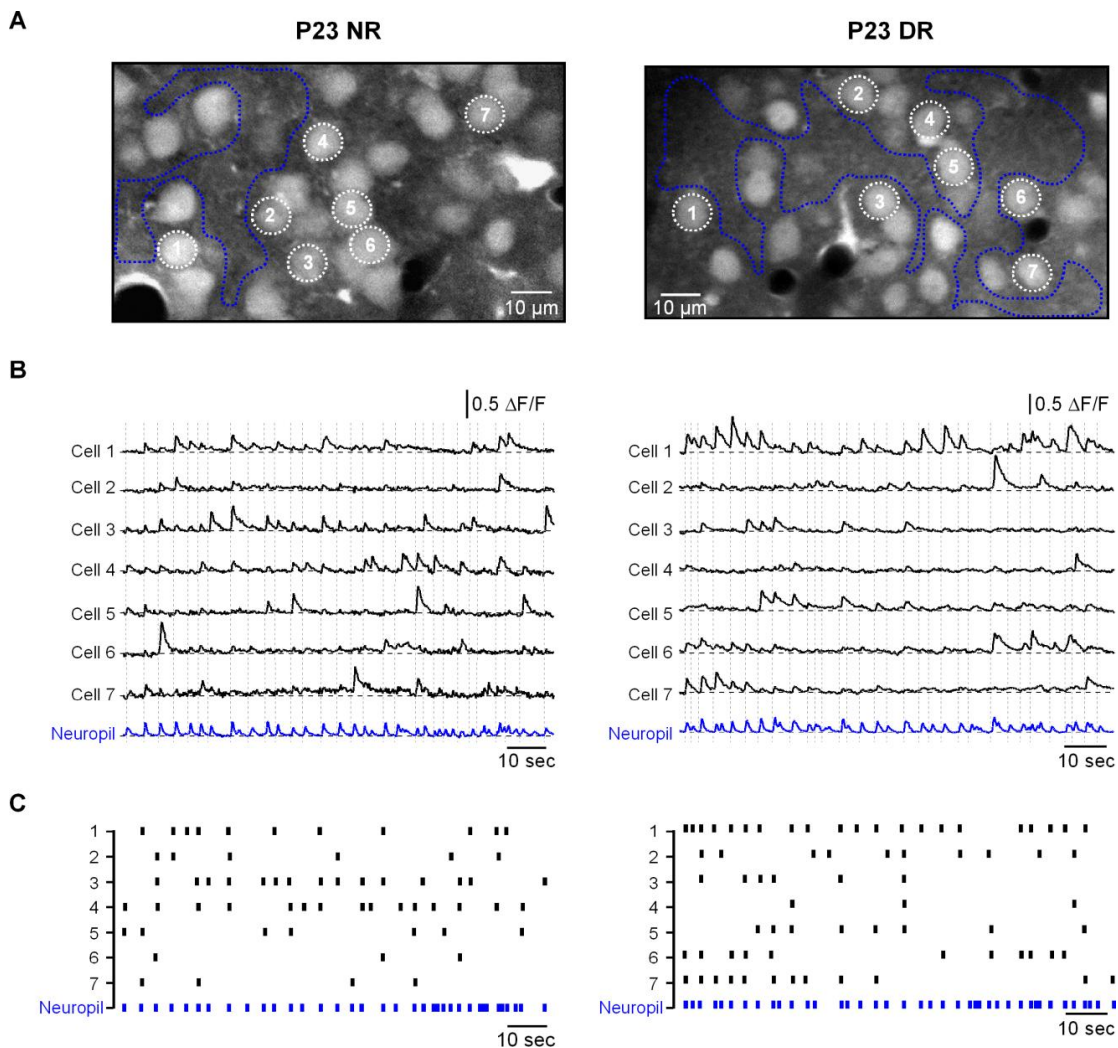
(A, B, C) Summary of the gabazine effect ( $n=4$  for P11-12,  $n=5$  for P20-29). Bar graphs presenting the mean value of the fraction of cells simultaneously activated during a given  $\text{Ca}^{2+}$  wave in control and during gabazine application at P11-12 (left) and at P20-29 (right) (A), the mean relative (normalized to control) frequency of  $\text{Ca}^{2+}$  waves detected in neuropil (B) and in single cells (C) at P11-12 and at P20-29 in the presence of gabazine. Significant effect of gabazine was observed for the fraction of active cells (A, right panel;  $p=3 \times 10^{-5}$ , Student's *t*-test) and for the cell frequency (C,  $p=0.005$ ) at P20-29.

The first attempts to investigate the effect of removing the  $\text{GABA}_A$  receptor-dependent inhibition were done with another  $\text{GABA}_A$  receptor antagonist bicuculline (20mM). However, it was shown that bicuculline do not only antagonizes the effect of GABA on the  $\text{GABA}_A$  receptor, but it rather has a more general effect, blocking also the currents produced by other compounds on the  $\text{GABA}_A$  receptor. Unlike bicuculline, gabazine selectively antagonizes GABA-induced  $\text{Cl}^-$  currents (Uchida et al., 1996), being more suited for studying the specific effect of endogenous GABA neurotransmitter release. The iontophoretic bicuculline release onto neurons in the cortical layer 2/3 in mice belonging to the age group P20-29 yielded similar results like the gabazine application (data not shown).

These results demonstrate that, by removing postsynaptic inhibition mediated by  $\text{GABA}_A$  receptors, neurons in layer 2/3 in the adult visual cortex can return to an immature pattern of spontaneous activation. This data suggests that the maturation of GABAergic inhibition causes the developmental switch in the pattern of the spontaneous  $\text{Ca}^{2+}$  waves.

#### 4.2.5.2. Mechanism Underlying the Sparsification of Spontaneous Neuronal Activity: No Role for Visual Experience

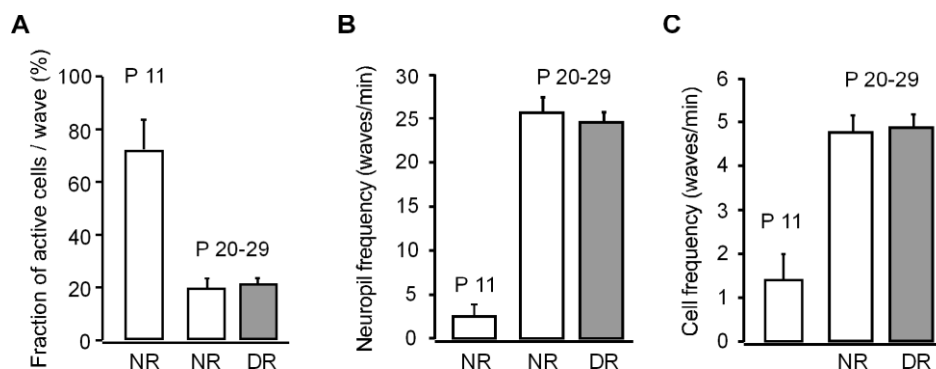
To determine whether the sparsification process requires visual experience the patterns of spontaneous activity in mice raised under normal lighting conditions were compared with those of mice reared in the dark. The impact of dark-rearing was examined at the age when the wave-associated spontaneous somatic  $\text{Ca}^{2+}$  transients were already sparse, that is at the end of the third postnatal week. Five mice aged between P22-P28 were included in this series of experiments. They were kept in total darkness from birth until the moment when the experiments were performed. The same loading procedure with the  $\text{Ca}^{2+}$  indicator dye OG-1 AM was carried out and the spontaneous  $\text{Ca}^{2+}$  activity within the loaded layer 2/3 neurons was recorded in the visual cortex. The results were compared with the ones obtained in the experiments done in the corresponding age group mice reared with normal visual experience (P20-29, n=10 animals).



**Figure 32: Spontaneous activity is comparable in normal and in dark reared mice.**

(A) Images presenting MCBL-loaded cells in the cortical layer 2/3 of the visual cortex in two different mice at P23, one control (*left*) and one dark reared (*right*). (B) Spontaneous wave-associated  $\text{Ca}^{2+}$  transients in individual neurons (*black*, mark with corresponding numbers in the images above) and in neuropil (*blue*) recorded from the experiments in (A). (C) Raster plots calculated from the  $\text{Ca}^{2+}$  traces presented in (B). Every dot corresponds to a detected  $\text{Ca}^{2+}$  transient in single cells (*black*) or in the neuropil (*blue*).

Surprisingly, the spatio-temporal patterns of cell activation within the spontaneous  $\text{Ca}^{2+}$  waves were qualitatively indistinguishable from their age-matched controls in the visually deprived mice. **Fig. 32** illustrates a comparison of spontaneous activity measured in individual neurons and in the neuropil in two animals at the same age, one reared in the dark, another one in normal lighting conditions. To quantify the effect of visual deprivation the following parameters were calculated and compared: the fraction of neurons participating in a given  $\text{Ca}^{2+}$  wave, wave and cell frequency. None of these three parameters were significantly different between the normal and dark reared mice (**Fig. 33**).

**Figure 33: Spontaneous  $\text{Ca}^{2+}$  waves are not influenced by dark rearing.**

Bar graphs summarizing the mean value of the fraction of cells activated during a given  $\text{Ca}^{2+}$  wave (A), averaged neuropil frequency (B) and averaged cell frequency (C) in control (normally reared, NR) mice (n=10) and in dark reared (DR) mice (n=5) at P20-P29. The corresponding data for P11 are shown for comparison. No significant difference in the activity pattern between control and dark-reared mice was observed (p=0.6 for the fraction of activated cells, p=0.6 for neuropil frequency, and p=0.8 for cell frequency, respectively; Student's t test).

These data indicate that visual experience has no major role on the maturation of the spontaneous activity in the visual cortex, at least during the first three postnatal weeks. Thus, it appears that sparsification is a more general developmental process that marks, perhaps, the onset of adult-type information processing in the brain.

Taken together, the results presented in this section reveal a novel type of large scale spontaneous  $\text{Ca}^{2+}$  waves that emerge in the visual cortex around P8. The spontaneous  $\text{Ca}^{2+}$  waves require activation of voltage-gated  $\text{Na}^+$  channels, glutamatergic synaptic transmission and, importantly, rely upon activation of NMDA receptor-channels. Around eye opening

(P12-14) there is a developmental switch in the pattern of spontaneous  $\text{Ca}^{2+}$  waves, from a profuse activation of the neuronal network into a sparse one, process paralleled by the development of GABAergic inhibition and independent of visual experience.

### 4.3. Development of the Light Evoked Activity in the Mouse Visual Cortex

Next, the neuronal  $\text{Ca}^{2+}$  responses to light stimulation in the superficial layer 2/3 of the visual cortex were also studied *in vivo* during development. This set of experiments was carried out in mice ranging from one week till two months old. Neurons were loaded with the  $\text{Ca}^{2+}$  indicator OG-1 AM and visual stimulations, consisting of 100 ms long light flashes produced by a photo-diode, were performed. The light source was placed at a distance of about 35-40 cm and at an angle of 35-50° laterally from the right eye of the mouse (**Fig. 34A**). In very young animals (P7-P10) the photo-diode had to be placed immediately in front of the mouse's eye in order to produce a visual response. Measurements were performed in the line-scan mode with a high sampling rate of 200 Hz that enabled the precise measurement of the responses' delays and kinetics. Usually 3-10 pyramidal neurons were included in one scanned line and the changes in intracellular  $\text{Ca}^{2+}$  concentration from each neuron was calculated and expressed as the relative change in fluorescence,  $\Delta F/F$ .

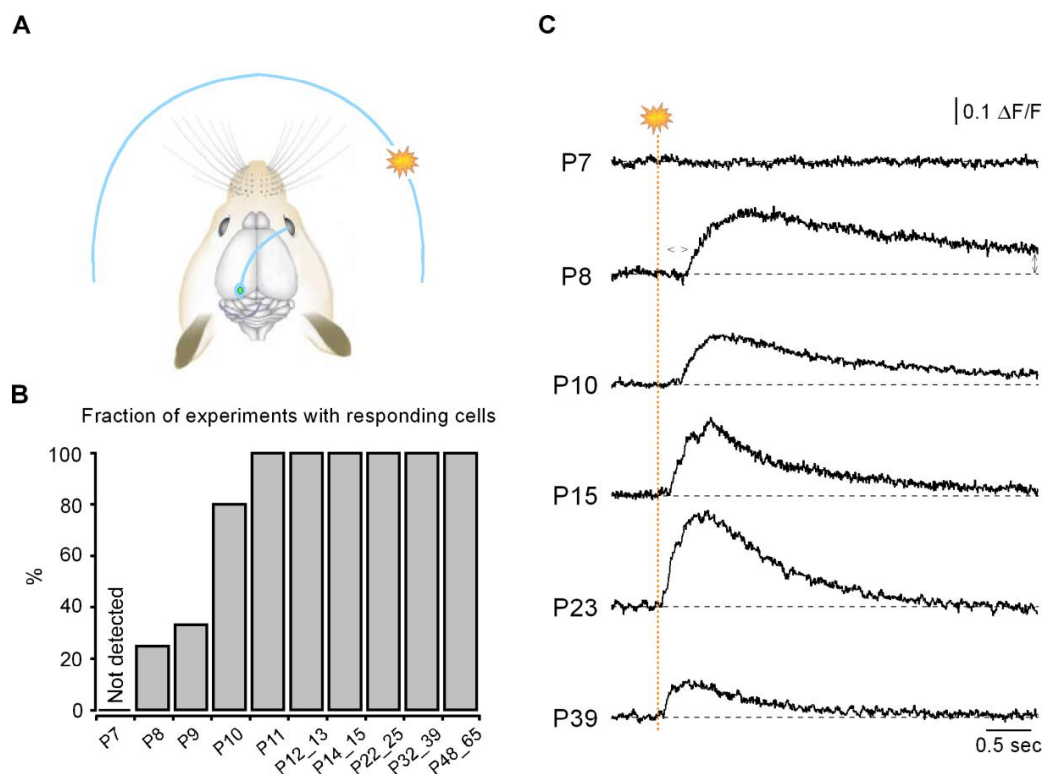


**Figure 34: Sensory-driven activity in the mouse visual cortex.**

(A) Diagram of the visual cortex and of the stimulation procedure. A brief (100 ms long) light-flash is produced by a LED which is placed 35-40 cm laterally from the contra lateral eye of the mouse. (B) Bar graph indicating at each age tested the fraction of experiments in which light-evoked responses could be detected in single cells (n=2 mice, 4, 3, 5, 3, 8, 5, 8, 4, 6 from left to right). (C) Flash-evoked  $\text{Ca}^{2+}$  transients from individual cortical neurons at different ages. Recordings are done in line-scan mode and represent for each age the average of successful trials (in which the stimulus elicited a somatic  $\text{Ca}^{2+}$  transient) out of 20 consecutive stimulations. The time point of the light stimulation is indicated by the yellow dotted line. Note the long delay (*arrow*) and duration of the responses at very young ages (P8-P10), before eye-opening.

Visually responsive cortical neurons in layer 2/3 were first identified before eye opening, at P8 (**Fig. 34B** and **C**). As in the case of the spontaneous activity, neuronal  $\text{Ca}^{2+}$  responses to flash stimulations could not be detected between P8 and P10 in each experiment (**Fig. 34B**).

A detailed developmental analysis revealed that the features of the neuronal responses induced by visual stimulation changed during development in the cortical layer 2/3 neurons. Before eye opening (P12-14), the light-evoked responses were sluggish with long latencies (approximate 300ms) and slow kinetics, measured as decay time constant (**Fig. 34C**, **Fig. 35A** and **B**). Often long intervals were required between stimulations to produce reliable neuronal responses. Many presentations of the light flash were not able to elicit  $\text{Ca}^{2+}$  responses in neurons, but when neurons responded, the responses usually had large amplitude. **Fig. 36A** shows, at each age tested, the fraction of stimulation trials in which no cellular  $\text{Ca}^{2+}$  response could be observed (failures). Note the high failure rate of light stimulations (around 80-90%) between P8 to P10. After eye opening, the percentage of stimulations that failed to produce a neuronal  $\text{Ca}^{2+}$  response decreased to approximately 30%.

After eye opening, the latency of the  $\text{Ca}^{2+}$  responses to light stimulations decreased steeply to a constant mean value of approximately 100 ms (**Fig. 35A**). Also their kinetics changed, showing a rapid decrease in duration, from over 2 sec before eye opening to approximately 1 sec afterwards (**Fig. 35B**). The third parameter calculated to characterize the changes in neuronal responses to light-flash stimulation during development was the amplitude of  $\text{Ca}^{2+}$  responses in individual neurons. The amplitude had a tendency to decrease after eye opening, but this decrease was not so prominent (**Fig. 35C**).



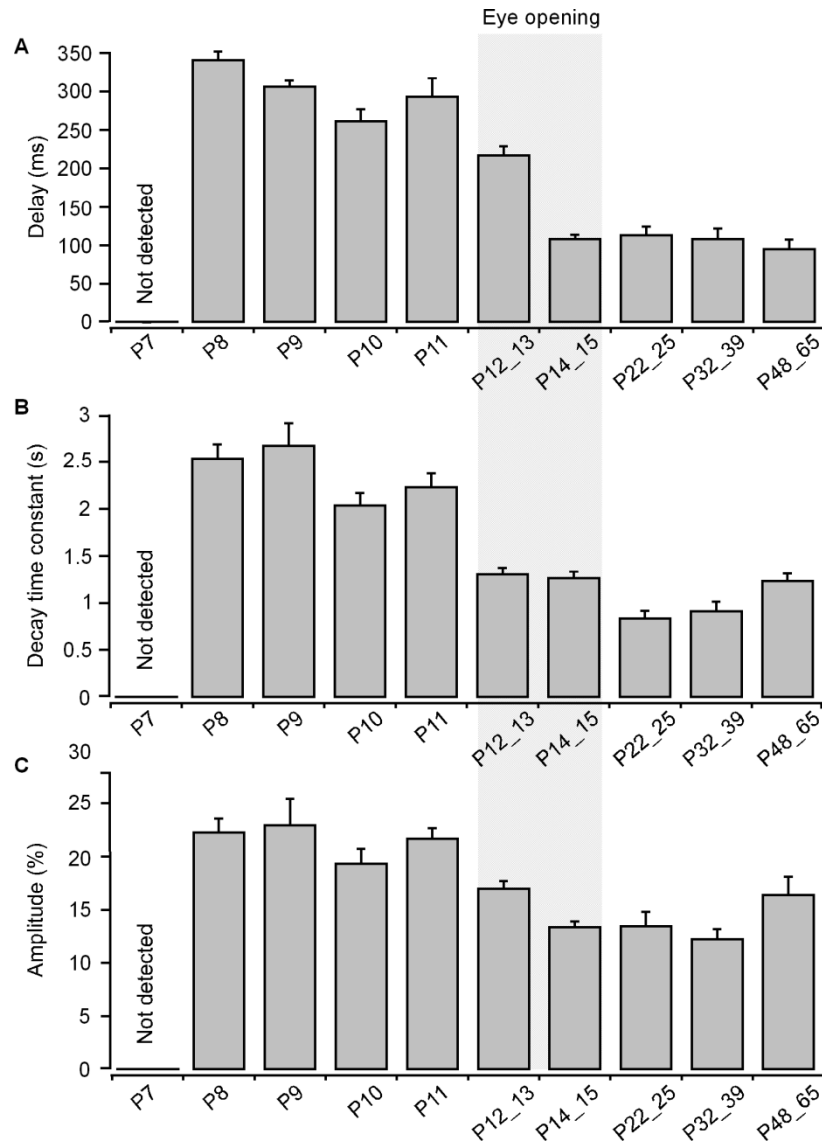


**Figure 35: Development of latency, decay time constants and amplitude of the neuronal  $\text{Ca}^{2+}$  responses evoked by visual stimulation.**

(A) Bar graphs showing at each age tested the averaged delay (A), decay time constant (B) and amplitude (C) of the somatic  $\text{Ca}^{2+}$  transients recorded in individual layer 2/3 neurons and evoked by light-flash stimulation. (n=14 cells, 8, 33, 21, 52, 39, 21, 14, 24 from left to right).

Remarkably, the pattern of neuronal  $\text{Ca}^{2+}$  responses to light flashes differed before and after eye opening. At earliest ages, when  $\text{Ca}^{2+}$  responses could be elicited, the majority of neurons were consistently activated and responded with  $\text{Ca}^{2+}$  transients to the light stimulation. In the older animals after eye opening, the percentage of neurons simultaneously activated by the light stimulation decreased (**Fig. 36B**).

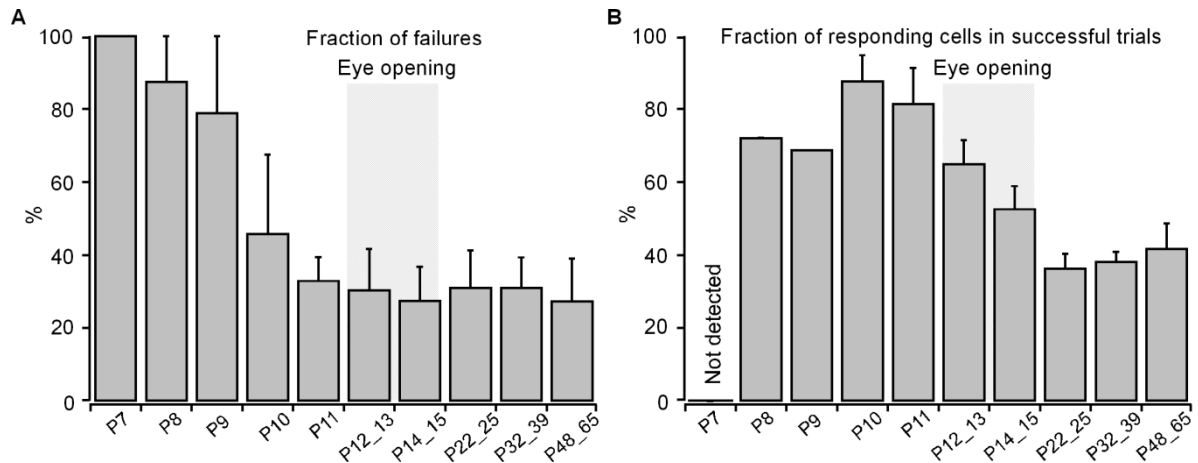


**Figure 36: Development of light evoked  $\text{Ca}^{2+}$  signals.**

(A) Plot of the fraction of trials in which no cellular  $\text{Ca}^{2+}$  response could be evoked. (B) Bar graph showing at every analyzed age the percentage of cells in one trial that responded to the light flash with a  $\text{Ca}^{2+}$  transient. Only those trials in which at least one cell was activated are included.

**Fig. 37** illustrates representative examples of neuronal  $\text{Ca}^{2+}$  responses to light presentation at early and at late developmental stages. Whereas before eye opening (P8) the majority of neurons responded with relatively homogenous large  $\text{Ca}^{2+}$  transients, at later ages neurons behaved differently: there were neurons that reliably responded to the light stimulations, other reacted only sporadically and with very small amplitudes of the  $\text{Ca}^{2+}$  transients, and there were also non-responding neurons. Thus, as in the case of the spontaneous activity, in the mouse visual cortex there is a developmental switch in the pattern of neuronal responses to light stimulation, from a dense activation before eye opening (P8) to a more restricted, sparse one in the adult mice.

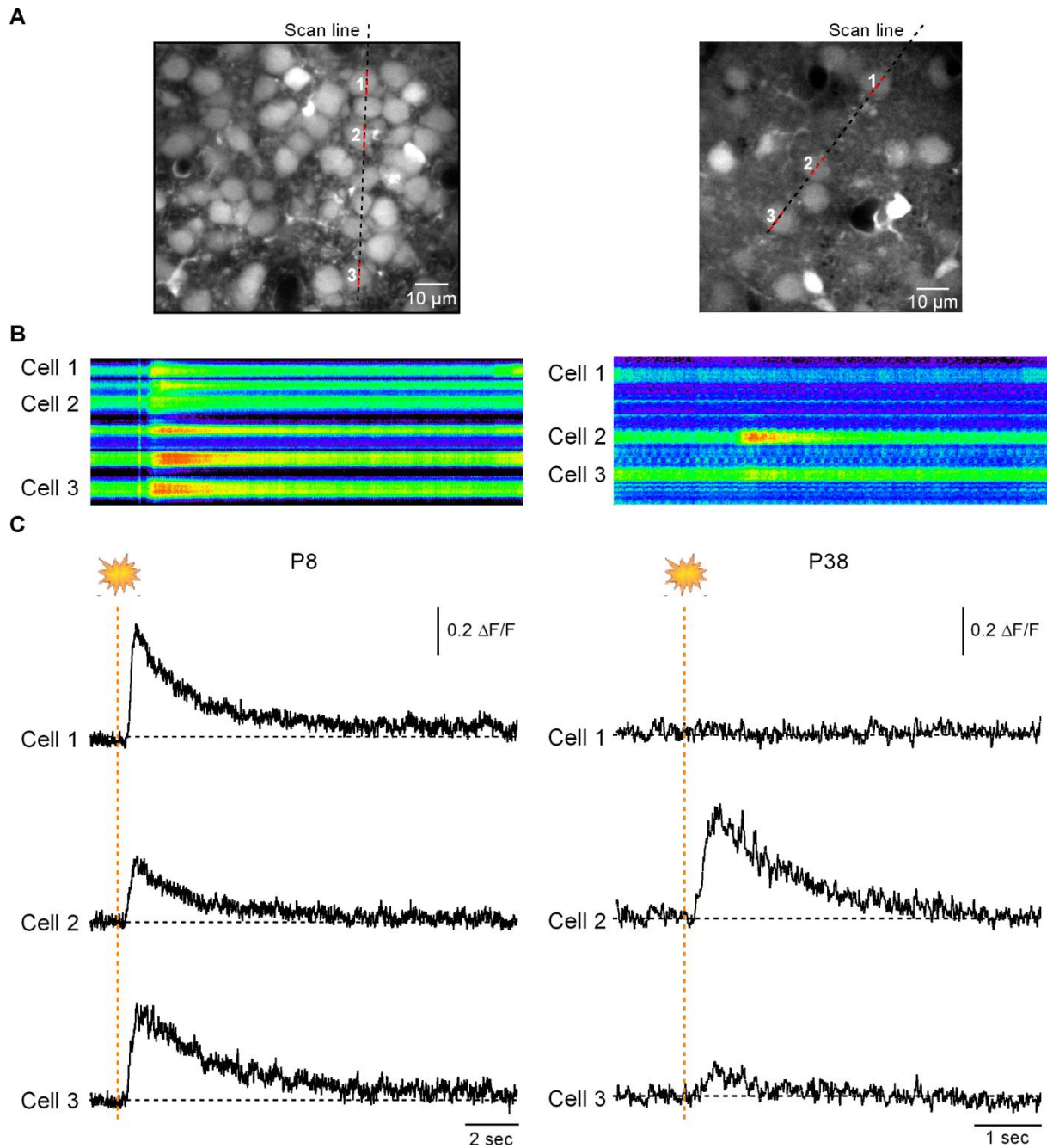


**Figure 37: Developmental switch in neuronal  $\text{Ca}^{2+}$  response patterns.**

(A) High-magnification images of layer 2/3 neurons *in vivo* in the mouse visual cortex taken at P8 (*left*) and P38 (*right*), respectively. (B) Line-scan recordings of  $\text{Ca}^{2+}$  transients evoked in each age by one light flash. The images are displayed in arbitrary units, color-coded with warmer colors coding for increases in fluorescence. (C) Examples of normalized fluorescent  $\text{Ca}^{2+}$  transients in three cortical neurons from the line-scan recordings in (B). The time of light stimulation is represented by the dotted yellow line, the position of the scan lines and the cells analyzed are indicated in (A).

NMDA receptor activation is required for the experience-dependent development of the visual cortex (Bear et al., 1990). Therefore, the dependency of the visual evoked  $\text{Ca}^{2+}$  responses upon NMDA receptors activation was tested by bath applications of the competitive NMDA receptor antagonists APV (50-100 $\mu\text{M}$ , n=3 experiments, P13-24) or CGP (25 $\mu\text{M}$ , n=1 experiment, P12). During the drug applications, the visually evoked neuronal  $\text{Ca}^{2+}$  responses

were dramatically, but reversibly blocked ( $80.33 \pm 10.44\%$  reduction in cellular responsiveness to stimuli presentation under APV compared to control; **Fig. 38**).

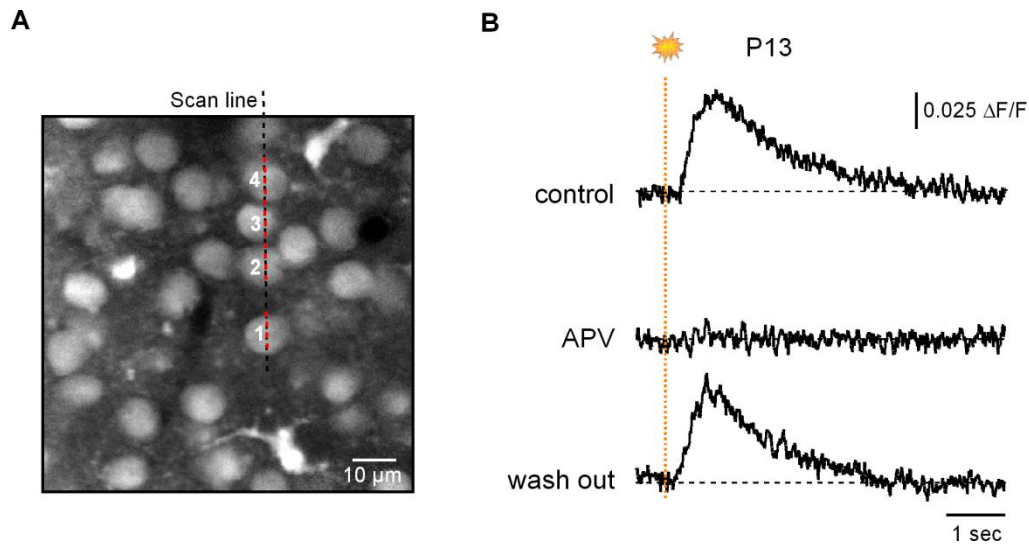


**Figure 38: Flash-evoked Ca<sup>2+</sup> responses require the activation of NMDA receptors.**

(A) *In vivo* image acquired in layer 2/3 of the visual cortex in a P13 mouse. (B) Ca<sup>2+</sup> responses to flash stimulations taken in control (*upper trace*), in the presence of 100 μM APV (*trace in the middle*) and after wash out of APV (*lower trace*). Each trace is the average of the Ca<sup>2+</sup> responses from 20 consecutive trials and measured in the 4 neurons marked with the respective numbers in (A).

Taking together, these results reveal that as early as P8 visual stimuli presented through the closed eyelids can drive neuronal activity in the visual cortex of mice. At these early ages before eye opening there is a robust neuronal activation to light stimulation. After eye opening, there is a sparsification in the neuronal responses, from a general activation to a more restricted one in adults. Similar to the spontaneous activity in the visual cortex, the light-evoked neuronal Ca<sup>2+</sup> responses essentially depend on activation of NMDA receptors.

## Chapter 5

### Discussion

This thesis presents progresses achieved by imaging *in vivo* calcium signals from large neuronal circuits with single-cell resolution. The main achievements described in this work include: (i) improvement of MCBL technique through the introduction of multicolor imaging and cell-specific staining; (ii) functional analysis of  $\text{Ca}^{2+}$  signaling in highly confined brain regions during rapid and multiple pharmacological manipulations in live experiments; (iii) enabling of *in vivo*  $\text{Ca}^{2+}$  imaging of dendrites and spines in transgenic mice expressing genetically encoded fluorescent  $\text{Ca}^{2+}$  indicator proteins (FCIPs); (iv) measurement of functional somatic and dendritic FCIPs-based  $\text{Ca}^{2+}$  signals; (v) characterization of spontaneous and light evoked activity patterns in the developing visual cortex and (vi) discovery of the phenomenon of sparsification.

#### 5.1 New Applications of the Multi-Cell Bolus Loading Technique

Two-photon  $\text{Ca}^{2+}$  imaging *in vivo* using targeted bulk loading of cortical cells with small molecule  $\text{Ca}^{2+}$  indicators is a powerful approach for high-resolution *in vivo* imaging of cortical network function. MCBL permits simultaneous recordings of spontaneous and sensory-driven  $\text{Ca}^{2+}$ -transients from tens to hundreds of individual neurons. So far applications of MCBL were used in the mammalian brain *in vivo* (i) to characterize spontaneous and sensory-driven activity in the somatosensory and motor cortices of rats and mice (Stosiek et al., 2003; Nimmerjahn et al., 2004; Kerr et al., 2005), (ii) to detect spontaneous  $\text{Ca}^{2+}$  transients in rat Purkinje cell dendrites (Sullivan et al., 2005), (iii) for monitoring spontaneous and light-evoked responses in the mouse visual cortex (Garaschuk et al., 2006b), (iv) to visualize the relation between neurons and plaques, the histological

hallmark of Alzheimer's disease, in transgenic mice carrying mutations associated with Alzheimer's disease (Garaschuk et al., 2006b) (v) for the characterization of direction selectivity of layer 2/3 neurons in the visual cortex of rats and cats (Ohki et al., 2005), (vi) to determine the microstructure of pinwheel centers with single cell resolution in cat visual cortex (Ohki et al., 2006), (vii) to investigate neuronal responsiveness during ocular dominance plasticity in mouse visual cortex (Mrsic-Flogel et al., 2007) and (viii) to test for the orientation selectivity of EGFP-positive GABAergic interneurons in layer 2/3 of the visual cortex (Sohya et al., 2007). All these studies were done under anesthesia, but MCBL proved its applicability also in awake, behaving animals. In combination with brain microendoscopy, MCBL was used to characterize the macroscopic properties of neuronal networks by monitoring  $\text{Ca}^{2+}$  signals in nonanesthetized mouse pups (Adelsberger et al., 2005).

As presented in section 4.1.1.2., one of the major advantages of MCBL is that it is not age dependent, being able to stain not only newborn and juvenile tissue, but also adult and even aged tissue. This quality renders MCBL especially useful to study the *in vivo* functional properties of neuronal networks in mutant mice carrying gene mutations relevant for different age-associated human diseases, such as Alzheimer's disease (Garaschuk et al., 2006b).

MCBL stains relative homogeneously all the cells present in the target brain region. One can circumvent the lack of cell-specificity by combining it with additional specific cellular markers, like for example the astroglial marker sulforhodamine 101 (Nimmerjahn et al., 2004). This study describes a procedure which simplifies and speeds-up the neuron/glia-specific staining by combining both dyes in the same injection pipette. The double-colored images (e.g. **Fig. 11A**) disclose many specific details (for example, processes of glial cells) and thus significantly improve the discrimination of functional properties of neuronal and astrocytic networks. As we could show (Garaschuk et al., 2006b), cell-type-specific analyses of neurons belonging to different subclasses is enabled by applying MCBL in mutant mice expressing genetically encoded fluorescent markers in a defined neuronal subclass. Recently, a similar approach was applied to study the difference in orientation-selectivity between the GABA-ergic interneurons and excitatory neurons in layer 2/3 of the visual cortex in transgenic mice in which the GABA-ergic interneurons expressed EGFP (Sohya et al., 2007).

As shown above, the experiments using MCBL could be easily combined with applications of pharmacological substances directly to the cells of interest. Drugs could be added to the preheated ACSF solution that continuously perfused the brain, procedure similar to the bath application of drugs in conventional brain slice experiments. Under *in vivo* conditions, the cortex is exposed through the small craniotomy performed for dye loading,

which is sufficiently large to allow an effective access of drugs to the brain parenchyma. The water soluble drugs (like for example APV or TTX) elicited their effects soon after they were present in the recording chamber. The lipophilic drugs (like for example CNQX) required application in high concentrations, presumably because of the poorer diffusion properties they have inside the brain tissue. This *in vivo* ‘bath application’ method enabled rapid pharmacological manipulations, including application and wash out of multiple drugs at controlled concentrations. Thus, the ‘bath application’ presents several advantages over other techniques available for the pharmacological treatment of brain cells *in vivo*, where drugs are usually administered via intravenous or intraperitoneal injections. The limitations of such “systemic” drug administration include the possibility of applying only those drugs that cross the blood-brain barrier, the delayed effect and unknown concentration at the site of interest, and possible systemic side effects. A very similar technique was also used by Minlebaev et al. (Minlebaev et al. 2007). As the perfusion chamber, a plastic cylinder with fine mesh at its bottom was gently pressed onto the surface of the barrel cortex, so that the mesh prevented the brain pulsations. This construction also allowed application of drugs directly on the cortical surface (Minlebaev et al. 2007).

An alternative method for drug delivery directly to the cells of interest was the local application. This was performed by inserting a pipette filled with the drug through the same craniotomy used for MCBL dye delivery. The drug was subsequently released onto the cells either by iontophoresis or by pressure-application. This approach had two advantages over the bath application: it could be successfully used for local application of any type of drug (including the lipophilic ones) and by carefully controlling the application parameters (like for example duration, diameter of the tip of the pipette, amount of ejecting current) the drugs could exert their action in highly confined brain regions (down to a few cells).

In conclusion, recent improvements of MCBL have following advantages: in combination with other labeling techniques, in particular with those involving the use of genetically encoded, green-fluorescence-protein-based indicators, MCBL provides useful tools needed for the functional analysis of  $\text{Ca}^{2+}$  signaling in identified subclasses of neurons and glia cells *in vivo*; MCBL can be used in a variety of animal models at different ages; MCBL allows to visualize cells, which are transiently treated pharmacologically in a live experiment.

However, even with an improved technique it was still not possible to overcome some general limitations of MCBL. One of them is that imaging of processes of individual neurons is difficult, presumably because all processes have same brightness of staining thus

forming a rather homogenous neuropil. Another limitation refers to the fact that all cells and structures in a given volume are stained and under high-power excitation out-of-focus light may substantially contribute to the recorded signal (Helmchen and Denk, 2005).

## 5.2. Advances in Imaging Calcium Signals Using the New Genetically Encoded Fluorescent Calcium Biosensor CerTN-L15

Another methodological improvement of the *in vivo* two-photon  $\text{Ca}^{2+}$  imaging presented in this thesis is the characterization of the cortical expression patterns and the functional properties of a novel troponin C-based  $\text{Ca}^{2+}$  biosensor (Heim and Griesbeck, 2004), CerTN-L15. CerTN-L15 had a long-lasting stable expression in brains of transgenic mice (Heim et al., 2007). With the use of the Thy-1 promoter (Caroni, 1997; Feng et al., 2000), the expression was purely neuronal as proved by counterstaining with the glial specific marker sulforhodamine 101. CerTN-L15 produced intense labeling in the majority of brain areas including cortex, hippocampus, cerebellum and brain stem (Heim et al., 2007). Within individual neurons CerTN-L15 was homogeneously distributed in the cytosol, allowing *in vivo* visualization of individual cortical layer 2/3 neurons, their dendrites and dendritic spines. The sensor was excluded from the cell nucleus, aspect that caused a ring-like appearance of cortical cells somata under *in vivo* conditions, where cells were usually viewed from above.

The favorable fluorescence properties and the relatively high  $\text{Ca}^{2+}$  sensitivity of CerTN-L15 enabled functional *in vivo* imaging of single neurons. Moreover, the sensitivity of CerTN-L15 was well within the range of the sensitivity of the commonly employed small molecule  $\text{Ca}^{2+}$  indicators used for *in vivo* recordings, like Fura-2 and Oregon Green BAPTA-1 (2-15%, Smetters et al., 1999; Kerr et al., 2005; Garaschuk et al., 2006a). The decay time constants of glutamate-evoked somatic CerTN-L15-mediated  $\text{Ca}^{2+}$  transients were around 1.6 s *in vivo* and were, thus, only two times slower than the decay time constants of spontaneous  $\text{Ca}^{2+}$  transients measured *in vivo* with Oregon Green BAPTA-1 (0.8 s, Kerr et al., 2005).

So far, FCIP-mediated  $\text{Ca}^{2+}$  signals from neuronal structures *in vivo* were measured just in the olfactory bulb using camgaroo-2 and inverse pericam (Hasan et al., 2004) and in beams of parallel fibers using GCaMP2 (Diez-Garcia et al., 2007). However, those  $\text{Ca}^{2+}$  signals were integrated over populations of cells and did not have single-cell resolution. In contrast, CerTN-L15 provided discernable  $\text{Ca}^{2+}$  signals from small dendritic segments (approx.  $1 \times 35 \mu\text{m}$ ). To our knowledge, this is the first example of FCIP-based *in vivo*  $\text{Ca}^{2+}$  signals of spiny dendrites. Noteworthy, the quality of these recordings (signal amplitude,



signal-to-noise ratio) is very similar to the quality of dendritic recordings from neurons, pipette-filled with the small molecule  $\text{Ca}^{2+}$  indicator Oregon Green BAPTA-1 (Waters and Helmchen, 2004).

These results are in clear contrast to results obtained with cameleons, which have consistently shown a marked reduction in  $\text{Ca}^{2+}$  sensitivity in transgenic mice (Hasan et al., 2004; Nagai et al., 2004). As mentioned in the introduction, CerTN-L15 and cameleons have a very similar architecture and differ only in the  $\text{Ca}^{2+}$  binding moiety. Instead of using TnC, cameleons employ the interaction of CaM with the CaM binding peptide M13 (Miyawaki et al., 1997; Miyawaki et al., 1999). Calmodulin, however, is a ubiquitous signal transduction protein that is highly regulated on many levels and activates many  $\text{Ca}^{2+}$ -dependent responses within cells (Griesbeck, 2004). It is a multifunctional protein that can bind to at least 30 different target enzyme and proteins (Jurado et al., 1999). On the other side, it is itself tightly regulated by the host cell biochemistry through extensive phosphorylation on serine/threonine and tyrosine residues (Benaim and Villalobo, 2002). Moreover, competition by endogenous calmodulin at the level of the calmodulin target peptide, which would markedly decrease probe signal strength, is also expected (Kotlikoff, 2007). These uncontrolled intracellular interactions may explain the failure in obtaining full functionality of CaM-based  $\text{Ca}^{2+}$  sensors when they were expressed in the mouse.

In conclusion, the new FCIP mouse line that expresses the troponin C-based  $\text{Ca}^{2+}$  biosensor CerTN-L15 provides important improvements for the analysis of  $\text{Ca}^{2+}$  signaling in the intact brain. These include a homogeneous and bright staining of the entire cytosol of individual neurons down to secondary/tertiary dendrites and the full functionality of the sensor protein allowing *in vivo*  $\text{Ca}^{2+}$  imaging with single cell and even subcellular resolution. The cellular expression pattern of CerTN-L15 with bright dendrites and dye-free nuclei renders the dye particularly suitable for dendritic recordings. Thus, for a comprehensive cellular analysis, CerTN-L15-based labeling may be combined with the bolus labeling of cells with small molecule indicators, which provides good results for the staining of cell somata, but not that of dendrites.

### 5.3. Endogenous Network Activity in the Developing Visual Cortex

Benefiting from the new applications of MCBL a detailed analysis of the spontaneous activity in the visual cortex of mice during development was performed. This study revealed by means of *in vivo* two-photon functional  $\text{Ca}^{2+}$  imaging the presence of a

novel type of large scale spontaneous  $\text{Ca}^{2+}$  waves in the upper layers of the developing mouse visual cortex *in vivo*. These novel  $\text{Ca}^{2+}$  waves have following distinct properties:

- they emerge at the beginning of the second postnatal week and before eye opening recruit the entire neuronal network
- they increase their frequency during development gradually switching from sub-delta to delta range
- require action potential firing and glutamatergic synaptic transmission
- critically depend upon activation of NMDA receptor-channels
- switch from profuse to sparse around eye opening
- the decline in cellular synchronicity seen during development (the ‘sparsification’ process) is independent of visual experience
- the sparsification process is closely paralleled by the maturation of the GABAergic inhibition

### 5.3.1. Patterns of Spontaneous Network Activity in the Developing Visual Cortex

The earliest form of patterned spontaneous cortical activity is represented by the “early network oscillations” or ENOs (Garaschuk et al., 2000). They consist of  $\text{Ca}^{2+}$  waves involving the entire network of neurons in all cortical layers almost simultaneously and propagating from the posterior cortex along its longitudinal axis, crossing the anatomical boundaries between different cortical subregions (Garaschuk et al., 2000). ENOs are detected in the cortex of rodents at embryonic day 16 (Corlew et al., 2004) and persist until the end of the first postnatal week (Garaschuk et al., 1998; Garaschuk et al., 2000; Corlew et al., 2004), during the period at which GABAergic transmission is depolarizing (Garaschuk et al., 2000; McCabe et al., 2007). Based on optical fiber  $\text{Ca}^{2+}$  measurements, ENOs were identified to be present also *in vivo* in the temporal cortex of new born non-anesthetized mice (Adelsberger et al., 2005). ENOs are detected primarily during sleep-like resting states and are absent when the animals moved. In addition, ENOs are very sensitive to anesthetics and are completely abolished in anesthetized animals (Adelsberger et al., 2005).

Eventually, the adult neocortex is characterized by slow (0.2-0.5 Hz) depolarizing-hyperpolarizing (or Up-Down) wave activity (Steriade et al., 1993; Steriade and Timofeev, 2003), where sparse firing of action potentials predominates (Margrie et al., 2002; Petersen et

al., 2003; Kerr et al., 2005). The Up-Down state activity is detected under different anesthetics (Steriade et al., 1993; Lampl et al., 1999; Petersen et al., 2003; Kerr et al., 2005), during natural sleep (Steriade and Timofeev, 2003) and quiet wakefulness (Petersen et al., 2003).

The results presented in this thesis reveal a novel type of large scale spontaneous  $\text{Ca}^{2+}$  waves, which emerges in the visual cortex at the beginning of the second postnatal week and develop in the adult ages, bridging the gap between ENOs and the adult slow wave cortical activity. After ENOs have disappeared around P7, the newly described large scale slow spontaneous  $\text{Ca}^{2+}$  waves were detected throughout big regions in layer 2/3 of the visual cortex of anesthetized mice. These  $\text{Ca}^{2+}$  waves showed an increase in frequency during later stages of development, from a sub-delta (0.5 waves/min at P8) to a delta (30 waves/min or 0.5 Hz at P21) range of cortical wave activity. The  $\text{Ca}^{2+}$  waves persisted at this frequency in adult mice.

The nature of the spontaneous  $\text{Ca}^{2+}$  waves was exclusively neuronal, as glial cells, specifically labeled with sulforhodamine 101, showed different  $\text{Ca}^{2+}$  dynamics. Interestingly, the  $\text{Ca}^{2+}$  waves could be detected in the surrounding neuropil, whose *in vivo* spontaneous  $\text{Ca}^{2+}$  signals were previously demonstrated to be predominantly of axonal origin, thus representing the input activity into the local layer 2/3 neuronal network (Kerr et al., 2005). The sensitivity to TTX of the slow spontaneous  $\text{Ca}^{2+}$  waves and the dependence on activation of ionotropic glutamate receptors suggest that they require excitatory synaptic transmission for the recruitment of layer 2/3 neurons into the wave activity.

A major finding of this study is that the pattern of neuronal activation within the spontaneous  $\text{Ca}^{2+}$  waves changes during development. Before eye opening the  $\text{Ca}^{2+}$  waves recruited most of cortical neurons (70-75%), and each cell participated with a  $\text{Ca}^{2+}$  transient in almost every wave. The amount of synchronously active neurons dropped dramatically after eye opening, so that only 15-20% of the cells participated in a given  $\text{Ca}^{2+}$  wave at P16-19 and at the later ages tested. The spatial pattern of cellular activation at these later ages showed a stochastic behavior, the subset of activated neurons changing continually over time. Thus, in the mouse visual cortex there is a developmental switch in the pattern of endogenous activity transforming “dense” activation of the neuronal network into a sparse and heterogeneous one.

The process of sparsification was not influenced by the visual experience, as mice reared in the dark showed similar developmental pattern of the spontaneous  $\text{Ca}^{2+}$  wave. Conversely, the mechanism underlying the decline in cellular synchronicity after eye-opening was triggered by the developmental strengthening of the synaptic inhibition. Interestingly, a

presumably different set of inhibitory mechanisms, which rely strongly on visual experience (Katagiri et al., 2007), control the transition from the precritical to the critical period for monocular deprivation in the developing visual cortex (Hensch et al., 1998; Hensch, 2005).

The finding that the synchronicity of spontaneous activity in the visual cortex is reduced with maturation shows similarities between the development of spontaneous cortical and retinal activity. Using multi-electrode array recordings, Demas et al. (2003) found that in normally reared mice the synchronous firing of retinal ganglion cells (RGCs) occurs in the form of retinal waves at P9. The synchronicity of RGCs begins to break down shortly after eye opening (around P15) and by P21 is comparable with that observed in adult mice. The sparsification process of RGCs activation was also not influenced by visual experience (Demas et al., 2003). A similar development of cortical neuronal activity in the visual cortex was also found in the cat, where the maturational changes in the spontaneous neuronal activity consisted of a decrease in synchrony, paralleled by an increase in the frequency of neuronal discharges (Huttenlocher, 1966, 1967). Taken together, these data suggest that in the visual system the maturation in the endogenous activity pattern, represented by sparsification of the neuronal activation, is a more general process, which has a similar evolution during development and marks, perhaps, the onset of adult-type information processing in the brain.

In conclusion, the new form of slow spontaneous  $\text{Ca}^{2+}$  wave activity described here shares similarities with the early occurring ENOs, but also with the slow wave (or Up-Down) activity found in adults. Its ultra-slow rate of repetition (0.5-2.7 wave/min at P8-P11) and the large fraction of active cells/wave during the second postnatal week are similar to the ENOs. The persistence in the presence of anesthetics, the frequency at later developmental stages and the sparse pattern of neuronal activation after eye-opening were similar to the classical slow wave activity reported previously in adults.

### 5.3.2. Possible Physiological Function of the Spontaneous Calcium Waves

The accurate assembly of neuronal connections is generally thought to critically depend early in development on patterns of neuronal activity, generated either by intrinsically generated spontaneous activity (Katz and Shatz, 1996), or by early experience (Akerman et al., 2002). In particular, as postulated by Hebb, correlations in presynaptic and postsynaptic activity patterns strengthen and retain ‘correct’ synapses and eliminate ‘inappropriate’ connections (Katz and Crowley, 2002). The correlated, global mode of neuronal activation

seen during the newly described spontaneous  $\text{Ca}^{2+}$  waves is restricted in the visual cortex to the precritical period for monocular deprivation (Feller and Scanziani, 2005) and is completely gone at the end of the third postnatal week. During the precritical period, a complex interaction between the spontaneous activities in the afferent sensory pathways, including retina and the lateral geniculate nucleus, but also with the neighboring cortical areas, establishes the coarse connectivity and the sensory maps in the visual system (Sur and Leamey, 2001; Katz and Crowley, 2002; Feller and Scanziani, 2005; Sur and Rubenstein, 2005).

A remarkable feature of the slow wave activity in this period is the requirement of NMDA receptor-activation for wave-associated  $\text{Ca}^{2+}$  signaling. Hebbian postulate requires a mechanism for detecting coincident pre- and post-synaptic activity. The NMDA receptor is the main candidate for a coincident detector at synapses in the CNS, because it can only be activated by both glutamate and post-synaptic depolarization. If NMDA receptor contributes to the mechanisms underlying the activity-dependent cortical circuit formation, then pharmacological blockade of the receptor might be expected to prevent the normal course of this process. Indeed, evidence confirming this hypothesis came from studies where inhibition of NMDA receptors prevented the proper development and maintenance of precise connectivity of retino-tectal (Cline and Constantine-Paton, 1989; Ruthazer et al., 2003) or retino-collicular (Simon et al., 1992) projections. Blockade of NMDA receptors abolished the activity-dependent elimination of axon terminals from the territories dominated by the opposite eye in the binocular innervated optic tectum of *Xenopus* tadpoles (Ruthazer et al., 2003). The finding that the slow spontaneous  $\text{Ca}^{2+}$  waves are abolished by NMDA receptor blockers strongly indicates that in the mammalian visual system, like in the developing *Xenopus* retino-tectal system (Ruthazer et al., 2003), spontaneous activity may regulate axonal growth through activation of NMDA receptors and, thereby, the pattern of innervation territories in the cortex.

Sparsification of spontaneous neuronal activity seems to be a general motif of cortical development. Here evidence for such a switch in the visual cortex is provided, while others have shown sparsification of neuronal activity at later developmental stages in the retina (Demas et al., 2003), as well as a sparse activation pattern during adult Up-Down states in the somatosensory (Kerr et al., 2005) and motor cortex (Brecht et al., 2004; Kerr et al., 2005). After eye-opening, the ongoing spontaneous cortical activity is not a simply noise on which sensory responses are superimposed, but it has an essential role for encoding stimulus-evoked sensory information (Anderson et al., 2000). For example, the spontaneous

depolarization during the Up states enhanced the visual responsiveness of cortical neurons to stimuli of varying contrasts (Haider et al., 2007). Also, a set of dynamically switching cortical states can emerge during the ongoing spontaneous cortical activity, many of which correspond to orientation maps in the visual cortex (Kenet et al., 2003). In the rodent somatosensory cortex, the sensory responses during the Up states depend on the features of the whisker stimulation (Hasenstaub et al., 2007). Brief whisker stimuli evoke postsynaptic potentials containing a greater proportion of inhibition and the sensory responses are inhibited. In contrast, the prolonged and variable whisker stimulation during network activity increases the overall cortical responsiveness, dynamic range, and correlation between action potential response and speed of whisker movement (Hasenstaub et al., 2007). Thus, neuronal activity during Up-Down states can influence in a complex manner the responsiveness of cortical neurons to various sensory stimulations.

#### 5.4. Maturation of Neuronal Responses to Light Stimulation in the Mouse Visual Cortex

Besides the characterization of the spontaneous activity patterns, the features of neuronal  $\text{Ca}^{2+}$  responses to light stimulation in the superficial layer 2/3 of the mouse visual cortex were also studied here *in vivo* during development. Neuronal  $\text{Ca}^{2+}$  responses to light flash stimulation could be recorded already one week after birth, as early as P8, at the time when the mouse's eyelids are still closed. At this age, the large majority of photoreceptors in the mouse's retina are differentiated (Young, 1985) and the retinogeniculate projections are by now separated into eye-specific regions in dLGN (Godement et al., 1984). The latencies of visual responses through the closed eyelids were very long compared to the ones after eye-opening. The long latencies are likely to originate from the deficit of myelination, which begins in the optic nerve of mice around P7 and progressively increases thereafter (Foran and Peterson, 1992).

Previous studies had shown that visual responses can be elicited through the closed eyelids in kittens (Huttenlocher, 1966, 1967) and in ferrets (Krug et al., 2001; Akerman et al., 2002). In the ferret before eye-opening, many cortical, but not geniculate, neurons show selectivity to the orientation of gratings presented through closed eyelids, selectivity which improves with age (Krug et al., 2001). Moreover, dark-rearing of ferrets before eye-opening affects the normal segregation of On and Off inputs in the retinogeniculate pathway, indicating that visual experience through closed eyelids is developmentally important

(Akerman et al., 2002). Thus, in the mouse visual system, like in the ferret visual system, the responses through unopened eyelids could pattern neuronal activity and consequently provide developmentally relevant information for the refinement of functional connections.

Blockade of NMDA receptors in young animals 2 to 3 weeks old abolished the neuronal  $\text{Ca}^{2+}$  responses to light flash stimulation. Data obtained by other groups also showed that intracortical infusion of APV, a blocker of the NMDA receptor, profoundly suppressed the responses to visual stimulation (Fox et al., 1989), or disrupted the experience-dependent plasticity and the development of orientation selectivity (Kleinschmidt et al., 1987; Bear et al., 1990) in the kitten striate cortex. Altogether, these data indicate that NMDA receptor activation is required for the experience-dependent development of the visual cortex.

In the immature animals prior to eye-opening, the flash responses in cortical neurons were difficult to be elicited, but when they were present they encompassed the majority of neurons. The fraction of activated neurons by one light flash decreased as maturation progressed, similar to the decrease in neuronal activation during the spontaneous activity. The beginning of the sparse mode of activity of layer 2/3 neurons in the visual cortex around the end of the third postnatal week, that is one week after eye-opening, coincides quite well with the time point at which mice start to exhibit a refined visual performance. Thus, in elegant behavioral experiments Prusky and colleagues (Prusky et al., 2004) have shown that after eye-opening the visual acuity in mice improves steeply, reaching adult type-levels within about 8-10 days.

The important question which arises is what developmental significance has the sparsification process? Sparse coding in the primary visual cortex during natural vision has been proposed based both on the theoretical and experimental evidence (Vinje and Gallant, 2000; Olshausen and Field, 2004). This 'sparse coding' refers to the fact that neurons might encode sensory information using a small number of active neurons at any given point in time. This strategy could possibly confer several advantages. Sparse representations as a model of sensory signaling provide a means of efficiently forming associations and storing memories, and all of this is achieved using relatively small amounts of energy (Olshausen and Field, 2004).

In conclusion, two distinct forms of neuronal activity (spontaneous and light evoked) in the mouse visual cortex during development were identified. Before eye-opening, a dense mode of neuronal activity may primarily underlie the coarse wiring of remote brain regions. After eye-opening, sparse spontaneous activity, in concert with sparse coding of stimulus-

evoked activity may be the basis for the feature-selective activation of individual cortical neurons (Quiroga et al., 2005).



## Bibliography:

**Adams, S.R.** (2000). In *Imaging Neurons: A Laboratory Manual* (eds. Yuste, R., Lanni, F. & Konnerth, A.), Cold Spring Harbor Press, Cold Spring Harbor, New York, 30.1-30.7.

**Adelsberger, H., Garaschuk, O., and Konnerth, A.** (2005). Cortical calcium waves in resting newborn mice. *Nat Neurosci* 8, 988-990.

**Akerman, C.J., Smyth, D., and Thompson, I.D.** (2002). Visual experience before eye-opening and the development of the retinogeniculate pathway. *Neuron* 36, 869-879.

**Anderson, J., Lampl, I., Reichova, I., Carandini, M., and Ferster, D.** (2000). Stimulus dependence of two-state fluctuations of membrane potential in cat visual cortex. *Nat Neurosci* 3, 617-621.

**Antonini, A., Fagiolini, M., and Stryker, M.P.** (1999). Anatomical correlates of functional plasticity in mouse visual cortex. *J Neurosci* 19, 4388-4406.

**Ashworth, S.L., and Tanner, G.A.** (2006). Fluorescent labeling of renal cells in vivo. *Nephron Physiol* 103, 91-96.

**Ashworth, S.L., Sandoval, R.M., Tanner, G.A., and Molitoris, B.A.** (2007). Two-photon microscopy: Visualization of kidney dynamics. *Kidney Int.* 72, 416-421.

**Baird, G.S., Zacharias, D.A., and Tsien, R.Y.** (1999). Circular permutation and receptor insertion within green fluorescent proteins. *Proc Natl Acad Sci U S A* 96, 11241-11246.

**Bansal, A., Singer, J.H., Hwang, B.J., Xu, W., Beaudet, A., and Feller, M.B.** (2000). Mice lacking specific nicotinic acetylcholine receptor subunits exhibit dramatically altered spontaneous activity patterns and reveal a limited role for retinal waves in forming ON and OFF circuits in the inner retina. *J Neurosci* 20, 7672-7681.

**Bear, M.F., Kleinschmidt, A., Gu, Q.A., and Singer, W.** (1990). Disruption of experience-dependent synaptic modifications in striate cortex by infusion of an NMDA receptor antagonist. *J Neurosci* 10, 909-925.

**Benaim, G., and Villalobo, A.** (2002). Phosphorylation of calmodulin. Functional implications. *Eur J Biochem* 269, 3619-3631.

- Ben-Ari, Y.** (2001). Developing networks play a similar melody. *Trends Neurosci* 24, 353-360.
- Bezprozvanny, I., and Hayden, M.R.** (2004). Deranged neuronal calcium signaling and Huntington disease. *Biochem Biophys Res Commun* 322, 1310-1317.
- Boissonnas, A., Fetler, L., Zeelenberg, I.S., Hugues, S., and Amigorena, S.** (2007). In vivo imaging of cytotoxic T cell infiltration and elimination of a solid tumor. *J Exp Med* 204, 345-356.
- Bonhoeffer, T., and Grinvald, A.** (1991). Iso-orientation domains in cat visual cortex are arranged in pinwheel-like patterns. *Nature* 353, 429-431.
- Brecht, M., Schneider, M., Sakmann, B., and Margrie, T.W.** (2004). Whisker movements evoked by stimulation of single pyramidal cells in rat motor cortex. *Nature* 427, 704-710.
- Buzsaki, G., and Draguhn, A.** (2004). Neuronal oscillations in cortical networks. *Science* 304, 1926-1929.
- Cahalan, M.D., and Parker, I.** (2006). Imaging the choreography of lymphocyte trafficking and the immune response. *Curr Opin Immunol* 18, 476-482.
- Cahalan, M.D., Parker, I., Wei, S.H., and Miller, M.J.** (2003). Real-time imaging of lymphocytes in vivo. *Curr Opin Immunol* 15, 372-377.
- Cang, J., Renteria, R.C., Kaneko, M., Liu, X., Copenhagen, D.R., and Stryker, M.P.** (2005). Development of precise maps in visual cortex requires patterned spontaneous activity in the retina. *Neuron* 48, 797-809.
- Caroni, P.** (1997). Overexpression of growth-associated proteins in the neurons of adult transgenic mice. *J Neurosci Methods* 71, 3-9.
- Catalano, S.M., and Shatz, C.J.** (1998). Activity-dependent cortical target selection by thalamic axons. *Science* 281, 559-562.
- Chandrasekaran, A.R., Plas, D.T., Gonzalez, E., and Crair, M.C.** (2005). Evidence for an instructive role of retinal activity in retinotopic map refinement in the superior colliculus of the mouse. *J Neurosci* 25, 6929-6938.
- Chapman, B., and Stryker, M.P.** (1993). Development of orientation selectivity in ferret visual cortex and effects of deprivation. *J Neurosci* 13, 5251-5262.
- Chapman, B., Gödecke, I., and Bonhoeffer, T.** (1999). Development of orientation preference in the mammalian visual cortex. *J Neurobiol* 41, 18-24.
- Chapman, B., Stryker, M.P., and Bonhoeffer, T.** (1996). Development of orientation preference maps in ferret primary visual cortex. *J Neurosci* 16, 6443-6453.
- Charpak, S., Mertz, J., Beaupaire, E., Moreaux, L., and Delaney, K.** (2001). Odor-evoked calcium signals in dendrites of rat mitral cells. *Proc Natl Acad Sci U S A* 98, 1230-1234.

- Cline, H.T., and Constantine-Paton, M.** (1989). NMDA receptor antagonists disrupt the retinotectal topographic map. *Neuron* 3, 413-426.
- Corlew, R., Bosma, M.M., and Moody, W.J.** (2004). Spontaneous, synchronous electrical activity in neonatal mouse cortical neurones. *J. Physiol.* 560, 377-390.
- Crowley, J.C., and Katz, L.C.** (1999). Development of ocular dominance columns in the absence of retinal input. *Nat Neurosci* 2, 1125-1130.
- Crowley, J.C., and Katz, L.C.** (2000). Early development of ocular dominance columns. *Science* 290, 1321-1324.
- Daw, N.W., Gordon, B., Fox, K.D., Flavin, H.J., Kirsch, J.D., Beaver, C.J., Ji, Q., Reid, S.N., and Czepita, D.** (1999). Injection of MK-801 affects ocular dominance shifts more than visual activity. *J Neurophysiol* 81, 204-215.
- Debarbieux, F., Audinat, E., and Charpak, S.** (2003). Action potential propagation in dendrites of rat mitral cells in vivo. *J Neurosci* 23, 5553-5560.
- Demas, J., Eglén, S.J., and Wong, R.O.** (2003). Developmental loss of synchronous spontaneous activity in the mouse retina is independent of visual experience. *J Neurosci* 23, 2851-2860.
- Denk, W.** (2000). In *Imaging Neurons: A Laboratory Manual* (eds. Yuste, R., Lanni, F. & Konnerth, A.), Cold Spring Harbor Press, Cold Spring Harbor, New York, 17.1-17.8.
- Denk, W., and Svoboda, K.** (1997). Photon upmanship: why multiphoton imaging is more than a gimmick. *Neuron* 18, 351-357.
- Denk, W., Strickler, J.H., and Webb, W.W.** (1990). Two-photon laser scanning fluorescence microscopy. *Science* 248, 73-76.
- Diez-Garcia, J., Akemann, W., and Knöpfel, T.** (2007). In vivo calcium imaging from genetically specified target cells in mouse cerebellum. *Neuroimage* 34, 859-869.
- Diez-Garcia, J., Matsushita, S., Mutoh, H., Nakai, J., Ohkura, M., Yokoyama, J., Dimitrov, D., and Knöpfel, T.** (2005). Activation of cerebellar parallel fibers monitored in transgenic mice expressing a fluorescent Ca<sup>2+</sup> indicator protein. *Eur J Neurosci* 22, 627-635.
- Dräger, U.C.** (1975). Receptive fields of single cells and topography in mouse visual cortex. *J Comp Neurol* 160, 269-290.
- Dupont, E., Hanganu, I.L., Kilb, W., Hirsch, S., and Luhmann, H.J.** (2006). Rapid developmental switch in the mechanisms driving early cortical columnar networks. *Nature* 439, 79-83.
- Evans, R.M., and Zamponi, G.W.** (2006). Presynaptic Ca<sup>2+</sup> channels--integration centers for neuronal signaling pathways. *Trends Neurosci* 29, 617-624.
- Fagiolini, M., and Hensch, T.K.** (2000). Inhibitory threshold for critical-period activation in primary visual cortex. *Nature* 404, 183-186.

**Feller, M.B., and Scanziani, M.** (2005). A precritical period for plasticity in visual cortex. *Curr Opin Neurobiol* 15, 94-100.

**Feller, M.B., Wellis, D.P., Stellwagen, D., Werblin, F.S., and Shatz, C.J.** (1996). Requirement for cholinergic synaptic transmission in the propagation of spontaneous retinal waves. *Science* 272, 1182-1187.

**Feng, G., Mellor, R.H., Bernstein, M., Keller-Peck, C., Nguyen, Q.T., Wallace, M., Nerbonne, J.M., Lichtman, J.W., and Sanes, J.R.** (2000). Imaging neuronal subsets in transgenic mice expressing multiple spectral variants of GFP. *Neuron* 28, 41-51.

**Fields, R.D., Lee, P.R., and Cohen, J.E.** (2005). Temporal integration of intracellular  $Ca^{2+}$  signaling networks in regulating gene expression by action potentials. *Cell Calcium* 37, 433-442.

**Flecknell, P.A.** (2000). *Laboratory Animal anaesthesia*. Academic Press, London, UK.

**Foran, D.R., Peterson, A.C.** (1992). Myelin acquisition in the central nervous system of the mouse revealed by an MBP-Lac Z transgene. *J Neurosci* 12, 4890-4897.

**Fox, K., Sato, H., and Daw, N.** (1989). The location and function of NMDA receptors in cat and kitten visual cortex. *J Neurosci* 9, 2443-2454.

**Galli, L., and Maffei, L.** (1988). Spontaneous impulse activity of rat retinal ganglion cells in prenatal life. *Science* 242, 90-91.

**Garaschuk, O., Griesbeck, O., and Konnerth, A.** (2007). Troponin C-based biosensors: A new family of genetically encoded indicators for in vivo calcium imaging in the nervous system. *Cell Calcium* 42, 351-361.

**Garaschuk, O., Hanse, E., and Konnerth, A.** (1998). Developmental profile and synaptic origin of early network oscillations in the CA1 region of rat neonatal hippocampus. *J Physiol Lond* 507, 219-236.

**Garaschuk, O., Linn, J., Eilers, J., and Konnerth, A.** (2000). Large-scale oscillatory calcium waves in the immature cortex. *Nat Neurosci* 3, 452-459.

**Garaschuk, O., Milos, R.I., and Konnerth, A.** (2006a). Targeted bulk-loading of fluorescent indicators for two-photon brain imaging in vivo. *Nature Protocols* 1, 380-386.

**Garaschuk, O., Milos, R.I., Grienberger, C., Marandi, N., Adelsberger, H., and Konnerth, A.** (2006b). Optical monitoring of brain function in vivo: from neurons to networks. *Pflugers Arch* 453, 385-396.

**Göbel, W., Kampa, B.M., and Helmchen, F.** (2007). Imaging cellular network dynamics in three dimensions using fast 3D laser scanning. *Nat Methods* 4, 73-79.

**Godement, P., Salaün, J., and Imbert, M.** (1984). Prenatal and postnatal development of retinogeniculate and retinocollicular projections in the mouse. *J Comp Neurol* 230, 552-575.

- Gordon, J.A., and Stryker, M.P.** (1996). Experience-dependent plasticity of binocular responses in the primary visual cortex of the mouse. *J Neurosci* 16, 3274-3286.
- Griesbeck, O.** (2004). Fluorescent proteins as sensors for cellular functions. *Curr Opin Neurobiol* 14, 636-641.
- Grinvald, A., Lieke, E., Frostig, R.D., Gilbert, C.D., and Wiesel, T.N.** (1986). Functional architecture of cortex revealed by optical imaging of intrinsic signals. *Nature* 324, 361-364.
- Grutzendler, J., and Gan, W.B.** (2005). In *Imaging in Neuroscience and Development: A Laboratory Manual* (eds. Yuste, R., Konnerth, A.). Cold Spring Harbour Laboratory Press, US Chapter 22.
- Haider, B., Duque, A., Hasenstaub, A.R., Yu, Y., and McCormick, D.A.** (2007). Enhancement of visual responsiveness by spontaneous local network activity in vivo. *J Neurophysiol* 97, 4186-4202.
- Hanganu, I.L., Ben-Ari, Y., and Khazipov, R.** (2006). Retinal waves trigger spindle bursts in the neonatal rat visual cortex. *J Neurosci* 26, 6728-6736.
- Hasan, M.T., Friedrich, R.W., Euler, T., Larkum, M.E., Giese, G., Both, M., Duebel, J., Waters, J., Bujard, H., Griesbeck, O., et al.** (2004). Functional fluorescent Ca<sup>2+</sup> indicator proteins in transgenic mice under TET control. *PLoS Biol* 2, 763-775.
- Hasenstaub, A., Sachdev, R.N., and McCormick, D.A.** (2007). State changes rapidly modulate cortical neuronal responsiveness. *J Neurosci* 27, 9607-9622.
- Heim, N., and Griesbeck, O.** (2004). Genetically encoded indicators of cellular calcium dynamics based on troponin C and green fluorescent protein. *J Biol Chem* 279, 14280-14286.
- Heim, N., Garaschuk, O., Friedrich, M.W., Mank, M., Milos, R.I., Kovalchuk, Y., Konnerth, A., and Griesbeck, O.** (2007). Improved calcium imaging in transgenic mice expressing a troponin C-based biosensor. *Nat Methods* 4, 127-129.
- Helmchen, F., and Denk, W.** (2005). Deep tissue two-photon microscopy. *Nat Methods* 2, 932-940.
- Helmchen, F., and Waters, J.** (2002). Ca<sup>2+</sup> imaging in the mammalian brain in vivo. *Eur J Pharmacol* 447, 119-129.
- Helmchen, F., Imoto, K., and Sakmann, B.** (1996). Ca<sup>2+</sup> buffering and action potential-evoked Ca<sup>2+</sup> signaling in dendrites of pyramidal neurons. *Biophys J* 70, 1069-1081.
- Helmchen, F., Svoboda, K., Denk, W., and Tank, D.W.** (1999). In vivo dendritic calcium dynamics in deep-layer cortical pyramidal neurons. *Nat Neurosci* 2, 989-996.
- Hensch, T.K.** (2005). Critical period plasticity in local cortical circuits. *Nat Rev Neurosci* 6, 877-888.

**Hensch, T.K., Fagiolini, M., Mataga, N., Stryker, M.P., Baekkeskov, S., and Kash, S.F.** (1998). Local GABA circuit control of experience-dependent plasticity in developing visual cortex. *Science* 282, 1504-1508.

**Hirase, H., Qian, L., Bartho, P., and Buzsaki, G.** (2004). Calcium dynamics of cortical astrocytic networks in vivo. *PLoS Biol* 2, E96.

**Holthoff, K., Kovalchuk, Y., Yuste, R., and Konnerth, A.** (2004). Single-shock LTD by local dendritic spikes in pyramidal neurons of mouse visual cortex. *J Physiol* 560, 27-36.

**Horton, J.C., and Hocking, D.R.** (1996). An adult-like pattern of ocular dominance columns in striate cortex of newborn monkeys prior to visual experience. *J Neurosci* 16, 1791-1807.

**Hubel, D.H., and Wiesel, T.N.** (1959). Receptive fields of single neurones in the cat's striate cortex. *J Physiol* 148, 574-591.

**Hubel, D.H., and Wiesel, T.N.** (1962). Receptive fields, binocular interaction and functional architecture in the cat's visual cortex. *J Physiol* 160, 106-154.

**Hubel, D.H., and Wiesel, T.N.** (1968). Receptive fields and functional architecture of monkey striate cortex. *J Physiol* 195, 215-243.

**Hubel, D.H., and Wiesel, T.N.** (1969). Anatomical demonstration of columns in the monkey striate cortex. *Nature* 221, 747-750.

**Hübener, M.** (2003). Mouse visual cortex. *Curr Opin Neurobiol* 13, 413-420.

**Huttenlocher, P.R.** (1966). Development of neuronal activity in neocortex of the kitten. *Nature* 211, 91-92.

**Huttenlocher, P.R.** (1967). Development of cortical neuronal activity in the neonatal cat. *Exp Neurol* 17, 247-262.

**Jaubert-Miazza, L., Green, E., Lo, F.S., Bui, K., Mills, J., and Guido, W.** (2005). Structural and functional composition of the developing retinogeniculate pathway in the mouse. *Vis Neurosci* 22, 661-676.

**Jurado, L.A., Chockalingam, P.S., and Jarrett, H.W.** (1999). Apocalmodulin. *Physiological reviews* 79, 661-682.

**Kakizawa, S., Miyazaki, T., Yanagihara, D., Iino, M., Watanabe, M., and Kano, M.** (2005). Maintenance of presynaptic function by AMPA receptor-mediated excitatory postsynaptic activity in adult brain. *Proc Natl Acad Sci U S A* 102, 19180-19185.

**Kandler, K., and Katz, L.C.** (1995). Neuronal coupling and uncoupling in the developing nervous system. *Curr Opin Neurobiol* 5, 98-105.

**Kandler, K., and Katz, L.C.** (1998). Coordination of neuronal activity in developing visual cortex by gap junction-mediated biochemical communication. *J Neurosci* 18, 1419-1427.

- Katagiri, H., Fagiolini, M., and Hensch, T.K.** (2007). Optimization of somatic inhibition at critical period onset in mouse visual cortex. *Neuron* 53, 805-812.
- Katz, L.C., and Crowley, J.C.** (2002). Development of cortical circuits: lessons from ocular dominance columns. *Nat Rev Neurosci* 3, 34-42.
- Katz, L.C., and Shatz, C.J.** (1996). Synaptic activity and the construction of cortical circuits. *Science* 274, 1133-1138.
- Kenet, T., Bibitchkov, D., Tsodyks, M., Grinvald, A., and Arieli, A.** (2003). Spontaneously emerging cortical representations of visual attributes. *Nature* 425, 954-956.
- Kerr, J.N., Greenberg, D., and Helmchen, F.** (2005). Imaging input and output of neocortical networks in vivo. *Proc Natl Acad Sci U S A* 102, 14063-14068.
- Kleinfeld, D., Mitra, P.P., Helmchen, F., and Denk, W.** (1998). Fluctuations and stimulus-induced changes in blood flow observed in individual capillaries in layers 2 through 4 of rat neocortex. *Proc Natl Acad Sci U S A* 95, 15741-15746.
- Kleinschmidt, A., Bear, M.F., and Singer, W.** (1987). Blockade of "NMDA" receptors disrupts experience-dependent plasticity of kitten striate cortex. *Science* 238, 355-358.
- Knöpfel, T., Diez-Garcia, J., and Akemann, W.** (2006). Optical probing of neuronal circuit dynamics: genetically encoded versus classical fluorescent sensors. *Trends Neurosci* 29, 160-166.
- Komuro, H., and Kumada, T.** (2005). Ca<sup>2+</sup> transients control CNS neuronal migration. *Cell Calcium* 37, 387-393.
- Konur, S., and Ghosh, A.** (2005). Calcium signaling and the control of dendritic development. *Neuron* 46, 401-405.
- Kotlikoff, M.I.** (2007). Genetically encoded Ca<sup>2+</sup> indicators: using genetics and molecular design to understand complex physiology. *J Physiol* 578, 55-67.
- Krey, J.F., and Dolmetsch, R.E.** (2007). Molecular mechanisms of autism: a possible role for Ca<sup>2+</sup> signaling. *Curr Opin Neurobiol* 17, 112-119.
- Krug, K., Akerman, C.J., and Thompson, I.D.** (2001). Responses of neurons in neonatal cortex and thalamus to patterned visual stimulation through the naturally closed lids. *J Neurophysiol* 85, 1436-1443.
- LaFerla, F.M.** (2002). Calcium dyshomeostasis and intracellular signalling in Alzheimer's disease. *Nat Rev Neurosci* 3, 862-872.
- Lampl, I., Reichova, I., and Ferster, D.** (1999). Synchronous membrane potential fluctuations in neurons of the cat visual cortex. *Neuron* 22, 361-374.
- Lanni, F., and Keller, H.E.** (2000). In *Imaging Neurons: A Laboratory Manual* (eds. Yuste, R., Lanni, F. & Konnerth, A.), Cold Spring Harbor Press, Cold Spring Harbor, New York, 1.1-1.72.

**Liu, S.J., and Zukin, R.S.** (2007).  $\text{Ca}^{2+}$ -permeable AMPA receptors in synaptic plasticity and neuronal death. *Trends Neurosci* 30, 126-134.

**Llinas, R.R.** (1988). The intrinsic electrophysiological properties of mammalian neurons: insights into central nervous system function. *Science* 242, 1654-1664.

**Lohmann, C., Finski, A., and Bonhoeffer, T.** (2005). Local calcium transients regulate the spontaneous motility of dendritic filopodia. *Nat Neurosci* 8, 305-312.

**Maffei, L., and Galli-Resta, L.** (1990). Correlation in the discharges of neighboring rat retinal ganglion cells during prenatal life. *Proc Natl Acad Sci U S A* 87, 2861-2864.

**Majewska, A., Yiu, G., and Yuste, R.** (2000). A custom-made two-photon microscope and deconvolution system. *Pflugers Arch* 441, 398-408.

**Mangini, N.J., and Pearlman, A.L.** (1980). Laminal distribution of receptive field properties in the primary visual cortex of the mouse. *J Comp Neurol* 193, 203-222.

**Mank, M., Reiff, D.F., Heim, N., Friedrich, M.W., Borst, A., and Griesbeck, O.** (2006). A FRET-based calcium biosensor with fast signal kinetics and high fluorescence change. *Biophys J* 90, 1790-1796.

**Mao, B.Q., Hamzei-Sichani, F., Aronov, D., Froemke, R.C., and Yuste, R.** (2001). Dynamics of spontaneous activity in neocortical slices. *Neuron* 32, 883-898.

**Margrie, T.W., Brecht, M., and Sakmann, B.** (2002). In vivo, low-resistance, whole-cell recordings from neurons in the anaesthetized and awake mammalian brain. *Pflugers Arch* 444, 491-498.

**Masters, B.R., So, P.T., and Gratton, E.** (1998). Multiphoton excitation microscopy of in vivo human skin. Functional and morphological optical biopsy based on three-dimensional imaging, lifetime measurements and fluorescence spectroscopy. *Ann N Y Acad Sci* 838, 58-67.

**McCabe, A.K., Easton, C.R., Lischalk, J.W., and Moody, W.J.** (2007). Roles of glutamate and GABA receptors in setting the developmental timing of spontaneous synchronized activity in the developing mouse cortex. *Dev Neurobiol* 67, 1574-1588.

**McCormick, D.A.** (1999). Spontaneous activity: signal or noise? *Science* 285, 541-543.

**McLaughlin, T., Torborg, C.L., Feller, M.B., and O'Leary, D.D.** (2003). Retinotopic map refinement requires spontaneous retinal waves during a brief critical period of development. *Neuron* 40, 1147-1160.

**Meister, M., Wong, R.O., Baylor, D.A., and Shatz, C.J.** (1991). Synchronous bursts of action potentials in ganglion cells of the developing mammalian retina. *Science* 252, 939-943.

**Metin, C., Godement, P., and Imbert, M.** (1988). The primary visual cortex in the mouse: receptive field properties and functional organization. *Exp Brain Res* 69, 594-612.



**Miller, K.D., Chapman, B., and Stryker, M.P.** (1989). Visual responses in adult cat visual cortex depend on N-methyl-D-aspartate receptors. *Proc Natl Acad Sci U S A* 86, 5183-5187.

**Minlebaev, M., Ben-Ari, Y., and Khazipov, R.** (2007). Network mechanisms of spindle-burst oscillations in the neonatal rat barrel cortex in vivo. *J Neurophysiol* 97, 692-700.

**Miyawaki, A.** (2005). Innovations in the imaging of brain functions using fluorescent proteins. *Neuron* 48, 189-199.

**Miyawaki, A., Griesbeck, O., Heim, R., and Tsien, R.Y.** (1999). Dynamic and quantitative  $\text{Ca}^{2+}$  measurements using improved cameleons. *Proc Natl Acad Sci USA* 96, 2135-2140.

**Miyawaki, A., Llopis, J., Heim, R., McCaffery, J.M., Adams, J.A., Ikura, M., and Tsien, R.Y.** (1997). Fluorescent indicators for  $\text{Ca}^{2+}$  based on green fluorescent proteins and calmodulin. *Nature* 388, 882-887.

**Mooney, R., Penn, A.A., Gallego, R., and Shatz, C.J.** (1996). Thalamic relay of spontaneous retinal activity prior to vision. *Neuron* 17, 863-874.

**Mrsic-Flogel, T.D., Hofer, S.B., Creutzfeldt, C., Cloëz-Tayarani, I., Changeux, J.P., Bonhoeffer, T., and Hübener, M.** (2005). Altered map of visual space in the superior colliculus of mice lacking early retinal waves. *J Neurosci* 25, 6921-6928.

**Mrsic-Flogel, T.D., Hofer, S.B., Ohki, K., Reid, R.C., Bonhoeffer, T., and Hübener, M.** (2007). Homeostatic regulation of eye-specific responses in visual cortex during ocular dominance plasticity. *Neuron* 54, 961-972.

**Muir-Robinson, G., Hwang, B.J., and Feller, M.B.** (2002). Retinogeniculate axons undergo eye-specific segregation in the absence of eye-specific layers. *J Neurosci* 22, 5259-5264.

**Nagai, T., Sawano, A., Park, E.S., and Miyawaki, A.** (2001). Circularly permuted green fluorescent proteins engineered to sense  $\text{Ca}^{2+}$ . *Proc Natl Acad Sci U S A* 98, 3197-3202.

**Nagai, T., Yamada, S., Tominaga, T., Ichikawa, M., and Miyawaki, A.** (2004). Expanded dynamic range of fluorescent indicators for  $\text{Ca}^{2+}$  by circularly permuted yellow fluorescent proteins. *Proc Natl Acad Sci U S A* 101, 10554-10559.

**Nagayama, S., Zeng, S., Xiong, W., Fletcher, M.L., Masurkar, A.V., Davis, D.J., Pieribone, V.A., and Chen, W.R.** (2007). In vivo simultaneous tracing and  $\text{Ca}^{2+}$  imaging of local neuronal circuits. *Neuron* 53, 789-803.

**Nakai, J., Ohkura, M., and Imoto, K.** (2001). A high signal-to-noise  $\text{Ca}^{2+}$  probe composed of a single green fluorescent protein. *Nat Biotechnol* 19, 137-141.

**Nevian, T., and Helmchen, F.** (2007). Calcium indicator loading of neurons using single-cell electroporation. *Pflugers Arch* 454, 675-688.

**Nicolelis, M.A., and Ribeiro, S.** (2002). Multielectrode recordings: the next steps. *Curr Opin Neurobiol* 12, 602-606.

**Nimmerjahn, A., Kirchhoff, F., Kerr, J.N.D., and Helmchen, F.** (2004). Sulforhodamine 101 as a specific marker of astroglia in the neocortex in vivo. *Nature Methods* *1*, 31-37.

**Ohki, K., Chung, S., Ch'ng, Y.H., Kara, P., and Reid, R.C.** (2005). Functional imaging with cellular resolution reveals precise micro-architecture in visual cortex. *Nature* *433*, 597-603.

**Ohki, K., Chung, S., Kara, P., Hübener, M., Bonhoeffer, T., and Reid, R.C.** (2006). Highly ordered arrangement of single neurons in orientation pinwheels. *Nature* *442*, 925-928.

**Olshausen, B.A., and Field, D.J.** (2004). Sparse coding of sensory inputs. *Curr Opin Neurobiol* *14*, 481-487.

**Orbach, H.S., Cohen, L.B., and Grinvald, A.** (1985). Optical mapping of electrical activity in rat somatosensory and visual cortex. *J Neurosci* *5*, 1886-1895.

**Paxinos, G., and Franklin, K.B.J.** (2001). *The Mouse Brain in Stereotaxic Coordinates*. Academic Press, San Diego, CA.

**Peinado, A.** (2000). Traveling slow waves of neural activity: a novel form of network activity in developing neocortex. *J Neurosci* *20*, RC54.

**Persico, A.M., Calia, E., and Keller, F.** (1997). Implants for sustained drug release over the somatosensory cortex of the newborn rat: a comparison of materials and surgical procedures. *J Neurosci Methods* *76*, 105-113.

**Petersen, C.C., Hahn, T.T., Mehta, M., Grinvald, A., and Sakmann, B.** (2003). Interaction of sensory responses with spontaneous depolarization in layer 2/3 barrel cortex. *Proc Natl Acad Sci U S A* *100*, 13638-13643.

**Polsky, A., Mel, B.W., and Schiller, J.** (2004). Computational subunits in thin dendrites of pyramidal cells. *Nat Neurosci* *7*, 621-627.

**Prusky, G.T., Alam, N.M., Beekman, S., and Douglas, R.M.** (2004). Rapid quantification of adult and developing mouse spatial vision using a virtual optomotor system. *Invest Ophthalmol Vis Sci* *45*, 4611-4616.

**Purves, D.** (2004). *Neuroscience*, third edition. Sinauer Associates Inc. *Sunderland Massachusetts USA*.

**Quiroga, R.Q., Reddy, L., Kreiman, G., Koch, C., and Fried, I.** (2005). Invariant visual representation by single neurons in the human brain. *Nature* *435*, 1102-1107.

**Redmond, L., Kashani, A.H., and Ghosh, A.** (2002). Calcium regulation of dendritic growth via CaM kinase IV and CREB-mediated transcription. *Neuron* *34*, 999-1010.

**Reiprich, P., Kilb, W., and Luhmann, H.J.** (2005). Neonatal NMDA receptor blockade disturbs neuronal migration in rat somatosensory cortex in vivo. *Cereb Cortex* *15*, 349-358.

**Rossi, F.M., Pizzorusso, T., Porciatti, V., Marubio, L.M., Maffei, L., and Changeux, J.P.** (2001). Requirement of the nicotinic acetylcholine receptor beta 2 subunit for the anatomical and functional development of the visual system. *Proc Natl Acad Sci U S A* 98, 6453-6458.

**Rudolf, R., Magalhaes, P.J., and Pozzan, T.** (2006). Direct in vivo monitoring of sarcoplasmic reticulum  $\text{Ca}^{2+}$  and cytosolic cAMP dynamics in mouse skeletal muscle. *J Cell Biol* 173, 187-193.

**Ruthazer, E.S., Akerman, C.J., and Cline, H.T.** (2003). Control of axon branch dynamics by correlated activity in vivo. *Science* 301, 66-70.

**Ruthazer, E.S., and Stryker, M.P.** (1996). The role of activity in the development of long-range horizontal connections in area 17 of the ferret. *J Neurosci* 16, 7253-7269.

**Schuett, S., Bonhoeffer, T., and Hübener, M.** (2002). Mapping retinotopic structure in mouse visual cortex with optical imaging. *J Neurosci* 22, 6549-6559.

**Simon, D.K., Prusky, G.T., O'Leary, D.D., and Constantine-Paton, M.** (1992). N-methyl-D-aspartate receptor antagonists disrupt the formation of a mammalian neural map. *Proc Natl Acad Sci US A* 89, 10593-10597.

**Smetters, D., Majewska, A., and Yuste, R.** (1999). Detecting action potentials in neuronal populations with calcium imaging. *Methods* 18, 215-221.

**Smith, A.L., Cordery, P.M., and Thompson, I.D.** (1995). Manufacture and release characteristics of Elvax polymers containing glutamate receptor antagonists. *J Neurosci Methods* 60, 211-217.

**Soeller, C., and Cannell, M.B.** (1996). Construction of a two-photon microscope and optimisation of illumination pulse duration. *Pflugers Arch* 432, 555-561.

**Sohya, K., Kameyama, K., Yanagawa, Y., Obata, K., and Tsumoto, T.** (2007). GABAergic neurons are less selective to stimulus orientation than excitatory neurons in layer II/III of visual cortex, as revealed by in vivo functional  $\text{Ca}^{2+}$  imaging in transgenic mice. *J Neurosci* 27, 2145-2149.

**Squirrell, J.M., Wokosin, D.L., White, J.G., and Bavister, B.D.** (1999). Long-term two-photon fluorescence imaging of mammalian embryos without compromising viability. *Nat Biotechnol* 17, 763-767.

**Steriade, M.** (2000). Corticothalamic resonance, states of vigilance and mentation. *Neuroscience* 101, 243-276.

**Steriade, M., and Timofeev, I.** (2003). Neuronal plasticity in thalamocortical networks during sleep and waking oscillations. *Neuron* 37, 563-576.

**Steriade, M., Nunez, A., and Amzica, F.** (1993). A novel slow (1 Hz) oscillation of neocortical neurons in vivo: depolarizing and hyperpolarizing components. *J Neurosci* 13, 3252-3265.

**Stosiek, C., Garaschuk, O., Holthoff, K., and Konnerth, A.** (2003). In vivo two-photon calcium imaging of neuronal networks. *Proc Natl Acad Sci U S A* *100*, 7319-7324.

**Sullivan, M.R., Nimmerjahn, A., Sarkisov, D.V., Helmchen, F., and Wang, S.S.** (2005). In vivo calcium imaging of circuit activity in cerebellar cortex. *J Neurophysiol* *94*, 1636-1644.

**Sur, M., and Leamey, C.A.** (2001). Development and plasticity of cortical areas and networks. *Nat Rev Neurosci* *2*, 251-262.

**Sur, M., and Rubenstein, J.L.** (2005). Patterning and plasticity of the cerebral cortex. *Science* *310*, 805-810.

**Sur, M., Angelucci, A., and Sharma, J.** (1999). Rewiring cortex: the role of patterned activity in development and plasticity of neocortical circuits. *J Neurobiol* *41*, 33-43.

**Svoboda, K., Denk, W., Kleinfeld, D., and Tank, D.W.** (1997). In vivo dendritic calcium dynamics in neocortical pyramidal neurons. *Nature* *385*, 161-165.

**Svoboda, K., Helmchen, F., Denk, W., and Tank, D.W.** (1999). Spread of dendritic excitation in layer 2/3 pyramidal neurons in rat barrel cortex in vivo. *Nat Neurosci* *2*, 65-73.

**Takano, T., Han, X., Deane, R., Zlokovic, B., and Nedergaard, M.** (2007). Two-photon imaging of astrocytic Ca<sup>2+</sup> signaling and the microvasculature in experimental mice models of Alzheimer's disease. *Ann N Y Acad Sci* *1097*, 40-50.

**Talcott, B., and Moore, M.S.** (1999). Getting across the nuclear pore complex. *Trends Cell Biol* *9*, 312-318.

**Theer, P., Hasan, M.T., and Denk, W.** (2003). Two-photon imaging to a depth of 1000 microm in living brains by use of a Ti:Al<sub>2</sub>O<sub>3</sub> regenerative amplifier. *Opt Lett* *28*, 1022-1024.

**Torborg, C.L., and Feller, M.B.** (2005). Spontaneous patterned retinal activity and the refinement of retinal projections. *Prog Neurobiol* *76*, 213-235.

**Tsien, R.Y.** (1981). A non-disruptive technique for loading calcium buffers and indicators into cells. *Nature* *290*, 527-528.

**Tsien, R.Y.** (1989). Fluorescent probes of cell signaling. *Annu Rev Neurosci* *12*, 227-253.

**Tsien, R.Y.** (2000). In *Imaging Neurons: A Laboratory Manual* (eds. Yuste, R., Lanni, F. & Konnerth, A.), Cold Spring Harbor Press, Cold Spring Harbor, New York, 55.1-55.10.

**Uchida, I., Cestari, I.N., and Yang, J.** (1996). The differential antagonism by bicuculline and SR95531 of pentobarbitone-induced currents in cultured hippocampal neurons. *Eur J Pharmacol* *307*, 89-96.

**Valverde, F.** (1968). Structural changes in the area striata of the mouse after enucleation. *Exp Brain Res* *5*, 274-292.

**Valverde, F.** (1998). *Golgi Atlas of the Postnatal Mouse Brain*. Springer Verlag.

- Vinje, W.E., and Gallant, J.L.** (2000). Sparse coding and decorrelation in primary visual cortex during natural vision. *Science* 287, 1273-1276.
- Wagor, E., Mangini, N.J., and Pearlman, A.L.** (1980). Retinotopic organization of striate and extrastriate visual cortex in the mouse. *J Comp Neurol* 193, 187-202.
- Waters, J., and Helmchen, F.** (2004). Boosting of action potential backpropagation by neocortical network activity in vivo. *J Neurosci* 24, 11127-11136.
- Weliky, M.** (1999). Recording and manipulating the in vivo correlational structure of neuronal activity during visual cortical development. *J Neurobiol* 41, 25-32.
- Weliky, M.** (2000). Correlated neuronal activity and visual cortical development. *Neuron* 27, 427-430.
- Weliky, M., and Katz, L.C.** (1999). Correlational structure of spontaneous neuronal activity in the developing lateral geniculate nucleus in vivo. *Science* 285, 599-604.
- Wessels, J.T., Busse, A.C., Mahrt, J., Dullin, C., Grabbe, E., and Mueller, G.A.** (2007). In vivo imaging in experimental preclinical tumor research-A review. *Cytometry A* 71, 542-549.
- Wiesel, T.N., and Hubel, D.H.** (1963). Single-Cell Responses in Striate Cortex of Kittens Deprived of Vision in One Eye. *J Neurophysiol* 26, 1003-1017.
- Williams, R.M., Piston, D.W., and Webb, W.W.** (1994). Two-photon molecular excitation provides intrinsic 3-dimensional resolution for laser-based microscopy and microphotochemistry. *FASEB J* 8, 804-813.
- Wise, F.** (2000). In *Imaging Neurons: A Laboratory Manual* (eds. Yuste, R., Lanni, F. & Konnerth, A.), Cold Spring Harbor Press, Cold Spring Harbor, New York, 18.1-18.9.
- Wong, E.H., Kemp, J.A., Priestley, T., Knight, A.R., Woodruff, G.N., and Iversen, L.L.** (1986). The anticonvulsant MK-801 is a potent N-methyl-D-aspartate antagonist. *Proc Natl Acad Sci U S A* 83, 7104-7108.
- Wong, R.O.** (1999). Retinal waves and visual system development. *Annu Rev Neurosci* 22, 29-47.
- Wong, R.O.** (2000). In *Imaging Neurons: A Laboratory Manual* (eds. Yuste, R., Lanni, F. & Konnerth, A.), Cold Spring Harbor Press, Cold Spring Harbor, New York, 41.1-41.7.
- Wong, R.O., Chernjavsky, A., Smith, S.J., and Shatz, C.J.** (1995). Early functional neural networks in the developing retina. *Nature* 374, 716-718.
- Wong, R.O., Meister, M., and Shatz, C.J.** (1993). Transient period of correlated bursting activity during development of the mammalian retina. *Neuron* 11, 923-938.
- Woodruff, G.N., Foster, A.C., Gill, R., Kemp, J.A., Wong, E.H., and Iversen, L.L.** (1987). The interaction between MK-801 and receptors for N-methyl-D-aspartate: functional consequences. *Neuropharmacology* 26, 903-909.

**Young, R.W.** (1985). Cell differentiation in the retina of the mouse. *Anat Rec* 212, 199-205.

**Yuste, R., and Denk, W.** (1995). Dendritic spines as basic functional units of neuronal integration. *Nature* 375, 682-684.

**Yuste, R., and Sur, M.** (1999). Development and plasticity of the cerebral cortex: from molecules to maps. *J Neurobiol* 41, 1-6.

**Yuste, R., Lanni, F., and Konnerth, A.** (2000). In *Imaging Neurons: A Laboratory Manual* (eds. Yuste, R., Lanni, F. & Konnerth, A.), Cold Spring Harbor Press, Cold Spring Harbor, New York, 34.1-34.9.

**Yuste, R., Nelson, D.A., Rubin, W.W., and Katz, L.C.** (1995). Neuronal domains in developing neocortex: mechanisms of coactivation. *Neuron* 14, 7-17.

**Yuste, R., Peinado, A., and Katz, L.C.** (1992). Neuronal domains in developing neocortex. *Science*, 665-669.

**Zhang, J., Campbell, R.E., Ting, A.Y., and Tsien, R.Y.** (2002). Creating new fluorescent probes for cell biology. *Nat Rev Mol Cell Biol* 3, 906-918.

## Appendix A

### List of Publications:

#### Publications in Peer Reviewed Journals:

Garaschuk O.\*, **Milos R.I.\***, Marandi N., Rochefort N., Pichler B., Konnerth, A. 'Sparsification' of neuronal activity in the visual cortex at eye opening. Submitted to Science

\* These authors contributed equally to this work

Heim N., Garaschuk O., Friedrich M.W., Mank M., **Milos R.I.**, Kovalchuk Y., Holbro N., Oertner T.G., Konnerth A., Griesbeck O. (2007) Improved calcium imaging in transgenic mice expressing a troponin C-based FRET biosensor. *Nature Methods* - 4,127-129.

Garaschuk O., **Milos R.I.**, Grienberger C., Marandi N., Adelsberger H., Konnerth A. (2006) Optical monitoring of brain function in vivo: from neurons to networks. *Pflügers Arch - Eur. J. Physiol.* 453: 385-396.

Garaschuk O., **Milos R.I.**, Konnerth A. (2006) Targeted bulk-loading of fluorescent indicators for two-photon brain imaging *in vivo*. *Nature Protocols* 1, 380-386.

#### Manuscripts in Preparation:

Adelsberger H., Grienberger C., **Milos R.I.**, Garaschuk O., Konnerth A. Optic fiber based detection of brain calcium signals in vivo.

#### Posters, Presentations:

Adelsberger H., Schierloh A., Grienberger C., **Milos R.I.**, Garaschuk O., Konnerth A. (2007) Long-range calcium waves in the brain of adult mice. Göttingen Meeting of the German Neuroscience Society 2007, T30-2C

**Milos R.I.**, Garaschuk O., Marandi N., Konnerth A. (2006) Endogenous network activity in the developing visual cortex at the onset of the critical period. FENS Forum 2006, A179.17

Adelsberger H., Grienberger C., **Milos R.I.**, Konnerth A. (2006) Spontaneous and sound evoked calcium transients in the auditory cortex of mice *in vivo*. FENS Forum 2006, A034.3

**Milos R.I.**, Garaschuk O., Marandi N., Konnerth A. (2006) Developmental switch of visual cortex network activity at the onset of the critical period. Supplement to *Acta Physiologica*, Vol. 186, PW07A-1

Garaschuk O., Busche M.A., **Milos R.I.**, Marandi N., Konnerth A. (2006) Mechanisms of calcium signaling in the *in vivo* mouse visual cortex. Supplement to Acta Physiologica, Vol. 186, OM04-23

Marandi N., **Milos R.I.**, Garaschuk O., Konnerth A. (2006) Light-evoked calcium signals in the developing mouse visual cortex precede eye-opening. Supplement to Acta Physiologica, Vol. 186, PW07P-2

**Milos R.I.** (2005) Calcium waves in the developing visual cortex. Neuroscience 2005. International Symposium Timisoara-München (Co-organizer)

Adelsberger H., Garaschuk O., **Milos R.I.**, Enache A., Konnerth A. (2005) A new method for *in vivo* monitoring of calcium signals in behaving mice. 2<sup>nd</sup> e.IP workshop at the annual meeting of the German Physiology Society.

Adelsberger H., Garaschuk O., **Milos R.I.**, Enache A., Konnerth A. (2004) *In vivo* monitoring of calcium waves in behaving mice. FENS Forum 2004, A148.2

Adelsberger H., Garaschuk O., **Milos R.I.**, Enache A., Konnerth A. (2004) Optic fiber-based calcium imaging *in vivo*. SFB 391 Symposium Synapses, 2004

Adelsberger H., Garaschuk O., **Milos R.I.**, Enache A., Konnerth A. (2004) A new method for monitoring *in vivo* Ca<sup>2+</sup> signaling. Supplement to Eur. J. Physiol. Vol. 447: P09-3

**Milos R.I.**, Radulescu A. (2002) Study of the correlations between clinical aspects, risk factors and osteodensimetry in osteoporosis. 6<sup>th</sup> International Medical Students and Young Doctors Meeting MEDIS 2002, Timisoara, Romania

**Milos R.I.**, Stirban C. (2000) Diagnosis of the vasovagal syncope using the tilt-test technique. 4<sup>th</sup> International Medical Students and Young Doctors Meeting MEDIS 2000, Timisoara, Romania (*First Prize* at the Internal Medicine Section).



# Targeted bulk-loading of fluorescent indicators for two-photon brain imaging *in vivo*

Olga Garaschuk<sup>1</sup>, Ruxandra-Iulia Milos<sup>2</sup> & Arthur Konnerth<sup>2</sup>

<sup>1</sup>Institut für Physiologie, Ludwig-Maximilians Universität München, Pettenkoferstrasse 12, 80336 München, Germany. <sup>2</sup>Institut für Neurowissenschaften, Technische Universität München, Biedersteinerstrasse 29, 80802 München, Germany. Correspondence should be addressed to A.K. (arthur.konnerth@lrz.tum.de).

Published online 27 June 2006; doi:10.1038/nprot.2006.58

One of the challenges for modern neuroscience is to understand the rules of concerted neuronal function *in vivo*. This question can be addressed using noninvasive high-resolution imaging techniques like two-photon microscopy. This protocol describes a versatile approach for *in vivo* two-photon calcium imaging of neural networks, stained with membrane-permeant fluorescent-indicator dyes. It is based on a targeted pressure ejection of the dye into the tissue of interest and can be used for a large spectrum of indicator dyes, including Oregon Green 488 BAPTA-1 acetoxymethyl ester and Fura-2 acetoxymethyl ester. Through the use of dye mixtures and multicolor imaging, this technique allows the visualization of distinct neurons and glial cells up to 500  $\mu\text{m}$  below the brain surface. It is suitable for staining the brain tissue of various different species (e.g., mouse, rat, cat and zebrafish) at all developmental stages. When combined with brain microendoscopy, it allows the monitoring of intracellular calcium signals in awake, behaving animals. The total time required to carry out the protocol, including dissection and cell staining, is  $\sim 2$  h. Thereafter, imaging experiments might be performed for at least 6 h.

## INTRODUCTION

This protocol describes an approach for *in vivo* two-photon  $\text{Ca}^{2+}$  imaging of large neuronal circuits at a single-cell level of resolution. Cells are stained by a brief ‘bolus’ injection of a membrane-permeant  $\text{Ca}^{2+}$ -indicator dye into the extracellular space (Fig. 1). The injected dye diffuses into the cells of interest, where it is hydrolyzed by intracellular esterases<sup>1</sup>. The activity-dependent  $\text{Ca}^{2+}$  transients in stained cells are then monitored using two-photon laser-scanning microscopy. This approach was initially developed for *in vivo* imaging of the mouse cortex, and is termed multicell bolus loading (MCBL)<sup>2</sup>. Over the past years, it has been successfully applied to the cerebral and cerebellar cortices of other species, such as rats and cats<sup>3–6</sup>. Interestingly, the same staining protocol is applicable to lower vertebrates and was used, for example, for *in vivo* imaging of the spinal cord<sup>7</sup>, olfactory bulb<sup>8</sup> and tectal<sup>9</sup> neurons in zebrafish larvae.

MCBL differs from other staining methods utilizing membrane-permeant acetoxymethyl (AM) ester-based indicator dyes<sup>10,11</sup> in that the indicators are delivered for a short period directly to the target cells (see also the method of Regehr and Tank<sup>12</sup>). The targeted delivery minimizes the loss of the dye due to diffusion, nonspecific and/or glial uptake, and so on. MCBL can be applied at various developmental stages (Fig. 2). Remarkably, there is also efficient staining of neurons in the adult and aged brain. This is in contrast to the more conventional techniques of AM ester dye loading, which work well only in the immature tissue<sup>10</sup>. Additional advantages of MCBL include the need for only minor surgery, the possibility of restaining neurons and, thus, the ability to conduct long-lasting, perhaps even chronic, recordings<sup>13</sup>.

While MCBL allows many cell bodies to be imaged simultaneously, the method is not sensitive enough to be used for the analysis of subcellular structures. There are two obvious reasons for this reduced sensitivity. First, the image contrast is reduced due to the relatively high background staining of the surrounding neuropil. Second, the dye concentration in MCBL-loaded cells is low, on average 20  $\mu\text{M}$  of the indicator dye<sup>2</sup>. These limitations restrict the use of MCBL to *in vivo* imaging of somatic  $\text{Ca}^{2+}$  transients. Note, however, that  $\text{Ca}^{2+}$ -indicator dyes also act as  $\text{Ca}^{2+}$  buffers, the presence of which within the cells perturbs the amplitude and kinetics of the  $\text{Ca}^{2+}$  signals under study<sup>14</sup>. From this point of view, low intracellular levels of indicator dyes (such as those achieved using MCBL) become an advantage.

To study neuronal  $\text{Ca}^{2+}$  dynamics in awake, behaving animals, the MCBL technique was recently combined with *in vivo* brain endoscopy<sup>15</sup>. A thin (diameter, 200  $\mu\text{m}$ ) optical fiber was implanted into the brain area with cells stained using MCBL. The optical fiber was used both for transmitting the excitation light and for collecting the emitted light. The authors detected fluorescence signals with a single photomultiplier and, thus, monitored the compound activity of a large neuronal population. Such an optical fiber can be implanted at any desired depth, allowing the detection of calcium responses in deep and/or hidden brain regions. This approach can be developed further by substituting a single optical fiber with fiber bundles and/or gradient refractive index (GRIN) fibers<sup>16</sup>. Such new approaches might soon allow the monitoring of behavior-related  $\text{Ca}^{2+}$  signals in individual neurons of any brain region.



## MATERIALS

### REAGENTS

- Experimental animals (see REAGENT SETUP)
- Anesthetic agent (e.g., isoflurane, ketamine/xylazine or urethane)
- Local anesthetic agent (e.g., lidocaine)
- Membrane-permeable calcium-indicator dye (e.g., Oregon Green 488 BAPTA-1 AM (OG-1 AM), Calcium Green-1 AM, Fura-2 AM, Fura-PE3 AM, Fluo-4 AM or Indo-1 AM from Molecular Probes or Teflabs)
- Sulforhodamine 101 (SR101; Sigma)
- 20% Pluronic F-127 in DMSO (e.g., 2 g Pluronic F-127 in 10 ml DMSO; Sigma) **! CAUTION** Strong detergent; skin, eye and respiratory system irritant. Wear suitable protective clothing
- Standard pipette solution: 150 mM NaCl, 2.5 mM KCl and 10 mM HEPES
- Standard external saline: 125 mM NaCl, 4.5 mM KCl, 26 mM NaHCO<sub>3</sub>, 1.25 mM NaH<sub>2</sub>PO<sub>4</sub>, 2 mM CaCl<sub>2</sub>, 1 mM MgCl<sub>2</sub>, 20 mM glucose, pH 7.4, when bubbled with 95% O<sub>2</sub> and 5% CO<sub>2</sub>
- Low melting point agarose (Invitrogen GmbH)

### EQUIPMENT

- Recording chamber with central access opening: custom-made from a standard tissue-culture dish (diameter, 35 mm<sup>2</sup>)
- Glass capillaries (e.g., from Hilgenberg GmbH)
- Pipette puller (e.g., PP830 from Narishige)
- Brain atlas (e.g., from Academic Press)
- Surgical equipment, including a stereotaxic instrument, drill and warming blanket to ensure a constant body temperature; available from many providers (e.g., TSE-Systems)
- LN-Mini manipulator (Luigs & Neumann GmbH)
- Picospritzer II (General Valve) or pneumatic drug-ejection system (NPI)
- Patch-clamp amplifier (e.g., from HEKA)
- Two-photon laser-scanning microscope commercially available from several providers (e.g., Zeiss)
- Felt polisher (e.g., from Dr. Ihde Dental)

## PROCEDURE

### Preparation

**1|** Anesthetize the animal and place it onto a warming blanket (38 °C) in front of the oxygen supply<sup>22</sup>. Affix the sensors of the anesthesia-monitoring system. Ensure that the surgical level of anesthesia has been reached (e.g., by testing the pinch withdrawal and the eyelid reflex). We anesthetize mice by inhalation of isoflurane (1–1.5% (vol/vol) in pure O<sub>2</sub>). Alternatively, adult mice can be anesthetized with either ketamine/xylazine or urethane (0.1/0.01 and 1.9 mg per g body weight, respectively, i.p.).

- Cyanoacryl glue (available from many providers; e.g., UHU GmbH)
- Millipore filter (Millipore)

### REAGENT SETUP

**Experimental animals** So far, the protocol has been tested in mice, rats, cats and zebrafish. **! CAUTION** All experiments must be performed in accordance with the relevant authorities' guidelines and regulations.

### EQUIPMENT SETUP

**Anesthesia unit** Including a chamber for pre-anesthetic medication, a flow meter and a vaporizer (the latter items are for volatile anesthetic agents only). Consult the literature (e.g., ref. 17) for the best choice of anesthesia for each species.

**Anesthesia-monitoring system** Used to measure the blood pressure, arterial oxygen concentration, body temperature, and respiratory and pulse rate of the animal. The monitoring equipment is available from many providers, but it is not always suitable for small laboratory animals (e.g., mice and neonatal rats). We use equipment from ADI Instruments to monitor the respiratory and pulse rate, body temperature and blood pressure in mice.

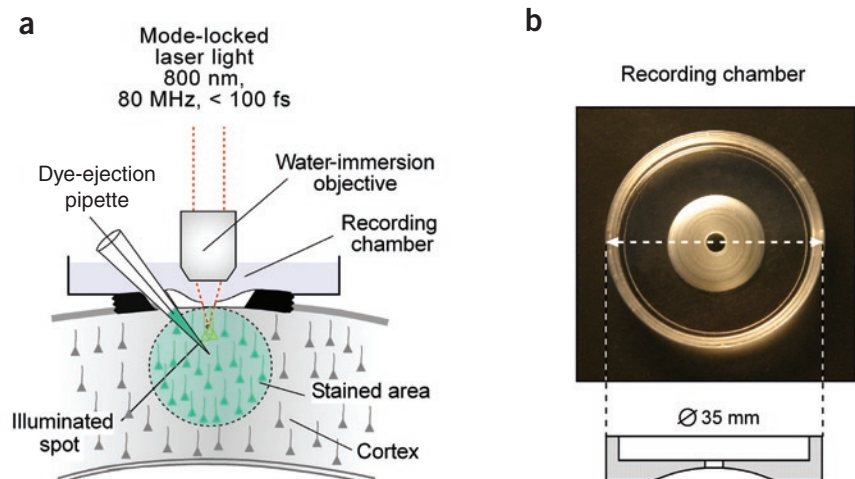
**Manipulator and pressure-application device** To inject the staining solution into the brain we use the LN-Mini manipulator and either Picospritzer II or the pneumatic drug-ejection system.

**Patch-clamp amplifier** Used to monitor the resistance of the pipette during dye injection. Monitoring of the pipette resistance is not mandatory, but is advisable because it allows pipette clogging to be recognized and the point when the pipette reaches the surface of the cortex to be estimated.

**Two-photon laser-scanning microscope** We use a custom-built microscope based on a mode-locked laser system operating at 710–920 nm wavelength (MaiTai, Spectra Physics) and a laser-scanning system (Fluoview, Olympus) coupled to an upright microscope (BX51WI, Olympus). Such a custom-built system can be assembled following the instructions in refs. 18,19.

**Brain atlas** Used to obtain stereotaxic coordinates of the respective brain region (for example, see refs. 20,21).

**Figure 1 |** Experimental arrangement for *in vivo* staining of neuronal populations with Ca<sup>2+</sup>-indicator dyes. **(a)** A custom-made recording chamber is glued to the skull to allow head fixation and the use of a water-immersion objective. The chamber is perfused with warm (37 °C) standard external saline. Two small craniotomies are performed: one for the insertion of the staining-patch micropipette (obligatory) and one above the field of view for improvement of the imaging depth (optional). Cells, stained using MCBL, are shown in green. The stained area has a diameter of 200–400 μm. Modified from ref. 2. **(b)** Photograph of the recording chamber (upper panel) and schematic drawing of its cross-section (lower panel). Note that a circular region around the perforation is thinned to fit the curvature of the animal's skull.



2| Use a stereotaxic device to identify the location of the brain area of interest. Inject ~ 50  $\mu$ l local anesthetic agent (e.g., 2% lidocaine; 20 mg lidocaine in 1 ml standard external saline) subcutaneously at the location where the skin is to be removed (optional).

3| Remove the skin above the desired brain area. Decide whether to image through the skull; the stability of the preparation is higher when imaging through the skull (lower impact of heart beat and breathing artifacts), but the efficiency of photon detection is higher when the skull is removed (images are crisper and imaging depth is greater).

4| Thin the skull and polish it with a felt polisher. Imaging through the thinned skull provides optimal results when the skull is thinned down to 10–20  $\mu$ m<sup>2</sup>. We suggest stopping thinning as soon as the bone bends when gently touched with the tweezers. If the skull is to be removed, less thinning is necessary.

▲ **CRITICAL STEP** The skull thinning must be performed as gently as possible; never press onto the skull. Inaccurate thinning often causes brain damage.

5| Use cyanoacryl glue to adhere the custom-made recording chamber to the skull.

6| Transfer the animal into the recording set-up (we use a set-up similar to that described in ref. 23, equipped with a two-photon laser-scanning microscope; see above) and place it onto a warming blanket (38 °C). Affix the sensors of the anesthesia-monitoring system. If necessary, adjust supply of anesthetic to keep physiological levels of monitored parameters.

▲ **CRITICAL STEP** The quality of recordings critically depends on the good condition of the experimental animal. Therefore, starting now, continuously monitor the following vital parameters: respiratory and pulse rate, body temperature, arterial oxygen concentration and blood pressure.

7| Perfuse the recording chamber with a warm (37 °C) standard external saline.

8| Perform a craniotomy above an area devoid of large blood vessels. This should be small ( $\leq 0.5$  mm) for imaging through the skull and larger (or two small craniotomies should be performed near each other; **Fig. 1**) for 'open-access' imaging.

▲ **CRITICAL STEP** Do not remove the dura mater; removal is not required for cell staining and strongly enhances movement artifacts. The stability of recordings also critically depends on the diameter of the craniotomy. Thus, openings larger than 1 mm in diameter are often accompanied by large movement artifacts occurring at the heartbeat frequency.

### Staining neurons with a calcium-indicator dye

9| Dissolve AM ester of the preferred indicator dye (e.g., OG-1 AM) in the solution containing 20% Pluronic F-127 in DMSO (e.g., 2 g Pluronic F-127 in 10 ml DMSO) to yield a dye concentration of 10 mM. Dilute this solution 1/10 to 1/100 with the standard pipette solution to prepare the

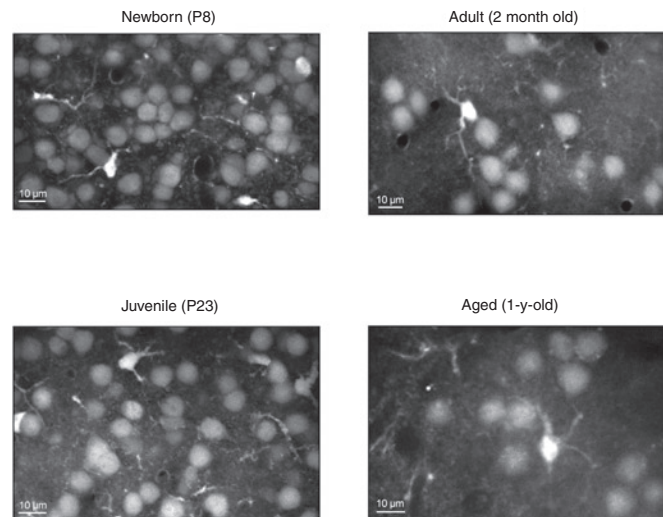


**Figure 2** | MCBL allows staining of cortical tissue at various developmental stages. The microphotographs illustrate layer 2/3 cells in the visual cortex of mice at different ages. Cells were stained using OG-1 AM and images were taken using a 60 $\times$  Nikon water-immersion objective (1.0 NA).

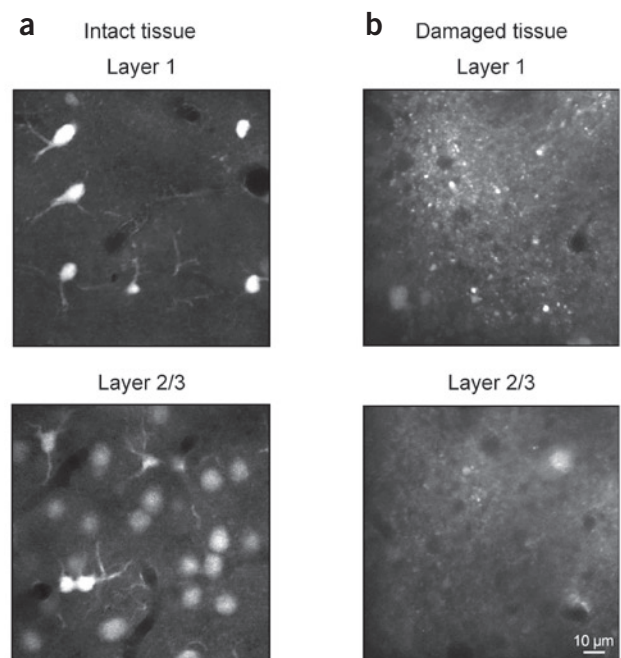


**Figure 3** | Assessment of the staining quality. (a,b) High-magnification images of cells in layer 1 (upper panels) and in layer 2/3 (lower panels) taken at two different locations in the visual cortex of a 64-d-old mouse. Both areas were stained using the same protocol, but in (b) a large brain vessel was damaged prior to staining.

**Figure 4** | Spontaneous  $\text{Ca}^{2+}$  transients in the visual cortex of an adult mouse. Spontaneously occurring  $\text{Ca}^{2+}$  transients (lower panel) in seven individual layer 2/3 neurons, marked with corresponding numbers in the upper panel. Data are derived from a series of time-lapse images recorded at 10 Hz.

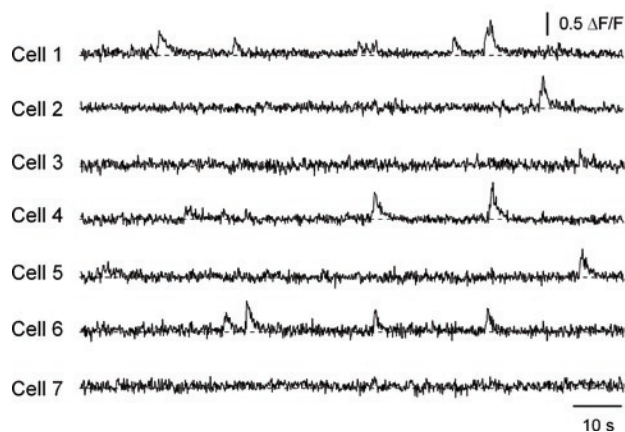
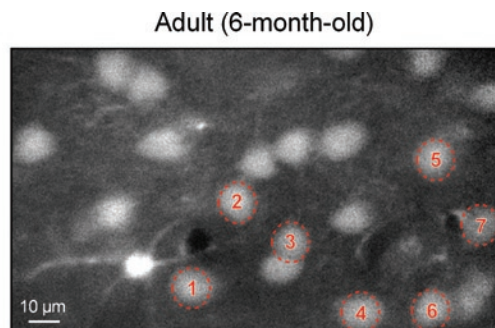
staining solution. The same recipe is used to dissolve other  $\text{Ca}^{2+}$ -indicator dyes (e.g., Fura-2 AM, Fluo-4 AM, Calcium Green-1 AM, Indo-1 AM, Fura-PE3 AM, Fura Red AM and Magnesium Green AM)<sup>2,7</sup>.

▲ **CRITICAL STEP** Note that the standard pipette solution (a simplified  $\text{Ca}^{2+}$ -free Ringer's solution) is designed to minimize precipitation of the dye. Filter the staining solution if necessary (we use a Millipore filter with a pore diameter of 0.45  $\mu\text{m}$ ).

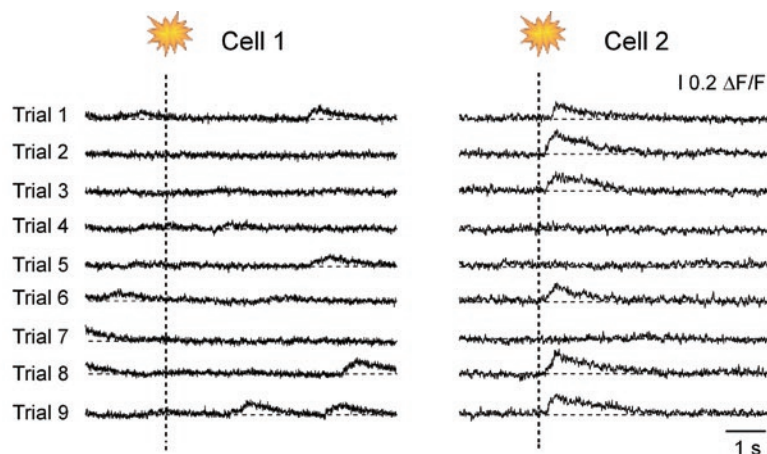
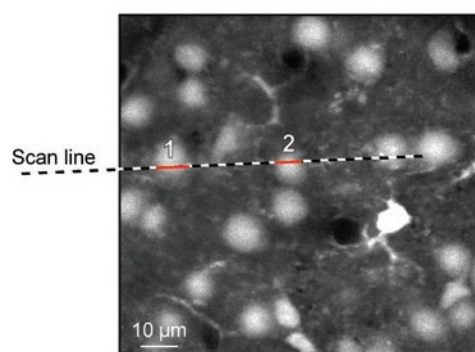
### ? TROUBLESHOOTING

**10** | Pull a staining micropipette from a glass capillary using a pipette puller (we use standard-patch pipettes with a resistance of 6–9  $\text{M}\Omega$  when filled with standard pipette solution). Fill with staining solution. Insert the pipette into the cortex (under an angle of, for example, 30°) while monitoring the pipette resistance with a patch-clamp amplifier. The pipette resistance can increase slightly (up to 15  $\text{M}\Omega$ ) when penetrating the dura mater, but must decrease to the initial level either immediately thereafter or, at the latest, upon the application of ejection pressure (see below). Advance the pipette along its axis until it reaches the desired depth (**Fig. 1**). With the dye-application pipette located 150–200  $\mu\text{m}$  below the cortical surface, all cortical cells between the surface and a 400- $\mu\text{m}$  depth are stained<sup>2</sup>. For staining the cells in deeper cortical layers, the pipette is positioned 650–750  $\mu\text{m}$  below the pia<sup>3</sup>. Apply a pressure pulse (1 min, 70 kPa) to eject ~400 femtoliters staining solution near the cells of interest (see ref. 3 for the slightly modified protocol for labeling deep cortical layers). Remove the pipette.

■ **PAUSE POINT** Wait ~1 h to obtain a stable maximal fluorescence level in stained cells<sup>2</sup>. This protocol yields a stained area with a diameter of 200–400  $\mu\text{m}$ .



### Juvenile (P38)

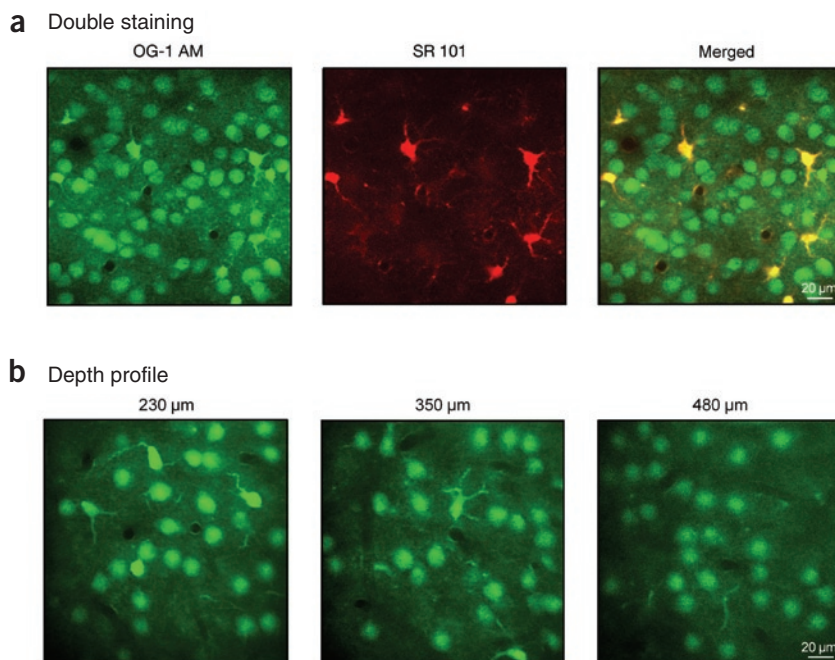


**Figure 5** |  $\text{Ca}^{2+}$  transients in the individual cortical neurons evoked by sensory stimulation. Line-scan recordings of  $\text{Ca}^{2+}$  transients (sampled at 200 Hz; right panel) in two layer 2/3 neurons of the mouse visual cortex marked with the respective numbers in the left panel. The vertical broken line in the right panel marks the beginning of a brief (100 ms) light flash. Note that whereas cell 2 responded reliably to this stimulus, no responses were seen in the neighboring cell 1, which instead exhibited frequent spontaneous  $\text{Ca}^{2+}$  transients.

**Figure 6** | Double staining and depth profile.

(a) Microphotographs of layer 2/3 cells in the mouse visual cortex (30-d-old mouse) stained simultaneously using a dye mixture containing OG-1 AM and the glial marker SR101. The fluorescence of OG-1 AM was directed to the green channel (left) and the fluorescence of SR101 was directed to the red channel (middle). The merged image on the right shows neurons in green and glial cells in yellow.

(b) Microphotographs of the visual cortex of a juvenile (32-d-old) mouse taken at different depths. The excitation light's pulse width under the objective was optimized by compensating group-velocity dispersion with a pair of prisms<sup>28</sup>.

**Two-photon imaging of stained cells**

**11** | Choose the wavelength of the excitation light (depends on the indicator dye used). Consult ref. 24 for two-photon excitation spectra of common Ca<sup>2+</sup>-sensitive dyes. Excitation light of 800 nm can be used for the initial visualization of neurons stained with the following indicator dyes: Fura-PE3 AM, Fura Red AM, Indo-1 AM, Calcium Green-1 AM, OG-1 AM, Fluo-4 AM and Magnesium Green AM.

**12** | Check the average power of the excitation light under the objective (must be at least 50–70 mW). Reduce the excitation power to the minimum and focus the objective (for example Nikon, 60×, numerical aperture (NA) 1.0, water immersion) of the two-photon microscope onto the brain surface. Raise the excitation power carefully (to avoid dye bleaching) and inspect the upper cortical layers using high-resolution settings (frame rate, 1 Hz). The following structures become clearly visible: large epithelial cells on the top of the cortex; layer 1 cells up to the depth of 100–200 μm, depending on the age of the animal (**Fig. 3a**, upper panel); and layer 2/3 cells (**Figs. 2–7**). When imaging through the

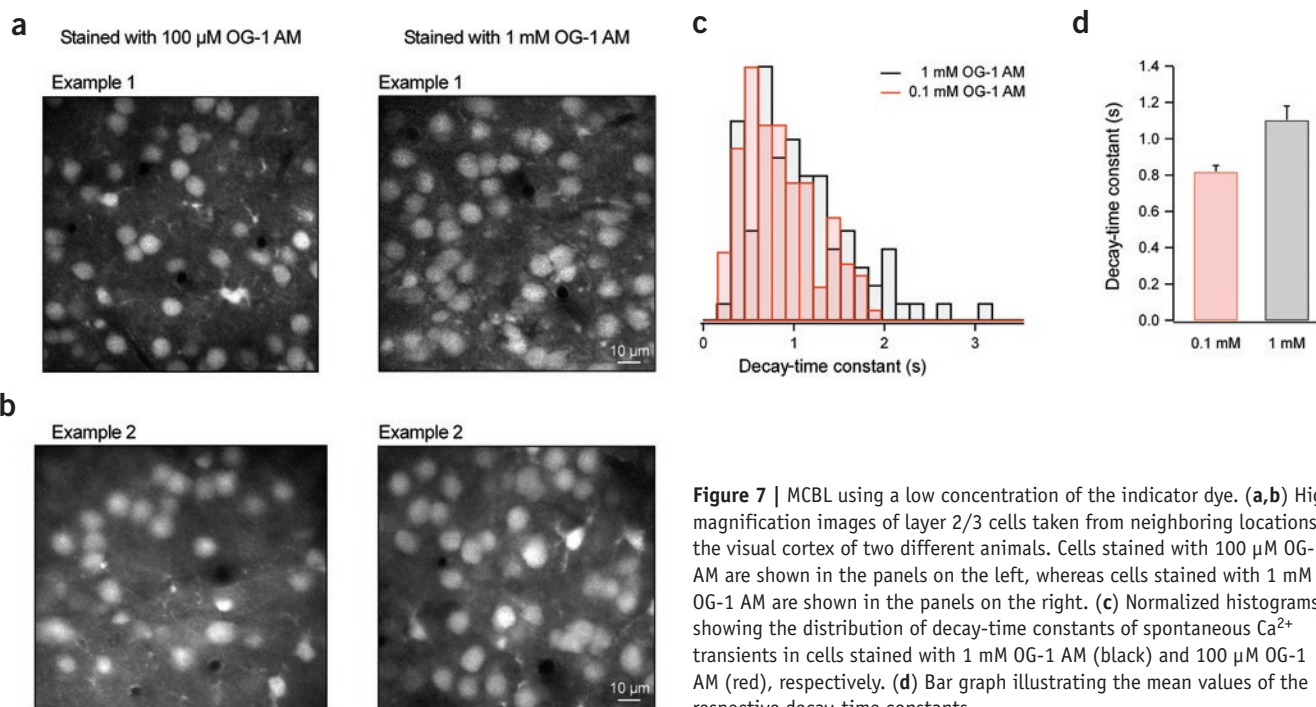


**Figure 7** | MCBL using a low concentration of the indicator dye. (a,b) High-magnification images of layer 2/3 cells taken from neighboring locations in the visual cortex of two different animals. Cells stained with 100 μM OG-1 AM are shown in the panels on the left, whereas cells stained with 1 mM OG-1 AM are shown in the panels on the right. (c) Normalized histograms showing the distribution of decay-time constants of spontaneous Ca<sup>2+</sup> transients in cells stained with 1 mM OG-1 AM (black) and 100 μM OG-1 AM (red), respectively. (d) Bar graph illustrating the mean values of the respective decay-time constants.

thinned skull, individual cells can be well resolved up to 250  $\mu\text{m}$  below the cortical surface. Removing the skull above the imaging field further improves depth resolution. The maximal depth at which individual cells can be resolved depends on the shape and density of cells, the density of blood vessels in the imaged region and the age of the animal. In juvenile and young adult animals, the depth limit for single-cell imaging in the cortex is  $\sim 500 \mu\text{m}$  (**Fig. 6b**; consult ref. 25 for optimization of the imaging depth). In general, all cells in the preparation are stained; the only dark areas correspond to blood vessels, which are easily identified when focusing through the tissue. Furthermore, characteristic astrocytes often surround the blood vessels (see below).

### ? TROUBLESHOOTING

**13** | Monitor  $\text{Ca}^{2+}$  transients of interest, for example, with a frame rate of 10 Hz. Use online brightness-versus-time analyses to monitor photobleaching. Adjust excitation power to levels just below the bleaching ‘threshold’. Use a commercially available software package for collection of time-lapse images and online data analyses.

### ? TROUBLESHOOTING

#### ● TIMING

Dissection (Steps 1–8), 1h

Staining (Steps 9–10), 1h

Imaging (Steps 11–13), at least 6 h

### ? TROUBLESHOOTING

See **Table 1**.

**TABLE 1** | Troubleshooting table.

PROBLEM	SOLUTION
Step 9: the staining patch micropipette gets clogged	Clean glass capillaries used to manufacture the pipettes; dissolve $\text{Ca}^{2+}$ -indicator dyes immediately before use; filter the staining solution before use (e.g., with a Millipore filter; pore diameter, 0.45 $\mu\text{m}$ )
Step 12: cells are not, or are only poorly, stained	There are two likely scenarios, either (i) the tissue is intact but the dye delivery failed, or (ii) the tissue is damaged ( <b>Fig. 3</b> ); for (i) monitor the pipette resistance during dye injection (a value above 20 $\text{M}\Omega$ indicates that the pipette is clogged); for (ii) check the anesthesia monitoring parameters, try to thin the skull as gently as possible, avoiding damage to large blood vessels, and increase the speed of dissection and staining (the latter should be accomplished in less than 2 h)
Step 13: recording conditions are unstable; occurrence of high-frequency vibrations of cells and/or slow drift of the plane of focus	These problems are more profound when the skull is removed; cover the skull opening with 2% low melting point agarose (e.g., 20 mg in 1 ml standard external saline) and keep the temperature of the external saline stable (with a precision of 0.1 $^{\circ}\text{C}$ ); the high-frequency vibrations are usually the result of heart-beat pulsation (compare with measurements of the anesthesia-monitoring system) and are more profound in regions with a high density of blood vessels

### ANTICIPATED RESULTS

**Figures 2–5** illustrate MCBL-stained layer 2/3 cells in the visual cortex of mice of different ages. At each age, stained cortical neurons show spontaneous (**Fig. 4**) as well as light-evoked (**Figure 5**)  $\text{Ca}^{2+}$  transients. Data shown in **Figure 4** are derived from a series of time-lapse images recorded at 10 Hz. Light-evoked responses in **Fig. 5** were recorded as a series of line scans at 200 Hz. Note that in each case, the signal-to-noise ratio is sufficient to allow individual non-averaged somatic  $\text{Ca}^{2+}$  transients to be distinguished clearly from the background. As was shown by Kerr *et al.*<sup>3</sup> in rat somatosensory cortex, spontaneous  $\text{Ca}^{2+}$  transients reflect action-potential firing. Also, in the mouse visual cortex, both spontaneous (**Fig. 4**) and light-evoked (**Fig. 5**)  $\text{Ca}^{2+}$  transients required firing of action potentials (O.G. and A.K., unpublished observations).

As mentioned above, the MCBL technique is not cell-type specific. It provides a relatively homogeneous staining of different cell types (although glial cells are generally brighter than neurons). An identification of the various cell types can be achieved using additional markers (e.g., cell-type specific expression of green fluorescent protein) and multicolor two-photon imaging. A versatile approach for distinguishing between neuronal cells and astrocytes was developed by Nimmerjahn *et al.*<sup>5</sup> and is based on the use of the astrocyte-specific marker SR101, which emits fluorescence light at



wavelengths (550–750 nm) that are significantly longer than those of common Ca<sup>2+</sup> indicators. For targeted SR101 staining, we modify the protocol of Nimmerjahn *et al.*<sup>5</sup>. We dilute 1 mg SR101 in 4 ml standard pipette solution and use it to dilute the concentrated solution containing 10 mM Ca<sup>2+</sup> indicator (Step 9). The combined staining cocktail, containing SR101 and the Ca<sup>2+</sup>-sensitive dye, is then injected into the brain (Step 10). This results in a good loading of neurons and glia cells with the Ca<sup>2+</sup> indicator, and specific staining of glia cells with SR101 in the same brain region (**Fig. 6a**).

The MCBL technique was originally designed to apply 400 femtoliters of the concentrated Ca<sup>2+</sup>-indicator dye-containing solution (yielding a final pipette concentration of the dye of 1 mM). Because membrane-permeant Ca<sup>2+</sup>-indicator dyes are dissolved in DMSO, the staining solution also contained 10% DMSO (vol/vol). Although similar and/or higher detergent concentrations are routinely used to stain intact tissues with indicator dyes<sup>11,26,27</sup>, we recently found that such a high dye/detergent concentration is not needed. As shown in **Figure 7a,b**, the MCBL protocol can provide high-quality staining of the mouse cortex with 100 μM OG-1 AM and 1% DMSO (vol/vol)-containing pipette solution. However, the use of the lower dye concentration imposes higher demands on the quality of preparation. The time constants of spontaneous Ca<sup>2+</sup> transients were, on average, 0.81 ± 0.04 s (*n* = 123) in cells stained with 100 μM OG-1 AM and 1.10 ± 0.08 s (*n* = 88) in cells stained with 1 mM OG-1 AM (**Fig. 7c,d**). This similarity suggests that the intracellular indicator levels obtained with 100 μM OG-1 AM-containing staining solutions are nearly as high as those reached with 1 mM OG-1 AM-containing solutions (in the range of 20 μM<sup>2</sup>).

**ACKNOWLEDGMENTS** We thank M.A. Busche for help with experiments shown in **Figure 6b**. This work was supported by grants from the Deutsche Forschungsgemeinschaft (SFB 391 and SFB 596) and the Bundesministerium für Bildung und Forschung (NGFN-2).

**COMPETING INTERESTS STATEMENT** The authors declare that they have no competing financial interests.

Published online at <http://www.natureprotocols.com>  
Rights and permissions information is available online at <http://npg.nature.com/reprintsandpermissions>

- Tsien, R.Y. A non-disruptive technique for loading calcium buffers and indicators into cells. *Nature* **290**, 527–528 (1981).
- Stosiek, C., Garaschuk, O., Holthoff, K. & Konnerth, A. *In vivo* two-photon calcium imaging of neuronal networks. *Proc. Natl. Acad. Sci. USA* **100**, 7319–7324 (2003).
- Kerr, J.N., Greenberg, D. & Helmchen, F. Imaging input and output of neocortical networks *in vivo*. *Proc. Natl. Acad. Sci. USA* **102**, 14063–14068 (2005).
- Ohki, K., Chung, S., Ch'ng, Y.H., Kara, P. & Reid, R.C. Functional imaging with cellular resolution reveals precise micro-architecture in visual cortex. *Nature* **433**, 597–603 (2005).
- Nimmerjahn, A., Kirchhoff, F., Kerr, J.N.D. & Helmchen, F. Sulforhodamine 101 as a specific marker of astroglia in the neocortex *in vivo*. *Nat. Methods* **1**, 31–37 (2004).
- Sullivan, M.R., Nimmerjahn, A., Sarkisov, D.V., Helmchen, F. & Wang, S.S. *In vivo* calcium imaging of circuit activity in cerebellar cortex. *J. Neurophysiol.* **94**, 1636–1644 (2005).
- Brustein, E., Marandi, N., Kovalchuk, Y., Drapeau, P. & Konnerth, A. 'In vivo' monitoring of neuronal network activity in zebrafish by two-photon Ca<sup>2+</sup> imaging. *Pflügers Arch.* **446**, 766–773 (2003).
- Li, J. *et al.* Early development of functional spatial maps in the zebrafish olfactory bulb. *J. Neurosci.* **25**, 5784–5795 (2005).
- Niell, C.M. & Smith, S.J. Functional imaging reveals rapid development of visual response properties in the zebrafish tectum. *Neuron* **45**, 941–951 (2005).
- Yuste, R. in *Imaging: A Laboratory Manual* (eds. Yuste, R., Lanni, F. & Konnerth, A.) 34.1–34.9 (Cold Spring Harbor Press, Cold Spring Harbor, New York, 2000).
- Wong, R.O. in *Imaging: A Laboratory Manual* (eds. Yuste, R., Lanni, F. & Konnerth, A.) 41.1–41.7 (Cold Spring Harbor Press, Cold Spring Harbor, New York, 2000).
- Regehr, W.G. & Tank, D.W. Selective fura-2 loading of presynaptic terminals and nerve cell processes by local perfusion in mammalian brain slice. *J. Neurosci. Methods* **37**, 111–119 (1991).
- Christie, R.H. *et al.* Growth arrest of individual senile plaques in a model of Alzheimer's disease observed by *in vivo* multiphoton microscopy. *J. Neurosci.* **21**, 858–864 (2001).
- Neher, E. The use of fura-2 for estimating Ca<sup>2+</sup> buffers and Ca<sup>2+</sup> fluxes. *Neuropharmacology* **34**, 1423–1442 (1995).
- Adelsberger, H., Garaschuk, O. & Konnerth, A. Cortical calcium waves in resting newborn mice. *Nat. Neurosci.* **8**, 988–990 (2005).
- Flusberg, B.A. *et al.* Fiber-optic fluorescence imaging. *Nat. Methods* **2**, 941–950 (2005).
- Flecknell, P. *Laboratory Animal Anaesthesia* (Academic Press, San Diego, 2000).
- Majewska, A., Yiu, G. & Yuste, R. A custom-made two-photon microscope and deconvolution system. *Pflügers Arch.* **441**, 398–408 (2000).
- Nikolenko, V. & Yuste, R. in *Imaging in Neuroscience and Development: A Laboratory Manual* (eds. Yuste, R. & Konnerth, A.) 75–78 (Cold Spring Harbor Press, Cold Spring Harbor, New York, 2005).
- Paxinos, G. & Watson, C. *The Rat Brain in Stereotaxic Coordinates* (Academic Press, San Diego, CA, 2004).
- Paxinos, G. & Franklin, K.B.J. *The Mouse Brain in Stereotaxic Coordinates* (Academic Press, San Diego, CA, 2001).
- Vender, J.R., Hand, C.M., Sedor, D., Tabor, S.L. & Black, P. Oxygen saturation monitoring in experimental surgery: a comparison of pulse oximetry and arterial blood gas measurement. *Lab. Anim. Sci.* **45**, 211–215 (1995).
- Eilers, J., Schneggenburger, R. & Konnerth, A. in *Single-Channel Recording* (eds. Sakmann, B. & Neher, E.) 213–229 (Plenum Press, New York, 1995).
- Xu, C. in *Imaging: A Laboratory Manual* (eds. Yuste, R., Lanni, F. & Konnerth, A.) 19.1–19.9 (Cold Spring Harbor Press, Cold Spring Harbor, New York, 2000).
- Helmchen, F. & Denk, W. Deep tissue two-photon microscopy. *Nat. Methods* **2**, 932–940 (2005).
- Ikegaya, Y. *et al.* Synfire chains and cortical songs: temporal modules of cortical activity. *Science* **304**, 559–564 (2004).
- Hirase, H., Qian, L., Bartho, P. & Buzsaki, G. Calcium dynamics of cortical astrocytic networks *in vivo*. *PLoS Biol.* **2**, E96 (2004).
- Soeller, C. & Cannell, M.B. Construction of a two-photon microscope and optimisation of illumination pulse duration. *Pflügers Arch.* **432**, 555–561 (1996).

# Optical monitoring of brain function in vivo: from neurons to networks

Olga Garaschuk · Ruxandra-Iulia Milos ·  
Christine Grienberger · Nima Marandi ·  
Helmuth Adelsberger · Arthur Konnerth

Received: 7 July 2006 / Accepted: 2 August 2006 / Published online: 18 October 2006  
© Springer-Verlag 2006

**Abstract** The precise understanding of the cellular and molecular basis of brain function requires the direct assessment of the activity of defined cells in vivo. A promising approach for such analyses is two-photon microscopy in combination with appropriate cell labeling techniques. Here, we review the multi-cell bolus loading (MCBL) method that involves the use of membrane-permeant fluorescent indicator dyes. We show that this approach is useful for the functional analysis of clusters of neurons and glial cells in vivo. Work from our and other laboratories shows that the techniques that were previously feasible only in brain slices, like targeted patch clamp recordings from identified cells or pharmacological manipulations in confined brain regions, can now be used also in vivo. We also show that MCBL and two-photon imaging can be easily combined with other labeling techniques, particularly with those involving the use of genetically encoded, green-fluorescent-protein-based indicators. Finally, we examine recent applications of MCBL/two-photon imaging for the analysis of various brain regions, including the somatosensory and the visual cortex.

**Keywords** Calcium imaging · Two-photon microscopy · Bolus loading · Functional architecture of neural networks

## Introduction

Our understanding of the function of neural circuits in situ has benefited greatly from data obtained using two versatile techniques that were introduced 25 years ago: (1) the ‘giga-seal’ whole-cell patch clamp technique [1] and (2) the use of fluorescent indicator dyes [2]. Thus, neural networks in culture and/or brain slices are often studied either by means of  $\text{Ca}^{2+}$  imaging (after staining the cells with membrane-permeant  $\text{Ca}^{2+}$  indicator dyes; for review see [3]) or by means of simultaneous patch-clamp recordings of connected neurons (for review, see [4, 5]). With the development of two-photon laser scanning microscopy [6], such studies became feasible even in vivo in anesthetized and, potentially, also in awake animals.

The initial in vivo studies combined two-photon calcium imaging with microelectrode [7, 8] or whole-cell patch-clamp [9, 10] recordings. The microelectrodes or the patch pipettes were used not only for recording electrical signals from the cells of interest, but also, and equally important, for filling the cells with a calcium indicator dye, thus allowing high-resolution  $\text{Ca}^{2+}$  imaging in neurons and their processes. The use of membrane-permeant  $\text{Ca}^{2+}$  indicator dyes in vivo was introduced by Stosiek et al. [11]. This technique, termed multi-cell bolus loading (MCBL), enabled the targeted labeling of intact neuronal circuits in the living animal. The technique is applicable in various neuronal tissues and in a variety of species from lower vertebrates to mammals [12–18]. When combined with appropriate detection techniques, like two-photon laser scanning microscopy and/or brain endoscopy [19, 20], it allows the monitoring of both the ‘macroscopic’ function of brain circuits [20] and the ‘microscopic’ behavior of individual cells [11, 13]. In this paper, we review recent data obtained with high-resolution in vivo  $\text{Ca}^{2+}$  imaging of

O. Garaschuk · R.-I. Milos · C. Grienberger · N. Marandi ·  
H. Adelsberger · A. Konnerth (✉)  
Institut für Neurowissenschaften,  
Technische Universität München,  
Biedersteinerstr. 29,  
80802 Munich, Germany  
e-mail: arthur.konnerth@lrz.tum.de



neural circuits. We provide some new technical aspects of cell staining, describe approaches used to identify different cell types, and illustrate new applications arising from the combination of MCBL with other techniques.

### The MCBL approach

Figure 1a illustrates an experimental arrangement used for in vivo MCBL. A dye ejection pipette, similar to those used for patch clamp recordings, containing a concentrated solution of a  $\text{Ca}^{2+}$  indicator dye (for example, Oregon

Green 488 BAPTA-1 acetoxymethyl ester [OG-1 AM]) is inserted into the brain through a small skull opening, and the dye is pressure-ejected into the brain area of interest. Within the brain, the dye diffuses into the cells and becomes hydrolyzed by endogenous esterases [2]. This procedure results in a rather uniform staining of cells within the targeted area (Fig. 1b). Originally we used 1 mM of the indicator dye for the pressure ejection [11]. Recent data, however, have shown that a dye concentration of 100  $\mu\text{M}$  often produces similarly good results [21]. Other groups adapted our technique and used similar recipes for in vivo staining of cortical neurons in rats and

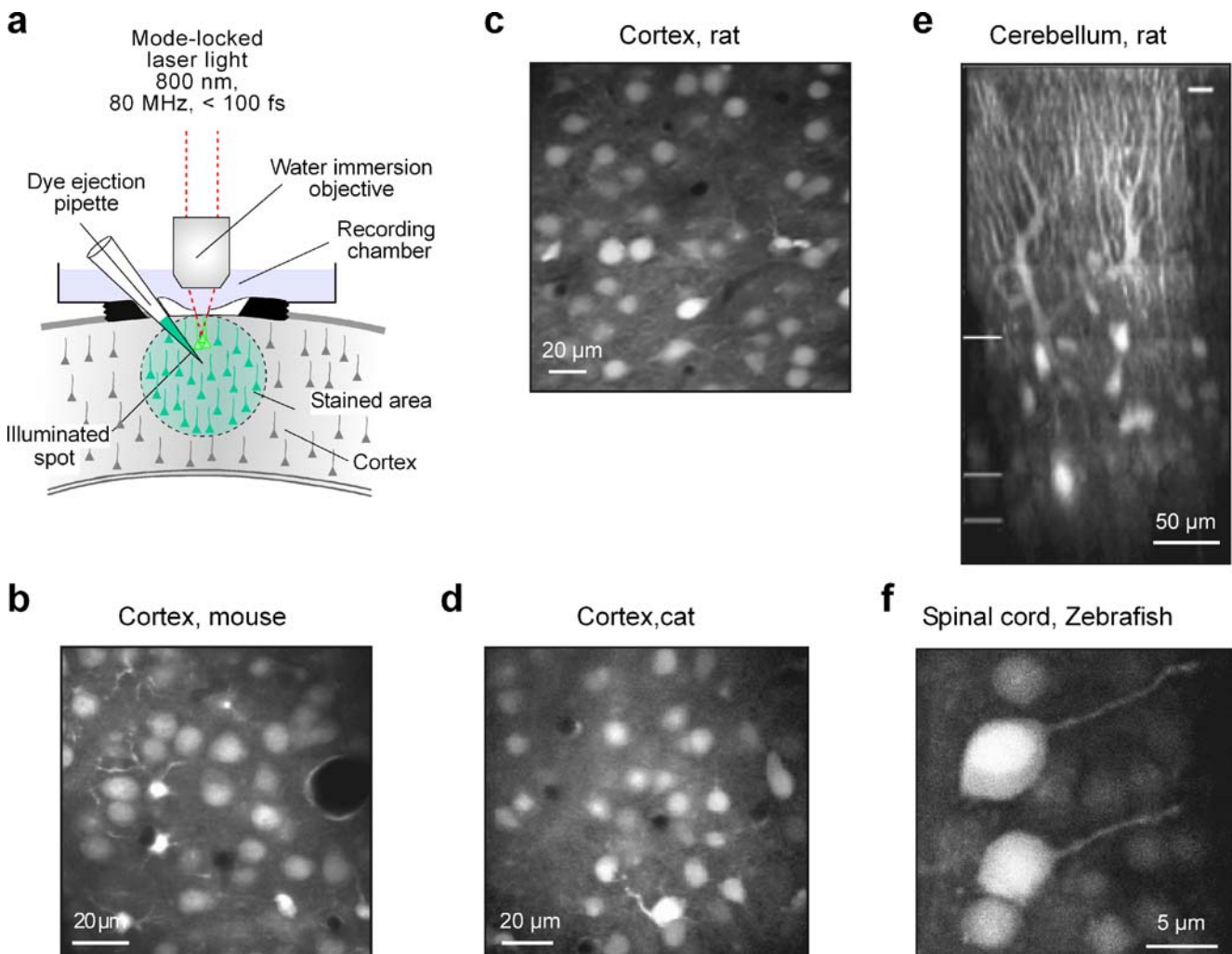


**Fig. 1** MCBL enables in vivo staining of neural networks in different species. **a** Schematic drawing of the experimental arrangement. Reproduced, with permission from Macmillan Publishers Ltd, from [21]. **b–f** In vivo images of stained cells in the cerebral cortex of a mouse (**b**), a rat (**c**), and a cat (**d**), as well as in the rat cerebellum (**e**) and in the spinal cord of a zebrafish larva (**f**). The cells in **b–e** were stained with OG-1 AM and those in **f** with Fura PE3 AM. All images were obtained

using two-photon laser scanning microscopy and are reproduced (with permission from Macmillan Publishers Ltd; National Academy of Sciences USA, copyright 2003, 2005; and the American Physiological Society) from references [11, 13, 15, 16], respectively. Note that both dyes stained all structures within a respective tissue; the only *dark areas* correspond to many small and one large **b** brain vessels. Here and below, all imaged preparations were stained using MCBL

cats (Fig. 1c and d; [13]) and for dye labeling of rat cerebellar neurons (Fig. 1e; [15]). As already mentioned, the staining protocol is also applicable in lower vertebrates and was used, for example, for staining neurons in the spinal cord (Fig. 1f; [16]), olfactory bulb [17], and tectum [18] of zebrafish larvae. Interestingly, unlike other common protocols for labeling brain tissue with AM esters of  $\text{Ca}^{2+}$  indicator dyes [22], MCBL-based staining shows little age dependence and can be used not only for staining newborn and juvenile tissues but also for staining adult and even aged tissues [21].

Figure 2a shows the time course of an MCBL-based staining of the mouse visual cortex with Fura PE3 AM. The left panel of Fig. 2a illustrates a very early time point, immediately after dye ejection, in which the dye is located extracellularly. Within a few minutes, the dye starts to accumulate in the cells and is gradually removed from the extracellular space (Fig. 2a, middle and right panel). This removal process is the result of the cellular uptake of the dye and, importantly, the clearing of the extracellular space by the vascular system. To estimate the kinetics of the removal process, we pressure-ejected the membrane-impermeant fluorescent dye Alexa Fluor 594 into the mouse cortex and monitored its removal by the use of two-photon imaging (Fig. 2b). The removal process had a double exponential time course, with the mean decay time constants of  $2.3 \pm 0.1$  and  $13.3 \pm 0.7$  s ( $n=33$  samples), respectively (Fig. 2c and d). In conclusion, dye removal from the extracellular space under *in vivo* conditions is very efficient and rapid, contributing to the good contrast between stained cells and the surrounding tissue.

### Identification of different cell types *in vivo*

The MCBL procedure leads to the staining of virtually all cells in the targeted brain area. Although glial cells tend to accumulate higher concentration of indicator dyes [11, 23], their unequivocal identification requires the use of a specific marker and multicolor imaging. It was recently reported that glial and neuronal cells can be easily separated *in vivo* by using the specific glial marker sulforhodamine 101 [14]. Sulforhodamine 101 emits light in the red portion of the spectrum, and, therefore, it can be easily used in combination with any common  $\text{Ca}^{2+}$  indicator (e.g. OG-1 AM, Fura 2 AM, etc.). Glial cells stained both with OG-1 AM and sulforhodamine 101 appear yellow on the merged image (Fig. 3a), while neurons stained with OG-1 AM only appear green. To simplify and speed-up the staining procedure, we co-ejected both indicator dyes from the same pipette and

simultaneously labeled the cells with sulforhodamine 101 and OG-1 AM [21].

Although separation of neurons and glial cells can be easily achieved, it is still rather difficult to discriminate between different types of neurons. One method of cell-type-specific labeling involves the use of mutant mice expressing a specific fluorescent marker as, for example, enhanced green fluorescent protein (EGFP). This genetically encoded indicator was used in a variety of transgenic mice to mark GABAergic interneurons in general [24, 25], as well as parvalbumin- [26] or somatostatin-positive (Fig. 3b; [27]) interneuronal subtypes. Figure 3b shows an example of an EGFP-labeled somatostatin-positive GABAergic cell (blue) in the mouse visual cortex stained with OG-1 AM (green).

A certain degree of cell specificity can also be achieved when using MCBL and confining dye delivery, as good as possible, to specific anatomical subregions. For example, for studying  $\text{Ca}^{2+}$  signals in the dendrites of layer 5 pyramidal neurons of the rat motor cortex (Fig. 3c), Kerr et al. [12] ejected the indicator dye at the level of layer 5 (650–750  $\mu\text{m}$  below the pia). One hour after dye ejection, the dendrites of layer 5 cells became discernable at the level of layer 2/3 and were studied using two-photon imaging.

### Targeted whole-cell patch clamp recordings in MCBL-stained tissues

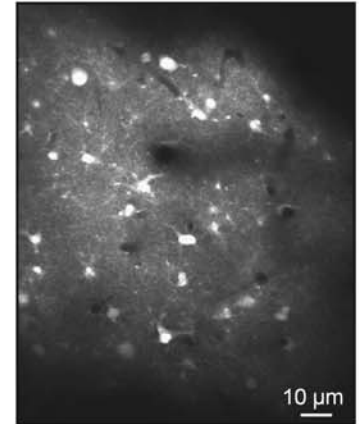
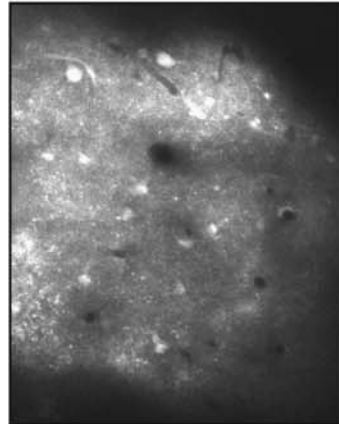
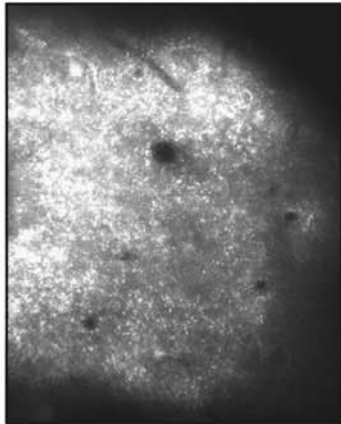
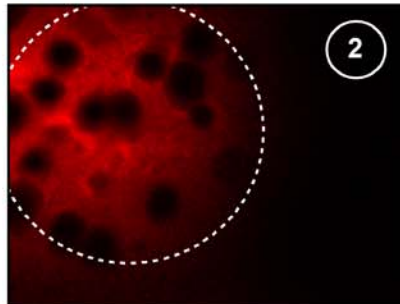
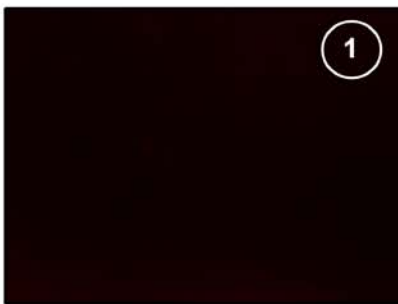
Originally, *in vivo* whole-cell patch clamp recordings in the mammalian brain were introduced as a ‘blind’ approach [28–31]. Thereby, the patch pipette is placed in the brain area of interest (e.g. within a given cortical area at a given depth) and is then slowly advanced forwards to hit a cell on its way. This approach gives good results if one aims at recording from any cell belonging to an abundant cell population. For recordings from cells belonging to a specific subclass of neurons, Margrie et al. [32] introduced a few years ago the so-called two-photon targeted patching approach. This procedure combines whole-cell patch clamp recordings with *in vivo* two-photon imaging of EGFP-positive neurons. An EGFP-positive neuron and a patch pipette filled with a fluorescent intracellular solution are brought into close proximity under the visual control using two-photon imaging (see also [33]). This allows *in vivo* whole-cell patch clamp recordings from defined cells, such as, for example, parvalbumin-positive GABAergic neurons [32]. The basic requirement for the two-photon targeted patching is the ability to visualize and preselect a cell of interest before a whole-cell recording configura-

**a**

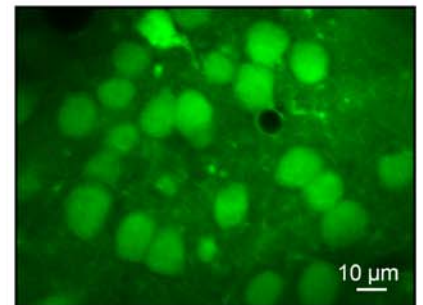
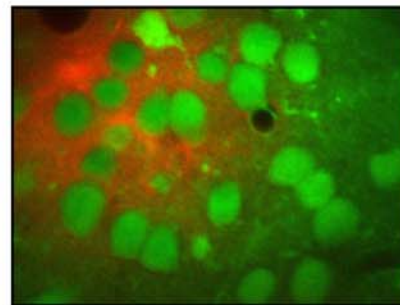
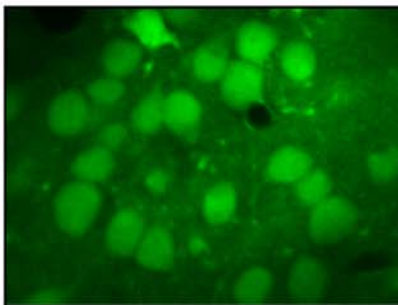
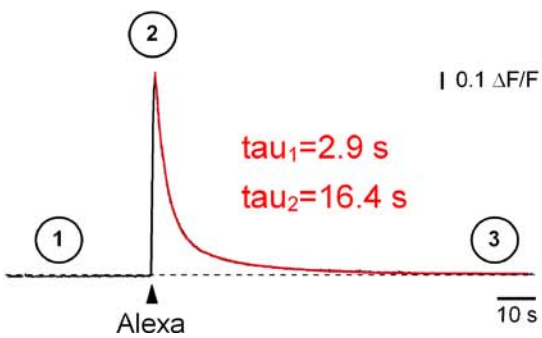
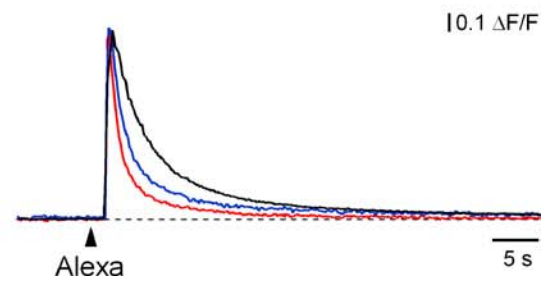
1 min after dye injection

5 min

20 min

**b** Red channel: (Alexa Fluor 594)

Merged

**c****d**

◀ **Fig. 2** Removal of extracellular dye molecules by microcirculation. **a** Images of layer 2/3 cells in the mouse visual cortex taken in vivo 1, 5, and 20 min after a bolus injection of Fura PE3 AM. Note gradual removal of the dye from the extracellular space and an increasing brightness of individual cells. **b** In vivo images of the mouse visual cortex obtained before (1) during (2) and after (3) a 500 ms long injection of a red fluorescent dye Alexa Fluor 594 into the extracellular space (*upper panel*). Merged images on the *lower panel* show the fluorescence spot caused by Alexa injection (*red*) in relation to individual cortical cells present in this region (stained with OG-1 AM, *green*). **c** The time course of the Alexa 594-based fluorescence transient. *Numbers* on the trace show the time points at which images in **b** were taken. **d** Three Alexa 594-based fluorescence transients, each obtained in a separate experiment, covering the entire range of the kinetics observed

tion is established. As shown in Fig. 4, a similar procedure can be used with MCBL-based staining. In these examples, a neuron (Fig. 4a–c) and a glia cell (Fig. 4d,e) were patched under visual control and identified based on their morphology and, more importantly, on how they responded to sulforhodamine 101 staining (Fig. 4d). The electrical responses recorded subsequently in the whole-cell configuration showed the behavior characteristic for neurons (Fig. 4b and c; up-

and-down states [34]) and glia cells (Fig. 4e; [35]), respectively. In addition to the ability to select cells based on anatomical and/or molecular markers, MCBL allows to preselect the cells for targeted patching based on their calcium signaling properties.

### Somatic calcium signaling in vivo requires action potential firing

By conducting simultaneous cell-attached electrical recordings and two-photon  $\text{Ca}^{2+}$  imaging in neurons stained with OG-1 AM in the rat somatosensory/motor cortex (Fig. 5a), Kerr et al. [12] showed that the probability of detecting a  $\text{Ca}^{2+}$  transient associated with a single action potential is as high as 97%. The probability of detecting short bursts of two to four action potentials was even higher, approaching almost 100%. In vivo  $\text{Ca}^{2+}$  transients evoked by single action potentials had mean amplitudes of approximately 10% (Fig. 5b) and mean decay time constants of 800 ms [12]. Similar results were also obtained in the mouse visual cortex (O.

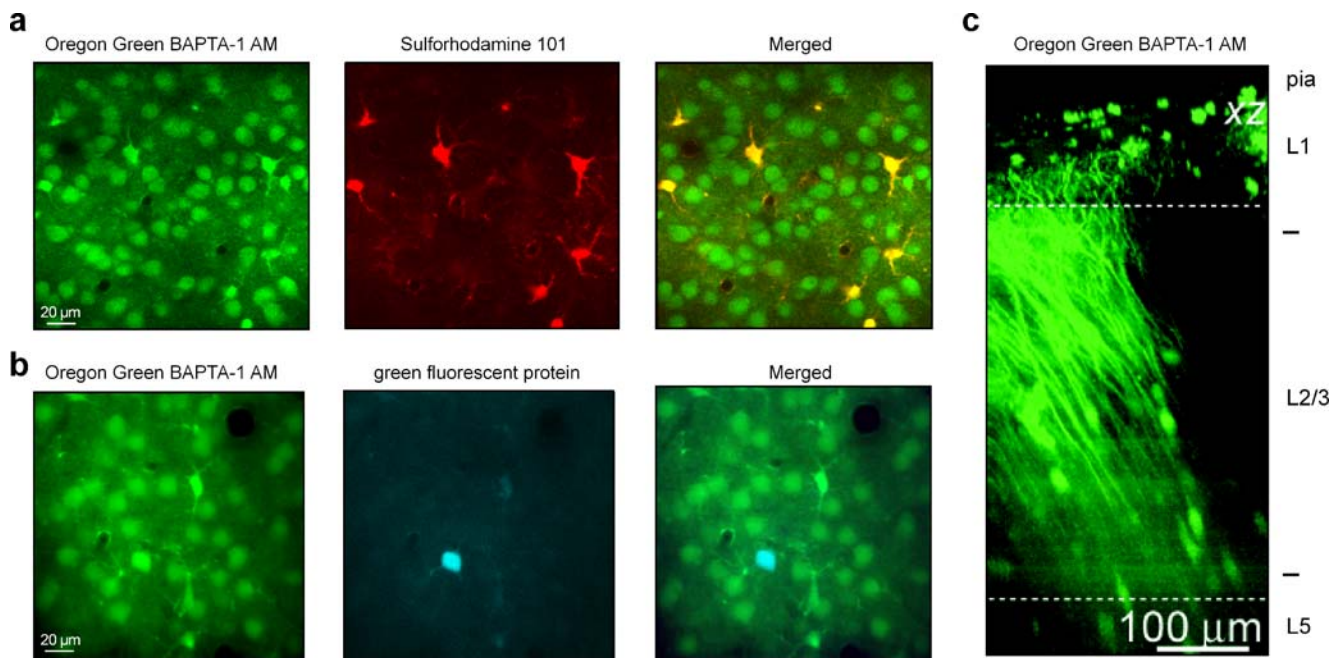


**Fig. 3** Imaging of identified cell types. **a** Microphotographs of layer 2/3 cells in the mouse visual cortex stained with MCBL technique using a dye mixture containing OG-1 AM and a glial marker sulforhodamine 101. The fluorescence of OG-1 AM was directed to the *green channel* (*left*) and the fluorescence of sulforhodamine 101 to the *red one* (*middle*). The merged image on the right shows neurons in *green* and glial cells in *yellow*. **b** Microphotographs illustrating OG-1 AM-based staining of layer 2/3 cells (*left*) in a transgenic mouse

expressing EGFP (*middle*) selectively in somatostatin-positive GABAergic interneurons. The merged image on the *right* shows all cells in *green* and a somatostatin-positive interneuron in *light blue*. **c** A side projection of dendrites of layer 5 pyramidal neurons stained with OG-1 AM. **a**, **c** Reproduced (with permission from Macmillan Publishers Ltd; National Academy of Sciences USA, copyright 2005) from [12, 21], respectively

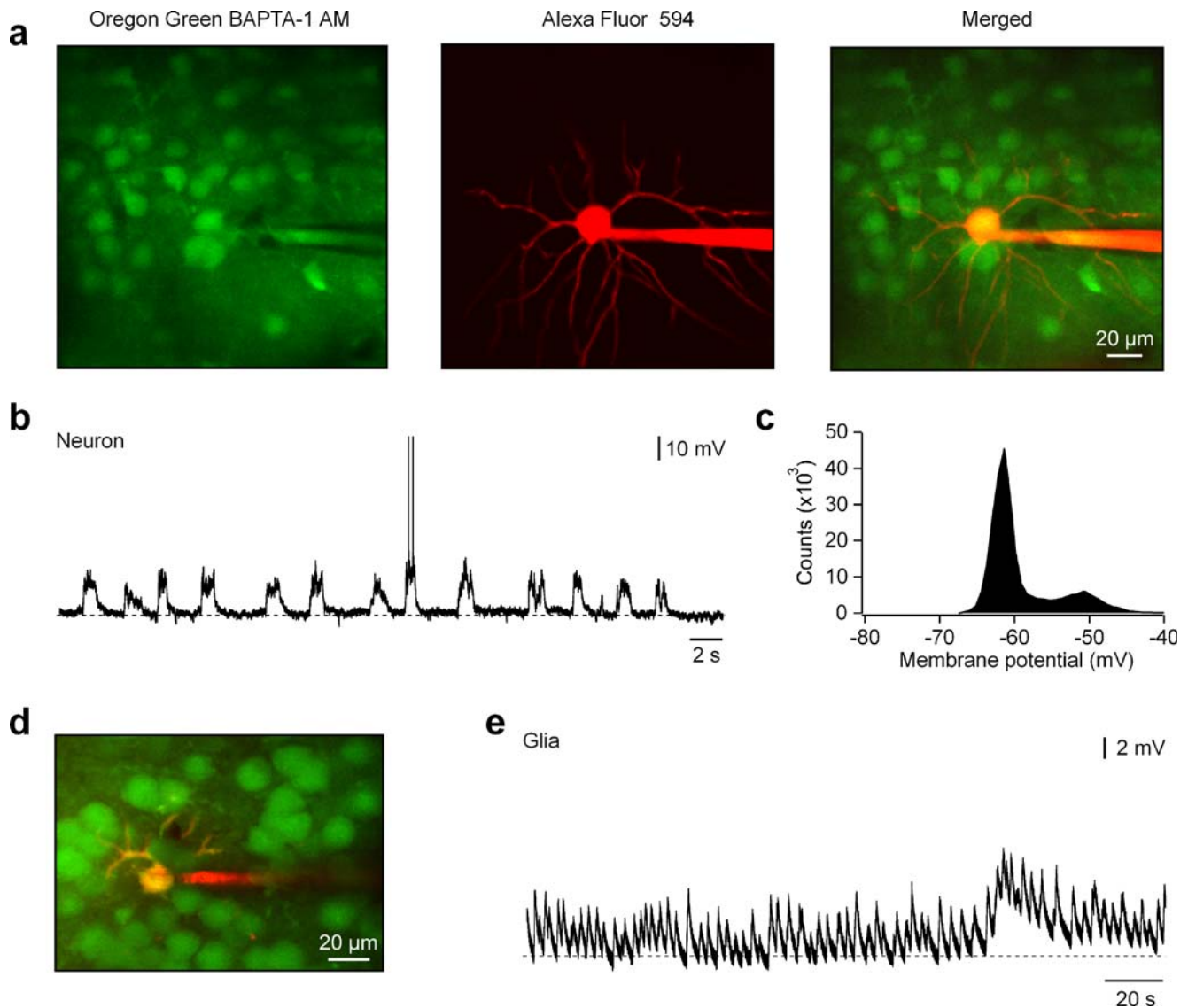


**Fig. 4** Targeted in vivo patch-clamp analysis using MCBL. **a** A microphotograph of layer 2/3 cells stained with OG-1 AM (*green channel, left*). A neuron in the middle of the image was patched with a pipette containing Alexa Fluor 594 (*red channel, middle*). The image on the *right* is an overlay of the two images. **b** Whole-cell membrane potential recordings from the neuron in **a**. **c** A histogram of the

membrane potential measurements in **b** showing two peaks at  $-51$  mV (up state) and  $-62$  mV (down state). **d** An overlay image showing OG-1 AM stained neurons in *green* and a patched glial cell filled with Alexa Fluor 594 in *red*. Before patching, the cell was labeled with S101. **e** Whole-cell recordings of the membrane potential of the glial cell shown in **d**

Garaschuk and A. Konnerth, unpublished observations). These in vivo results confirm earlier findings obtained in brain slices that also showed a strict dependence of somatic  $\text{Ca}^{2+}$  signals on action potential firing (Fig. 5c; [36]). Thus, it appears that under in vivo conditions, dendritic  $\text{Ca}^{2+}$  signals that involve  $\text{Ca}^{2+}$  entry through ligand-gated channels, for example, *N*-methyl-D-aspartate (NMDA) receptor channels (e.g. [37]), do not contribute measurably to  $\text{Ca}^{2+}$  signals detected in MCBL stained cells. The minor contribution of these dendritic  $\text{Ca}^{2+}$  signals is most probably due to the fact that the dye

concentration in MCBL stained cells is too low (approximately  $20 \mu\text{M}$ ; [11]) for dendritic recordings.

### In vivo pharmacology

Although in vivo preparations are, in general, less accessible for controlled pharmacological manipulations as compared to cell cultures and tissue slices, there are several different techniques available for the pharmacological treatment of brain cells in vivo. Most often, drugs are administered in

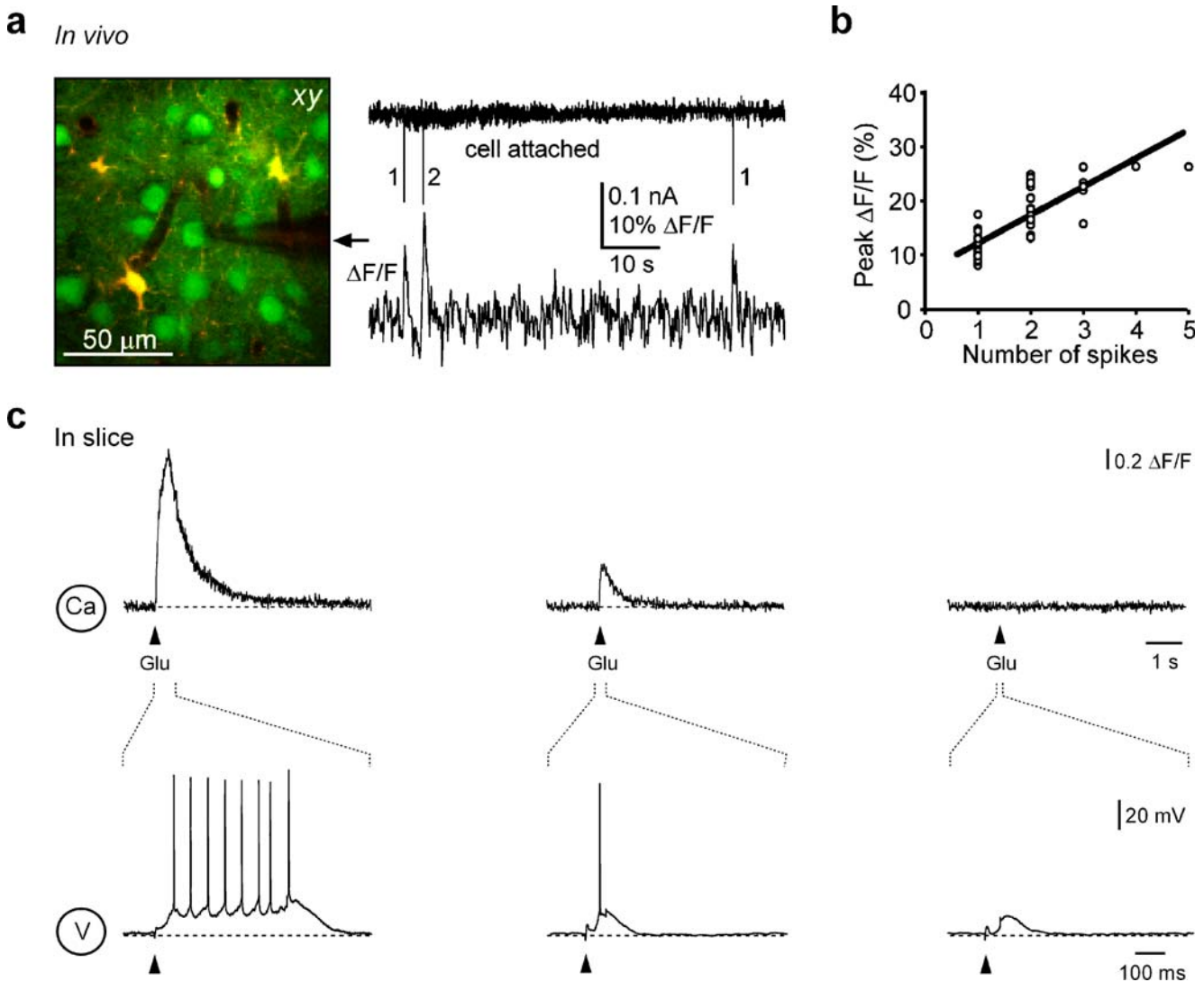


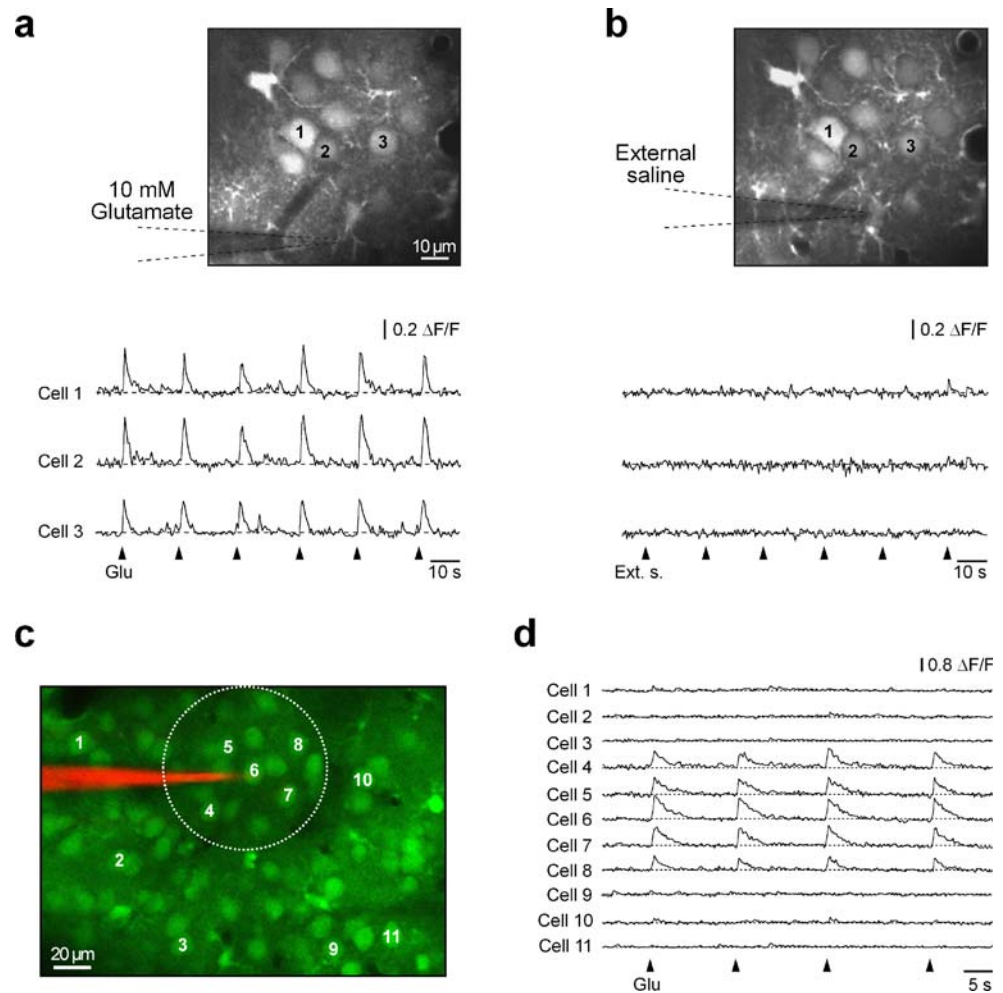
**Fig. 5** Somatic  $\text{Ca}^{2+}$  signals in MCBL-stained cells require action potentials. **a** *Left panel*: a merged image of layer 2/3 cells in the rat somatosensory cortex stained *in vivo* with OG-1 AM (green) and sulforhodamine 101 (red). Neurons are green and astrocytes are yellow. *Right panel*: a simultaneous recording of action potentials in the cell-attached configuration (*upper trace*) and associated  $\text{Ca}^{2+}$  transients (*lower trace*) obtained from the neuron in the middle. The

position of the patch pipette is indicated by an *arrow*. **b** Amplitudes of *in vivo* calcium transients plotted as a function of the number of action potentials detected in simultaneous cell-attached recordings. **a**, **b** Reproduced, with permission from National Academy of Sciences USA, copyright 2005, from [12]. **c** Glutamate-evoked  $\text{Ca}^{2+}$  transients and corresponding changes in the membrane potential recorded in a cortical slice obtained from a brain stained *in vivo* with OG-1 AM

*vivo* via intravenous or intraperitoneal injections. The drugs used in such experiments have to be able to cross the blood–brain barrier; their action is delayed and their concentration at the site of action is largely unknown. In addition, such treatments often cause systemic side effects. Therefore, the systemic drug administration has strong limitations when studying fast cellular responses. A convenient alternative method, which is particularly useful when performing imaging experiments with single cell resolution, is the local application of drugs directly to the cells of interest (Fig. 6). In experiments using MCBL, the craniotomy used for dye loading can be also used for the insertion of an iontophoresis or a pressure-application pipette. As shown in Fig. 6c

and d, such applications can exert their action in highly confined brain regions, with a spherical shape and a diameter of around 100  $\mu\text{m}$ . The use of a recording chamber, as that illustrated in Fig. 1a, allows an even simpler method for drug application. Drugs can be simply added to preheated artificial cerebrospinal fluid, which is used for continuous perfusion. This approach is similar to the bath application of drugs in conventional brain slice experiments. We found that under *in vivo* conditions, the small craniotomy used for MCBL-based cell staining is sufficiently large to allow an effective access of drugs to the brain parenchyma. In our experience, water-soluble drugs (e.g. the NMDA receptor antagonist 2-amino-5-

**Fig. 6** In vivo pharmacology. **a, b** In vivo  $\text{Ca}^{2+}$  recordings from layer 2/3 cells of the mouse somatosensory cortex stained with OG-1 AM. The cells (marked with the respective numbers in the corresponding image) were stimulated either with an iontophoretic application of 10 mM glutamate (**a**) or with an iontophoretic application of external saline (**b**). **c, d**  $\text{Ca}^{2+}$  transients in layer 2/3 cells of the mouse visual cortex (stained with OG-1 AM and marked with corresponding numbers in **c**) caused by a local iontophoretic coapplication of 25  $\mu\text{M}$  Alexa Fluor 594 and 100 mM glutamate. The circle in **c** delineates the area in which glutamate-evoked  $\text{Ca}^{2+}$  transients were detected



phosphonopentanoic acid [APV] or the sodium channel blocker tetrodotoxin [TTX]) start acting within the intact brain as soon as they are present in the recording chamber and, thus, within time frames that are comparable to those observed in brain slices. However, to achieve in vivo drug effects similar to those observed in slices, a two- to threefold increase in the concentration of the drug is required. The use of lipophilic drugs (e.g. the voltage-gated  $\text{Ca}^{2+}$  channel blocker nitrendipine or the AMPA receptor antagonist CNQX) turned out to be more difficult. The required drug dosages were higher, most probably because of the poor diffusion properties of these substances.

#### Monitoring sensory-driven neuronal activity with single cell resolution

To this end, MCBL and two-photon imaging were used (a) for the characterization of spontaneous and sensory-driven activity in the somatosensory and motor cortices of rats and

mice (Fig. 7a; [11, 12]), (b) for monitoring light-evoked responses in the mouse visual cortex (Fig. 7b), and (c) for the characterization of direction selectivity of the layer 2/3 neurons in the visual cortex of rats and cats (Fig. 7c; [13]). In zebrafish larvae, the approach was used for the analysis of light-evoked responses in the optic tectum [18], odor-evoked activity patterns in the olfactory bulb [17], and air puff-evoked  $\text{Ca}^{2+}$  signals in spinal cord neurons [16].

Two-photon imaging studies in rodent primary sensory cortices have established that the coding of spontaneous as well as sensory-driven activity in the upper cortical layers is sparse. Thus, only 10% of neurons participated in the spontaneous up states in rat somatosensory cortex [12]. Similarly, rather few cells responded to orientations of moving bars in rat visual cortex [13]. In contrast, the percentage of responsive cells in cat visual cortex was rather high, reaching even 100% in some experiments [13].

Another interesting feature revealed by two-photon imaging of neuronal networks in vivo is the heterogeneous distribution of activity in space and time across individual

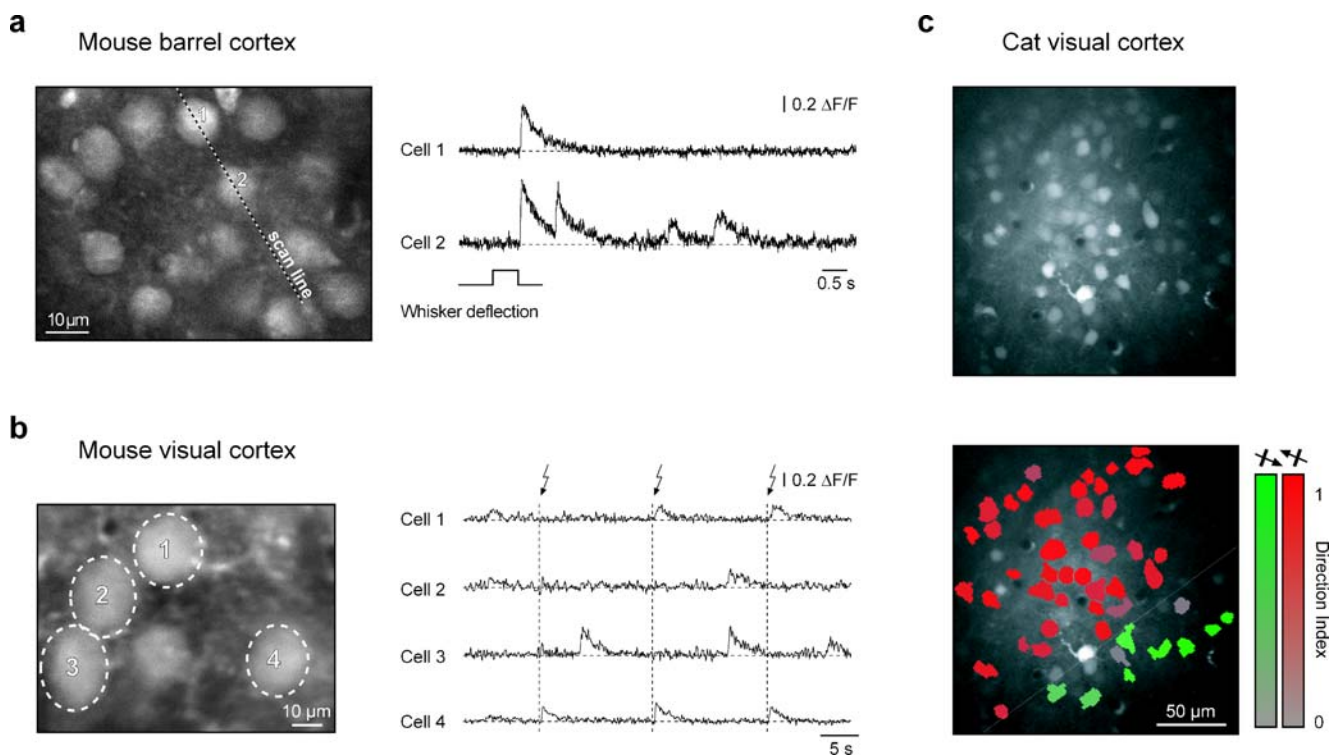


**Fig. 7** Sensory-driven  $\text{Ca}^{2+}$  transients in individual cortical neurons. **a** Individual neurons in the mouse barrel cortex (*left*) and the corresponding  $\text{Ca}^{2+}$  transients (*right*) evoked by the deflection of the majority of whiskers at the contralateral side of the snout. The transients were recorded using the line-scan mode (5 ms/line). The position of the scanned line is indicated. **b** Individual neurons in the mouse visual cortex (*left*) and the corresponding  $\text{Ca}^{2+}$  transients (*right*) evoked by brief light flashes. Light flashes were applied every

10 s (indicated as a *dotted line*). **c** A high-resolution image of the cat visual cortex (*upper panel*). On the *lower panel*, all cells responding to a given direction of the visual stimulus were color-coded in *red* and *green*. The cells responding to both directions are displayed as *gray*, according to their direction index (see color scale on the *right*). **a** Reproduced, with permission from National Academy of Sciences USA, copyright 2003, from [11]. **c** Reproduced, with permission from Macmillan Publishers Ltd, from [13]

neurons. For example, continuously changing ‘mosaic’ activation patterns were observed in rat and mouse somatosensory cortex during spontaneous [12] as well as sensory-driven [11] activity. These data indicated that such activities are not generated by a particular subset of neurons, but rather are produced by dynamically reorganizing neuronal subpopulations. Interestingly, the results concerning the organization of the orientation- and direction-selectivity maps at a single cell level show species specificity. Thus, in the optic tectum of zebrafish larvae as well as in the rat visual cortex, direction- or orientation-selectivity maps are locally disordered with neighboring cells, often highly tuned to different directions and/or orientations [13, 18]. In contrast, in the cat visual cortex, orientation- and direction-selectivity maps are highly organized (Fig. 7c; [13]). Orientation and direction selectivity varies slowly over the distance; the transitions between different preferred directions are smooth and ordered with each cell responding similarly to its nearest neighbors. Interestingly, the boundaries between neuronal clusters responding to different directions are

extremely narrow (20–50  $\mu\text{m}$ ) and are populated by cells responding rather equally to both directions (Fig. 7c).

### Monitoring $\text{Ca}^{2+}$ signals in awake behaving animals

To measure macroscopic properties of neural networks in nonanesthetized animals, Adelsberger et al. [20] combined MCBL with in vivo brain microendoscopy. The tip of a thin flexible optic fiber ( $\varnothing=200 \mu\text{m}$ ; numerical aperture = 0.48) was implanted into the brain region stained with OG-1 AM (Fig. 8a) and was used both for excitation of the fluorescent dye and for the collection of the emitted light. The use of a single detector (photomultiplier or avalanche photodiode) allowed recording a compound  $\text{Ca}^{2+}$  signal from all cells within the illuminated volume, thus severely reducing the susceptibility of recordings to movement artifacts. This in vivo microendoscope was recently used to record spontaneous  $\text{Ca}^{2+}$  waves in the cortex of nonanesthetized mouse pups (Fig. 8b). The waves occurred mainly during sleep



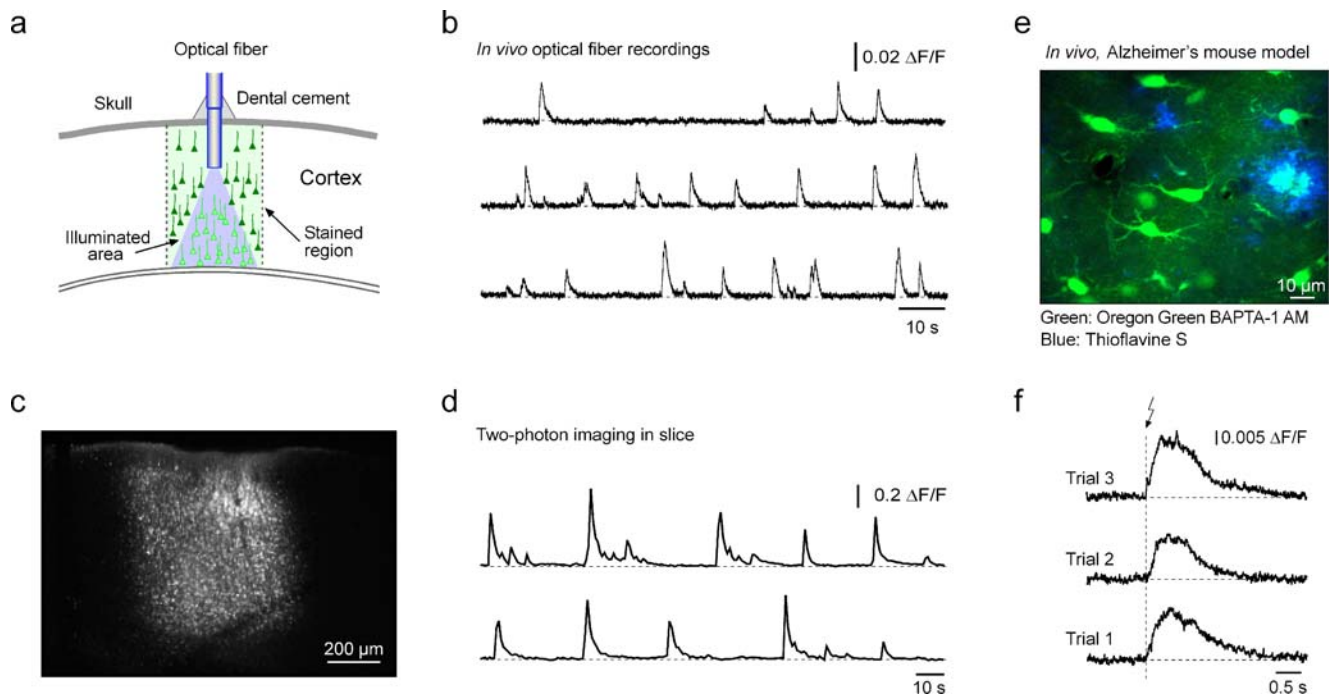


**Fig. 8** In vivo brain microendoscopy. **a** A schematic drawing illustrating an implanted optical fiber. **b** In vivo recordings of spontaneous cortical  $\text{Ca}^{2+}$  waves in a nonanesthetized newborn mouse. **c**, **d** A two-photon image of the in vivo stained cortical area (**c**), where the  $\text{Ca}^{2+}$  waves shown in **d** were recorded from. **e** A high-resolution in vivo image of the layer 1 in the visual cortex of a mouse model of

like resting states and vanished or became inhibited during animal's movements [20]. Remarkably, similar  $\text{Ca}^{2+}$  waves were present in cortical slices obtained from mice stained in vivo (Fig. 8c and d). They closely resembled the early network oscillations initially found in cortical slices of newborn rats [38].

In addition to monitoring  $\text{Ca}^{2+}$  signals in awake, behaving animals, the microendoscopic approach can be performed anywhere in the brain, even in deep and hidden regions. However, its limitation is that it currently allows just a single point detection. Spatially resolved recordings may be obtained either through the implantation of an array of fibers, or through the substitution of a single optical fiber by fiber bundles [39], and/or by using gradient refractive index fibers [40].

### Monitoring $\text{Ca}^{2+}$ signals in aged and diseased brain

It is difficult to establish a good experimental model for studying neuronal aging in vitro because of the high fragility of aged neuronal tissue. By contrast, in vivo studies, like the ones using MCBL, are feasible also in aged animals [21]. Figure 8e displays cortical cells in vivo in the visual cortex of a 1-year-old mouse mutant, which represents a mouse model of Alzheimer's disease. These

Alzheimer's disease [41]. Cells are stained with OG-1 AM (green) and amyloid depositions are stained with thioflavine S (blue). **f** Light-evoked population  $\text{Ca}^{2+}$  transients recorded with an endoscopic fiber in the visual cortex of a mouse model of Alzheimer's disease. Cortical cells were stained with OG-1 AM. **a–d** Reproduced, with permission from Macmillan Publishers Ltd, from [20]

mice overexpress a human amyloid precursor protein (APP) with the Swedish double mutation (at positions 670/671) that is associated with a familiar form of Alzheimer's disease [41]. As a result of the mutation, the cortex is enriched with accumulations of the amyloid- $\beta$  protein, so-called dense core plaques. The plaques represent a histological hallmark of Alzheimer's disease [42]. For two-photon in vivo imaging studies, the plaques can be stained with specific fluorescent markers like, for example, thioflavine S [43]. We found that the diffusion of thioflavine S within the brain is rather restricted, and, therefore, the in depth staining of the brain tissue is better achieved by the bolus ejection technique (Fig. 8e; O. Garaschuk, R.I. Milos, and A. Konnerth, unpublished observations). The in vivo functional properties of neuronal networks in mutant animals can be studied both at the 'macroscopic' level using brain endoscopy (Fig. 8f) and at the level of individual neurons when using two-photon imaging (Fig. 8e).

### Conclusions

Two-photon  $\text{Ca}^{2+}$  imaging using targeted bulk loading of  $\text{Ca}^{2+}$  indicators is a useful approach for high-resolution in vivo imaging of network function. The advantages of the

approach include the relatively high temporal resolution (frame rates of up to 100/s), the good spatial resolution allowing the discrimination of single cells, and its high versatility that allows its use in a variety of animal models and at different ages. It is foreseeable, however, that the development of genetically encoded fluorescent protein sensors with improved properties will open exciting new possibilities in the nearest future [44–46]. Genetically encoded indicators, not just for calcium but also for other second messengers (e.g. [47–49]), can, in principle, be targeted to specific subclasses of neurons or even to small neuronal subcompartments, like dendrites and dendritic spines. The combination of bolus loading techniques with various methods like targeted expression of genetically encoded indicators will soon open entirely new avenues for the in vivo analysis of brain function.

**Acknowledgements** This study was supported by grants of the Deutsche Forschungsgemeinschaft (SFB 391 and SFB 596) and the Bundesministerium für Bildung und Forschung (NGFN-2). R.I.M. was supported by Marie Curie Fellowship. We thank M. Staufenbiel and D. Abramowski for APP mice.

## References

- Hamill OP, Marty A, Neher E, Sakmann B, Sigworth FJ (1981) Improved patch-clamp techniques for high-resolution current recording from cells and cell-free membrane patches. *Pflügers Arch* 391:85–100
- Tsien RY (1981) A non-disruptive technique for loading calcium buffers and indicators into cells. *Nature* 290:527–528
- Cossart R, Ikegaya Y, Yuste R (2005) Calcium imaging of cortical networks dynamics. *Cell Calcium* 37:451–457
- Feldmeyer D, Lubke J, Silver RA, Sakmann B (2002) Synaptic connections between layer 4 spiny neurone-layer 2/3 pyramidal cell pairs in juvenile rat barrel cortex: physiology and anatomy of interlaminar signalling within a cortical column. *J Physiol* 538:803–822
- Silberberg G, Grillner S, LeBeau FE, Maex R, Markram H (2005) Synaptic pathways in neural microcircuits. *Trends Neurosci* 28:541–551
- Denk W, Strickler JH, Webb WW (1990) Two-photon laser scanning fluorescence microscopy. *Science* 248:73–76
- Svoboda K, Denk W, Kleinfeld D, Tank DW (1997) In vivo dendritic calcium dynamics in neocortical pyramidal neurons. *Nature* 385:161–165
- Svoboda K, Helmchen F, Denk W, Tank DW (1999) Spread of dendritic excitation in layer 2/3 pyramidal neurons in rat barrel cortex in vivo. *Nat Neurosci* 2:65–73
- Waters J, Helmchen F (2004) Boosting of action potential backpropagation by neocortical network activity in vivo. *J Neurosci* 24:11127–11136
- Waters J, Larkum M, Sakmann B, Helmchen F (2003) Supralinear  $Ca^{2+}$  influx into dendritic tufts of layer 2/3 neocortical pyramidal neurons in vitro and in vivo. *J Neurosci* 23:8558–8567
- Stosiek C, Garaschuk O, Holthoff K, Konnerth A (2003) In vivo two-photon calcium imaging of neuronal networks. *Proc Natl Acad Sci USA* 100:7319–7324
- Kerr JN, Greenberg D, Helmchen F (2005) Imaging input and output of neocortical networks in vivo. *Proc Natl Acad Sci USA* 102:14063–14068
- Ohki K, Chung S, Ch'ng YH, Kara P, Reid RC (2005) Functional imaging with cellular resolution reveals precise micro-architecture in visual cortex. *Nature* 433:597–603
- Nimmerjahn A, Kirchhoff F, Kerr JND, Helmchen F (2004) Sulforhodamine 101 as a specific marker of astroglia in the neocortex in vivo. *Nat Methods* 1:31–37
- Sullivan MR, Nimmerjahn A, Sarkisov DV, Helmchen F, Wang SS (2005) In vivo calcium imaging of circuit activity in cerebellar cortex. *J Neurophysiol* 94:1636–1644
- Bruste E, Marandi N, Kovalchuk Y, Drapeau P, Konnerth A (2003) 'In vivo' monitoring of neuronal network activity in zebrafish by two-photon  $Ca^{2+}$  imaging. *Pflügers Arch* 446:766–773
- Li J, Mack JA, Souren M, Yaksi E, Higashijima S, Mione M, Fetcho JR, Friedrich RW (2005) Early development of functional spatial maps in the zebrafish olfactory bulb. *J Neurosci* 25:5784–5795
- Niell CM, Smith SJ (2005) Functional imaging reveals rapid development of visual response properties in the zebrafish tectum. *Neuron* 45:941–951
- Mehta AD, Jung JC, Flusberg BA, Schnitzer MJ (2004) Fiber optic in vivo imaging in the mammalian nervous system. *Curr Opin Neurobiol* 14:617–628
- Adelsberger H, Garaschuk O, Konnerth A (2005) Cortical calcium waves in resting newborn mice. *Nat Neurosci* 8:988–990
- Garaschuk O, Milos RI, Konnerth A (2006) Targeted bulk-loading of fluorescent indicators for two-photon brain imaging in vivo. *Nat Prot* 1:380–386
- Yuste R (2000) Loading brain slices with AM esters or calcium indicators. In: Yuste R, Lanni F, Konnerth A (eds) *Imaging: a laboratory manual*. Cold Spring Harbor Press, Cold Spring Harbor, New York, pp 34.31–34.39
- Hirase H, Qian L, Bartho P, Buzsaki G (2004) Calcium dynamics of cortical astrocytic networks in vivo. *PLoS Biol* 2:E96
- Lopez-Bendito G, Sturgess K, Erdelyi F, Szabo G, Molnar Z, Paulsen O (2004) Preferential origin and layer destination of GAD65-GFP cortical interneurons. *Cereb Cortex* 14:1122–1133
- Tamamaki N, Yanagawa Y, Tomioka R, Miyazaki J, Obata K, Kaneko T (2003) Green fluorescent protein expression and colocalization with calretinin, parvalbumin, and somatostatin in the GAD67-GFP knock-in mouse. *J Comp Neurol* 467:60–79
- Meyer AH, Katona I, Blatow M, Rozov A, Monyer H (2002) In vivo labeling of parvalbumin-positive interneurons and analysis of electrical coupling in identified neurons. *J Neurosci* 22:7055–7064
- Oliva AA Jr, Jiang M, Lam T, Smith KL, Swann JW (2000) Novel hippocampal interneuronal subtypes identified using transgenic mice that express green fluorescent protein in GABAergic interneurons. *J Neurosci* 20:3354–3368
- Pei X, Volgushev M, Vidyasagar TR, Creutzfeldt OD (1991) Whole cell recording and conductance measurements in cat visual cortex in-vivo. *NeuroReport* 2:485–488
- Ferster D, Jagadeesh B (1992) EPSP-IPSP interactions in cat visual cortex studied with in vivo whole-cell patch recording. *J Neurosci* 12:1262–1274
- Brecht M, Sakmann B (2002) Dynamic representation of whisker deflection by synaptic potentials in spiny stellate and pyramidal cells in the barrels and septa of layer 4 rat somatosensory cortex. *J Physiol* 543:49–70
- Margrie TW, Brecht M, Sakmann B (2002) In vivo, low-resistance, whole-cell recordings from neurons in the anaesthetized and awake mammalian brain. *Pflügers Arch* 444:491–498

32. Margrie TW, Meyer AH, Caputi A, Monyer H, Hasan MT, Schaefer AT, Denk W, Brecht M (2003) Targeted whole-cell recordings in the mammalian brain in vivo. *Neuron* 39:911–918
33. Komai S, Denk W, Osten P, Brecht M, Margrie TW (2006) Two-photon targeted patching (TPTP) in vivo. *Nat Prot* 1: 647–652
34. Petersen CC, Hahn TT, Mehta M, Grinvald A, Sakmann B (2003) Interaction of sensory responses with spontaneous depolarization in layer 2/3 barrel cortex. *Proc Natl Acad Sci USA* 100: 13638–13643
35. Amzica F (2002) In vivo electrophysiological evidences for cortical neuron-glia interactions during slow (<1 Hz) and paroxysmal sleep oscillations. *J Physiol Paris* 96:209–219
36. Smetters D, Majewska A, Yuste R (1999) Detecting action potentials in neuronal populations with calcium imaging. *Methods* 18:215–221
37. Kovalchuk Y, Eilers J, Lisman J, Konnerth A (2000) NMDA receptor-mediated subthreshold  $Ca^{2+}$  signals in spines of hippocampal neurons. *J Neurosci* 20:1791–1799
38. Garaschuk O, Linn J, Eilers J, Konnerth A (2000) Large-scale oscillatory calcium waves in the immature cortex. *Nat Neurosci* 3:452–459
39. Bharali DJ, Klejbor I, Stachowiak EK, Dutta P, Roy I, Kaur N, Bergey EJ, Prasad PN, Stachowiak MK (2005) Organically modified silica nanoparticles: a nonviral vector for in vivo gene delivery and expression in the brain. *Proc Natl Acad Sci USA* 102:11539–11544
40. Flusberg BA, Cocker ED, Piyawattanametha W, Jung JC, Cheung EL, Schnitzer MJ (2005) Fiber-optic fluorescence imaging. *Nat Methods* 2:941–950
41. Sturchler-Pierrat C, Abramowski D, Duke M, Wiederhold KH, Mistl C, Rothacher S, Ledermann B, Burki K, Frey P, Paganetti PA, Waridel C, Calhoun ME, Jucker M, Probst A, Staufenbiel M, Sommer B (1997) Two amyloid precursor protein transgenic mouse models with Alzheimer disease-like pathology. *Proc Natl Acad Sci USA* 94:13287–13292
42. Alzheimer A (1911) Über eigenartige Krankheitsfälle des späteren Alters. *Z Gesamte Neurol Psychiatr* 4:356–386
43. Christie RH, Bacskai BJ, Zipfel WR, Williams RM, Kajdasz ST, Webb WW, Hyman BT (2001) Growth arrest of individual senile plaques in a model of Alzheimer's disease observed by in vivo multiphoton microscopy. *J Neurosci* 21:858–864
44. Hasan MT, Friedrich RW, Euler T, Larkum ME, Giese G, Both M, Duebel J, Waters J, Bujard H, Griesbeck O, Tsien RY, Nagai T, Miyawaki A, Denk W (2004) Functional fluorescent  $Ca^{2+}$  indicator proteins in transgenic mice under TET control. *PLoS Biol* 2:e163
45. Diez-Garcia J, Matsushita S, Mutoh H, Nakai J, Ohkura M, Yokoyama J, Dimitrov D, Knopfel T (2005) Activation of cerebellar parallel fibers monitored in transgenic mice expressing a fluorescent  $Ca^{2+}$  indicator protein. *Eur J Neurosci* 22:627–635
46. Mank M, Reiff DF, Heim N, Friedrich MW, Borst A, Griesbeck O (2006) A FRET-based calcium biosensor with fast signal kinetics and high fluorescence change. *Biophys J* 90:1790–1796
47. Yasuda R, Harvey CD, Zhong H, Sobczyk A, van Aelst L, Svoboda K (2006) Supersensitive Ras activation in dendrites and spines revealed by two-photon fluorescence lifetime imaging. *Nat Neurosci* 9:283–291
48. Zaccolo M, De Giorgi F, Cho CY, Feng L, Knapp T, Negulescu PA, Taylor SS, Tsien RY, Pozzan T (2000) A genetically encoded, fluorescent indicator for cyclic AMP in living cells. *Nat Cell Biol* 2:25–29
49. Gorbunova YV, Spitzer NC (2002) Dynamic interactions of cyclic AMP transients and spontaneous  $Ca^{2+}$  spikes. *Nature* 418:93–96

# Improved calcium imaging in transgenic mice expressing a troponin C-based biosensor

Nicola Heim<sup>1,3</sup>, Olga Garaschuk<sup>2,3</sup>, Michael W Friedrich<sup>1</sup>, Marco Mank<sup>1</sup>, Ruxandra I Milos<sup>2</sup>, Yury Kovalchuk<sup>2</sup>, Arthur Konnerth<sup>2</sup> & Oliver Griesbeck<sup>1</sup>

**Fluorescent Ca<sup>2+</sup> indicator proteins (FCIPs) are attractive tools for studying Ca<sup>2+</sup> dynamics in live cells. Here we describe transgenic mouse lines expressing a troponin C (TnC)-based biosensor. The biosensor is widely expressed in neurons and has improved Ca<sup>2+</sup> sensitivity both *in vitro* and *in vivo*. This allows FCIP-based two-photon Ca<sup>2+</sup> imaging of distinct neurons and their dendrites *in vivo*, and opens a new avenue for structure-function analysis of intact neuronal circuits.**

Genetically encoded FCIPs<sup>1,2</sup> can be targeted to specific tissues and/or cellular subcompartments enabling high-resolution analyses of the intracellular Ca<sup>2+</sup> dynamics. Thus far, however, their use in the mammalian brain and many other tissues *in vivo* was mostly disappointing as a result of sensor inactivation or reduced dynamic range after transgenic expression<sup>3–5</sup>. Therefore, the detection of Ca<sup>2+</sup> signals from distinct neurons and their cellular subcompartments (for example, dendrites) *in vivo* has not been feasible.

Recently we generated a family of calcium biosensors based on variants of TnC, the Ca<sup>2+</sup> sensor protein in skeletal and cardiac muscle<sup>6</sup>. In the present study we increased the brightness of the sensor by replacing the donor cyan fluorescent protein by Cerulean<sup>7</sup>. Additionally, we introduced the common folding mutations V163A and S175G into acceptor protein Citrine<sup>8</sup> to enhance folding and brightness. These modifications resulted in the sensor termed CerTN-L15, which shared many properties with the parental TN-L15, but showed enhanced brightness when expressed in dissociated neurons (**Supplementary Fig. 1** online).

To generate transgenic mice expressing CerTN-L15, we used the Thy-1 expression cassette<sup>9</sup>. Altogether, we generated 17 independent lines of Thy1-CerTN-L15 mice that differed in expression patterns and strength of expression owing to the strong context sensitivity of the Thy1 expression cassette. In all mouse lines

expression patterns were widespread and involved many major areas of the central nervous system, such as cortex, hippocampus, cerebellum, brain stem, retina, spinal cord and several more peripheral structures such as the trigeminal ganglia (**Supplementary Table 1** online).

For an in-depth analysis we focused on the transgenic line C because this line had the highest expression level of the transgene (**Fig. 1a**). Western blot analysis of cortical tissue showed that the onset of CerTN-L15 expression in line C was around birth. The amount of transgene increased during the first two postnatal weeks and remained stable for up to 11 months, the latest time point tested (data not shown). We detected no signs of degradation of the sensor, as verified by western blot analysis (**Fig. 1b**).

To test for correct folding and basic sensor functionality, we measured two-photon emission spectra of cultured hippocampal neurons acutely transfected with CerTN-L15 (**Fig. 1c** and **Supplementary Methods** online). We compared these spectra with those obtained in individual hippocampal and cortical neurons in brain slices of transgenic mice (**Fig. 1c**). Emission spectra taken in the absence of extracellular Ca<sup>2+</sup> (blue lines) were comparable for acutely transfected and transgenically expressed Ca<sup>2+</sup> indicator protein. Moreover, depolarization of neurons in slices and in transfected cultures with high K<sup>+</sup> concentration solution resulted in decreased donor emission and increased acceptor emission with a comparable change in Citrine/Cerulean emission ratio of 70–95% (**Fig. 1c**). Thus, we concluded that CerTN-L15 was stably expressed in the brain of transgenic mice, well folded, fully functional compared to the acutely transfected sensor, and was not inactivated or degraded during transgenic expression.

Within the brains of transgenic line C mice, the indicator was widely expressed in many types of neurons of the central nervous system, most prominently in the pyramidal neurons of the hippocampus and the neocortex (**Supplementary Fig. 2** online). Distribution of CerTN-L15 in the cytosol was homogenous, with no signs of aggregation or compartmentalization. The nucleus was devoid of CerTN-L15.

To analyze functional properties of CerTN-L15, we first tested its Ca<sup>2+</sup> sensitivity in acute cortical slices. For this purpose, we performed simultaneous two-photon imaging and whole-cell patch clamp recordings from labeled layer 2/3 pyramidal cells in the temporal/parietal cortex (**Fig. 2** and **Supplementary Methods**). The patched neurons had normal electrophysiological properties with a threshold for action potential generation of  $-41.9 \pm 1.8$  mV, action potential amplitude of  $96.3 \pm 4.5$  mV and action potential half-width of  $1.01 \pm 0.14$  ms ( $n = 7$  cells). We stimulated the neurons either by direct current injections (**Fig. 2a,b**) or by iontophoretic glutamate applications (**Fig. 2c**). Both stimulation

<sup>1</sup>Max Planck Institute of Neurobiology, Am Klopferspitz 18, 82152 Martinsried, Germany. <sup>2</sup>Institute of Neuroscience, Technical University Munich, Biedersteinerstr. 29, 80802 Munich, Germany. <sup>3</sup>These authors contributed equally to this work. Correspondence should be addressed to O.G. (griesbeck@neuro.mpg.de) or A.K. (arthur.konnerth@lrz.tu-muenchen.de).

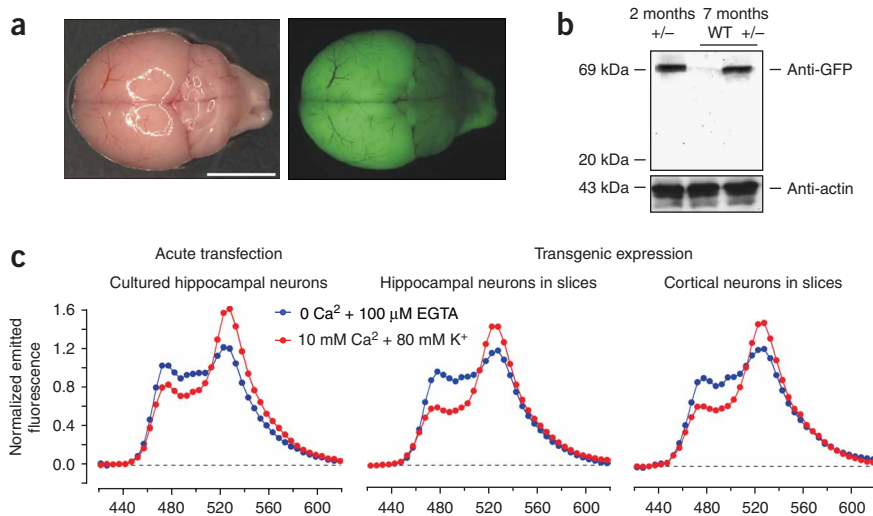


**Figure 1** | Characterization of Thy1-CerTN-L15 transgenic mice. **(a)** Bright field (left) and fluorescence (right; Citrine emission) images of whole brain of a mouse (line C). All analyzed mice were heterozygous (CerTN-L15<sup>+/-</sup>). Scale bar, 5 mm. **(b)** Western blot analysis of cortical tissue of transgenic line C mouse (taken at 2 and 7 months) using an antibody against GFP. The indicator band runs at the expected molecular weight of 69 kDa. WT, wild type. +/-, CerTN-L15. **(c)** Comparison of averaged emission spectra of CerTN-L15 in acutely transfected cultured neurons (left) with averaged emission spectra of CerTN-L15 transgenically expressed in hippocampal (middle) and cortical (right) neurons in brain slices (from left to right  $n = 20$ , 105 and 21 cells, respectively). Blue spectra were measured with Ca<sup>2+</sup>-free external solution whereas red spectra were measured with a depolarizing external solution (see **Supplementary Methods**).

paradigms evoked trains of action potentials that were associated with characteristic changes in the fluorescence of Cerulean and Citrine (**Fig. 2b,c**). Brief trains of 2–3 action potentials evoked clear changes in the ratio of Citrine/Cerulean fluorescence in single trials (**Fig. 2b**), whereas fluorescence changes caused by single action potentials were not reliably detected. The relation between the number of action potentials and the amplitude of the associated Ca<sup>2+</sup> transients was linear in all cells tested ( $n = 11$ ; **Fig. 2d**). The slope of the fit line, however, was slightly different in different cells (mean fractional change in emission ratio expressed as  $\Delta R/R$  change per one action potential =  $4.2 \pm 0.6\%$ ,  $n = 6$ ; **Supplementary Methods**). The mean decay time constant of the Ca<sup>2+</sup> transients was  $1.5 \pm 0.1$  s ( $n = 11$ ). There was no substantial correlation between the magnitude of the decay time constant and the number of action potentials in the underlying burst (**Fig. 2e**), suggesting that under our experimental conditions saturation of CerTN-L15 is negligible.

Next we examined fluorescence properties of CerTN-L15 *in vivo* (**Fig. 3** and **Supplementary Fig. 3** online). We used iontophoretic glutamate applications to probe for functional responses of CerTN-L15. When analyzing neurons in layer 2/3 of the visual cortex *in vivo*, we had to use stimulation pulse durations, which were two times longer compared to those used in cortical slices (see **Supplementary Methods**). The resulting amplitudes ( $\Delta R/R$ ) of the Ca<sup>2+</sup> transients were also twice as large ( $63.7 \pm 5.1\%$ ,  $n = 11$  *in vivo* compared to  $33.2 \pm 2.2\%$ ,  $n = 6$  *in vitro*). In layer 1 (**Fig. 3b**), however, stimulation parameters were comparable to those used in brain slices. These data suggest that the Ca<sup>2+</sup>

sensitivity of the sensor was comparable *in vivo* and *in vitro*, but Ca<sup>2+</sup> measurements at greater depth *in vivo* had a higher detection threshold (probably owing to higher baseline noise and/or photon scattering). The time courses of somatic glutamate-evoked Ca<sup>2+</sup> transients were similar *in vivo* and *in vitro*. Thus, the decay

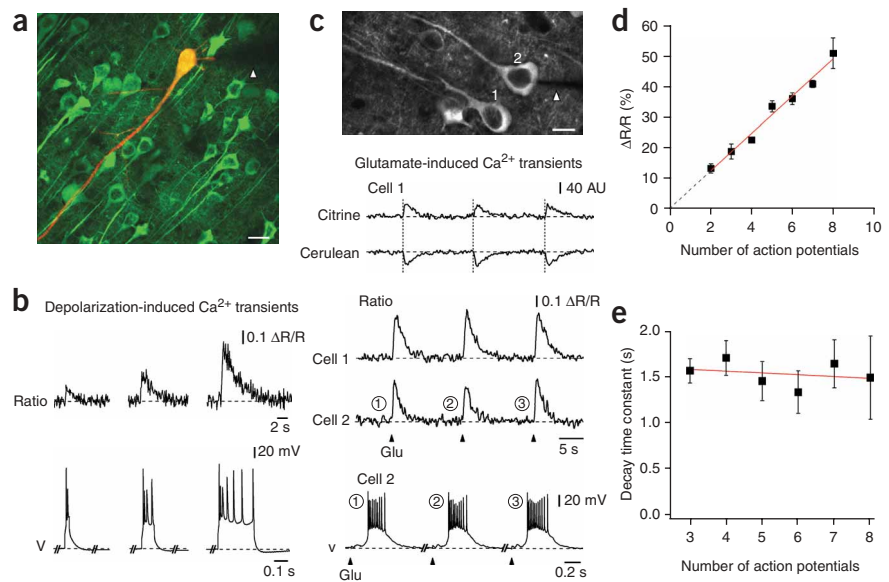


**Figure 2** | Ca<sup>2+</sup> sensitivity of CerTN-L15. **(a)** A merged image of layer 2/3 neurons in a cortical slice (37-day-old mouse). CerTN-L15 labeling is shown in green. A pyramidal neuron patched with internal saline containing 100  $\mu\text{M}$  Alexa Fluor 594 is shown in yellow. Arrowhead, shadow of the patch pipette. Scale bar, 20  $\mu\text{m}$ . **(b)** Relative changes in the Citrine/Cerulean ratio (top) and corresponding membrane depolarizations (bottom; accompanied by 2, 4 and 7 action potentials, respectively) caused by three current injections (35, 100 and 300 ms long). **(c)** Microphotograph of two layer 2/3 cortical neurons (47-day-old mouse); cell 1 is intact whereas cell 2 is patched (top). Arrowhead, shadow of the patch pipette. Scale bar, 10  $\mu\text{m}$ . Original traces showing changes in fluorescence of donor and acceptor proteins in response to a 100-ms-long iontophoretic glutamate application (cell 1) and corresponding ratio changes (cells 1 and 2; middle). Underlying bursts of action potentials recorded simultaneously from cell 2 (bottom). Note similarity of ratio changes in the intact (cell 1) and patched (cell 2) cell. Circled numbers mark responses to individual glutamate puffs of patched cell 2. **(d,e)** Dependence of the amplitude of Citrine/Cerulean ratio (**d**;  $n = 25$  depolarization steps to the cell shown in **a**) and the decay time constant of the ratio changes (**e**;  $n = 11$  neurons) on the number of underlying action potentials. Red lines are linear least-square fits to the respective sets of data. Data are mean  $\pm$  s.e.m.

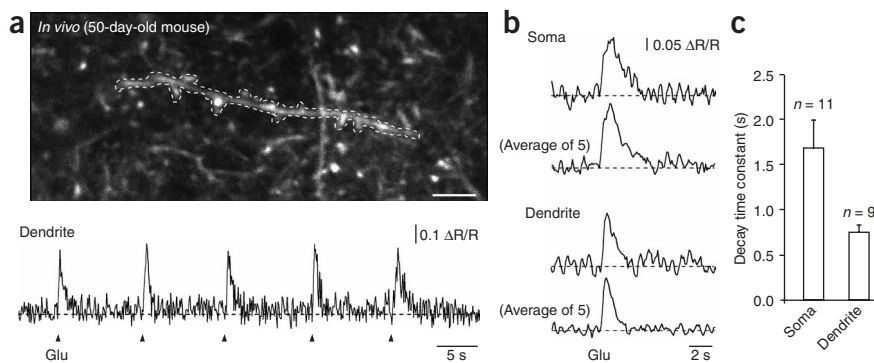


**Figure 3** | CerTN-L15-based Ca<sup>2+</sup> measurements *in vivo*. **(a)** Micrograph of a spiny dendrite located 30 μm below the cortical surface (top). Ca<sup>2+</sup> transients recorded from the region of interest delineated in the top panel, and caused by five consecutive 40-ms-long iontophoretic glutamate applications (bottom). **(b)** Individual and averaged Ca<sup>2+</sup> transients recorded simultaneously in the soma (upper traces) and in a neighboring dendrite of another cell (lower traces) in response to 30-ms-long iontophoretic glutamate applications. **(c)** Summary of decay time constants of somatic and dendritic glutamate-activated Ca<sup>2+</sup> transients recorded *in vivo*. Data are mean ± s.e.m.

time constant of somatic Ca<sup>2+</sup> transients was on average  $1.68 \pm 0.3$  s ( $n = 11$ ) *in vivo* (Fig. 3c) and  $1.63 \pm 0.2$  s ( $n = 34$ ) *in vitro*. For comparison, see also the *in vitro* dissociation time constant of recombinant CerTN-L15 (Supplementary Fig. 1).

We attempted to measure Ca<sup>2+</sup> signals in spiny dendrites, sites of initial processing of synaptic signals. The concentration of the indicator protein within secondary/tertiary dendrites and the dendrite-to-background fluorescence ratio allowed clear visualization of spiny dendrites in CerTN-L15 expressing mice (Fig. 3a). Brief (30–50 ms) iontophoretic glutamate pulses evoked dendritic Ca<sup>2+</sup> transients with mean amplitudes of  $48.8 \pm 7\%$  ( $n = 9$ ) and decay time constants of  $0.76 \pm 0.07$  s ( $n = 9$ ). Notably, the signal-to-noise ratio was sufficient to distinguish individual, nonaveraged Ca<sup>2+</sup> transients from the background noise (Fig. 3a).

The high Ca<sup>2+</sup> sensitivity of the TnC-based sensor both *in vivo* and *in vitro* are in clear contrast to results obtained with the analogous cameleons, which have consistently shown a marked reduction in Ca<sup>2+</sup> sensitivity in transgenic mice<sup>3,4</sup>. Cameleons use the interaction of calmodulin (CaM) with the CaM binding peptide M13. Calmodulin, however, is highly regulated by phosphorylation and sequestration by a plethora of CaM binding proteins<sup>10,11</sup>. These uncontrolled intracellular interactions may explain difficulties in obtaining full functionality of various CaM-based Ca<sup>2+</sup> sensors expressed in the mouse as well as cell-type to cell-type variations in performance<sup>4,5</sup>. The cellular expression pattern of CerTN-L15—bright dendrites (Fig. 3b,c) and dye-free nuclei—renders this indicator particularly suitable for dendritic recordings, and complements other methods such as bolus labeling of cells with small-molecule indicators<sup>12,13</sup>, which allows good staining of cell somata but not of dendrites.

In conclusion, the new FCIP mouse line provides important improvements for the analysis of Ca<sup>2+</sup> signaling in the intact brain. These include (i) a homogeneous and bright staining of the entire cytosol of individual neurons down to secondary and tertiary dendrites, (ii) the full functionality of the sensor protein allowing

measurement of small suprathreshold depolarizations consisting of as few as 2–3 action potentials, (iii) the linear response properties of CerTN-L15 within a physiologically relevant activity range, and (iv) the possibility of *in vivo* Ca<sup>2+</sup> imaging with single-cell and even subcellular resolution.

*Note: Supplementary information is available on the Nature Methods website.*

#### ACKNOWLEDGMENTS

We thank M. Bösl for doing pronucleus injections, and A. Schulze-Schenke and S. Direnberger for assistance. Supported by grants of the Deutsche Forschungsgemeinschaft (SFB 391 and SFB 596) and the Bundesministerium für Bildung und Forschung (NGFN-2).

#### AUTHOR CONTRIBUTIONS

N.H., M.W.F., M.M. and O.G. generated transgenic mice and performed biochemical and spectroscopic characterization; O.Ga., R.I.M., Y.K. and A.K. performed electrophysiology and two-photon imaging.

#### COMPETING INTERESTS STATEMENT

The authors declare that they have no competing financial interests.

Published online at <http://www.nature.com/naturemethods/>  
Reprints and permissions information is available online at  
<http://npg.nature.com/reprintsandpermissions>

- Zhang, J., Campbell, R.E., Ting, A.Y. & Tsien, R.Y. *Nat. Rev. Mol. Cell Biol.* **3**, 906–918 (2002).
- Miyawaki, A. *Neuron* **48**, 189–199 (2005).
- Nagai, T., Yamada, S., Tominaga, T., Ichikawa, M. & Miyawaki, A. *Proc. Natl. Acad. Sci. USA* **101**, 10554–10559 (2004).
- Hasan, M.T. *et al. PLoS Biol.* **2**, 763–775 (2004).
- Diez-Garcia, J. *et al. Eur. J. Neurosci.* **22**, 627–635 (2005).
- Heim, N. & Griesbeck, O. *J. Biol. Chem.* **279**, 14280–14286 (2004).
- Rizzo, M.A., Springer, G.H., Granada, B. & Piston, D.W. *Nat. Biotechnol.* **22**, 445–449 (2004).
- Griesbeck, O., Baird, G.S., Campbell, R.E., Zacharias, D.A. & Tsien, R.Y. *J. Biol. Chem.* **276**, 29188–29194 (2001).
- Caroni, P. *J. Neurosci. Methods* **71**, 3–9 (1997).
- Jurado, L.A., Chockalingam, P.S. & Jarrett, H.W. *Physiol. Rev.* **79**, 661–682 (1999).
- Benaim, G. & Villalobo, A. *Eur. J. Biochem.* **269**, 3619–3631 (2002).
- Garaschuk, O., Milos, R.I. & Konnerth, A. *Nat. Protocols* **1**, 380–386 (2006).
- Stosiek, C., Garaschuk, O., Holthoff, K. & Konnerth, A. *Proc. Natl. Acad. Sci. USA* **100**, 7319–7324 (2003).

# Appendix B

## Curriculum Vitae

### Personal Data:

Name:	Ruxandra-Iulia Miloş
Date of Birth:	03.07.1977
Place of Birth:	Timisoara (Temeschburg), Romania
Marital Status:	married

---

### Education:

09 / 1984 - 06 / 1992	General School No. 22, Timisoara, Romania
09 / 1992 - 06 / 1996	“Colegiul Banatean” High School, Timisoara, Romania
7 / 1996	School leaving examination (Abitur)
10 / 1996 - 09 / 2002	University of Medicine and Pharmacy “Victor Babes” Timisoara, Romania, Faculty of General Medicine
10 / 1999 - 09 / 2004	University of Medicine and Pharmacy “Victor Babes” Timisoara Romania, Faculty of Physiokinetotherapy

---

### Experience:

07 / 2001 - 08 / 2001	internship at the Hospital de Santa Maria, University of Lisbon, Portugal
10 / 2002 - 03 / 2003	doctoral study in the Department of Pathophysiology, University of Medicine and Pharmacy “Victor Babes” Timisoara, Romania
04 / 2003 - 03 / 2004	Marie Curie Fellow at Marie Curie Training Site „Cellular Signalling in Human Diseases”, Ludwig-Maximilians- University Munich, Germany
04 / 2004 - 12 / 2005	doctoral study in the Institute for Cellular Physiology, Faculty of Medicine, Ludwig-Maximilians-University Munich, Germany
01 / 2006 - 09 / 2007	doctoral study in the Institute for Neuroscience, Faculty of Medicine, Technical University, Munich, Germany
01 / 2008	resident in Radiology, Emergency County Hospital Timisoara, Romania

## Acknowledgements:

This work was carried out under the supervision of Prof. Dr. Arthur Konnerth and Prof. Dr. Olga Garaschuk. My special thanks go to Professor Arthur Konnerth for his exceptional generosity in offering me the possibility to get a top research training in the field of neuroscience, for his encouragement to learn innovative and new techniques, for the discussions we had, that taught me how to critically evaluate scientific results and not the last, for his constant effort to support and develop new scientific projects in Timisoara.

I want to warmly thank Professor Olga Garaschuk for her mentorship, for teaching me the discipline and accuracy essentially requested in producing valuable scientific results and in the art of describing them suitably, for her advices and help in solving difficult technical or theoretical problems, as well as for her outstanding personal commitment and support.

I am deeply grateful to Professor Helmuth Adelsberger, who, at the beginning of my training, introduced me in the basics of neuroscience and calcium imaging, and offered me constantly, during my entire stay in the lab, his great personal support and encouragement.

I want to thank also Professor Alexandru Cristescu, the first coordinator of my doctoral thesis from the Pathophysiology Department of the Medical University in Timisoara, all members of the Institute for Neuroscience of the Technical University in Munich and The Marie Curie Fellowships for funding me during the first year of my doctoral study.

Personal thanks go to all my friends in Munich who created for me the greatest atmosphere to work and enjoy my staying in this beautiful town and to my family, who always did the best for me. In particular, I am grateful to my grandfather, who taught me that no other profession is more beautiful than medicine and to whom I want to dedicate this work.